Structure-Function Relationships of Membrane Proteins - Spectroelectrochemical Investigation of Artificial Membranes

vorgelegt von
Diplom-Chemiker
Jacek Artur Kozuch
aus Lublinitz

von der Fakultät II – Mathematik und Naturwissenschaften
der Technischen Universität Berlin
zur Erlangung des akademischen Grades

Doktor der Naturwissenschaften
– Dr. rer. nat. –

genehmigte Dissertation

Promotionsausschuss:

Vorsitzender:	Prof. Dr. Reinhard Schomäcker
Berichter:	Prof. Dr. Peter Hildebrandt
Berichter:	Prof. Dr. Claudia Steinem

Tag der wissenschaftlichen Aussprache: 30.11.2012

Berlin 2013
D 83

Moim rodzicom

Follow your passion...

Abstract

Membrane proteins exert a variety of fundamental functions, such as proton and electron transfer, voltage-gated ion translocation and enzymatic reactions. Since most of these processes can be monitored and controlled by electrochemical techniques, substantial efforts have been made to engineer membrane models on electrodes, providing a biocompatible environment for membrane proteins, e.g. tethered bilayer lipid membranes (tBLMs).

To date, electrochemical impedance spectroscopy (EIS) has been extensively used to study integral proteins in such devices. However, this methodology cannot provide structural insights, which are required to understand the molecular basis of the proteins' functions. To overcome this limitation, in this work, surface-enhanced infrared absorption (SEIRA) spectroscopy, combined with EIS, was applied. Here a nanostructured Au film, the supporting material for the tBLM, served as the IR signal amplifier of adsorbed molecules and as the working electrode in the same setup.

In this work, for the first time, the assembly of stable tBLMs on nanostructured Au films is demonstrated, allowing for the structural and functional spectroelectrochemical characterization of a membrane-embedded protein. The tBLM, composed of (cholesterylpolyethylenoxy)thiol (CPEO3), 6-mercaptohexanol (6MH), and 1-palmitoyl-2-oleoyl-sn-glycero-3-phosphocholine (POPC), showed a capacitance of C_{tBLM} = 0.6 - 0.7 μF cm^{-2} and, due to the presence of inevitable defects, a moderate resistance of R_{Bilayer} = (21 $\pm$ 2) kΩ cm^2. The combined spectroscopic and electrochemical analysis provided novel insight into molecular details of the formation process of the tBLM, revealing a two-step process of vesicle adsorption onto 6MH fragments and the spreading to cover the CPEO3 SAM.

As a proof-of-concept, the cation-channel forming peptide gramicidin A (gA) was integrated into the tBLMs and analyzed in terms of specific cation-peptide and cation-lipid interactions that are essential for the function of the channel-forming gA and the membrane structure, respectively. On the basis of EIS and SEIRA spectroscopy, the functionality of gA, acting as an ion channel for monovalent cations, was analyzed and correlated to the structural alterations.

The combined approach was further extended to the human voltage-gated anion channel (hVDAC) which, besides its central key role in apoptosis, is proposed to be involved in the voltage-controlled ion flux across the membrane. This protein was used to study the direct proteo-tBLM formation from hVDAC-containing vesicles, the suitability of this tBLM system for potential-dependent SEIRA difference spectroscopy, and the mechanism of voltage-gating. Fusion and spreading of hVDAC-containing vesicles result in tBLMs with capacitances and resistances of C_{tBLM} = 0.6 - 0.7 μF cm^{-2} and R_{Bilayer} = (14 $\pm$ 2) kΩ cm^2, respectively, as well as in potential-dependent variations of the bilayer resistance. The results prove the presence of hVDAC within the POPC-POPC bilayer fragments of the tBLM. Potential-dependent SEIRA difference spectra demonstrate the motion of the bilayer towards or away from the Au surface for positive and negative potential differences, respectively. In addition, small potential-dependent changes of the protein structure were observed pointing at a mechanism of voltage-gating that involves a distortion of the β-barrel structure. This structural change may be caused either by elongation and compression (for positive and negative potentials) of the channel or by bending of the hVDAC-bilayer network leading to a cone-shaped structure. Both hypotheses are in line with the asymmetry of voltage-gating, however, only the latter describes the low gating probability reported previously.

Altogether, the present study has demonstrated the great potential of the combined EIS/SEIRA approach for studying structure-function relationships of membrane proteins.

Zusammenfassung

Membranproteine üben eine Vielzahl fundamentaler Funktionen aus, wie z. B. den Protonen- und Elektronentransfer, den spannungsgesteuerten Ionentransport oder enzymatische Reaktionen. Da diese Prozesse in der Regel mit elektrochemischen Techniken untersucht werden können, wurden verschiedene Membranmodelle entwickelt, um eine biokompatible Umgebung für die Rekonstitution von Membranproteinen auf Elektroden zu schaffen. Besonders interessant sind dabei die trägerfixierten Lipiddoppelschichtmembranen (tethered bilayer lipid membranes - tBLMs).

Bislang wurde überwiegend die elektrochemische Impedanzspektroskopie (EIS) für die Untersuchung von membrangebundenen Proteinen verwendet. Diese Methode liefert allerdings keine strukturellen Informationen, die für das Verständnis der molekularen Grundlagen der biologischen Prozesse erforderlich sind. In dieser Arbeit wurde daher, in Kombination mit der EIS, die oberflächenverstärkte Infrarotabsorptions-Spektroskopie (surface-enhanced infrared absorption - SEIRA) eingesetzt. Bei dieser Technik dient ein nanostrukturierter Au Film, der als Träger der tBLMs verwendet wird, sowohl als IR-Signalverstärker wie auch als Arbeitselektrode in einer elektrochemischen Zelle.

Die vorliegende Arbeit zeigt erstmals den Aufbau einer stabilen tBLM auf einer nanostrukturierten Au-Schicht und ihre Verwendung für die spektroelektrochemische Charakterisierung der Struktur und Funktion von membrangebundenen Proteinen. Die tBLM, aufgebaut aus (Cholesterylpolyethylenoxy)thiol (CPEO3), 6-Mercaptohexanol (6-MH) und 1-Palmitoyl-2-oleoyl-sn-glycero-3-phosphocholin (POPC), wies eine spezifische Kapazität von $C_{\mathrm{tBLM}} = 0.6$ - $0.7\ \mu\mathrm{F\ cm}^{-2}$ und, aufgrund der unvermeidbaren Defekte, moderate Widerstände von $R_{\mathrm{Bilayer}} = (21 \pm 2)\ \mathrm{k\Omega\ cm}^2$ auf. Die spektroelektrochemische Untersuchung der tBLMs lieferte neue Informationen zum Prozess der tBLM-Bildung, der mit der Adsorption der Vesikel auf 6MH-besetzten Bereichen und der nachfolgenden Spreitung und Benetzung des CPEO3-SAMs in zwei Schritten abläuft.

Als "Proof-of-Concept" wurde das Peptid Gramicidin A (gA), das kationenselektive Kanäle bildet, in die tBLM eingebaut und EIS/SEIRA-spektroskopisch hinsichtlich der spezifischen Kation-Peptid- und Kation-Lipid-Wechselwirkungen untersucht, die essentiell für die Funktion des Ionenkanals und die Struktur der Membran sind. Dabei konnten die funktionellen und strukturellen Eigenschaften des gA korreliert werden.

Der kombinierte spektroskopisch-elektrochemische Ansatz wurde zudem auf die Untersuchung des spannungsgesteuerten Anionenkanals (human voltage-gated anion channel - hVDAC) ausgedehnt, der neben seiner Rolle in der Apoptose den Ionentransport über die äußere Mitochondrienmembran spannungsabhängig zu steuern scheint. Die Arbeiten am hVDAC zielten darauf ab, die direkte Bildung von Proteo-tBLMs durch Spreiten von hVDAC-rekonstituierten Vesikeln, den Mechanismus des spannungsabhängigen Ionentransports und die Anwendbarkeit dieses tBLM-Systems für die spannungsabhängige SEIRA Differenzspektroskopie zu untersuchen. Das Spreiten der hVDAC-POPC-Vesikel resultierte in tBLMs mit Kapazitäten und Widerständen von $C_{\mathrm{tBLM}} = 0.6$ - $0.7\ \mu\mathrm{F\ cm}^{-2}$ und $R_{\mathrm{Bilayer}} = (14 \pm 2)\ \mathrm{k\Omega\ cm}^2$ und spannungsabhängigen Variationen des tBLM Widerstandes. Die Ergebnisse beweisen die Integration von hVDAC in die POPC-POPC Doppelschichtfragmente der tBLM. Potentialabhängige SEIRA Differenzspektren zeigen die Bewegung

der Doppelschichten bei positiven Potentialdifferenzen zur Au Elektrode hin und bei negativen von ihr weg. Zusätzlich lassen die SEIRA-spektroskopischen Resultate auf eine spannungsabhängige Verzerrung der β-Barrelstruktur schließen. Diese kann zum einen auf einer Dehnung bei positiven und einer Kompression bei negativen Potentialen des hVDAC-Doppelschichtnetzwerks oder zum anderen auf dessen Krümmung beruhen, welche zu einer keilförmigen Struktur des Kanals führt. Beide Hypothesen stimmen mit der Asymmetrie des spannungsabhängigen Schließens von hVDAC überein. Letztere erklärt zusätzlich auch die niedrige Schließwahrscheinlichkeit von hVDAC.

Insgesamt demonstriert die vorliegende Arbeit das große Potential des kombinierten EIS/SEIRA-spektroskopischen Ansatzes für die Untersuchung von Struktur-Funktions-Beziehungen in Membranproteinen.

Publications

Parts of this work are published in the following articles:

1. Kozuch, J.; Steinem, C.; Hildebrandt, P.; Millo, D. Combined Electrochemistry and Surface-enhanced Infrared Absorption Spectroscopy of Gramicidin A Incorporated into Tethered Bilayer Lipid Membranes. *Angew. Chem.* **2012**, 51, 8114–8117.
2. Kozuch, J.; Weichbrodt, C.; Steinem, C.; Hildebrandt, P.; Millo, D. SEIRA spectro-electrochemical Investigation of Human Voltage-Gated Anion Channel Incorporated into tBLMs. **2012**, *in prepareation*.

Other publications in peer-reviewed journals:

1. Sivanesan, A.; Ly, H. K.; Kozuch, J.; Sezer, M.; Kuhlmann, U.; Fischer, A.; Weidinger, I. M. Functionalized Ag nanoparticles with tunable optical properties for selective protein analysis. *Chem. Commun.* **2011**, 47, 3553–3555.
2. Sivanesan, A.; Kozuch, J.; Ly, H K.; Kalaivani, G.; Fischer, A.; Weidinger, I. M. Tailored silica coated Ag nanoparticles for non-invasive surface enhanced Raman spectroscopy of biomolecular targets. *RSC Adv* **2012**, 2, 805-808.
3. Kozuch, J.; von der Hocht, I.; Hilbers, F.; Michel, H.; Weidinger, I. Resonance Raman Characterization of Novel Artificial Intermediates of Cytochrome c Oxidase from *Paracoccus Denitrificans*. **2012** *in prepareation*.

Oral presentation:

1. *"Merging functional and structural information on membrane proteins: Combined Electrochemistry and Surface-enhanced Infrared Absorption of Gramicidin A Incorporated into Tethered Bilayer Lipid Membranes"*, Campus d'exellència internacional catalunya sud (CEICS) Nobel Campus, July 1st - 4th, 2012, Tarragona (Spain).
2. *"Combined Electrochemistry and Surface-enhanced Infrared Absorption of Gramicidin A Incorporated into Tethered Bilayer Lipid Membranes"*, Berlin International Graduate School of Natural Sciences and Engineering (Big-NSE) Mid-term Symposium, March 12th, 2012, Berlin (Germany).
3. *"Biomimetic Membranes for Vibrational Spectroscopic Investigations of Membrane Proteins"*, Berlin International Graduate School of Natural Sciences and Engineering (Big-NSE) Mid-term Symposium, July 1st, 2011, Berlin (Germany).
4. *"Biomimetic Membranes for Vibrational Spectroscopic Investigations of Membrane Proteins"*, Berlin International Graduate School of Natural Sciences and Engineering (Big-NSE) PhD Proposal Workshop, October 9th, 2009, Berlin (Germany).

Poster contributions:

1. Engineering Lipid Bilayer, September 7th - 9th, 2012, Leeds (United Kingdom)
2. Campus d'exellència internacional catalunya sud (CEICS) Nobel Campus, July 1st - 4th, 2012, Tarragona (Spain)
3. ISSHC XV: International Symposium on the Relations between Heterogeneous and Homogeneous Catalysis, September 11th - 16th, 2011, Berlin (Germany)
4. Unifying Concepts in Catalysis (UniCat) Colloquium, May 20th, 2010, Berlin (Germany)

Contents

Abstract III

Zusammenfassung V

Publications VII

Contents XI

Abbreviations XIII

1. Introduction and Motivation 1

I. Theoretical Background 5

2. Theory 7
- 2.1. Vibrational Spectroscopy 7
  - 2.1.1. Theory of Vibrational Spectroscopy 7
  - 2.1.2. Infrared Spectroscopy 11
    - 2.1.2.1. Fourier Transform Infrared Spectroscopy 11
    - 2.1.2.2. Attenuated Total Reflexion-Infrared Spectroscopy 13
    - 2.1.2.3. Surface-enhanced Infrared Absorption Spectroscopy 14
- 2.2. Electrochemical Impedance Spectroscopy 16
  - 2.2.1. Electrode Interfaces 16
  - 2.2.2. The Theory of Electrochemical Impedance Spectroscopy 17
    - 2.2.2.1. The Electrical Impedance 18
    - 2.2.2.2. Representations of Impedance Spectra 19
    - 2.2.2.3. Evaluation and Physical Relevance of tBLMs 20

3. Artificial Membrane Systems 25
- 3.1. Structure and Assembly of Lipids 25
  - 3.1.1. Phospholipids 26
  - 3.1.2. Self-assembly of Phospholipids 26
  - 3.1.3. The Transmembrane Potential 28
- 3.2. Solid-Supported Membranes 29
  - 3.2.1. Tethered Bilayer Lipid Membranes 31
- 3.3. Infrared Spectroscopy of Phospholipid Membranes 33

4. Membrane Proteins 35
- 4.1. Structure of proteins 35
  - 4.1.1. Infrared Spectroscopy of Proteins 36

4.2. Gramicidin A from *Bacillus brevis* 41
  4.2.1. Polymorphism of Gramicidin A 43
    4.2.1.1. Double Helix - The Pore 43
    4.2.1.2. Helix Dimer - The Channel 44
  4.2.2. Infrared Spectroscopy of Gramicidin A 46
4.3. Human Voltage-Gated Anion Channel 47
  4.3.1. Structure of the Human Voltage-Gated Anion Channel 49
  4.3.2. Infrared Spectroscopy of the Human Voltage-Gated Anion Channel 50

II. Experimental Section 53

5. Experimental Details 55
5.1. Chemicals and Preparation Tools 55
5.2. Instrumentation 56
  5.2.1. Surface-Enhanced Infrared Absorption Spectroscopy 56
  5.2.2. Electrochemistry 57
5.3. Preparation 60
  5.3.1. Membrane Proteins Incorporated into tBLMs 60
5.4. Execution of Experiments 61
  5.4.1. Spectroelectrochemistry of Membrane Proteins Incorporated into tBLMs 61

III. Results and Conclusions 65

6. Results 67
6.1. Construction of tBLMs on the nanostructured SEIRA Au film 67
  6.1.1. Formation of the CPEO3/6MH SAM 68
    6.1.1.1. EIS of CPEO3/6MH SAMs 68
    6.1.1.2. SEIRA spectroscopy of CPEO3/6MH SAMs 71
  6.1.2. Formation of tBLMs on nanostructured Au 73
  6.1.3. Summary 82
6.2. Spectroelectrochemistry of gA Incorporated into tBLMs 84
  6.2.1. Incorporation of gA into tBLMs 84
  6.2.2. Structure-Function Relationship of tBLM-embedded gA 91
  6.2.3. Cation-Phospholipid Interactions 95
  6.2.4. Summary 95
6.3. Spectroelectrochemistry of hVDAC Incorporated into tBLMs 97
  6.3.1. Formation of hVDAC-containing tBLMs 97
  6.3.2. Structure-Function Relationship of hVDAC in tBLMs 104
  6.3.3. Summary and Discussion 111

7. Conclusions 113

Bibliography 117

Acknowledgements 125

Abbreviations

6MH	6-mercaptohexanol
AFM	atomic force microscopy
ATR	attenuated total reflexion
CD	circular dichroism
CPE	constant phase element
CPEO3	(cholesterylpolyethyleneoxy)thiol
DMPC	1,2-dimyristoyl-sn-glycero-3-phosphocholine
ECT	electrochemical treatment
EIS	electrochemical impedance spectroscopy
EM	electromagnetic
FT	Fourier transform
FTIR	Fourier transform infrared
gA	gramicidin A
hVDAC	human voltage-gated anion channel
IR	infrared
IRE	internal reflexion element
lh	left-handed
lt	lipid-tethered
MIM	mitochondrial inner membrane
MOM	mitochondrial outer membrane
NMR	nuclear magnetic resonance
OCP	open circuit potential
OD	optical density
PL	phospholipid
POPC	1-palmitoyl-2-oleyl-sn-glycero-3-phosphatidylcholine
pt	protein-tethered
PZC	potential of zero charge
QCM	quartz-crystal microbalance
rh	right-handed
RR	resonance Raman
SAM	self-assembled monolayer
SDS	sodium dodecyl sulfate
SEIRA	surface-enhanced infrared absorption
SER	surface-enhanced Raman
SERR	surface-enhanced resonance Raman
SPR	surface-plasmon resonance
SSM	solid-supported membrane
tBLM	tethered bilayer lipid membrane

1. Introduction and Motivation

Membrane proteins play an essential role in life. They are responsible for a wide range of fundamental functions, such as proton and electron transfer, voltage-gated ion or metabolite translocation, and enzymatic reactions. Furthermore, they represent the target of more than 45 % of currently used drugs.[1] Therefore, the understanding of structure-function relationships of membrane proteins is of utmost importance for elucidating the molecular basis of essential biological processes, not only in fundamental and but also in applied life sciences.[2] Prominent examples for applications of biological systems range from clean energy conversion and storage to the design and screening of novel pharmaceutical agents. In any case, it is a prerequisite to preserve the structure and function of the target protein which usually requires its incorporation into a lipid bilayer membrane as its (quasi-)native environment. The bilayer matrix plays a crucial role in stabilizing the three-dimensional structure of the protein as well as for controlling the function, e.g. via generating and modulating transmembrane potentials or formation of domains which allow for specific lipid-protein interactions.

In the past decades, vibrational spectroscopy has made substantial contributions to elucidate the molecular mechanisms of biological processes. Unlike other methods, Raman and in particular infrared (IR) spectroscopy represent non-invasive techniques providing molecular structure information with high temporal resolution. They allow for the investigation of the dynamics of molecular processes with a sensitivity to structural details that goes beyond that of X-ray crystallography. As an additional advantage, application of vibrational spectroscopies is not restricted to highly purified samples like other techniques in structural biology but can be employed under quite different experimental conditions such as solutions, solid phase, and interfaces. Accordingly, they are ideal tools for probing structure and reactions of membrane proteins in biomimetic devices that mimic the native biological environment. These are in particular membrane models that allow for peripheral or integral immobilization of proteins.[3,4] So far, these constructs were usually characterized by electrochemical techniques, such as protein-film voltammetry or electrochemical impedance spectroscopy, and imaging methods including atomic force and fluorescence microscopy, whereas vibrational spectroscopies have only rarely been applied. Since potential-dependent processes such as redox reactions, voltage-gated mass transfer, or the modulation of the activity due to changes of the transmembrane potential, are nearly ubiquitously present in biological systems, so-called tethered bilayer lipid membranes (tBLMs) assembled on a conductive support, e.g. a Au electrode, are particularly interesting membrane models. Applying vibrational spectroscopies to study proteins in such devices is, however, a considerable challenge since conventional IR and Raman spectroscopy lack the sensitivity for molecular targets at sub-monolayer coverages.

This drawback can be overcome by exploiting the surface enhancement of radiation provided by nanostructured noble metals. Specifically, surface-enhanced infrared absorption (SEIRA) spectroscopy is ideally suited in this respect since optimum enhancement of the IR signals is obtained for molecules in the vicinity of nanostructured Au surfaces[5] a metal that is often used as a solid support for tBLMs. Depositing a signal-amplifying nanostructured Au film on a silicon prism, which is used as the optical element in attenuated total reflection (ATR) IR spectroscopy, SEIRA spectroscopy solely probes the molecules close to the solid surface without inference from the bulk species. Furthermore, the Au film can be used as the working electrode in an electrochemical setup. In this way, electrochemical and spectroscopic data can be obtained from protein (sub-)monolayers at the same time. However, the nanostructured surface morphology of the Au film is both a blessing and a curse at the same time, since, to date, the roughness has impeded the construction of a closed bilayer lipid membrane.

In this work, for the first, a time stable tBLM was assembled on nanostructured SEIRA-active Au films and applied to study formation and properties of the phospholipid bilayer, the incorporation of membrane proteins, and their function within this biomimetic construct. The former is comprised of extracting crucial parameters such as the composition of the self-assembled monolayer (SAM). Here, the lipid-tether (cholesterylpolyethyleneoxy)thiol (CPEO3) was used together with the short hydrophilic-headed spacer 6-mercaptohexanol (6MH) to provide a stable CPOE3-supported system coexisting with quasi free-standing phospholipid-phospholipid bilayer fragments for the insertion of membrane proteins. To examine the suitability of these tBLMs to act as realistic model membranes for functional and structural investigations, gramicidin A (gA) was incorporated into these tBLMs as a proof-of-concept. GA is a linear pentadecapeptide that is involved in gene regulation and, thus, in engendering the transition between vegetative growth and sporulation of its host organism *Bacillus brevis*. Furthermore, gA is known for its antibacterial activity and was found to exhibit anti-HIV antiviral properties.[6] Besides its original and clinical importance, the peptide has attracted the attention of scientists due to its property of forming various helical structures. In particular, the helical dimer structure, adopted in bilayer membranes and denoted as a channel, was subject of extensive investigations. This conformation is capable of translocating specifically monovalent cations across the bilayer membrane with increasing conductance for higher ionic radii.

A second system studied in this work is the human voltage-gated anion channel (hVDAC) also known as the mitochondrial porin. This channel is located in the mitochondrial outer membrane and is the main gate keeper for the exchange of metabolites between mitochondria and the cytosol. Furthermore, hVDAC plays an essential role in mitochondria-mediated apoptosis and, thus, in cellular decision of life and death. Thus, this protein represents an important player in several diseases, neurodegenerative disorders, and viral infections ranging from cancer and Parkinson's diseases to Hepatitis B.[7] Electrochemical experiments performed in artificial membranes, revealed a further function, i.e. the voltage-gated transduction of ions across the membrane. The mechanism of the voltage-gating and the question why only a minority of incorporated channels respond to potentials is still matter of debate.

This work is comprised of 3 parts focusing on the theoretical background, experimental section, and the results and conclusions. The first part outlines the theoretical basics of the methods used in this work, i.e. electrochemical impedance spectroscopy (EIS) and SEIRA spectroscopy (chapter 2). Furthermore, artificial membrane systems (chapter 3) and membrane proteins (chapter 4) in general as well as specifically within the concept of tBLMs (section 3.2.1) are reviewed, complemented by a description of gA and hVDAC (sections 4.2 and 4.3, respectively). The second part deals with the experimental approaches and setups (chapter 5). The third part of this work presents the results and conclusions (chapter 6). The focus is laid on the construction of the tBLM system on the nanostructured SEIRA-acitve Au film and the application of the spectroelectrochemical SEIRA approach for studying artificial membrane systems. In section 6.1, the formation of tBLMs is characterized and the process of vesicle fusion and spreading is investigated. In the next step, gA is incorporated to demonstrate the suitability of this artificial membrane sys- tem for investigating structure-function relationships of transmembrane proteins (section 6.2). In addition to the analysis of the spontaneous incorporation process, the cation-peptide and cation-lipid interactions, essential for the functionality of transmembrane channels, were studied. In section

6.3, these investigations were extended to the voltage-gated pore hVDAC. First, the CPEO3-supported tBLM was examined for its suitability to employ potential-dependent SEIRA difference spectroscopy. Furthermore, the immobilization of hVDAC by spreading of hVDAC-containing vesicles was monitored by this spectroelectrochemical approach demonstrating the presence of hVDAC inside the quasi free-standing 6MH-supported bilayer fragments. Finally, the functionality and the structural changes associated with voltage-gated channel closing was monitored by electrochemistry and SEIRA spectroscopy. Chapter 7 summarizes the results and presents the conclusions.

Part I.

Theoretical Background

2. Theory

2.1. Vibrational Spectroscopy

In 1800, William Herschel laid the cornerstone for vibrational spectroscopy by discovering the infrared (IR) radiation in the spectrum of the sun. One century later, researchers began to analyze matter by its use, producing the first IR spectra and, by that, beginning to establish the technique of IR spectroscopy. In the 1920s, the discovery of the Raman effect by Chandrasekhara V. Raman gave birth to the second fundamental vibrational technique, Raman spectroscopy. However, due to the poor performance and sensitivity of the instruments, these techniques were used to study rather small molecules and inorganic materials.[8] In particular, the development of lasers, interferometers, as well as methods to purify biological samples finally allowed the application of vibrational spectroscopy in life sciences.

Nowadays, vibrational spectroscopy is among the most important techniques for the elucidation of structure-function relationships of biomolecules.[5] By the use of the resonance Raman (RR)[5] effect and the difference mode in IR spectroscopy (section 2.1.2.1 on page 11) it is possible to monitor structural features and even single bondings with a more detailed resolution than high-resolved crystal structures and without restrictions concerning the size of the sample. Moreover, these techniques can be combined with time-resolved experiments to study dynamic biological processes even in the time scale of femtoseconds.[9,10] Another advantage of vibrational spectroscopy is that it may be applied to solubilized, crystallized and immobilized molecules, whereby the latter is particularly interesting in the combination with the surface-sensitive techniques of surface-enhanced Raman (SER) and surface-enhanced infrared absorption (SEIRA) spectroscopy. These methodologies exploit the surface-enhancement of an appropriate metal surface acting also as electrode material and, thus, allow for the spectroelectrochemical characterization of protein monolayers.[11,12] In this work, SEIRA spectroscopy was used to study membrane-embedded proteins in a spectroelectrochemical manner.

2.1.1. Theory of Vibrational Spectroscopy

Vibrational spectroscopy is based on the interaction of electromagnetic radiation with matter which causes transitions between the vibrational states of molecules. This transitions may arise either from a resonant absorption of IR radiation (10 - 12500cm^{-1}) or from inelastic scattering.[5] The former takes place when the energy of a photon $h\nu_{\mathrm{IR}}$ of the polychromatic IR radiation matches the energy difference between an initial and final vibrational state ($h\nu_i$ and $h\nu_f$, respectively) and is the basis of IR spectroscopy:

$$h\nu_{\mathrm{IR}} = h\nu_f - h\nu_f. \tag{2.1}$$

In contrast to that, in Raman spectroscopy, monochromatic light is used to monitor the inelastic scattering. Due to the interaction with vibrational transitions, the energy of the scattered photons $h\nu_{\mathrm{R}}$ differs from that of the incident light $h\nu_0$:

$$h\nu_0 - h\nu_{\mathrm{R}} = h\nu_f - h\nu_i. \tag{2.2}$$

Both phenomena may be associated with rotational transitions that appear as a fine structure of the vibrational transition. However, as this effect might be resolved only in the gas phase, it is rather irrelevant for the study of biological samples. Since the IR absorption and Raman scattering differ in their underlying mechanisms, the information obtained from both techniques is, to some degree, complementary. Vibrational transitions are only IR-active when the excited vibrational mode is accompanied by a change of the dipole moment; Raman-active vibrations, however, exhibit a change of the polarizability. Due to this principle, IR and Raman spectra usually display different band patterns in respect to the relative intensities of the bands.

Molecular Vibrations Molecular vibrations can be described by the use of the model of the harmonic oscillator where the atoms are treated as point masses connected by mass-less springs.[13] The simplest case is the vibration of a diatomic molecule A-B. Here, the masses m_A and m_B are displaced along the x-axis from its equilibrium position by Δx. According to Hooke's law, $F_x = -f\Delta x$, the restoring force F_x antagonizes this movement due to the force constant f that reflects the strength of the bond. This treatment leads to the potential energy V of the vibrational motion:

$$V = \frac{1}{2} f \Delta x^2. \tag{2.3}$$

The kinetic energy of the atoms is dependent on the reduced mass $\mu = m_\mathrm{A} \cdot m_\mathrm{B} (m_\mathrm{A} + m_\mathrm{B})^{-1}$ and the velocity of their motions $\mathrm{d}\Delta x/\mathrm{d}t$:

$$T = \frac{1}{2} \mu \left(\frac{\mathrm{d}\Delta x}{\mathrm{d}t} \right)^2. \tag{2.4}$$

As the harmonic oscillator refers to an undamped vibration, the conservation of energy requires that the sum of the derivatives of the potential and kinetic energy equals zero

$$0 = \frac{\mathrm{d}V}{\mathrm{d}t} + \frac{\mathrm{d}T}{\mathrm{d}t} = f\Delta x + \mu \frac{\mathrm{d}^2\Delta x}{\mathrm{d}t^2} \tag{2.5}$$

and results in the Newton equation of motion

$$0 = \frac{f}{\mu}\Delta x + \frac{\mathrm{d}^2\Delta x}{\mathrm{d}t^2} \tag{2.6}$$

which can be solved by the cosine function

$$\Delta x = A \cdot \cos(\omega t + \theta). \tag{2.7}$$

Here, A, ω, and θ are the amplitude, the circular frequency, and the phase of the vibrational motion, respectively. Introducing equation 2.7 into 2.6 leads to a term describing the circular frequency:

$$\omega = \sqrt{\frac{f}{\mu}}. \tag{2.8}$$

It is common practice to express this term in wavenumbers (in cm^{-1}) which can be achieved by dividing the circular frequency with $2\pi c$ (here, c is the velocity of light):

$$\widetilde{\nu} = \frac{1}{2\pi c}\sqrt{\frac{f}{\mu}}. \tag{2.9}$$

This relation demonstrates very clearly that the wavenumber or frequency of a vibration increases with increasing bond strength and decreasing weight of the involved atoms.

Normal Modes The description of molecules containing more than two atoms represents a more elaborate subject. The maximum number of possible molecular vibrations can be calculated on the basis of the degrees of freedom of a molecule. Each atom might be displaced in three directions in space (in a Cartesian coordinate system), so that a molecule containing N atoms possesses $3N$ degrees of freedom. This number, however, has to be reduced by 6 degrees of freedom considering the translation and rotation in respect to the three axes in space, yielding in a total number of $3N-6$ vibrational degrees of freedom. Since linear molecules can rotate only in respect to two axes, they have $3N-5$ vibrational degrees of freedom. These vibrations are denoted as normal modes. To obtain the frequencies of the normal modes, the displacement of the Cartesian coordinates of all atoms of the molecule has to be considered. Here, the kinetic energy reads:

$$T=\frac{1}{2}\sum_{\alpha=1}^{N} m_\alpha \left[\left(\frac{\mathrm{d}\Delta x_\alpha}{\mathrm{d}t}\right)^2+\left(\frac{\mathrm{d}\Delta y_\alpha}{\mathrm{d}t}\right)^2+\left(\frac{\mathrm{d}\Delta z_\alpha}{\mathrm{d}t}\right)^2\right]. \tag{2.10}$$

By the use of the mass-weighted Cartesian displacement coordinates

$$q_i=\sqrt{m_i}\Delta x_i, \quad q_{i+1}=\sqrt{m_i}\Delta y_i, \quad q_{i+2}=\sqrt{m_i}\Delta z_i \quad \text{(for each atom } \alpha=i\text{)} \tag{2.11}$$

the expression for the kinetic energy gets simplified to

$$T=\frac{1}{2}\sum_{i=1}^{3N}\left(\frac{\mathrm{d}q_i}{\mathrm{d}t}\right)^2. \tag{2.12}$$

The potential energy is a more complex term as it involves all possible interaction between all atoms (covalent, but also electrostatic, van-der-Waals etc.) and can be expressed as a Taylor series:

$$V=V_0+\sum_{i=0}^{3N}\left(\frac{\partial V}{\partial q_i}\right)_0 q_i+\frac{1}{2}\sum_{i,j=1}^{3N}\left(\frac{\partial^2 V}{\partial q_i \partial q_i}\right)_0 q_i q_j+\ldots. \tag{2.13}$$

For the description of the vibrational potential energy, only changes in its value upon displacement of the atoms have to considered and, therefore, the first term (potential energy at the equilibrium) and the second term (as infinitesimal changes of q_i from the equilibrium position do not change V) are zero. According to the harmonic approximation, higher terms do not influence the potential energy substantially and can be neglected, so that V can be expressed as

$$V\approx\frac{1}{2}\sum_{i,j=1}^{3N}\left(\frac{\partial^2 V}{\partial q_i \partial q_i}\right)_0 q_i q_j=\frac{1}{2}\sum_{i,j=1}^{3N} f_{ij} q_i q_j. \tag{2.14}$$

In analogy to equation 2.6 the derivative of the kinetic and potential energy result in the Newton equation[5]

$$0=\frac{\mathrm{d}^2 q_j}{\mathrm{d}t^2}+\sum_{i=1}^{3N} f_{ij} q_i \tag{2.15}$$

comprised of $3N$ linear second order differential equations and its general solution

$$q_i=A_i\cos(\sqrt{\lambda}t+\theta). \tag{2.16}$$

Solving this system of differential equations leads to $3N$ solutions for λ representing $3N$ frequencies $\lambda^{\frac{1}{2}}$. 6 solutions (or 5, respectively; see section 2.1.1) equal zero as they refer to the translation and rotation of the molecule; $3N-6$ (or $3N-5$, respectively), however, yield the frequencies of the normal modes. With the knowledge of all frequencies, the amplitude of the displacement of each atom A_i for every normal mode can be calculated. Consequently, a normal mode presents an in-phase-oscillation of the entire molecule with a given frequency, but different amplitudes of certain segments of the molecule. As these amplitudes may differ substantially, these normal modes may be reduced approximately to the part of the molecule with the most pronounced motion, in some cases being ascribed to specific group vibrations or single bonds.

To simplify the description of the probability of vibrational transitions, the mass-weighted Cartesian coordinates can be converted into normal coordinates Q_k (for k normal modes) by the use of an orthogonal transformation

$$Q_k = \sum_{i=1}^{3N} l_{ik} q_i. \tag{2.17}$$

Choosing the transformation coefficient l_{ik} in such a way that T and V assume the shape of equations 2.12 and 2.14, and the potential energy does not depend on the cross products $Q_k \times Q_{k'}$ $(k \neq k')$ leads to the following solution of the Newton equation:

$$Q_k = K_k \cos(\sqrt{\lambda_k} t + \theta_k). \tag{2.18}$$

The Infrared Absorption As in other optical methods, the extent of the IR absorption is displayed as the absorbance A (in OD = optical density) by the use of the Lambert-Beer law:

$$A = -\lg\left(\frac{I}{I_{\mathrm{Ref}}}\right) = \varepsilon \cdot c \cdot d. \tag{2.19}$$

Here, I and I_{Ref} are the intensity of the IR radiation after passing through a solution with and without the analyte. On one hand the resulting absorbance is dependent on the conditions during the experiment reflected by the concentration c and the optical path length d and on the other hand on the molar absorption coefficient ε including the quantum mechanical probability of the transition between the initial and final vibrational state (see equation 2.1). The latter is given by the transition dipole moment

$$[\mu_q]_{if} = \langle \psi_f^* | \widehat{\mu}_q | \psi_i \rangle. \tag{2.20}$$

Here, ψ_f and ψ_i are the wave functions of the final and initial vibrational state and $\widehat{\mu}_q$ the operator of the electric dipole moment

$$\widehat{\mu}_q = \sum_{\alpha} e_\alpha \cdot q_\alpha. \tag{2.21}$$

with the charge e_α of the atom α and its distance q_α to the center of gravity of the molecule. By expanding the operator of the electric dipole moment $\widehat{\mu}_q$ in a Taylor series with respect to the normal coordinates Q_k the prerequisites for an IR-active absorption can be identified. For an harmonic oscillator only the linear terms of the Taylor series have to be considered, so that $\widehat{\mu}_q$ results in

$$\widehat{\mu}_q = \mu_q^0 + \sum_{k=1}^{3N-6} \widehat{\mu}_q^k \cdot Q_k \tag{2.22}$$

with

$$\widehat{\mu}_q^k = \left(\frac{\partial \mu_q}{\partial Q_k}\right)_0 . \tag{2.23}$$

In this way, the transition probability transforms into

$$[\mu_q]_{if} = \langle \psi_f^* | \widehat{\mu}_q | \psi_i \rangle = \mu_q^0 \langle \psi_f^* | \psi_i \rangle + \sum_{k=1}^{3N-6} \widehat{\mu}_q^k \langle \psi_f^* | Q_k | \psi_i \rangle . \tag{2.24}$$

Due to the orthogonality of the wavefunctions ψ_i and ψ_f, the first term of equation 2.24 equals zero and, therefore, only a non-zero transition probability (IR-active transition) is achieved when the second term is non-zero. This is only the case when (a) the electric dipole moment of the molecule changes during the vibrational displacement of the atoms ($\widehat{\mu}_q^k \neq 0$) and (b) the quantum number between the states i and f differ by one within the harmonic approximation ($< \psi_f^* | Q_k | \psi_i > \neq 0$). This consideration holds for all three Cartesian coordinates (q = x, y, z), so that the absorbance A of unpolarized light of randomly oriented molecules arises from the sum of the transition probabilities along all three components:

$$A \propto ([\mu_x]_{if}^2 + [\mu_y]_{if}^2 + [\mu_z]_{if}^2). \tag{2.25}$$

However, using linear polarized light on an oriented sample allows to address the individual components of the transition dipole moment $[\mu_q]_{if}$ and, by this, to obtain more detailed information about the studied system.

2.1.2. Infrared Spectroscopy

2.1.2.1. Fourier Transform Infrared Spectroscopy

The principle of the Fourier Transform (FT) IR Spectroscopy is applied in nearly all of today's IR spectrometers. Due to this approach, the measuring time can be drastically reduced, in contrast to the previous dispersive technique, leading to an improved signal-to-noise ratio.

The Michelson Interferometer A central building block of an FTIR spectrometer is the Michelson interferometer (figure 2.1) comprised of a beam splitter and two plane mirrors, i.e. a fixed and a movable mirror, oriented perpendicularly to each other. The beam splitter transmits and reflects the incoming polychromatic IR radiation, ideally divided in half, onto the two mirrors and subsequently recombines both beams directing the combined beam at the sample. With an optical path difference of $\delta = 0$, the distance between both mirrors and the beam splitter is equal leading to no phase difference between both beams and, therefore, the outgoing radiation equals the incoming one. Upon displacement of the movable mirror, however, the beams interfere with each other, so that each wavelength λ undergoes alternately constructive ($\delta = 2n \cdot \frac{1}{2}\lambda$) and destructive interference ($\delta = (2n+1) \cdot \frac{1}{2}\lambda$) and results in a δ-dependent cosinusoidal modulation reflecting the respective wavelength λ. The signal which is accumulated on the detector is a superposition of the cosine functions of all frequencies of the polychromatic IR radiation and is referred to as an interferogram (figure 2.1). Eventually, by the use of the Fourier transform, this optical path length dependent interferogram (time domain) is then transformed into a IR spectrum (frequency domain)

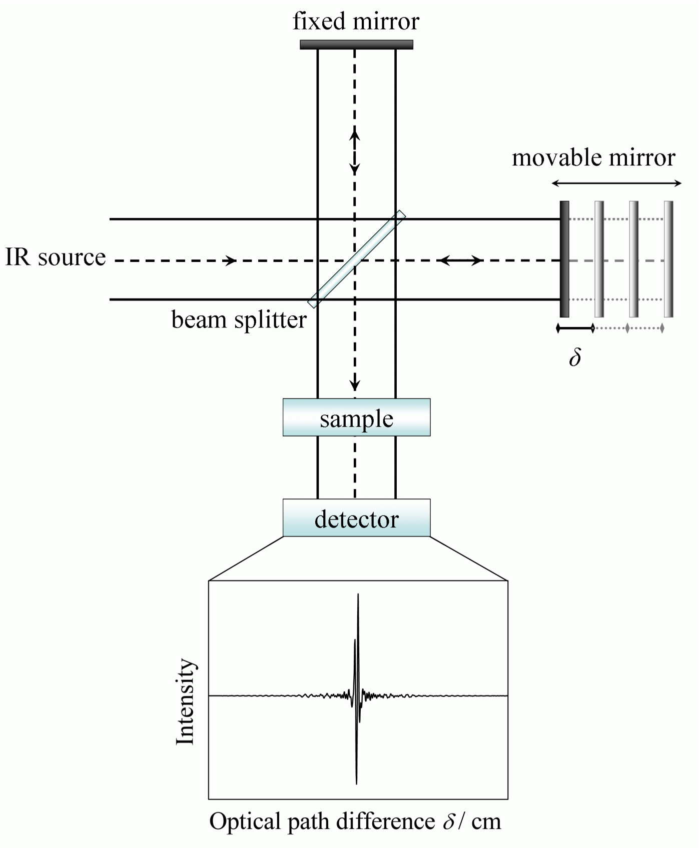

Figure 2.1: Michelson Interferometer: The IR radiation passes a beam splitter where it is divided into two parts and subsequently recombined directed at the sample. The movable mirror varies the optical path difference between the two beams generating an interferogram of the detected IR radiation

displaying the attenuation of the IR radiation depending on the wavenumber (reciprocal wavelength):

$$I(\widetilde{\nu}) = \int_{-\infty}^{+\infty} I(\delta)\cos(2\pi\widetilde{\nu})\mathrm{d}\delta. \tag{2.26}$$

This integral assumes an infinite motion of the movable mirror. Since the effective optical path difference is restricted to only a few centimeters, the interferogram has to be multiplied with an appropriate apodization function (i.e. a triangular function) to bring the edges of the interferogram smoothly to zero. With this procedure, artifacts in the spectrum are suppressed, but also the shape of spectral bands is manipulated.

Advantages of the Fourier Transform Infrared Spectroscopy FTIR spectroscopy presents several advantages over the dispersive approach:

- **Multiplex or Felgett advantage:** In dispersive spectrometers the complete noise intensity is recorded at each spectral data point. By the use of the FT, this total noise is distributed over the entire spectral range, so that the signal-to-noise ratio improves by $\sqrt{N}$ for an spectrum comprised of N elements.[5]
- **Throughput or Jacquinot advantage:** Due to the lack of a slit, that determines the resolution in dispersive devices and reduces the light throughput, large apertures can be used. By that, a largely increased amount of IR radiation reaches the detector not recording the intensity of single pixels but of the complete IR radiation spectrum.

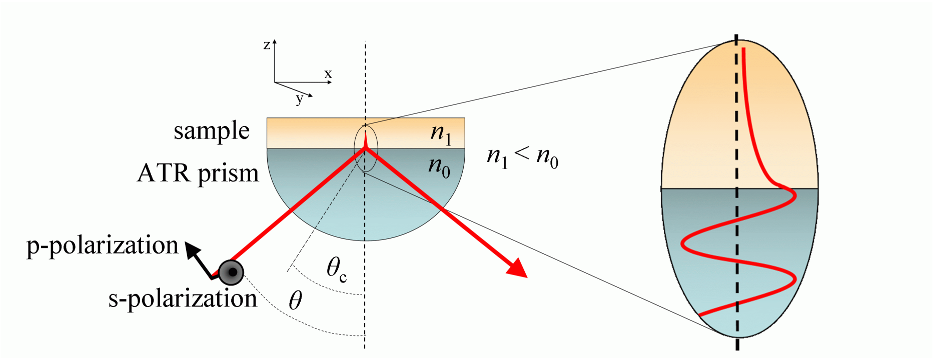

Figure 2.2: Schematic configuration for attenuated total reflexion-infrared (ATR-IR) spectroscopy. The incoming IR beam, composed of a perpendicular (s) and parallel (p) component (in respect to the plane of incidence) of the electromagnetic field, experiences total reflexion at the interface to an optically less dense medium, i.e. the sample, if the incident angle exceeds the critical angle θ_c

- **Connes advantage:** The simultaneously measured interferogram of a HeNe laser provides an internal calibration of the mirror position and, thus, the precise wavenumber of spectral features.

2.1.2.2. Attenuated Total Reflexion-Infrared Spectroscopy

In this work, the technique of surface-enhanced infrared absorption (SEIRA) was employed in the attenuated total reflexion (ATR) mode and, thus, a brief description of ATR-IR spectroscopy will be presented in this paragraph. Figure 2.2 presents a schematic representation of this approach comprised of the central building block, the internal reflection element (IRE) or ATR prism. As a general rule, the phenomenon of total reflexion only takes place at the interface to an optically less dense medium at an angle of incidence higher than the critical angle θ_c. Since the refractive index of biological systems lie in the region of $n_1 \sim 1.44$,[14] typically silicon ($n_{\mathrm{Si}} = 2.34$), germanium ($n_{\mathrm{Ge}} = 4.0$), or zinc selenide ($n_{\mathrm{ZnSe}} = 2.4$) are used as materials for the IRE.[5] A side effect of the total reflexion is the propagation of an evanescent wave through the interface into the less dense medium without carrying any energy. In this process, the amplitude of the electric field decays exponentially in the direction normal to the surface (i.e. in z-direction):

$$E = E_0 exp\left(-\frac{z}{d_{\mathrm{p}}}\right). \tag{2.27}$$

Here, d_{p} is the penetration depth at which the amplitude decayed to ca. 37 % ($\sim e^{-1}$) of its initial value and dependents on the angle of incidence θ, the wavelength of the radiation λ, and the ratio of the refractive indices n_1/n_0 (of the IRE and the optically rare medium, respectively):

$$d_{\mathrm{p}} = \frac{\lambda}{2\pi\sqrt{\sin^2\theta - \left(\frac{n_1}{n_0}\right)^2}}. \tag{2.28}$$

As a rule of thumb, the penetration depth lies in the range of the wavelength of the incident radiation. For instance, in the case of a Si prism, a incident angle of 60° (as used in this work), and a spectral region of 1000 to 4000 cm^{-1} (10 - 2.5 μm) the penetration depth of the evanescent wave is between 2.6 and 0.7 μm, respectively. An absorbing medium placed onto the surface of the IRE can couple with the electric field of the evanescent wave, absorb

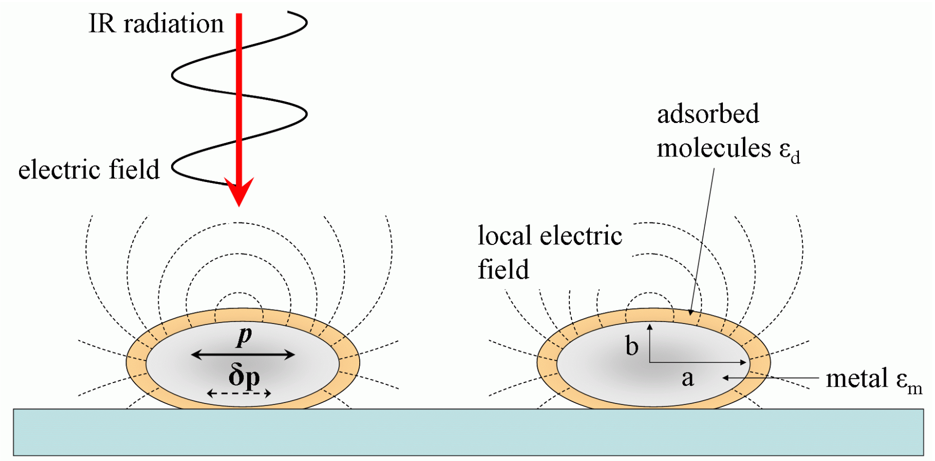

Figure 2.3: Schematic representation of the electromagnetic mechanism (EM) of surface-enhanced infrared absorption (SEIRA) originating from ellipsoidal metal particles. The electric field component of the incident IR radiation polarizes the metal islands. The dipole p generates an enhanced local electric field around the particles that excites the molecular vibrations of the absorbed molecules. Furthermore, the molecular vibrations induce an additional dipole δp and perturb the optical properties of the metal.

energy of the radiation and, thus, attenuate the total reflected beam. The parallel (p) and perpendicular (s) component of the incident radiation (in respect to the plane of incidence; see figure 2.2 cause a polarization of the evanescent wave in the x and z-directions, and in the y-direction.

The biggest advantage of the ATR technique is the accessibility to the studied sample that is put on the IRE. Therefore, the supernatant buffer solution can be exchanged very easily to study effects of the experimental conditions (pH, ionic strength etc.), binding of substrates, cofactors, and ligands or even reactions might be followed *in-situ*.[14] Furthermore, some samples such as membrane proteins can be oriented preferably on the IRE, so that additional information about the orientation of structural elements can be obtained by the use of polarized light.[15]

2.1.2.3. Surface-enhanced Infrared Absorption Spectroscopy

In 1980, Hartstein et al. discovered the surface-enhanced infrared absorption (SEIRA) effect in ATR-IR experiments of organic compounds adsorbed to Ag and Au films.[16] This effect, showing mechanistic similarities to surface-enhanced Raman scattering (SERS), yields enhancement factors of 10 to 1000 and selectively probes absorbed species in the vicinity of up to ca. 8 nm to the metal surface. Additionally, the Au film can also function as the working electrode for electrochemical investigations. With these prerequisites, SEIRA spectroscopy is very well suited for a wide range of applications including studies of biological systems.[17] To date, peripheral and integral membrane proteins, such as cytochrome c,[18] cytochrome c oxidase (CcO),[19] sensory rhodopsin II,[20] and hydrogenases,[21,22] were assembled by different approaches on nanostructured Au films and studied with electrochemistry and SEIRA in stationary and even time-resolved experiments, however, without the contribution of closed artificial membrane systems (see section 3.2 on page 29).[3,23]

Mechanisms of the Surface-Enhancement Similar as for SERS[5], surfaces composed of metal islands play a crucial role for the mechanism of the enhancement of SEIRA. Such a surface can be represented as an apposition of ellipsoidal metals particles depicted in figure

2.3. The total surface-enhancement in SEIRA, however, is provided by the sum of individual effects:[24,25]

- **Electromagnetic (EM) mechanism - plasmon resonance**
  The electric field of the incident IR radiation polarizes the metal islands by the excitation of collective electron resonances (localized plasmon modes). The dipole p, which is induced in the metal, generates a local EM field surrounding the particles. This induced local EM field is polarized perpendicularly to the surface at every point of the metal particle (surface selection rule) and its magnitude depends on the sixth power of the distance to the metal surface d

  $$|E_{\text{local}}|^2 = \frac{4p^2}{d^6} \tag{2.29}$$

  which is the origin for the short-range enhancement of this mechanism (up to ca. 8 nm from the surface). In this way, the enhancement factor F at a distance d to the surface of a nanoparticle with a radius of a_0 can be estimated to be

  $$F(d) = F(0) \cdot \left(\frac{a_0}{a_0 + d} \right)^6 . \tag{2.30}$$

  Adsorbed molecules can interact with this enhanced EM field and cause transitions between vibrational states. The extent of the enhancement is dependent on the dimensions and shape of the particles. Calculations using the Bruggemann effective medium theory have shown that ellipsoidal particles (high $\frac{a}{b} > 1$; see figure 2.3) yield larger enhancements.[26]

- **Electromagnetic (EM) mechanism - perturbation of optical properties of the metal**
  Additionally, the oscillating dipoles of adsorbed molecules can induce dipoles in the metal particles δp. This results in the change of the dielectric function of the metal and, thus, modulates the transmittance and reflectance of the metal film at the frequencies of the vibrations. Since the absorptivity of metals and its volume fraction is much larger than of the surface molecules, this will cause an effective enhancement of the IR absorption.

- **Chemical mechanism - donor-acceptor interaction and charge transfer**
  Molecules that are chemisorbed to metal surfaces experience larger enhancements than physisorbed ones. This can be understood on the basis of a donor-acceptor interaction between the adsorbate and the metal that changes the vibrational polarizability of the molecules. Furthermore, a charge transfer exhibited by charge oscillations between the molecular orbitals and the metal might increase the absorption coefficient.

- **Uniformal orientation**
  Chemisorption and physisorption often leads to an alignment of the molecular dipoles with a preferential orientation in respect to the metal surface. Due to the surface selection rule, vibrations perpendicularly oriented to the surface give rise to IR absorption that is three times higher than for the randomly oriented situation.

SEIRA employed in the ATR mode displays a strong dependence on the angle of incidence and the polarization of the IR radiation.[27] P-polarized IR radiation (see figure 2.2) leads to strongly enhanced IR signals that increase further using higher angles of incidence. The interaction with s-polarized IR radiation, however, does not yield any effective signal of the absorbed species. These characteristics of the setup for ATR-SEIRA spectroscopy are reviewed by Osawa.[28]

2.2. Electrochemical Impedance Spectroscopy

Since the mid-20th century, novel technological devices such as solid-state batteries, high-temperature electrochemical sensors, and fuel cells were developed at a fast pace. As a consequence, the characterization of solid-solid and solid-liquid interfaces became of major interest in the field of material sciences. Electrochemical Impedance Spectroscopy (EIS) is a powerful method that proved to be well-suited for this aim as it allows for the characterization of many electrical properties of materials and, even more importantly, of their interfaces with electronically conducting systems.[29] Even dynamic processes of bound and mobile charges may be investigated. Therefore, EIS experiments contribute to the understanding of important catalytic reactions such as the catalytic oxidation of methane[30] or ethene[31] using transition metals.

In recent decades, due to advances in the instrumentation, life sciences began to benefit from the advantages of EIS as well. Especially in the fields of biomedical research and the development of biosensors, this technique found increasing application,[32] as processes of biorecognition and modifications of target surfaces can be monitored in an non-invasive and label-free manner without the need of modifying biomolecules with fluorescence dyes, enzymes, redox or radioactive labels. In this way, for instance, researchers were able to follow the hybridization of DNA-strands on surfaces without the introduction of fluorescence labels that are unavoidable in other common methods.[33] However, this approach is not only restricted to biomolecules, such as DNA, enzymes or antibodies, whole cells can be studied as well. Asphahani et. al presented a platform on the basis of EIS that allows to monitor the response of cancer cells in consequence of the binding of the ion channel inhibitor chlorotoxin.[34] Furthermore, EIS is used routinely to characterize artificial membrane systems (see chapter 3 on page 25) and study membrane-embedded proteins such as ion channels.[35,36]

2.2.1. Electrode Interfaces

The immersion of a metal surface into an electrolyte-containing aqueous medium leads to a redistribution of charges and, thus, to a charged interface.[5] Depending on which metal is used, the electron density of the metal is either reduced or increased which leads to an excess concentration and even adsorption of oppositely charged ions to the electrode surface. This process does not require the application of external potentials and takes place already at open circuit conditions. The charge distribution in the bulk solution, shown in figure 2.4 (left), can be understood on the basis of the electrical double layer model which combines the approaches of the Helmholtz and the Gouy-Chapman concept. The first layer which is in direct contact to the electrode is composed of a compact film of specifically absorbed ions and a highly ordered water matrix. This structure is less than 1 nm thick and denoted as the inner Helmholtz or Stern layer. Its formation requires a gain in free energy that compensates the partial loss of the hydration shell and usually countervails the charge of the electrode resulting in a sharp potential drop. Adjacent to the inner Helmholtz layer is the outer Helmholtz or diffuse double layer. Here, the ions can diffuse freely still adopting to a concentration gradient determined by the interfacial electric field.

The potential distribution in the proximity of a metal can be described on the basis of a simple electrostatic model in which the charge densities σ_i at each interface have to be considered (see [Smith and White 1992][37]). The charge density of the metal σ_M is given by Gauss' law using the potential difference between the metal φ_M and the inner Helmholtz layer φ_M:

$$\sigma_\mathrm{M} = \frac{\varepsilon_0 \varepsilon_\mathrm{C}}{d_\mathrm{C}}(\varphi_\mathrm{M} - \varphi_\mathrm{C}). \tag{2.31}$$

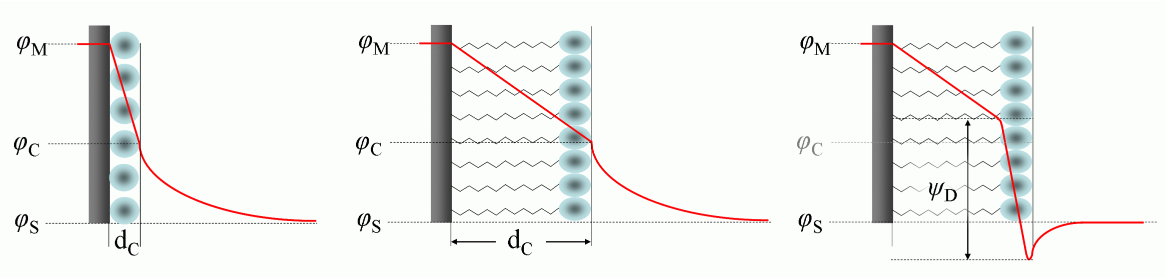

Figure 2.4: Schematic representation of the potential profile in the electrical double layer of a metal with absorbed ions (left), with a self-assembled monolayer with polar headgroups in a simplified model (middle), and in a more elaborate model (right)

Here, ε_0 is the permittivity, and ε_C and d_C the dielectric constant and thickness of the inner Helmholtz layer, respectively. The decay of the charge density inside the outer Helmholtz layer σ_S is dependent on the potential difference between the inner Helmholtz layer and the bulk solution at an infinite distance to the electrode φ_S:

$$\sigma_S = -\varepsilon_0 \varepsilon_S \kappa \frac{2kT}{e} \sinh\left(\frac{e}{2kT}(\varphi_C - \varphi_S)\right). \tag{2.32}$$

In this equation which is derived from Gouy-Chapman theory, ε_S is the dielectric constant of the solution, T the temperature, and k and e the Boltzmann constant and the elementary charge, respectively. The thickness of the outer Helmholtz layer is given by the Debye length κ that defines the exponential decay of the potential to ca. 37 % ($\sim e^{-1}$) of its initial value and is dependent of the ionic strength of the solution I:

$$\kappa = \sqrt{\frac{\varepsilon_0 \varepsilon_S kT}{I}}. \tag{2.33}$$

The charge density of the inner Helmholtz results σ_C results from the requirement of charge neutrality of the complete system:

$$\sigma_M + \sigma_C + \sigma_S = 0. \tag{2.34}$$

Applying an external potential difference to the metal electrode changes the potential of the metal φ_M. A particularly interesting state, the potential of zero charge (E_{PZC}), is achieved when φ_M equals φ_S and the absolute charge density on the metal surface and the effective electric field perturbing the solution becomes zero.

Coating the electrode with an amphiphilic self-assembled monolayer (SAM), as shown in figure 2.4 (middle), introduces a hydrophobic layer with a decreased dielectric constant ($\varepsilon_r \sim 2-3$) and, if necessary, with charged headgroups. Along this layer, the potential drops linearly according to this simple model. More elaborate models contain an additional component which is the dipole potential ψ_D generated by the polar headgroups (figure 2.4 (right)).[38] In this way, the profile of the potential is described more precisely and resembles model of the potential distribution across a phospholipid membrane (see 3.3 on page 29).

2.2.2. The Theory of Electrochemical Impedance Spectroscopy

EIS is an electrochemical technique that probes the dielectric properties of a medium as a function of the frequency. It is based on the interaction of an externally applied and alternating electric field with the electric dipole moments of the analyte or of a dielectric medium, such as the molecules within the inner Helmholtz layer as well as a SAM or a phospholipid membrane. The most common way of performing EIS is to apply an alternating voltage of small amplitude to the electrode and record the phase shift and amplitude, or the real and imaginary parts, of the resulting current. By scanning the frequency (in the range of 1 mHz and 1 MHz) a complete spectrum can be measured.

2.2.2.1. The Electrical Impedance

The impedance $Z(\omega)$ is the frequency-dependent resistance.[39] In analogy with Ohm's law, it can be calculated as the ratio of the alternating voltage and the resulting current:

$$Z(\omega) = \frac{U(\omega,t)}{I(\omega,t)}. \tag{2.35}$$

In an EIS experiment a monochromatic signal $U(t) = U_0 \sin(\omega t)$ with the a single frequency of $\nu = 2\pi\omega$ is applied and the current $I(t) = I_0 \sin(\omega t + \Theta(\omega))$ with a phase difference Θ is measured.[29,39,40] The resulting impedance is

$$Z(\omega) = \frac{U_0 \sin(\omega t)}{I_0 \sin(\omega t + \Theta(\omega))}. \tag{2.36}$$

For purely resistive behavior Θ is zero, and the responses of capacitive and inductive elements are $I(t) = [dU(t)/dt]C$ and $U(t) = [dI(t)/dt]L$, respectively (C is the capacitance and L the inductance). The analysis of a system using these differential equations can be very complex. Fortunately, the use of the Fourier transform simplifies this treatment by conversion into the frequency domain (which is also the variable in a EIS measurement) yielding to a voltage and current of $U(\omega) = U_0\pi$ and $I(\omega) = I_0\pi e^{i\omega}$, respectively, as well as to the solution of the differential equations for a resistive, capacitive and inductive behavior ($i = \sqrt{-1}$):

$$Z_\mathrm{R}(\omega) = R \qquad \text{with} \qquad \Theta = 0, \tag{2.37}$$

$$Z_\mathrm{C}(\omega) = (i\omega C)^{-1} \qquad \text{with} \qquad \Theta = -\frac{\pi}{2}, \tag{2.38}$$

$$Z_\mathrm{L}(\omega) = i\omega L \qquad \text{with} \qquad \Theta = +\frac{\pi}{2}. \tag{2.39}$$

The Complex Impedance The impedance is a complex quantity and, therefore, can be represented in the Cartesian coordinate system (figure 2.5) as the complex number

$$Z(\omega) = R(\omega) + iX(\omega) = \mathrm{Re}(Z(\omega)) + i\mathrm{Im}(Z(\omega)) \tag{2.40}$$

(in literature also referred to as $Z = Z' + iZ''$).

In this representation, the real part R and the imaginary part X are the resistance and the reactance, respectively. The latter is the magnitude providing information about the capacitive and inductive properties of a system (see equations 2.38 and 2.39). The two coordinate values of the vector which is depicted in figure 2.5 can be written as

$$\mathrm{Re}(Z) = R = |Z| \cos\Theta \quad \text{and} \quad \mathrm{Im}(Z) = X = |Z| \sin\Theta \tag{2.41}$$

with the phase angle Θ and the magnitude of the impedance $|Z|$

$$\Theta = \arctan\frac{X}{R} \quad \text{and} \quad |Z| = \sqrt{R^2 + X^2}. \tag{2.42}$$

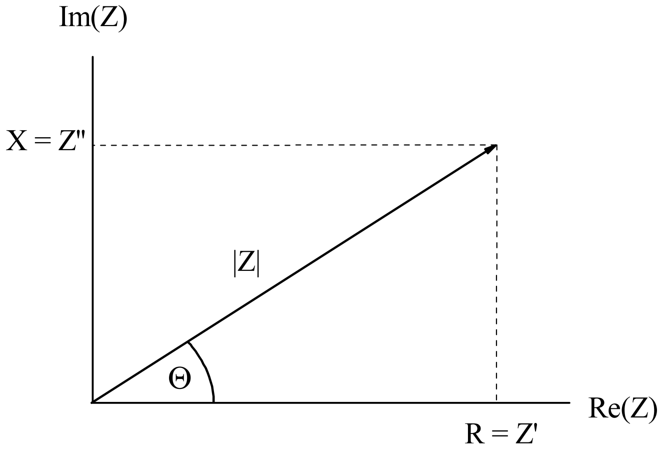

Figure 2.5: The vector of the impedance Z plotted in a Cartesian coordinate system

Through the use of the Euler rule the impedance Z may be rearranged in polar coordinates and expressed as

$$Z(\omega) = |Z|(\omega)e^{i\Theta(\omega)}. \tag{2.43}$$

The Admittance In the same way as the resistance can be rearranged to obtain the conductance, the inverse of the impedance yields the admittance Y:

$$Y = Z^{-1} = G + iB. \tag{2.44}$$

Here, the real part is the conductance G and the imaginary part B the susceptance and can be calculated using the partial fraction decomposition:

$$Y = Z^{-1} = \frac{1}{R+iX} = \frac{R}{R^2+X^2} + i\frac{-X}{R^2+X^2}. \tag{2.45}$$

A common way to express Z and Y is to distinguish between resistive and capacitive components in series $Z = R_{\mathrm{S}}(\omega) - iX_{\mathrm{S}}(\omega)$ or in parallel $Y = G_{\mathrm{P}}(\omega) - iB_{\mathrm{P}}(\omega)$. From this approach, the reactance and the susceptance result in the following quantities:

$$X_{\mathrm{S}}(\omega) = (\omega C_{\mathrm{S}}(\omega))^{-1} \quad \text{and} \quad B_{\mathrm{P}}(\omega) = \omega C_{\mathrm{P}}(\omega). \tag{2.46}$$

2.2.2.2. Representations of Impedance Spectra

In the previous section various mathematical ways to express the impedance were presented. Here, the most important graphical representations will be explained on the basis of the equivalent circuit shown in figure 2.6.[39] This circuit might be used as an approximation of the electrical properties of a functionalized electrode that is in contact to an electrolyte. In this analogy, R_0 represents the resistance of the electrolyte and R_1 and C_1 the resistance and the capacitance, respectively, e.g. of a tBLM (figure 2.6). Figure 2.7 shows the Nyquist, Bode, and Cole-Cole plot that correspond to this circuit.

Nyquist Plot The most common graphical representation is the Nyquist plot which is based on the complex impedance $Z = R + iX$ and the associated plotting shown in figure

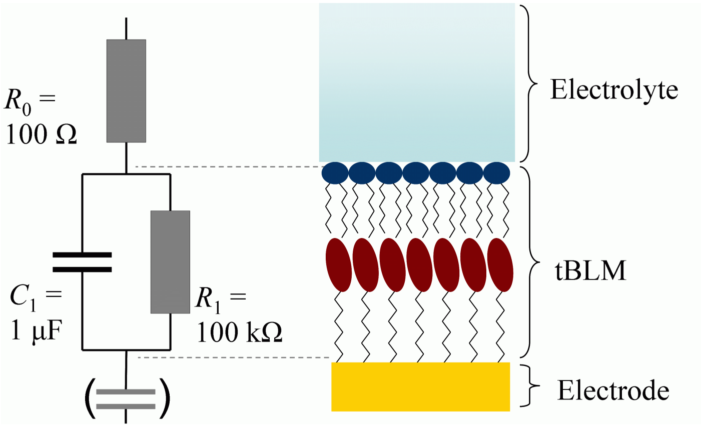

Figure 2.6: An electrical circuit consisting of the resistances $R_0 = 100\ \Omega$, $R_1 = 100\ \mathrm{k}\Omega$, and the capacitance $C_1 = 1\ \mu$F applied to the corresponding model of a tBLM that is supported by an electrode and in contact to an electrolyte

2.5. Here, the imaginary part of the impedance $Im(Z(\omega)) = X(\omega)$ is plotted against the real part $Re(Z(\omega)) = R(\omega)$ as a function of the angular frequency $\omega = (2\pi)^{-1}\nu$. The result of such a plot is a half circle holding the following properties:

- At high frequencies, the impedance curve intercepts with the $Re(Z)$-axis at the value of R_0,
- and at low frequencies at the sum of both resistances $R_0 + R_1$.
- The length of the vector of each data point is the magnitude of the impedance $|Z|$, and the angle with the $Re(Z)$-axis the phase difference Θ (see figure 2.5).
- The angular frequency ω_0 corresponds to the time constant $\tau = R_1 \cdot C_1$ of the R_1C_1-element

Bode Plot In the Bode plot, the magnitude of the impedance $|Z|$ and the phase difference Θ are plotted against the frequency ν. A simple Bode plot of the circuit in figure 2.6 can be subdivided into 3 regions:

- *I* and *III*: At very high and low frequencies, the impedance is independent of the frequency and shows pure resistive behavior ($\Theta = 0$). Equally to the Nyquist plot, the low resistance R_0 appears at high frequencies (*I*), and the sum of both resistances $R_0 + R_1$ at low frequencies (*III*).
- *II*: In the transient area, the impedance behaves frequency-dependent due to the presence of the capacitance C_1. According to equation 2.38 the phase difference approximates the value of $\Theta = -\frac{\pi}{2}$, and the capacitance can be calculated by $C_1 = (\omega|Z|)^{-1}$.

Cole-Cole Plot One of the admittance plots is the Cole-Cole plot where the imaginary and the real part are divided by the angular frequency. The advantage of this representation is the direct description of the capacitance C_1 either by the use of the point of intersection with the $-Im(Y)\omega^{-1}$ axis or the radius of the half circle.

2.2.2.3. Evaluation and Physical Relevance of tBLMs

The physical properties by which a membrane system can be characterized are its resistance and capacitance. An additional component that is inserted into the description is the resistance of the electrolyte which is observed at rather high frequencies due to its low magnitude

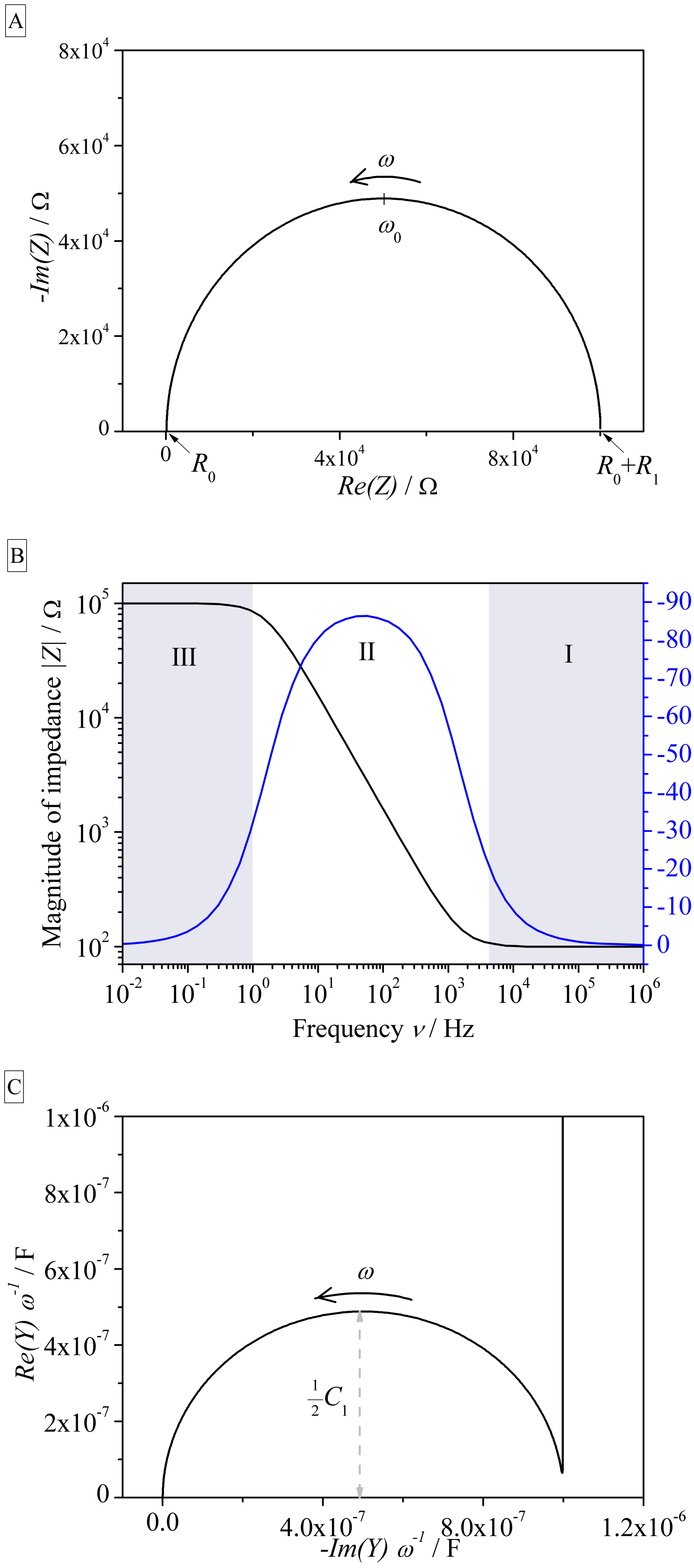

Figure 2.7: The Nyquist (**A**), Bode (**B**), and Cole-Cole plot (**C**) of the corresponding electric circuit in depicted in figure 2.6.

(see figure 2.6). However, by the use of EIS, the capacitance of the electrode as well as the properties of the Helmholtz layer or the ionic reservoirs beneath the bilayer may be monitored. Fortunately, these parts are usually not addressed in the same frequency range as the resistance and capacitance of the membrane and, therefore, can be neglected upon modeling the system. The presence of defects or pores, however, might intensify the influence of the sub-membrane region of tBLMs.[41]

These electrical properties can be extracted from the impedance spectrum manually on the basis of the different representations or by modeling of the studied system.[42] The latter can be done either on the basis of the continuum theory[29] or by the use of semi-empirical methods. In both cases, the system is approximated by an equivalent circuit that provides the mathematical equations for a fit to the data. Semi-empirical methods have the advantage of using already established and optimized models for certain properties of the system. In this work, a non-linear least squares fitting on the basis of the Levenberg-Marquardt algorithm was applied.[43] The following components were used to describe the tBLM.

Ohmic Resistance of a Membrane Due to its hydrophobic core, a lipid bilayer acts as a barrier for ions and other molecules. Therefore, it can be treated as an isolator with the ohmic resistance R.

Capacitance of a Membrane Furthermore, the membrane can be described as a capacitor with the capacitance C:

$$C = \varepsilon_\mathrm{r}\varepsilon_0\frac{A}{d}. \tag{2.47}$$

A and d are the area and the thickness of the membrane, respectively. Whereas A dependents on the dimensions of the experimental assembly, the thickness of a bilayer lies in the range of 4 - 6 nm depending on the phospholipid composition.[44] The dielectric constant of the hydrophobic core is $\varepsilon_\mathrm{r} = 2.1 - 2.8$, the one of the hydrophilic headgroup region of a thickness of 0.6 - 1 nm $\varepsilon_\mathrm{r} = 20$.[45] The latter value, however, may increase up to the dielectric constant of water ($\varepsilon_\mathrm{r} = 80$) depending on the level of solvation. Neglecting this contribution, the specific capacitance of a membrane with a hydrophobic part of 4 nm amounts to

$$C_{sp} = \frac{\varepsilon_\mathrm{r}\varepsilon_0}{d} \approx 0.5 - 0.6\mu\mathrm{F\,cm}^{-2} \tag{2.48}$$

which matches the values obtained from experiments.

Constant Phase Element In the case of an non-ideal capacitive behavior, the capacitance can be replaced by a constant phase element (CPE) that treats the dielectric constant as a complex magnitude on the basis of the Debye theory.[29] The advantage of this approach is a better fit that describes the system more precisely. The resulting impedance amounts to

$$Z_\mathrm{CPE}(\omega) = Q^{-1}(i\omega)^{-\alpha} \qquad \text{with} \qquad \Theta = -\alpha\frac{\pi}{2} \tag{2.49}$$

and α being a parameter with the property $0 < \alpha < 1$. For the case of $\alpha = 1$, this approach describes an ideal capacitor and Q equals the capacitance C (see equation 2.38); all other cases yield the quantity Q with the unit $Fs^{\alpha-1}$ which cannot be compared directly with C. Fortunately, both values might be related to each other when the CPE-element lies in parallel to an ohmic resistance:[46]

$$C = Q(\omega''_\mathrm{max})^{\alpha-1}. \tag{2.50}$$

Here, ω''_{max} is the frequency at which the imaginary part of the impedance $Im(Z)$ reaches its maximum value.

3. Artificial Membrane Systems

Biological membranes are ubiquitous components of living organisms and provide the structural matrix for various essential processes in nature, such as signal recognition, transduction and amplification as well as the generation of electrochemical gradients or ligand-receptor interactions.[47] The chemical transformations during the metabolism and photosynthesis are also linked to the properties of the membrane and even its separating function becomes of crucial importance during the life cycle of a biological cell when cell division, fusion of cell compartments, or apoptotic processes take place.[48] For membrane proteins, the incorporating membrane plays a fundamental role in stabilizing the structure of the protein and, thus, maintaining its function. The latter might be even modulated by the insulating properties of the membrane, for instance, by the generation of membrane potentials.[20] Therefore, the investigation of membrane proteins is tightly linked to its native environment, the lipid membrane. Furthermore, membrane proteins are the target of the majority of drugs, so that the construction and characterization of artificial membrane systems presents a very fascinating and challenging research field.

The modern picture of a biological membrane is based on the fluid-mosaic model by Singer and Nicolson[49] describing the membrane as a two-dimensional solution in which proteins and lipids are able to float freely. This model was modified by the introduction of dynamic structures that accumulate defined membrane components to form sub-micrometer-sized lipid-protein-rafts.[50] These lipid-protein-islands are of essential importance for the function of the membrane. The challenge in engineering artificial membranes is to mimic these properties of the membrane as close as possible to provide a native-like environment for investigations of membrane proteins and their applications in biotechnology. These artificial membrane systems can be subdivided into two classes: three-dimensional bodies resembling the cellular overall structure, such as vesicles or liposomes, and two-dimensional planar constructs that can be constructed as solid-supported or free-standing lipid membranes. Solid-supported membranes are highly demanding constructs for the investigation of structural and dynamic properties of membranes as well as the above mentioned processes involving membrane proteins[3], but also in view of future biotechnological and medical applications.[51] They can be prepared on various kinds of substrates, such as glass, indium tin oxide (ITO), and different metal surfaces allowing for a wide range of possible applications and studies with surface-sensitive methods. Moreover, due to the attachment to the substrate they exhibit a high long-term and mechanical stability, still provided with the needed flexibility and mobility of the lipid molecules when a subjacent thin water film and ionic reservoir is present.

3.1. Structure and Assembly of Lipids

The essential ability of lipids to self-organize into specific supramolecular aggregates results from its amphiphilic nature, i.e. a hydrophilic head group region and several hydrophobic tails. Although this class of biomolecules provides a wide range of diverse derivatives,[52–54] here, the focus of this section will be laid on quantitative description of phospholipids and phospholipid composites.[55]

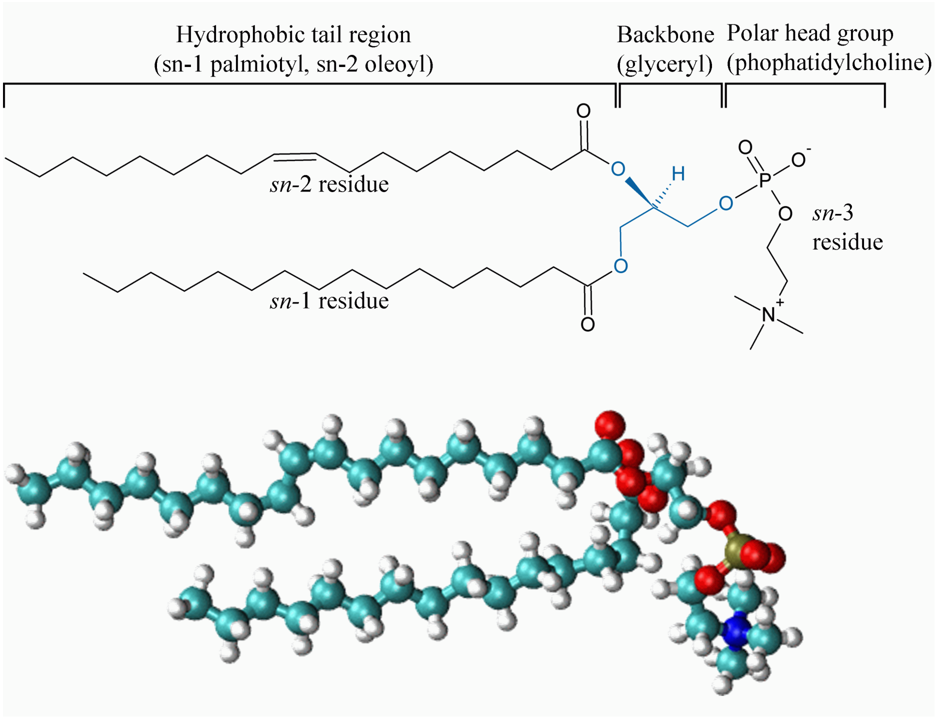

Figure 3.1: Chemical (top) and three-dimensional (bottom) structure of the phospholipid 1-palmitoyl-2-oleyl-sn-glycero-3-phosphatidylcholine (POPC) showing the three regions of the hydrophobic tails, the backbone, and the hydrophilic head group, i.e. a palmitoyl and an oleoyl chain, the glyceryl backbone (indicated in blue), and the phosphatidylcholine head group, respectively. The glyceryl backbone binds via its oxygen atom to the *sn*-1, *sn*-2, and *sn*-3 residues. (In the three-dimensional structure carbons are depicted in light blue, hydrogens in white, oxygens in red, the nitrogen in dark blue, and the phosphorus in yellow.)

3.1.1. Phospholipids

The most common class of lipids in nature are phospholipids (PL). They are composed of three essential structural elements (see figure 3.1): the polar head group, a hydrophobic tail region, and a connecting backbone.[55] Numerous variants result from different head and tail modifications. Some examples of head groups, shown in table 3.1 are choline, ethanolamine, and serine forming phosphatidylcholine, phosphatidylethanolamine, and phosphatidylserine, which render the lipids either zwitterionic or charged at a physiological pH. The hydrophobic tails composed of acyl chains may vary in length and the degree of unsaturation (table 3.2). The behavior of lipids in aqueous phase are dependent on these intrinsic parameters (head group polarity, size and charge; acyl chain length and branching; location and extend of unsaturation etc.) but also on extrinsic conditions such as concentration (lyotropism) and temperature (thermotropism).[52–54] In this work, 1-palmitoyl-2-oleyl-sn-glycero-3-phosphatidylcholine (POPC), which is depicted in figure 3.1, was used for all experiments.

3.1.2. Self-assembly of Phospholipids

Due to their amphiphilic nature, phospholipids tend to self-assemble in aqueous mediums and form mesophase structures, including monolayers, micelles, reverse micelles, bilayers, and hexagonal phases.[55] The driving force for the aggregation is the hydrophobic effect which is characterized by the large negative change of the entropy due to the arrangement of

Designation	structure	charge at neutral pH
Phosphatidylcholine (PC)	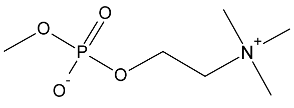	zwitterionic
Phosphatidylglycerol (PG)	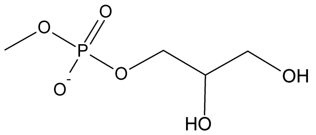	negative
Phosphatidylserine (PS)	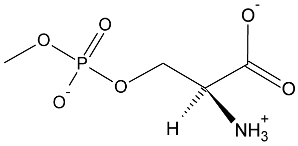	negative
Phosphatidylethanolamine (PE)	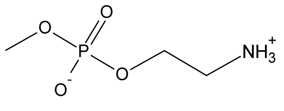	zwitterionic

Table 3.1: Nomenclature and structure of common headgroups present in phospholipids

Designation	structure	C atoms
Myristoyl (M)	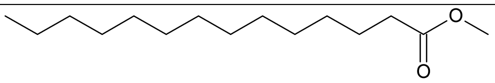	14
Palmitoyl (P)	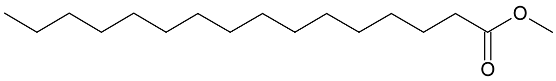	16
Stearoyl (S)	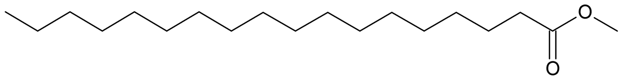	18
Oleoyl (O)	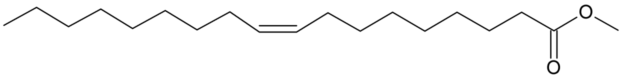	18

Table 3.2: Nomenclature and structure of common acyl chain present in phospholipids.

PL	T_m	PL	acyl chains	T_m	PL	acyl chains	T_m
POPC	-2	DLPC	12-12	-1	DSPC	18:0-18:0	55
POPG	-2	DMPC	14-14	23	-	18:1-18:0	9
POPS	14	DPPC	16-16	41	-	18:0-18:1	6
POPE	25	DSPC	18-18	55	DOPC	18:1-18:1	-20

Table 3.3: Transition temperatures T_m (in °C) of different phospholipids dependent on the headgroup (left), the acyl chain length (middle), and unsaturation within the acyl chains (right).[56,57] Acyl chain rows illustrate the acyl species: “C atoms”:“double bonds”

water dipoles around the fatty acid chains of the lipids. This loss of entropy is minimized in the course of the self-assembly. The shape of the aggregates is determined by shape factor P which is the ratio between the volume of the acyl chains V_C and the product of the head group area A_0 and the effective length of the acyl chains l_C:

$$P = \frac{V_\mathrm{C}}{A_0 \cdot l_\mathrm{C}}. \tag{3.1}$$

The dispersion of POPC, for instance, leads to the formation of multilamellar vesicles. By the use of high-frequency sonication or extrusion through polycarbonate filters these objects

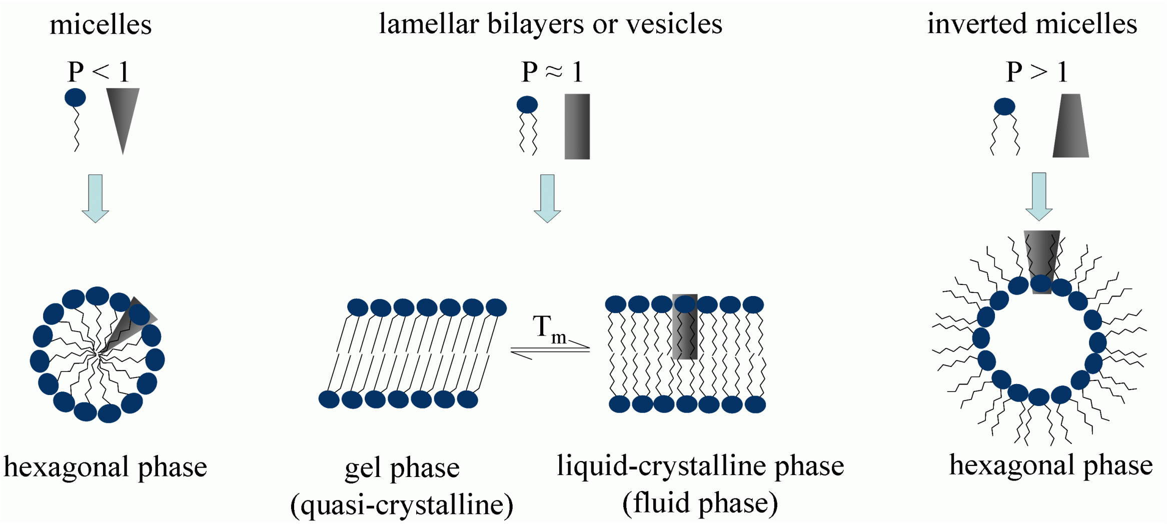

Figure 3.2: Schematic representation of lipid molecules with different shapes determined by the shape factor P (equation 3.1). Lipids with thin or bulky tails tend to form micelles or inverted micelles, respectively, which arrange in hexagonal phases. Lipids with a balanced head to tail size assemble to lamellar bilayers and vesicles. Below the transition temperature, the latter structures exist in a gel (quasi-crystalline), and above in the liquid-crystalline phase (fluid).

can be converted to stable unilamellar vesicles, in the latter case even with a defined size. However, the naturally most abundant architecture is bilayers, which can exist in different thermodynamic phases. The most important once are the gel phase (L_β) and liquid crystalline phase or fluid phase (L_α). These phases can be thought of as a "solid" and "liquid" phase in which the phospholipid are restricted in their mobility or allowed to exchange positions with its neighbors, respectively. The latter is the state prevailing in biological membranes. Influenced by its structure, every lipid has a characteristic transition ("melting") temperature T_m between the gel and fluid phase (table 3.3):

- Increasing acyl chain length, for instance, leads to higher transition temperatures of lipid bilayers, whereas unsaturation of bondings disrupts the molecular packing and ordering of the hydrophobic tails and decreases the melting point.[55]
- The extend of polarity of the head group and its size modulates the interaction between the headgroups among themselves and with water influencing the phase behavior as well.

The permeability of fluid bilayers is highly selective. For instance, water can pass a membrane relatively fast ($30-40\mu$m s^{-1})[58], whereas against ions, such as Na$^+$, Cl$^-$ ($10^{-10}\mu$m s^{-1} and $10^{-7}\mu$m s^{-1}, respectively)[59] the membrane highly is impermeable.[60] However, the insulating properties of a membrane are dependent on the composition of a membrane such as the cholesterol content (e.g. for H$^+$ and OH$^-$ the permeability ranges from 1 to $10^{-4}\mu$m s^{-1}).[61]

3.1.3. The Transmembrane Potential

The transmembrane potential difference $\Delta\psi_M$ regulates numerous processes of membrane proteins.[63] However, due to the structure of phospholipid membranes, consisting of the hydrophobic interior, the zwitterionic or charged head groups, and oriented water dipoles, the potential distribution across the membrane follows a complex profile, as depicted in figure 3.3:

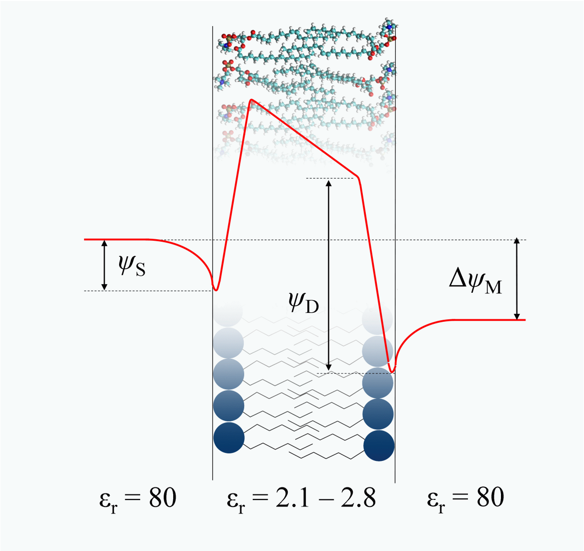

Figure 3.3: Schematic representation of the electrical potential profile across a phospholipid membrane.[62]

- The transmembrane potential difference $\Delta\psi_M$ is determined by the difference between the potential of the bulk solution on both sides of the bilayer. This potential is either generated by concentration gradients of ions or by the application of an external potential. The associated electric field strengths across the membrane lie in the range of 10^7 V m^{-1}.
- The potential of the polar headgroup region affects the concentration gradient of the bulk solution in a similar way as a metal electrode (see section 2.2.1 on page 16) giving rise to the surface potential ψ_S.
- Within the head group region, the alignment of the charged lipid residues and water dipoles cause a sharp increase in the potential by the so-called dipole potential ψ_D.
- Inside the hydrophobic part of the (symmetric) membrane, the potential drops linearly in analogy to equation 2.31 by the transmembrane potential difference $\Delta\psi_M$.

The potential of the polar head group region can be determined quite easily by electrophoretic measurement of the zeta potential.[64] The dipole potential, however, can be only obtained from theoretical calculations or from indirect experimental approaches (see [Clarke 2001][62] or [Wang 2012][65] for a recent review). These data yield values in the range of 200 - 500 mV with a positive sign in the interior of the membrane for saturated phosphatidylcholines. Due to the sharp drop along the short distance of the headgroup region, the associated electric fields are very strong with values between 10^8 and 10^9 V m^{-1}.

3.2. Solid-Supported Membranes

Solid-supported membranes (SSMs) are artificial membranes that are immobilized on appropriately prepared surfaces. Two types, shown in figure 3.4, can be distinguished: SSMs on hydrophilic materials such as glass and hybrid SSMs on hydrophobic functionalized noble metals. The advantage of these systems is the high long-term and mechanical stability, and the possibility of employing a wide range of surface-analytical and surface-sensitive techniques. To date, these systems were characterized by means of microscopic techniques, such as atomic force microscopy (AFM),[66] fluorescence microscopy, and imaging ellipsometry,[67] surface-sensitive surface-plasmon resonance (SPR) and quartz-crystal microbalance

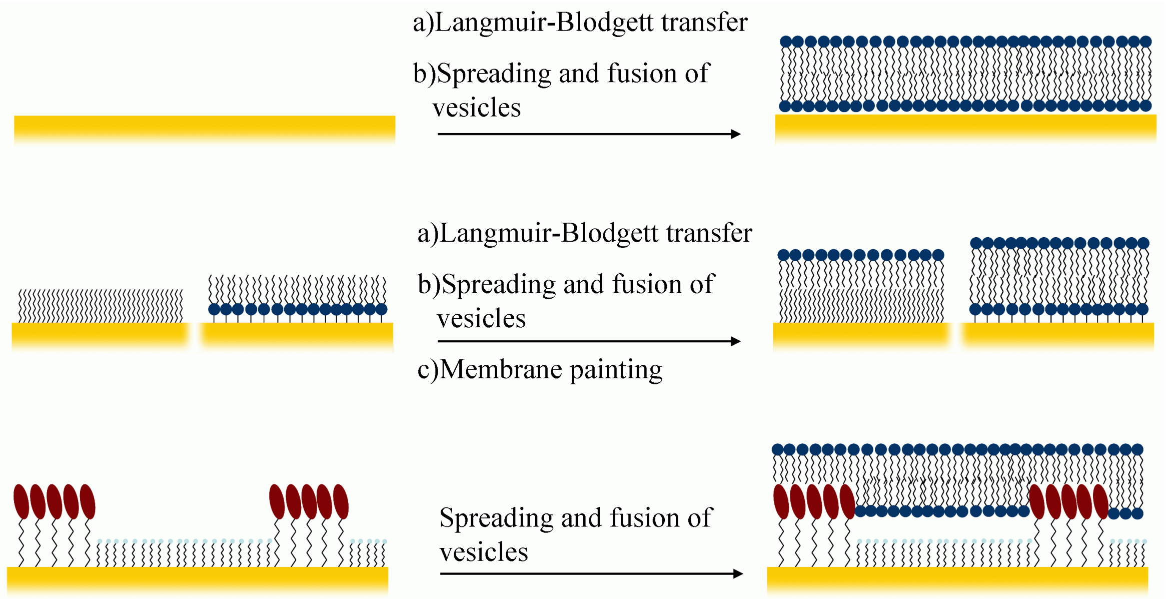
a)Langmuir-Blodgett transfer
b)Spreading and fusion of vesicles
a)Langmuir-Blodgett transfer
b)Spreading and fusion of vesicles
c)Membrane painting
Spreading and fusion of vesicles

Figure 3.4: Schematic representation of different solid-supported membranes (SSMs) and their formation procedures: SSMs on hydrophilic surfaces (top), hybrid SSMs on hydrophobic functionalized noble metals (middle), and tethered bilayer lipid membranes (tBLM) using a lipid-tether molecule and a spacer to create an aqueous reservoir.

(QCM),[68] and electrochemical impedance spectroscopy.[69] Furthermore, spectroscopic techniques such as surface-enhance resonance Raman scattering (SERRS)[70,71] and attenuated total reflexion infrared (ATR-IR) spectroscopy[72,73] were applied to study bilayer properties and attached proteins. This work presents a new and unique approach of combining electrical impedance spectroscopy (EIS) and surface-enhanced infrared absorption (SEIRA) to study membranes and integral membrane proteins in a spectroelectrochemical manner *in-situ* on the very same construct.[74] Several approaches exist to construct such kind of artificial membrane systems.

Solid-Supported Membranes on Hydrophilic Supports One method to form SSMs on hydrophilic supports is the Langmuir-Blodgett technique[75]. Here, a monolayer of lipids covering the water surface is transferred onto the support by traction and immersion through the water-air interface to form the support-facing and the solution-exposed layers, respectively. Alternatively, the monolayer-covered substrate can be pushed horizontally onto the monolayer-covered water surface to obtain the bilayer.[76] In this way, the construction of asymmetric bilayers can be achieved. Another method is based on the spreading and fusion of unilamellar vesicles.[77,78] Here, through adhesion forces vesicles interact with the hydrophilic surface causing ruptures and subsequent spreading. Due to the hydrophobic effect, the lacerated vesicles fuse and form a closed bilayer lipid membrane.

Hybrid Solid-Supported Membranes on Hydrophobic Functionalized Supports Hybrid SSMs are based on metal supports which are functionalized with alkanthiols or lipidthiols that interact quasi-covalently with the metal electrode.[79] The second layer can be obtained either by spreading of vesicles[69,80] or by painting membranes.[81] In the latter approach, lipids dissolved in *n*-decane are brought onto the hydrophobic functionalized electrode and mixed with water. The dilution of lipids leads to the self-assembly on the electrode resulting in the bilayer.

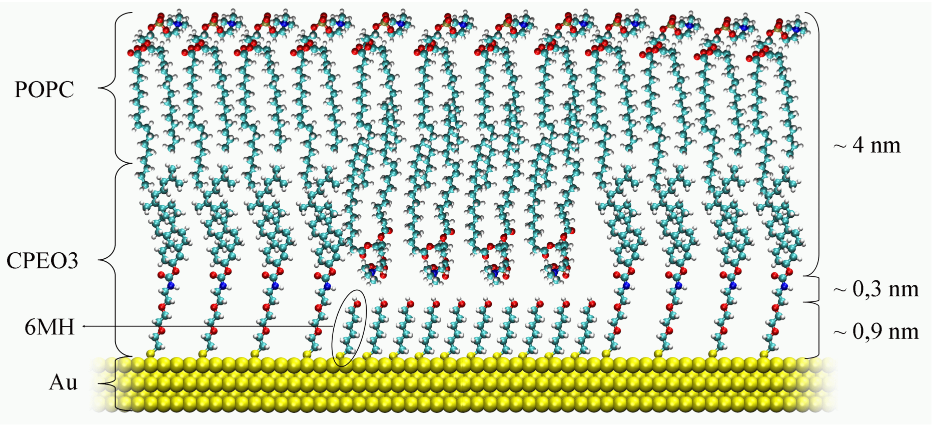

Figure 3.5: Schematic representation of CPEO3-tBLMs composed of a mixed self-assembled monolayer of (cholesterylpolyethyleneoxy)thiol (CPEO3) and 6-mercaptohexanol (6MH) and the lipid 1-palmitoyl-2-oleyl-sn-glycero-3-phosphatidylcholine (POPC). On the right hand side approximate sizes of the components are given: The thickness of the POPC-POPC and POPC-CPEO3 bilayer is ca. 4 nm,[82] and the one of the 6MH spacer ca. 0,9 nm. In between these two layers, a aqueous reservoir of at least 0.3 nm is situated.

The disadvantage of these systems is the close proximity to the substrate. Due to this fact, the natural properties of the biological membrane are not satisfactory reproduced which impedes the immobilization of membrane proteins protruding beyond the membrane surface. SSMs containing appropriate spacer molecules overcome this problem by providing an aqueous reservoir. These systems are denoted as tethered bilayer lipid membranes (tBLMs).

3.2.1. Tethered Bilayer Lipid Membranes

Tethered bilayer lipid membranes (tBLMs; figure 3.4) are constructs that combine the concepts of both types of SSMs plus introducing a spacer that creates an aqueous reservoir in between the bilayer and the supporting electrode. In this way, the disadvantage of the direct contact of the bilayer with the electrode is avoided, and even larger membrane proteins may be incorporated. In general, tBLMs can be subdivided into two groups, protein-tethered (pt) and lipid-tethered (lt) BLMs, although combined constructs are present in literature as well.[83]

Protein-Tethered Bilayer Lipid Membranes In ptBLMs, the membrane protein is linked via the tether to the electrode and the bilayer is constructed around it. A particularly interesting example was presented by Knoll and Naumann et al.[23] who used a His-tag tether to bind the membrane protein cytochrome c oxidase (CcO) via a Ni^+-NTA (nitrilotriacetic acid) linker to an Au electrode. The enormous advantage of this approach is the possibility of immobilizing proteins with a preferential orientation respect the surface, either with the C or the N-terminus. By this, the common problem of having a 50:50 mixture of the "‘up-down"’ and "‘down-up"’ orientation could be avoided efficiently. However, this system has several drawbacks. First of all, the protein mobility is restricted severely by the quasi-covalent attachment to the support. Furthermore, no or only weak electrical contact is present between the protein and the electrode.[84] The main drawback of this system, however, is the absence of a closed bilayer that was attempted to be constructed around the protein by lipid-detergent exchange; the electrical properties obtained from EIS were not indicative of a BLM formation, as also commented in a review by Jeuken.[3]

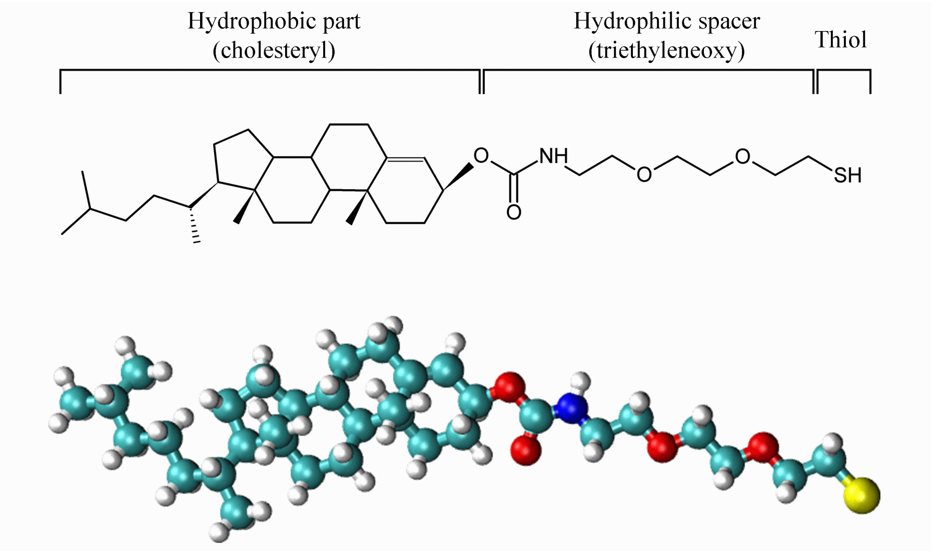

Figure 3.6: Chemical (top) and three-dimensional (bottom) structure of the lipid tether (cholesterylpolyethyleneoxy)thiol (CPEO3) showing the three regions of the hydrophobic cholesteryl part, the hydrophilic triethyleneoxy linker, and the thiol group that binds quasi-covalently to Au. (In the three-dimensional structure carbons are depicted in light blue, hydrogens in white, oxygens in red, the nitrogen in dark blue, and the sulfur in yellow.)

Lipid-Tethered Bilayer Lipid Membranes The other approach resulting in ltBLMs makes use of appropriately functionalized tethers or anchors. Such a tether molecule typically consists of three elements: a hydrophobic part that inserts into the BLM, a hydrophilic spacer, and a thiol group.[47] Among several different examples[85–88], a recent and very successful approach was established by Jeuken, Bushby, and Evans using the (cholesterylpolyethylenoxy)thiol or triethyleneoxythiol cholesterol (CPOE3 or EO_3C, respectively; see figure 3.6).[47] Figure 3.5 schematically presents the architecture of this system.[89] In these studies, a mixed self-assembled monolayer (SAM) of CPEO3 and the hydrophilic spacer 6-mercaptohexanol (6MH) was constructed. Due to phase separation of these two molecules, the SAM is composed of rafts of pure CPEO3 and pure 6MH. As a result, the BLM, which is formed upon spreading and fusion of phospholipid (PL) vesicles, consists of islands of quasi free-standing PL-PL bilayer patches surrounded by a supported PL-CPEO3 hybrid bilayer. This architecture implicates the presence of a aqueous reservoir in between the hydroxyl head groups of the 6MH spacer and the PL-PL bilayer which is the prerequisite for the incorporation of integral membrane proteins into an native-like environment.

To date, this system allowed for a very elegant electrochemical characterization of ion channels,[36] and redox enzymes[90] as well as for other studies not involving tBLMs.[47] The advantage of the CPEO3 over other lipid tethers, such as 1,2-dipamitoyl-*sn*-phophatidylthioethanol (DPPTE)[88] or 2,3-di-O-phytanyl-sn-glycerol-1-tetraethylene-glycol-DL-α-lipoic acid ester (DPTL)[87], is an easier synthesis (as none of them is available commercially), simplified purification and better storage properties.[47] Furthermore, CPEO3-tBLMs were characterized very thoroughly by Jeuken et al. using different methods, such as AFM,[91] ATR-IR,[92] and EIS[89], providing a sound basis for further studies.

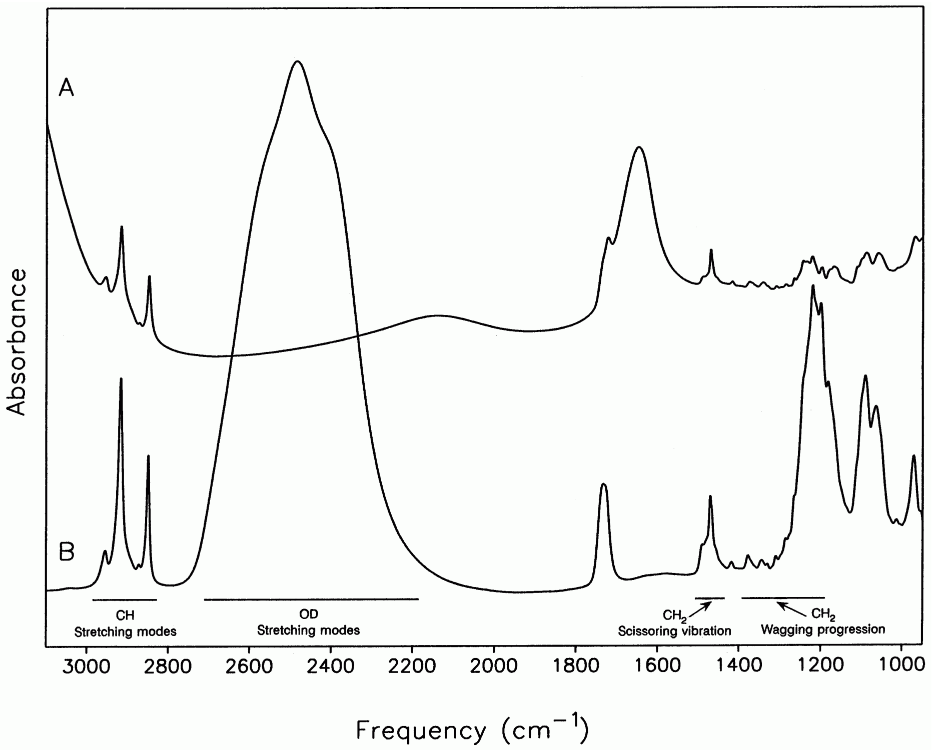

Figure 3.7: IR spectra of phospholipids in H_2O (A) and D_2O (B).[93] (Reprinted from Chem. Phys. Lipids, 94, T. Le Bihan, M. Pézolet, Study of structure and phase behavior of dipalmitoylphosphatidylcholine by infrared spectroscopy: characterization of the pretransition and subtransition, 13-33, Copyright (1998), with kind permission from Elsevier)

3.3. Infrared Spectroscopy of Phospholipid Membranes

In past decades, IR spectroscopy was used extensively to study the structure, conformation and the dynamics of phospholipids in lamellar phases.[94,97] A main focus were the structural changes associated with the transition from the quasi-crystalline gel phase to the fluid phase (see figure 3.2), in particular, the conformations of the phospholipids. However, different regions of the IR spectrum arise from different structural elements of the lipid and, thus, provide complementary information (see figure 3.7 and table 3.4):

The Acyl Chain CH_2 Stretching Region The symmetric and asymmetric CH_2 ($\nu_{as}(CH_2)$ and $\nu_s(CH_2)$, respectively) stretchings of the acyl chains provide very sensitive qualitative information about their static order.[98] The wavenumbers of these vibrations shift to higher values when the PL passes from the gel into the fluid phase. The reason for this effect is an increased disorder (in the fluid phase) reflected by a higher proportion of *gauche* conformers within the acyl chains. In addition, the CH_2 groups possess higher degree of motional freedom (rotation, translation, collision etc.), so that the increased wavenumber is accompanied with a broader band width.

The Acyl Chain CH_2 Bending and Wagging Region The CH_2-wagging ($\gamma_w(CH_2)_n$) can be used to quantify the degree of disorder within the acyl chains.[99–101] In this way, the number of different conformers composed of consecutive *gauche* and *trans* elements can be derived. Furthermore, the CH_2-scissoring motion ($\delta(CH_2)_n$) experience a correlation field splitting in certain conformations that indicate a highly ordered structure.

Average wavenumber	vibration	designation
3028	choline-CH_3-as-stretching	$\nu_{as}((CH_3)_3N^+)$ (w)
2956	CH_3-as-stretching	$\nu_{as}(CH_3)$ (s)
2920	CH_2-as-stretching	$\nu_{as}(CH_2)$ (s)
2886	head-CH_2-s-stretching	$\nu_s(h\text{-}CH_2)$ (m)
2875	CH_3-s-stretching	$\nu_s(CH_3)$ (s)
2850	CH_2-s-stretching	$\nu_s(CH_2)$ (s)
1740	ester-carbonyl-stretching	$\nu(C{=}O)$ (s)
1730	carboxylic acid-carbonyl-stretching	$\nu(C{=}O)$ (s)
1610	carboxylate-stretching	$\nu(COO)$ (s)
1485	choline-CH_3-as-bending	$\delta_{as}((CH_3)_3N^+)$ (m)
1470	CH_2-bending (scissoring)	$\delta(CH_2)_n$ (m)
1460	CH_3-as-bending	$\delta_{as}(CH_3)$ (m)
1380	CH_3-s-bending	$\delta_s(CH_3)$ (m)
1342-1180	CH_2-wagging (progression)	$\gamma_w(CH_2)_n$ (w)
1250-1220	phosphate-diester-as-stretching	$\nu_{as}(PO_2)$ (s)
1170	ester(C-O)-as-stretching	$\nu_{as}(CO\text{-}O\text{-}C)$ (m)
1086-1072	phosphate-diester-s-stretching	$\nu_s(PO_2^-)$ (m)
1085	ester(C-O)-s-stretching	$\nu_s(CO\text{-}O\text{-}C))$(m)
1070	phosphate-ester-stretching	$\nu(CO\text{-}PO_2^-)$ (m)
970	choline-as-stretching	$\nu_{as}(C\text{-}N^+)\text{-}C$ (m)
930	choline-s-stretching	$\nu_s(C\text{-}N^+)\text{-}C$ (m)

Table 3.4: Typical group vibrations of phospholipids. Here, “s” and “as” refer to symmetric and asymmetric vibration, respectively. (Data collected from [Blume 1996][94], [Tamm and Tatulian 1997][95], and [Krishnamurty et al. 2008][96])

The Acyl Chain Carbonyl Stretching In general, IR spectra of phospholipids exhibit a carbonyl stretching ($\nu(C{=}O)$) composed of two species. In earlier days, these two components were ascribed to the *sn*-1 and *sn*-2 ester carbonyl groups. Experiments with mixed $^{13}C{=}O$ and $^{12}C{=}O$ carbonyl groups in one lipid molecule,[102] however, revealed that it is not the different location in the *sn*-1 and *sn*-2 branch but the presence and quality of hydrogen bonding interactions with water molecules that cause shifts in the band position.[103]

Headgroup Phosphate Stretchings The position of the asymmetric stretching of the phosphate ($\nu_{as}(PO_2)$) dependents on the hydration or binding of cations. For instance, hydrating dry lipid samples shifts the wavenumber from 1250 to 1230 cm^{-1}.[94]

4. Membrane Proteins

Membrane proteins play an essential role in the function of a biological cell. They are responsible of carrying out a wide range of fundamental processes, such as proton and electron transfer, voltage-gated ion translocation, signal transduction, and enzymatic reactions. Moreover, they present also the target for more than 45 % of current drugs.[1] Therefore, membrane proteins are of utmost importance for biotechnological and medical applications such as, for instance, engineering of bio-fuel cells or the clinical use of enzymatic biosensors. Despite their biological, biotechnological, and medical significance, the structures of less than 1 % of all membrane proteins have been determined, yet.[104] This lack of knowledge can be traced back mainly to difficulties in the preparation, such as the purification and crystallization, and alternations of the structure and function once removed from their native environment. Consequently, the investigation of membrane proteins with non-invasive techniques, such as vibrational and electrochemical impedance spectroscopy, and at native-like conditions provided by artificial membranes is a seminal approach in life sciences.

4.1. Structure of proteins

Proteins are biopolymers that are constructed out of 20 different building blocks, the so-called proteinogenic L-α-amino acids. These amino acids are connected via a peptide (amide) bond that results from a condensation reaction between an amino and a carboxylic acid group. Due to the partial double bond character of the amide C-N, this bond is relatively strong (hydrolysis is kinetically hindered), planar, and is usually present in the *trans*-configuration.

The primary structure of a protein is defined by its amino acid sequence. Depending on the type of amino acids, specific interactions, particularly hydrogen bonds, emerge within the chain causing the peptide to fold into the so-called secondary structure. Typical secondary structure elements are the α-helix, β-sheet, turns, and random coils. α-helices are right-handed spiral-like structures that result from hydrogen bonds between the C=O of an amino acid and the N-H group of its third succeeding neighbor, and *vice versa*. In this way, each turn of the helix is composed of 3.6 amino acids. Due to the fact that the amide C=O bonds are aligned in parallel (all C=O bonds face towards the same direction, i.e. towards the C-terminus of the helix; see figure 4.3), all amino acid residues are oriented externally and might render, depending on the polarity of the residues, the α-helix either hydrophobic or hydrophilic. Membrane proteins are often constituted of helices with hydrophobic substituents, so that they can be incorporated and stabilized efficiently by the hydrophobic interior of the lipid membrane (see chapter 3 on page 25). β-sheets occur when several β-strands, which are linear peptide chains, arrange in parallel or antiparallel (with the same or reverse propagation direction of the chains, respectively) to each other. In each strand, all amide C=O bonds are aligned antiparallel to each other (facing alternately the "left" and "right" side of the strand), so that the residues are located at both sides of the β-strand. β-sheets are formed due hydrogen bonds between opposing peptide bonds. In the case of the antiparallel β-sheets, these hydrogen bonds are normal to the direction of the sheet and parallel to each other, whereas in parallel sheets the hydrogen bonds are oriented at distorted angles to the sheet direction causing a slightly less stable structure in the latter case. Turns are short segments that contain a maximum number of 5 amino acids, stabilize a U-like conformation and, thus, change the direction of propagation by 180°. Depending on the position of the hydrogen bonds, α, β, or γ-turns are formed. Random coils, eventually, do not possess a regular structure. A rather exotic structure is the β-helix. It is the result of the association of β-strands to a β-sheet that propagates in a helical pattern. In the case of, for instance, gramicidin a β-helix is set up by a primary structure composed of an alternate arrangement of L and D-amino acids, so that within one β-strand all amino acid residues face only one side of the strand and, thus, can "roll up" without any hindrance inside the helix. One can distinguish between parallel and antiparallel β-helices which differ substantially among each other, and can occur, both, in a left and right-handed manner.[105,106]

The tertiary structure is the consequence of the association of different secondary structure elements leading to a densely "bundled" protein. This association is brought about by different kinds of interplays, such as hydrophobic or electrostatic interactions, covalent (e.g. disulfide bonds between two cysteines), or hydrogen bondings.

The same interactions may lead to an arrangement of subunits or monomers of these tertiary structure elements forming the so-called quaternary structure, i.e. dimers, trimers, etc. A prominent example is hemoglobin.[107]

This complete structural hierarchy is essential for the function of proteins. Changes of these structural elements may lead to denaturation and, by this, to a loss of function, which is in most cases an irreversible process. This can be initiated by several extraneous influences, such as high temperatures, high electric fields, non-physiological pH values, organic solvents or the removal of membrane proteins from the plasma membrane.

4.1.1. Infrared Spectroscopy of Proteins

The IR spectrum of a protein is composed of the signals of the polyamide backbone (secondary and tertiary structure), of the residues of each single amino acid,[108] and, if present, of the prosthetic group. In the two latter cases, the respective vibrational features are usually

Designation	wavenumber	group vibrations
Amide A	3310-3270	N-H stretching (first component of the Fermi resonance with first overtone of the amide II)
Amide B	3010-3030	second component of the Fermi resonance of the N-H stretching with first overtone of the amide II
Amide I	1700-1600	C=O stretching with minor contributions of the N-H bending
Amide II	1580-1480	combination of N-H bending and C-N stretching
Amide III	1300-1230	combination of N-H bending and C-N stretching (with different signs and proportions)

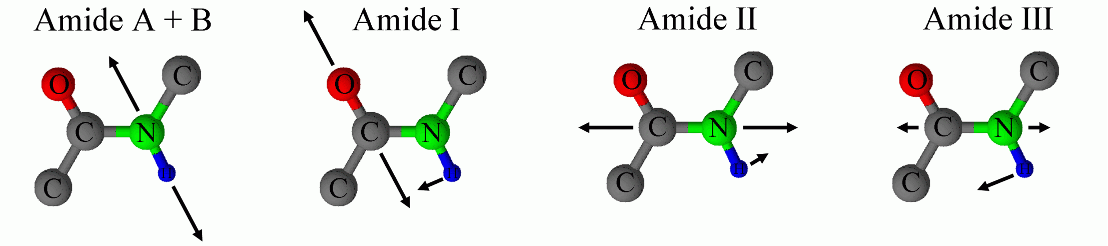

Table 4.1: Protein backbone (amide) vibrations with their typical wavenumber regions (in cm^{-1}) and the assignment to the particular group vibrations

perceived only in reaction-induced difference spectra as they originate from either a single or a small number of equivalents.[109] The protein backbone, however, pervades the entire protein and displays relatively strong intensities of the vibrations. These IR vibrations are denoted as amide bands (see figure table 4.1). The most important amide vibrations are the amide I and amide II which can be ascribed to the C=O stretching (with shares of the N-H bending), and a combination of N-H bending and C-N stretching, respectively. To date, the amide I band was investigated most extensively and allows for the most significant predications of the secondary and tertiary structure of the protein. The amide I vibration results from the C=O stretching and inferior contributions of the N-H bending and, thus, its position is strongly dependent on the hydrogen bonds between these two groups. In this way, it is possible to assign the components of the amide I band to structural elements, of which the most important ones are α-helices, β-sheets, turns, and random coils (see table 4.2). Beside the effect of hydrogen bonds, also transition dipole moment coupling within each structural element plays an important role and may lead to splitting of amide bands into an symmetric and asymmetric component (in-phase or out-of-phase, respectively) with different frequencies and polarizations.[108,110] On the basis of these two effects, the spectral composition of the amide I band can be analyzed theoretically and experimentally and allows for a prediction of the protein backbone structure.[108,111,112] The amide II band was not investigated as extensively as the amide I. However, theoretical calculations provided estimates for the position and polarization as well:[113]

α-helix The α-helix has a sole amide I IR absorption at frequencies between 1657 and 1648 cm^{-1}. The transition dipole moment is oriented in parallel to the helix axis.

The amide II band is located at ca. 1545 cm^{-1} with a perpendicular polarization.

β-sheet Due to dipole moment coupling, the amide I band experiences a splitting into two components.[108] The main absorption is located at ca. 1630 cm^{-1} and has a transition dipole moment perpendicular oriented to the propagation direction of the chain; the weaker absorption is at ca. 1685 cm^{-1} and has a direction of the transition dipole moment parallel along the chain. Although initially claimed by some authors,[114] the presence of the high frequency component is not a characteristic feature of parallel β-sheets. Therefore, there is no straightforward way to distinguish between parallel and anti-parallel sheets.

The amide II is split into two components as well: a strong at ca. 1524 cm^{-1} and a weaker at ca. 1555 cm^{-1} with parallel and perpendicular polarizations.

β-helix β-helical structures have not been investigated so extensively, yet, therefore it is difficult to specify a representative range. Previous studies, however, revealed common features as for β-sheets with a main and a minor component at ca. 1635 and 1690 cm^{-1}.[105] Due to their helical arrangement, the orientation of the transition dipole moment is perpendicular and parallel to the helix axis for these components, respectively.

For gramicidin A, which adopts β-helical structures, the amide II was found to be located at ca. 1550 cm^{-1}. The transition dipole moment for this absorption is oriented parallel in respect to the helix axis.[111,112]

Turn As turns may differ significantly in their hydrogen bonding network, they show an absorption in the complete amide I range between 1690 and 1630 cm^{-1}. Most often, however, the amide I absorption can be found between 1686 and 1662 cm^{-1}

Secondary structure	amide I (H_2O)	amide I (D_2O)	amide II (H_2O)
α-helix	1657-1648 ($\|$)	1660-1642 ($\|$)	$\sim$1545[113] ($\perp$)
β-sheet (main)	1641-1623 ($\perp$)	1638-1615 ($\perp$)	$\sim$1524[113] ($|$)
(minor)	1695-1674 ($\|$)	1692-1672 ($\|$)	$\sim$1555[113] ($\perp$)
β-helix (main)	1640-1630[105] ($\perp$)		$\sim$1550[111,112] ($|$)
(minor)	$\sim$1690[105] ($|$)		
turn	1686-1662	1692-1652	
random coil	1657-1642	1654-1639	

Table 4.2: Spectral position (in cm^{-1}) of the amide I and amide II band for different secondary structure elements in H_2O and D_2O.[115] $\perp$ and $\|$ refer to the orientation of the transition dipole moment in respect to either the helix axis or the sheet direction.

Random Coil The amide I band of random coils coincides with that of α-helices at ca. 1650 cm^{-1}. In membrane proteins, they are rather rare segments and, therefore, do not contribute to the total amide I band significantly.

Difference Spectroscopy IR spectroscopy is a very attractive method to study the structure and dynamics of proteins as it allows for the resolution of very subtle structural changes. For instance, a change of the distance of a hydrogen bonding by 0.002 Å may cause a band shift by 1 cm^{-1}. Other structural-analytical methods, such as x-ray diffraction, rarely reach resolutions below 1 Å. However, the IR spectrum of a protein results from an overlap of many signals impeding the conventional analysis of subtle modifications of the structure, as demonstrated in figure 4.1 left. Here, the absolute IR spectra of the membrane protein rhodopsin are shown before and after illumination.[5] Although involving major structural changes, both spectra do not show any visible differences. The construction of the difference solves this problem by displaying only IR absorptions of structural elements that underwent an alteration (see figure 4.1 right). In this way, even single bonds can be detected given that chemical modifications (e.g. protonation or deprotonation, electronic rearrangements, coupling and breaking of bonds etc.) or, in the case of linear polarized IR radiation, changes in the orientation occurred. These changes may occur in the backbone of the protein, altering the amide bands, in prosthetic group (when provided), or in the amino acid

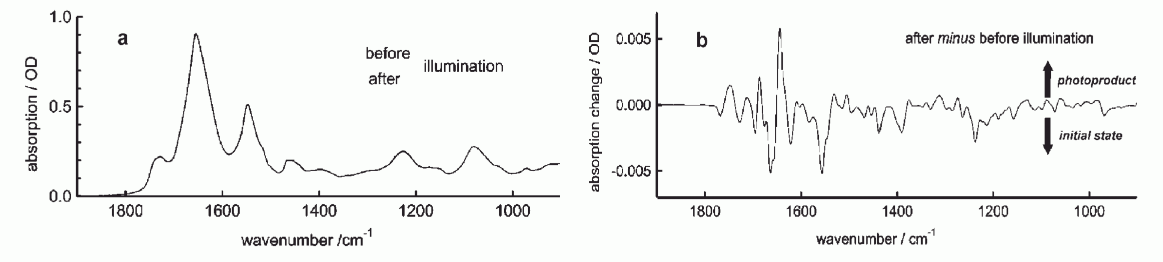

Figure 4.1: Left: Absolute IR spectra of rhodopsin before and after illumination. Right: Illuminated "minus" dark difference spectrum of rhodopsin revealing the light-induced changes that are not visible in the absolute spectra.[5] (Reprinted from F. Siebert, P. Hildebrandt, Vibrational Spectroscopy in Life Science, p. 196, 2008, Copyright (2008), with kind permission from Wiley-VCH Verlag GmbH & Co. KGaA)

residues (see Barth and Zscherp 2002 for a list of vibrations of all amino acid residues).[108] Such a difference spectrum describing the process $A \longrightarrow B$, results form the difference of the absorbance spectra of two states (A_A, A_B) and, therefore, from the intensities of both states (I_A, I_B):

$$\Delta A = A_B - A_A = -\lg\frac{I_B}{I_0} + \lg\frac{I_A}{I_0} = -\lg\frac{I_B}{I_A}. \tag{4.1}$$

In this way, the spectral contributions of the arising state B are displayed as positive and the ones of the disappearing state A as negative difference bands of the difference spectrum (see figure 4.1).

H/D-Effect Maintaining the natural structure and function of a biological sample requires the presence of an aqueous medium. However, water displays strong and broad IR adsorptions at ca. 3400 and 1650 cm^{-1} (O-H stretching ν(OH) and H-O-H bending/scissoring δ(HOH), respectively; see figure 4.2). In particular, the bending mode overlaps severely with the amide I and amide II band (1700-1600 cm^{-1} and 1580-1480 cm^{-1}, respectively) impeding the IR spectroscopic investigation of proteins. Using heavy water (D_2O or ^2H_2O) instead of H_2O, the stretching and bending vibration shifts to ca. 2500 and 1210 cm^{-1}, respectively. As also the amide functions of the backbone may be deuterated upon H/D-exchange, the amide I and II bands shifts as well, however, to less extend by ca. 0-10 and 100 cm^{-1}, respectively (denoted as amide I' and amide II'). In this way, the amide bands can be separated from the vibrations of the solvent facilitating the evaluation of the spectra. However, one has to be cautious, when working with H_2O-D_2O mixtures as the H-O-D bending coincides with the amide II' band at ca. 1450 cm^{-1}.

Mathematically, this effect is based on the change of the reduced mass of the oscillating group which determines the frequency of the vibration, as demonstrated by equation 2.9 on page 8.

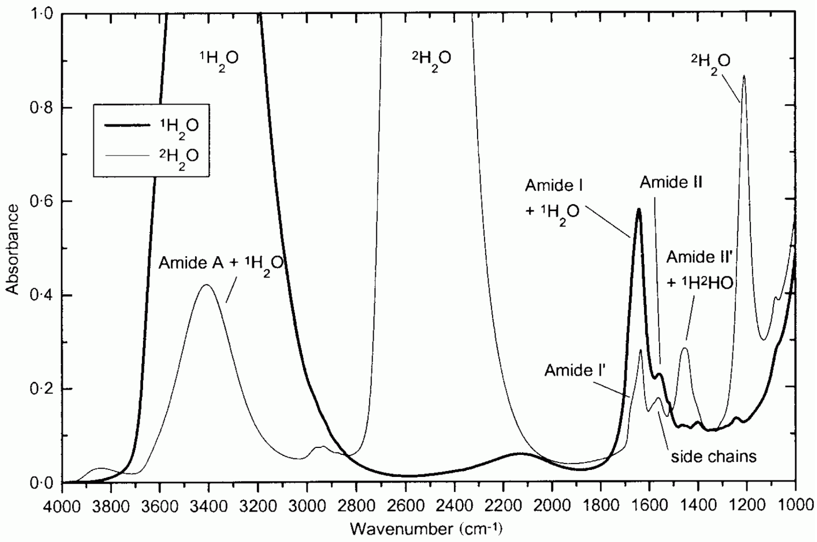

Figure 4.2: IR absorption spectra of the protein tendamistant in ^1H_2O (H_2O, bold line) and ^2H_2O (D_2O, thin line). The H-O-H bending at ca. 1650 cm^{-1} of H_2O overlaps strongly with the protein signals. By the use of D_2O this band shifts to ca. 1210 cm^{-1} unveiling the amide absorption bands.[108] (Reprinted from Quart. Rev. Biophys., 35, A. Barth, C. Zscherp, What vibrations tell us about proteins, 369-430, Copyright (2002), with kind permission from Cambridge University Press)

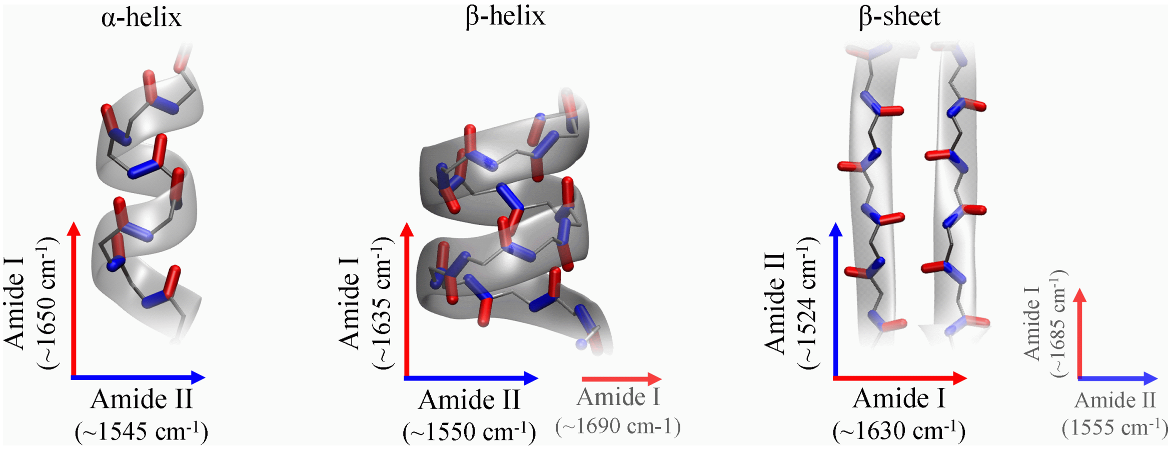

Figure 4.3: α-helix (left), β-helix (middle), and β-sheet (right) with C=O and C-N bondings highlighted in red and blue, respectively. Due to the periodical alignment of these bonds, the total dipole moments of the amide I and amide II of these secondary structure elements are oriented perpendicular to each other as indicated by the arrows. (PBD ids for the α-helix,β-helix, and β-sheet are 1KDL, 1MAG, and 1JY4, respectively)

Surface-Selection Rule As demonstrated in figure 2.3, the local EM field in SEIRA is polarized perpendicular (along the z-axis) to the metal surface at each point and, thus, leads to the surface selection rule. Beside the effect of higher IR absorptions for oriented molecules, the ratio of the relative intensities of signals in the spectra provides additional information about the fixed orientation of the absorbed molecules and processes involving reorientations of segments or groups. As a rule of thumb, structural elements with a dipole moment change associated with the excited vibrational transition oriented parallel to the metal surface (in the xy-plane) do not exhibit any effective IR absorption ($I_{\|} = 0$); those oriented perpendicularly to the surface display the highest intensity of the IR band ($I_{\perp}$; along z-direction). For orientations in between both of these situations, the intensity depends on the z-component of the dipole moment change and, hence, on the angle to the surface normal:

$$I_{\mathrm{IR},\theta} = I_{\mathrm{IR},\perp} \cdot \cos\theta. \tag{4.2}$$

The substantial part of the structure of integral membrane proteins is composed of helices or sheets in which the amino acids are arranged in a highly ordered manner. As demonstrated in table 4.1, the amide I and amide II vibrations are comprised mostly of the C=O and C-N stretchings, respectively. These groups appear in a periodical orientation in helices and sheets and experience a coupling of their dipole moments. This leads to a coupled oscillating system of amide I and amide II vibrations, respectively,[108] extending the entire secondary structure unit (see figure 4.3). Consequently, the total dipole moment changes of these amide bands show a specific orientation for helices and sheets (see figure 4.3):

- In α-helices, the dipole moment change of the amide I is oriented in parallel and the one of the amide II perpendicularly in respect to the axis of the helix.
- β-helices have a hydrogen bonding pattern as β-sheets, but an orientation of C=O (although, here, in an alternating "up and down" pattern) and C-N bonds as in α-helices. Hence, the dipole moment change of the main component of amide I (at ca. 1635 cm^{-1}) is oriented in parallel and the one of the amide II perpendicularly in respect to the axis of the helix; in the case of the minor component at ca. 1690 cm^{-1} the transition dipole moment is oriented perpendicular to the helix axis.

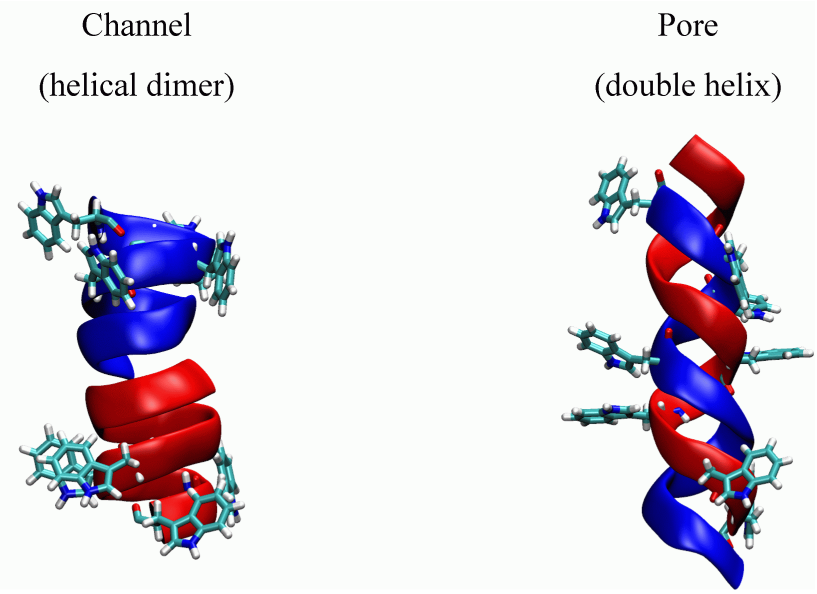

Figure 4.4: Structures of gramicidin A showing the two β-strands and the Trp residues. The channel (left) is a right-handed helical dimer formed by a N-terminus to N-terminus association two gramicidins in the upper and bottom leaflet of the bilayer membrane (PDB ID: 1NRM). Pores (right) are double helical structures composed of four species that may form in a parallel and antiparallel as well as in a right and left-handed manner (PDB ID: 1ALX).

- In β-sheets, the dipole moment change of the main amide I component absorbing at ca. 1630 cm^{-1} is oriented perpendicularly and the one of the main amide II at ca. 1524 cm^{-1} in parallel respect to the direction of the polyamide chain. The minor components of the amide I and II bands (ca. 1685 and ca. 1555 cm^{-1}, respectively) possesses an orientation of the transition dipole moments perpendicular to the main features and, therefore, in parallel for the amide I and perpendicular for the amide II with respect to the propagation direction of the chain.

On that basis, the analysis of the ratio of the intensities of the amide I and II band provides a tool to determine the orientation of these secondary structure elements within the protein or of the entire membrane protein within the membrane.[20,116–119]

4.2. Gramicidin A from *Bacillus brevis*

Gramicidin represents a family of linear, 15 amino acid-long, polypeptides from the soil bacterium *Bacillus brevis* regulating the transition between vegetative growth and sporulation. It is well known for its antibacterial activity[120] and was proposed as an anti-HIV antiviral agent.[121] The mechanisms of its original and clinical function involves gene regulation and inhibition of RNA polymerases.[6,122] Furthermore, when incorporated into membranes, helical membrane-spanning structures are formed that function as monovalent cation channels. Under this aspect, gramicidin was used to study extensively structural, functional, and dynamic properties and, thus, it represents the today's best understood ion channel. The detailed and diversified body of data and knowledge (see the elaborate review [B. A. Wallace 1998][106] and the list of reviews therein, or a more recent review by [Kelkar and Chattopadhyay 2007][123]) renders this peptide an ideal benchmark system to be used for the development of biotechnological devices.[3,48]

Phospholipid	$\beta^{6.3}\beta^{6.3}$	$\uparrow\uparrow \pi\pi^{5.6}$ (left-handed; species 1 + 2)	$\uparrow\downarrow \pi\pi^{5.6}$ (left-handed; species 3)
DPPC (TFE)	1	0	0
POPC (TFE)	0.95	0.03	0.02
DMPC (TFE)	0.85	0.06	0.09
DOPC (TFE)	0.82	0.09	0.09
DSPC (TFE)	0.66	0.24	0.10
Soybean PC (TFE)	0.35	0.32	0.33
Soybean PC (EtOH)	0.24	0.42	0.34
DLPC (TFE, 3h)	0.29	0.47	0.24
DLPC (TFE, 3h)	0.20	0.54	0.26
DLPC (EtOH)	0.18	0.33	0.49

Table 4.3: Composition of conformational states of gA in different phospholipid membranes (calculated from circular dichroism data; data taken from [Sychev et al. 1993][127]).

Directly isolated from the organism, gramicidin is composed of a heterogeneous mixture of its derivatives, gramicidin A, B, and C in a ratio of 80:5:15,[124] denoted as gramicidin D after its discoverer René Jules Dubos. All of them are linear pentadecapeptides varying in only one amino acid, in contrast to the cyclic decapeptide gramicidin S (Soviet). The primary structure of gramicidin A (gA) is composed of an alternating chain of L and D-amino acids:

formyl-L-Val-1–Gly-2–L-Ala-3–D-Leu-4–L-Ala-5–D-Val-6–L-Val-7–D-Val-8–L-Trp-9–
D-Leu-10–L-Trp-11–D-Leu-12–L-Trp-13–D-Leu-14–L-Trp-15–ethanolamine.

In gramicidin B and C, the tryptophan at position 11 is exchanged by phenylalanine and tyrosine, respectively. In addition, ca. 20 % of gramicidin D has a formyl-L-leucine at the first position. Since only gA was used in this work, this section will focus solely on this gramicidin variant.

The primary structure of gA shows several atypical features that have important implications for its structure and function. None of the amino acids carries a charged group which renders the peptide very hydrophobic. In addition, at the N- and C-termini (i.e. formyl-L-valine and ethanolamine, respectively) the amino group is blocked by a formyl group, and the carboxylic function of, essentially, the terminal glycine is reduced to an alcohol, respectively. In this way, gA cannot adopt a zwitterionic form, nor get charged at high or low pH values, leading to an even more hydrophobic nature which, however, is perfectly suited for incorporation into the hydrophobic core of a phospholipid membrane. Furthermore, the alternating chain of L and D-amino acids has significant structural consequences for the intramolecular hydrogen bond network and, thus, for its secondary structure: The formation of an α-helix is impeded as the side chains would protrude in both direction, to the outside and the inside of the helix. Consequently, a β-strand conformation is adopted, in which all amino acid residues point to only one side of the chain, and, as already proposed in the beginning of the 1970's by Urry[125] and Veatch[126], rolled up to form several β-helical structures (see figure 4.4). In this way, the interior of the helix is hydrophilic due to the backbone amide bonds, the surface, however, is covered by the hydrophobic side chains. It is clearly evident that this structure is ideally qualified to act as an ion channel when introduced into a phospholipid membrane. In fact, membrane-bound gA forms channel structures specific for the transport of monovalent cation across membranes. However, due to its small size and flexibility, it adopts several conformations depending on its environment.

4.2.1. Polymorphism of Gramicidin A

The polymorphism of gA manifests in solution, in the solid state and in membranes.[128] The two major types of secondary structure are the double helix and the helix dimer as depicted in figure 4.4. The former is established when two gA chains arrange to a parallel ($\uparrow\uparrow$) or anti-parallel ($\uparrow\downarrow$) β-sheet and twist in a right or left-handed direction to yield a double-stranded β-helix. These structures are referred to as, for instance, $\pi\pi^{5.6}$ where the superscript describes the number of residues per turn in each gA monomer and are designated as "the pore". Alternatively, one chain may form only intramolecular hydrogen bonds to create a single-stranded β-helix which dimerizes in a N-terminal to N-terminal antiparallel fashion. This helical dimer is denoted as "the channel" with the symbol $\beta^{6.3}\beta^{6.3}$ (in older literature also $\pi^{6.3}\pi^{6.3}$).

As a general rule, the double helical pore is predominant in organic solvents and the helical dimeric channel when incorporated in membranes. However, in the latter case, the solvent history and the type of phospholipid membrane plays a decisive role.[123] When gA is dissolved in, for instance, chloroform/methanol, benzene/methanol, or ethanol it tends to incorporate into membranes in non-channel conformations. Only by subsequent heating or sonication it is converted into the helical dimer. However, dissolving it in trifluoroethanol (TFE) promotes the direct formation of the channel structure as well as the presence of Cs^+ ions.[127] Moreover, the nature of the phospholipids, in particular the length of the acyl chains[129] and the membrane order, influences the structure of gA, so that mixtures of different composition are yielded as shown in table 4.3.

4.2.1.1. Double Helix - The Pore

The so-called pore conformations were first observed by Veatch et al.[126] in organic solvents as a mixture of four different states. Based on data from circular dichroism (CD), nuclear magnetic resonance (NMR), and IR spectroscopy double helical structures were proposed and later validated by structural investigations (see list of structures in the review by [B. A. Wallace 1998][106]. When gA is incorporated into membranes, theses states usually do not form or present a minor component (table 4.3).

Structures of the Double Helix States The pore structures consist of two strands that form a dimeric β-sheet with a parallel or antiparallel orientation of the monomers. This sheet may twist in left or right-handed manner into a helix:

- Species 1 und 2: left-handed parallel $\uparrow\uparrow$ $\pi\pi^{5.7}$ double helices differing in the alignment of the ends of the chains. Here, species 1 is 30 Å long.
- Species 3: left-handed antiparallel $\uparrow\downarrow$ $\pi\pi^{5.6}$ double helix; approximately 36 Å long with a maximum lumen diameter of 3.0 Å.
- Species 4: right-handed parallel $\uparrow\uparrow$ $\pi\pi^{5.7}$ double helix; approximately 27 Å long with a maximum lumen diameter of 2.6 Å.

As in β-sheets, the hydrogen bonds of antiparallel arrangements are normal to the direction of the sheet and parallel to each other, whereas in parallel sheets the hydrogen bonds are distorted in their orientation and render the helix slightly less stable. Due to the alternating L and D-amino acids, all residues point out of the surface of the tube with all Trp side chains being distributed along the entire length of the helix. This structure creates a homogenously hydrophobic surface which is favorable in organic solvents and thick membranes, where the complete pore is in a homogenous hydrophobic surrounding. In intermediately thick membranes with acyl chains composed of 18 to 14 C atoms,[129] this structure is unfavorable

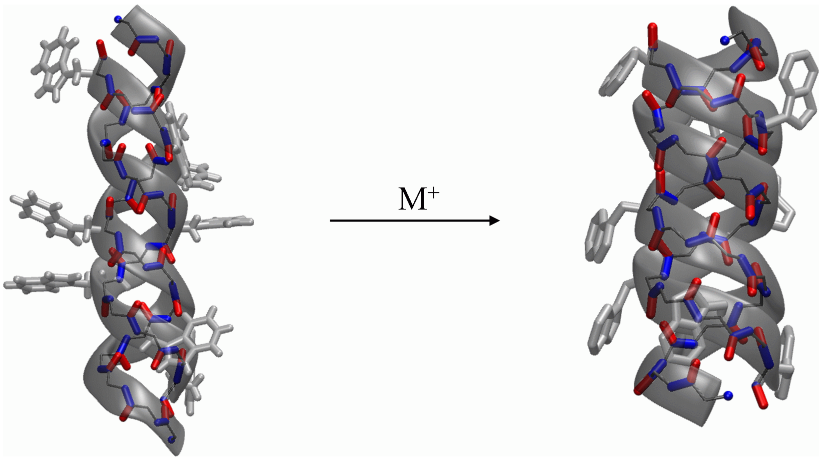

Figure 4.5: Structures of the "empty" and monovalent cation M^+-bound pore. Amide C=O bondings are highlighted in red; amide C-N bonds in blue. (PDB IDs of empty and M^+-bound channel are 1ALX and 1C4D, respectively)

as the ends of the pore get in contact with the polar headgroup region of the membrane. As will be described in the next section, in this case, the Trp residues tend to form hydrogen bondings with the polar groups and, therefore, inducing helical dimers.

Binding and Conductance of Cations Binding of monovalent ions leads to significant conformational changes, involving a rearrangement of the backbone (figure 4.5).[106] As a result, the helix is shortened to a length of 26 Å with 7.2 or 6.4 residues per turn. Furthermore, the lumen diameter is enlarged to a continuous and uniform hole of ≥ 3 Å, which allows, e.g., Cs^+ ions to pass through the peptide and, thus, designates this structure as "the pore". Within this pore, there are two binding sites symmetrically located in a distance of 7.2 Å way from the entrance, and 11.6 Å apart from each other. This site is produced by Trp-11 and Leu-4 of one strand and Val-1 and Ala-3 of the other strand by a reorientation of the carbonyl groups by an angle of 40° away from the helix axis and an associated distortion of the hydrogen bonding network. The binding affinity is related to the size of the cation in the order $Cs^+ \sim Rb^+ \gg K^+ > Li^+$, where an already bound ion promotes the binding of the second due to the already adopted "open pore" structure.

Bivalent cations, such as Ca^{2+}, block the channel by the formation of a structure with 5.7 residues per turn (30 Å long) and a inner diameter of 2.0 Å which is to small to permit ion transport. In this case, the binding site is located at the mouth of the pore involving the conjugation of Val-1 and Gly-2 from each chain.

4.2.1.2. Helix Dimer - The Channel

In 1972, D. W. Urry proposed the secondary structure of a helical dimer for gA.[125] This model was confirmed and improved by conductance,[130] NMR,[131] and CD studies[124] on gA incorporated into micelles and membranes as these data showed substantial differences in comparison to the results obtained for the double helix. More detailed and recent structures where obtained from solid-state NMR experiments of oriented and hydrated gA-containing DMPC bilayers.[132,133] When introduced into membranes, this structure acts as a ion channel for monovalent cations, whereas bivalent cations block the channel. For alkali cations, the conductivity increases with the ion size[134] and corresponds to the Hofmeister series (Tl^+ $>$) $Cs^+ > K^+ > Na^+ > Li^+$ which describes binding properties of ions to proteins.[135,136]

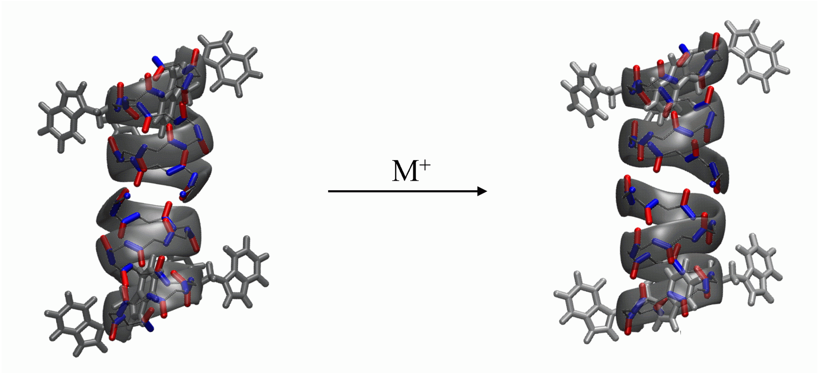

Figure 4.6: Structures of the “empty” and monovalent cation M^+-bound channel. Amide C=O bondings are highlighted in red; amide C-N bonds in blue. (PDB IDs of empty and M^+-bound channel are 1NRM and 1NMU, respectively)

Structure of the Double Helix States The helical dimer is the conformation present in phospholipid membranes. It is composed of two monomeric gA molecules, one in the upper and the other in the bottom leaflet of the membrane, that combine to an N-terminal to N-terminal dimer. In contradiction to the double helix, here, each monomer arranges to a sole β-strand, however, being still coiled in a β-helical way (by establishing 15 intramolecular hydrogen-bonds) and having placed all amino acid residues on the outside of the “tube”. This structure has 6.3 residues per turn (therefore denoted as $\beta^{6.3}$) and possesses a hydrophilic interior formed by the peptide backbone which is 3.6 Å in diameter and, thus, large enough to allow for the passage of monovalent ions.[123] However, with 13 Å in length, one monomer is to short to span the entire membrane and to conduct ions across it.

Active channels are formed spontaneously when two monomers in opposite membrane leaflets dimerize via six hydrogen bonds between their N-termini to yield in a 26 Å long dimer. Such a helix dimer is now able to span the entire hydrophobic part[129] of the membrane with an average lifetime of 0.5 seconds and a dimerization constant of $\sim 2 \cdot 10^{13} mol^{-1} cm^2$. All Trp residues are located at both ends of the dimer where the indole N-H groups are able to interact with the lipid head groups and water (figure 4.4). This renders the helical dimer as the thermodynamically stable state of gA when incorporated in membranes.

Binding and Conductance of Cations The transport of cations across the channel can be modeled as a three step process including two sites: ion diffusion and binding to the entry binding site of the channel, translocation through the channel to the exit binding site, and release and diffusion to the bulk. Although ^{13}C-NMR and X-ray data do not agree upon the exact interaction with certain amino acids, the approximate position of the binding site is located within the first turn of the helix. This position is ca. 9 to 10 Å away from the center of the channel[137] where the cation is coordinated by two carbonyl groups, one water in the channel, and at least one water on the bulk side. Here, the associated structural changes of gA are much smaller than in the case of the double helix, as only the outer helix turn rotates slightly into the channel accompanied by a slight reorientation of the carbonyl groups (figure 4.6). As a result the dimer shortens to ca. 22 Å and leads to a tightening of the membrane. The fact that the cation removes part of its solvation water, explains the conductance series $Tl^+ > Cs^+ > K^+ > Na^+ > Li^+$ as bigger cations carry a smaller and weaker solvation shell. The Trp residues that are located in the phospholipid headgroup region play a crucial role in the binding process due to its dipole moment of ca. 2 D. They produce a broad negative potential across the length of the channel which favors cation binding.

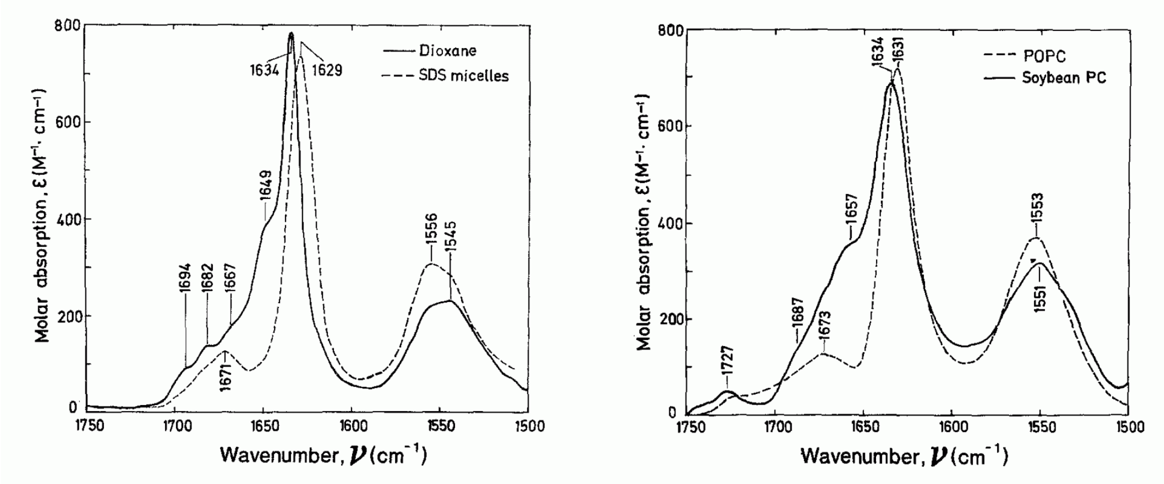

Figure 4.7: ATR-IR spectra of gA in dioxane and SDS micelles (left) and soybean PC and POPC liposomes (right).[127] (Reprinted from Eur. Biophys. J., 22, S. V. Sychev, L. I. Barsukov, V. T. Ivanov, 1993, 279-288, The double $\pi\pi 5.6$ helix of gramicidin A predominates in unsaturated lipid membranes, fig. 7 and fig. 8, Copyright (1993), with kind permission from Springer Science and Business Media)

Double occupancy (binding of a second ion to the binding site at the opposite side) causes probably an outward shift of both bound ions which leads to a weakening of the bonding. For instance, the binding constants of Na^+ to the first and the second (double occupied) site are 30 and 2.6 mol^{-1} dm^3. The kinetics of the process are modulated by double occupancy, as well: a Na^+ in the solely bound state has a exit rate of $3 \cdot 10^5$ s^{-1}, whereas in the doubly occupied situation it increases to $2 \cdot 10^7$ s^{-1}.[138,139] This observation is crucial for the understanding of the channel conductance: In a first step, a cation has to diffuse and bind to the channel, followed by a diffusive translocation of that ion to the binding site on the opposite side of the channel (with a rate constant of ca. 10^7 s^{-1}). Binding to the now unoccupied (first) site, weakens the ion-peptide interaction to release the conducted cation.

Ba^{2+} as a bivalent cation blocks the channel. Its binding site differs from the one of monovalent cations and is located at the outside of the channel, ca. 13 Å away from the center. The reason for this difference is the high affinity to water which stabilizes the solvation shell, thereby impairing penetration into the channel due to the large size of the hydrated ion.[137]

4.2.2. Infrared Spectroscopy of Gramicidin A

All double helical forms exhibit a strong amide I absorption between 1633 and 1638 cm^{-1} with intense shoulders close to 1650 cm^{-1} and a broad amide II band between 1551 and 1545 cm^{-1}.[126,127] In addition, species 3, the only antiparallel form shows a minor amide I component at 1680 cm^{-1} underlining the unique arrangement among the pore structures. These structures are formed when gA is dissolved in organic solvents or certain lipids such as dioxane or soybean PC, respectively (see figure 4.7). Binding of cations (e.g. Cs^+) shifts the positions of both amide bands to lower frequencies of ca. 1631 and 1540 cm^{-1} due to the widening of the pore.[112,127]

FTIR spectria of gA in SDS micelles and POPC liposomes showed that the amide I of the $\beta^{6.3}\beta^{6.3}$ helix dimer is located between 1631 and 1629 cm^{-1} with a visible weaker amide I component at ca. 1670 cm^{-1}.[127] The shoulder at ca. 1650 cm^{-1}, which is present in all double helix forms, is absent for the channel. The amide II band of the helical dimer

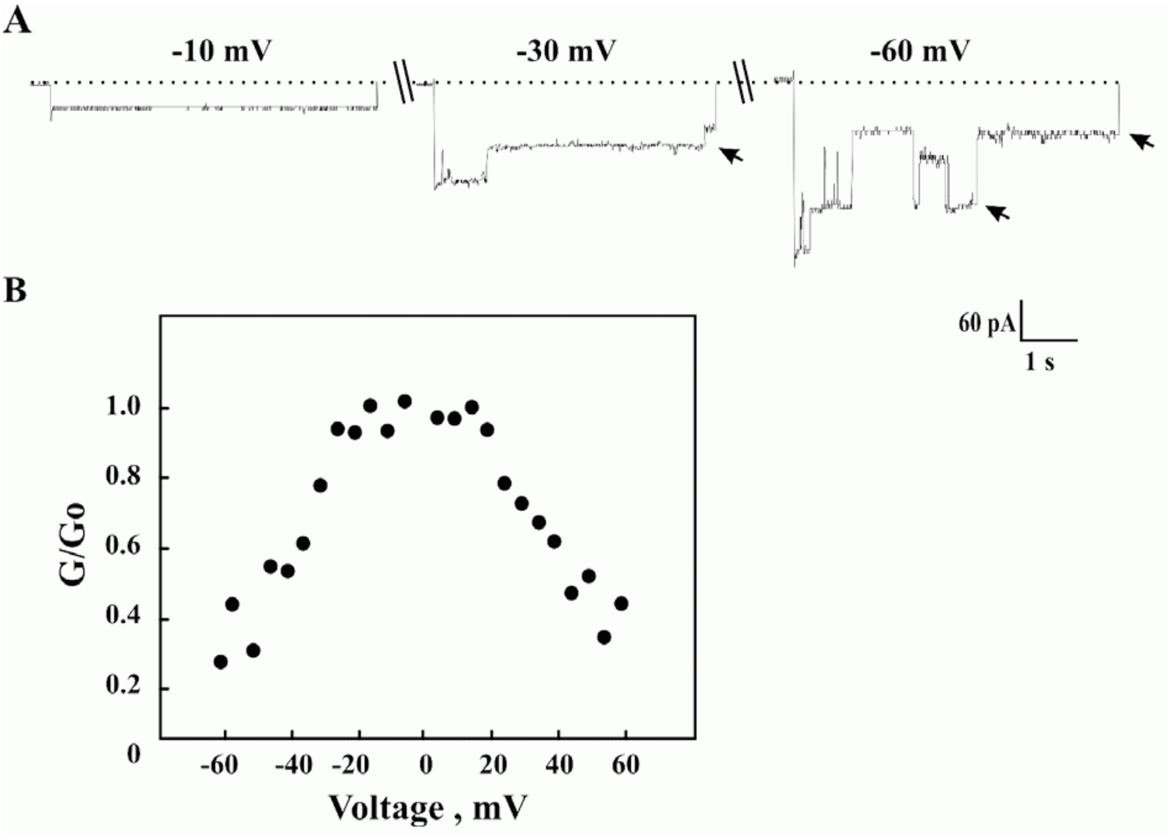

Figure 4.8: Channel activity of bilayer-reconstituted VDAC. A: Current traces during the application of potential steps form o mV to -10, -30, and -60 mV. At -10 mV the channel shows stable conductivity for several hours. At higher potentials VDAC adopts less conductive states. B: Voltage-dependent conductance of VDAC (G_0 represents the conductance at -10 mV).[7] (Reprinted from Mol. Asp. Med., 31, V. Shoshan-Barmatz, V. de Pinto, M. Zweckstetter, Z. Raviv, N. Keinan, N. Arbel, VDAC, a multi-functional mitochondrial protein regulating life and death, 227-285, Copyright (2010), with kind permission from Elsevier)

structure is shifted to higher wavenumbers and has a maximum at ca. 1553 - 1556 cm^{-1}. Binding of cations to membrane-embedded gA has not been studied that extensively with IR spectroscopy. It was observed that the presence of monovalent cations shift the equilibrium of gA conformation to the dimer helix state.[112] To date, however, structural changes of single amino acids were not in the focus of IR spectroscopic studies.

4.3. Human Voltage-Gated Anion Channel

The voltage-gated anion channel (VDAC), also known as the mitochondrial porin, is a membrane protein from the mitochondrial outer membrane (MOM). Its general function is to govern the exchange of metabolites and hence chemical energy between the mitochondrium and the cytosol. Moreover, it was found to play a key role in the regulation of mitochondria-mediated apoptosis (programmed cell death) which again is involved in the pathophysiology of several diseases and neurodegenerative disorders, such as heart attack, stroke, cancer, aging, and Parkinson's and Alzheimer's desease, as well as viral infection, e.g., Influenza A and Hepatitis B. In this way, hDVAC appears to be the linchpin for cellular decisions about life and death. Although the exact mechanistic details in apoptosis are still under debate,

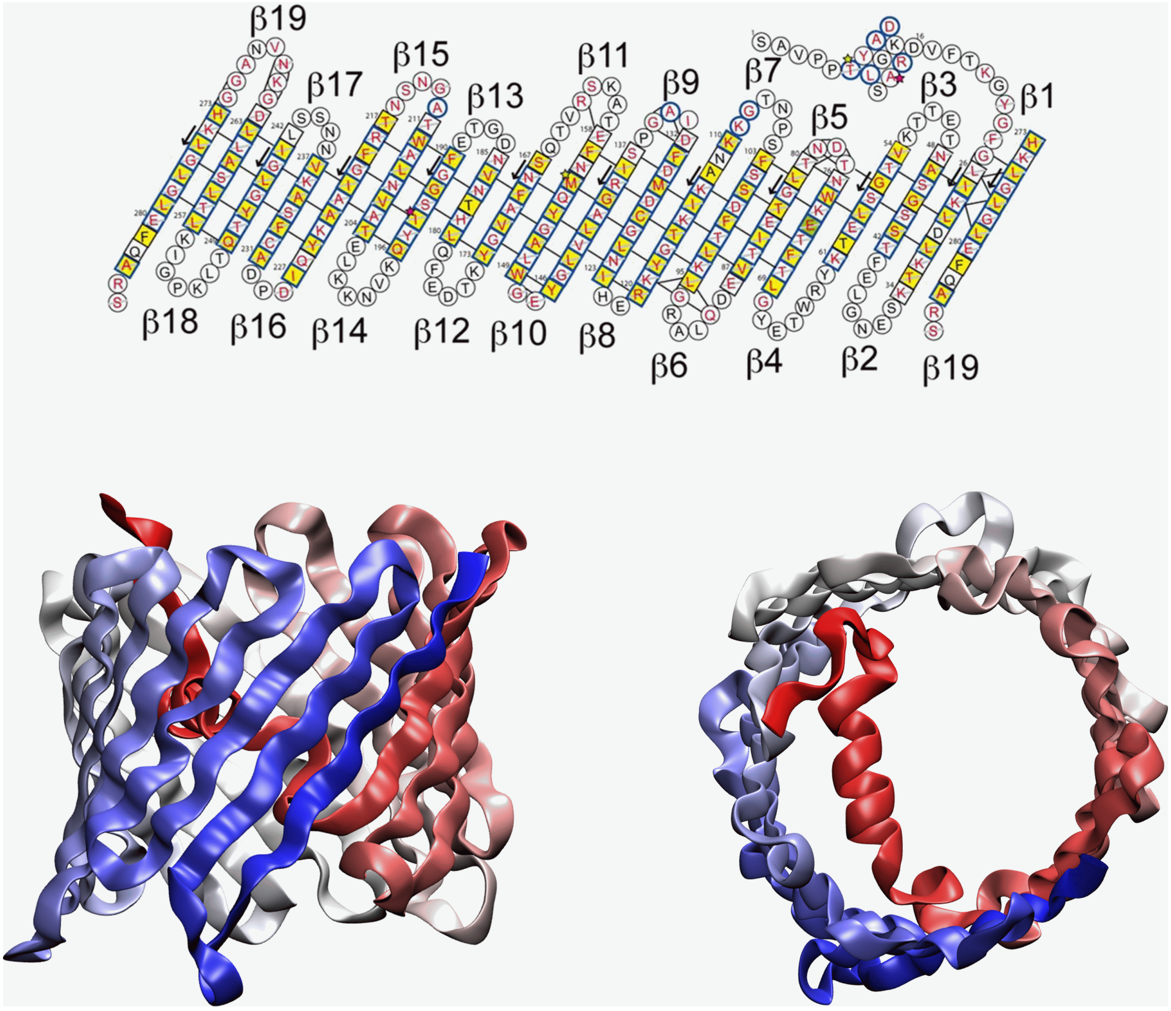

Figure 4.9: Top: 2D topology structure showing the amino acid sequence and arrangement of β-sheets of the human voltage-gated anion channel[140] (hVDAC; reprinted from Proc. Natl. Ac. Sci. USA, 105, M. Bayrhuber, T. Meins, M. Habeck, S. Becker, K. Giller, S. Villinger, C. Vonrhein, C. Griesinger, M. Zweckstetter, K. Zeth, Structure of the human voltage-dependent anion channel, 15370-15375, Copyright (2008), with kind permission from the National Acadamy of Science USA). The β-strands are enumerated with $\beta 1$ - $\beta 19$ from the N to the C-terminus. Bottom: 3D structure of hVDAC from the side (left) and from top (right). The N-terminus is located at the red part of the protein and the C-terminus at the blue part. (PDB ID: 2JK4)

VDAC is involved in the release of apoptotic proteins, such as cytochrome c, from mitochondria. For instance, by binding of the pro-apoptotic protein Bax to VDAC, oligomeric structures with pore sizes large enough to translocate the folded cytochrome c are formed and, thus, apoptosis can be initiated. However, apoptosis might also be impeded by the binding of hexokinases to VDAC which is one of the mechanisms to prevent cell death in carcinogenic cells. This renders VDAC a possible target for therapies of several diseases, such as cancer. Shoshan-Barmatz et al. present a detailed review about the importance and involvement of VDAC in regulating cell life and death.[7]

In this work, the focus is laid on the gating mechanism of VDAC. Although denoted as “anion channel”, in its open state, VDAC is permeable for small ions, such as Cl^-, K^+, and Na^+, as well as for large anions and cations. The latter include glutamate, ATP (adenosine-5’-triphosphate), or acetylcholine, dopamine, and Tris (tris(hydroxymethyl)aminomethane), respectively (see [Shoshan-Barmutz et al. 2010][7] and therein contained references). The slight anion selectivity (for KCl: P_{anion}/P_{cation}=2/1) is caused by several positively charged amino acid residues in the pore interior. This open state, with a single-channel conductance for KCl between 4 and 5 pS, is stable at low membrane potentials around 0 mV (< 10 mV, or > -10 mV, respectively). Upon increasing the potential in negative and positive manner, multiple sub-states with different ionic selectivities and permeabilities are generated. At higher potentials (> |±40 mV|), VDAC finally adopts the "closed state" with a specific conductance of 2 pS and a selectivity for cations (see figure 4.8). On the single channel level, these two states were reported to be observed as well with open probabilities of 100 % at 0 mV and ca. 60 % at potentials > |±40 mV|. Although, this is a generally accepted view, Steinem et al. shown that the channel closes only with a probability of 5 % (thus the open probability is 95 %) when the entire experiment was considered instead of only the periods in which closing events occurred (unpublished data). To date, this voltage-dependent conductivity of VDAC was observed only in *in-vitro*-experiments where the channel was incorporated into artificial membrane systems. Since it is not even known if the MOM exhibits a membrane potential, it is not clear if such a behavior takes place in mitochondria. However, it was speculated that the potential across mitochondrial inner membrane (MIM) may influence MOM.[141] Therefore it is postulated that at high MOM potentials, the metabolite flux is hindered and, thus, blocking larger molecules, in particular, nucleotides. Modeling of electrophysiological experiments yielded an energy for channel closure of ca. 7.7 kJ mol^{-1} which lies in the range of energy of one hydrogen bond. This indicates a low energy process involving the alternation of only 2 - 3 charged residues during the closing event.[142]

To date, three types of VDAC proteins were found, i.e. VDAC1, VDAC2 and VDAC3. VDAC1 is the most abundant and most active of these three, and probably the evolutionary youngest variant. In addition, studied were performed on channels from different organisms. In this work, human VDAC of the type 1 was investigated and will be denoted as hVDAC.

4.3.1. Structure of the Human Voltage-Gated Anion Channel

In 2008, the structure of hVDAC(1) (and murine VDAC1)[143] was resolved at atomic resolution using different approaches.[140,144] and is in line with predictions from previous experiments.[7] The 3D structure shown in figure 4.9 (bottom) unveiled a 19-stranded β-barrel with an N-terminal α-helix which is located inside the pore. These amphiphilic β-strands have an average length of ca. 10 amino acids, are tilted by 27° to 46° (37° on average) in respect to the barrel axis, and are connected by 18 flexible loops. Adjacent to the loops, two incomplete aromatic girdles around the barrel (parallel to the membrane plane) are formed and are separated by ca. 1.5 nm from each other. Due to the untypical uneven number of β-strands, which is in contrast to bacterial outer membrane pores, a parallel alignment of the strands $\beta 1$ and $\beta 19$ is formed, so that both, the N and C-terminus, face one side of the barrel opening. The barrel pore is approximately 4 nm long with an entrance size of ca. 3.1×3.5 nm, and a inner pore size of ca. 1.5×1 nm. This provides enough space for the translocation of small metabolites. This narrowing is achieved by the amphiphatic N-terminal α-helix (between Tyr-7 an Val-17 with an overall charge of zero) which is located horizontally, halfway through the pore. The preceding amino acids, Val-3 to Tyr-7 are only loosely attached to the barrel wall and point out of the barrel. The helix is fixed by a short stretch of negatively charged Asp that are aligned almost in parallel to the β-sheets and interact with highly conserved, hydrophilic amino acid residues of the barrel wall (His-181, Ser-193, Tyr-195, Lys-224), but is still provided with slight flexibility.[143] Positive amino acid residues of the helix are oriented towards the center of the barrel. As the primary structure of hVDAC from yeast to men is highly conserved, this structure is probably adopted by all VDAC isoforms in all eukaryotes.[145] Investigations of the orientation of VDAC inside the MOM lead to contradictory information about the C and N-termini facing the cytosol or the inter-membrane space, or even both in an anti-parallel dimeric structure.[146,147]

Gating Mechanism of the Human Voltage-Gated Anion Channel The lumen of the hVDAC pore is extensively hydrophilic. In the open state, the barrel walls are equipped with 15 positively charged and 11 negatively charged amino acid residues. Furthermore, the α-helix carries 3 positive and 2 negative groups: Lys-12, Lys-20, Arg-15, and Asp-9, Asp-16, respectively. In this way, the pore interior has a higher density of positive charges which is probably the reason for the anion selectivity. For the closed state, where the pore lowers its conductivity and becomes more cation selective, the N-terminal α-helix and also some β-strands are very important in voltage sensing. Mutation of Asp-16 and Lys-20 of the helix, as well as several lysines of the β-strands $\beta 1$ to $\beta 5$, for instance, had a strong influence on the function of VDAC.[148]

To date, several models for the gating mechanism were proposed based on the rearrangements of the α-helix or changes in the β-barrel structure. The former is based, on one hand, on the movement of the whole helix (or the residues 11-20) towards the center of the pore to create a steric hindrance associated with a partial or complete unfolding of the helix.[140,143,144] On the other hand, the electric field might interact with the dipole of the helix in such a way that its orientation is changed and hence the electrical properties of the channel are altered as well. The other model takes into account the less stable parallel β-strand alignment between strands $\beta 1$ and $\beta 19$ and the high amount of charges on $\beta 1$ to $\beta 8$.[140] This could enable the channel to adopt conformations that tighten the pore upon changes in the transmembrane potential.

A recent publication by Teijido et al.[149] showed that the model in which the helix moves independently is rather unlikely. In these studies, VDAC still exhibited voltage-dependent gating after covalent fixing of the helix to the wall. Furthermore, the α-helix and the β-strands $\beta 8$ - $\beta 15$ that flank the helix have a rather rigid structure which might indicate that the helix is important for stabilizing the integrity of the β-barrel.[150] Taking these data into account, a combined model is conceivable: Flexible parts of the VDAC β-barrel allow for a partial constriction that might induce an elongation along the barrel axis, and an associated, concerted pore narrowing and helix translocation.[149]

4.3.2. Infrared Spectroscopy of the Human Voltage-Gated Anion Channel

IR spectroscopy was used only sparsely to study the secondary structure of VDAC and the inclination of the complete barrel in respect to the membrane plane.[151] Figure 4.10 shows ATR-IR spectra of VDAC31 and VDAC32 from *P. vulgaris* reconstituted into asolectin bilayers. The main amide I component is located at 1631 cm^{-1} which is, together with the weaker component at ca. 1695 cm^{-1}, indicative of a β-sheet structure. The shoulder at ca. 1660 cm^{-1} can be assigned to the α-helix located within the VDAC pore. The broad amide II band (1570 - 1510 cm^{-1}) has a maximum at 1530 cm^{-1}. The comparison with the amide I of the β-barrel protein OmpF (1629 cm^{-1}) shows that VDAC has shorter β-strands ($\sim$ 10 amino acids) which is indeed the case as OmpF has an average β-strand length of 12 amino acids.

Dichroic spectra measured with ATR-IR allow for displaying only the absorption of the z-polarized component of the electromagnetic field by subtracting the spectrum with perpendicular polarized IR radiation from the one with parallel polarized IR radiation (see figure 4.10 right). In this spectrum, both the main β-sheet component of the amide I (at ca. 1630

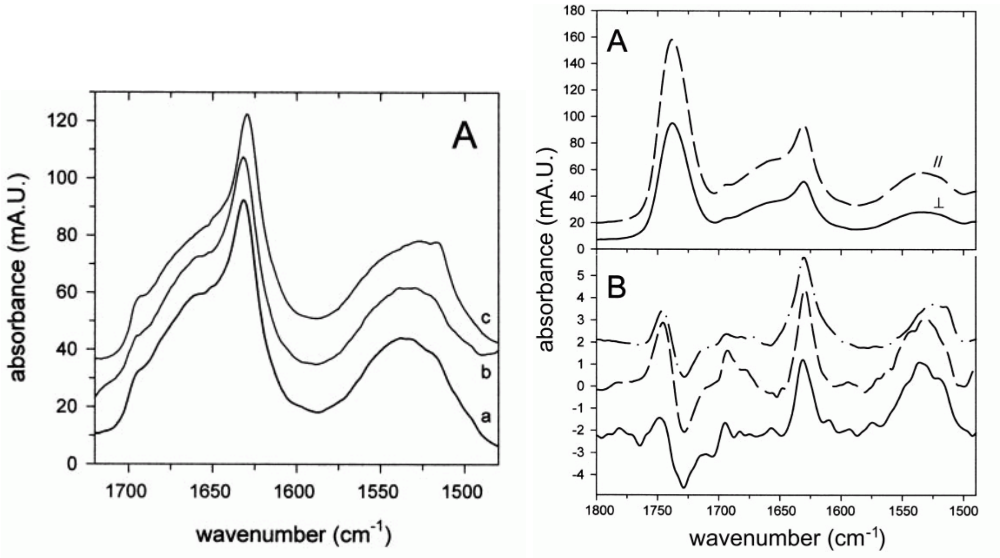

Figure 4.10: Left: ATR-IR spectra of the VDAC isofrom VDAC31 (a) and VDAC32 (b) *P. vulgaris*, and the β-barrel protein OmpF (c) reconstituted in asolectin with 5 % stigmasterol. Right: The top spectrum shows the ATR-IR spectrum recorded with perpendicular and parallel polarized light. The bottom spectra represent the dichroic spectra calculated as $A_{||}$ - $A_{\perp}$. This results in the spectrum of z-polarized component of the electromagnetic field: VDAC 31 (line), VDAC 32 (dashed line), and OmpF (dashed-dotted line).[151] (This research was originally published in J. Biol. Chem., H. Abrecht, E. Goormaghtigh, J.-M. Ruysschaert, F. Homble, Structure and Orientation of Two Voltage-dependent Anion-selective Channel Isoforms, 2000, 275, 40992-40999, Copyright (2000) with kind permission from the American Society for Biochemistry and Molecular Biology)

cm^{-1}) and the entire amide II band can be perceived. The remaining amide I components show rather weak intensity. Structural changes of VDAC upon changes of membrane potential have not been studied yet with IR spectroscopy due to the lack of spectroelectrochemical IR methods.

Part II.

Experimental Section

5. Experimental Details

5.1. Chemicals and Preparation Tools

Chemical	distributor
2-Propanol	Merck
6MH	Sigma Aldrich
Ag/AgCl reference electrode	World Precision Instruments, Inc.
$BaCl_2 \cdot 5H_2O$	Merck
Chloroform	Merck
CPEO3	provided by Prof. Claudia Steinem
CsCl	Merck
DCl	Sigma Aldrich
Deuterium oxide	Deutero GmbH
Extruder	Avestin
gA	provided by Prof. Claudia Steinem
HCl	Merck
HF	Fluka
hVDAC	provided by Prof. Claudia Steinem
K_2HPO_4	Merck
KCl	Sigma Aldrich
KH_2PO_4	Merck
LDAO	Sigma Aldrich
LiCl	Merck
$Na_2S_2O_3 \cdot 5H_2O$	Sigma Aldrich
Na_2SO_3	Merck
$NaAuCl_4 \cdot 2H_2O$	Sigma Aldrich
NaCl	Merck
NH_4Cl	Sigma Aldrich
NH_4F	Sigma Aldrich
Polycarbonate filters (100 nm)	Avestin
POPC	Avanti Polar Lipids
TlF	Alfa Aesar
Tris	Serva Electrophoresis GmbH

Table 5.1: Chemicals and preparation tools used in this work. All solutions were prepared using MilliQ water (> 18 mΩ).

Gramicidin A (gA) from *Bacillus brevis* and the human voltage-gated anion channel (hVDAC; type 1) were kindly provided by Prof. Claudia Steinem. hVDAC, containing an additional RGS-fragment at the N-terminus, was overexpressed in *Escherichia coli*, purified and refolded into LDAO micelles.[152]

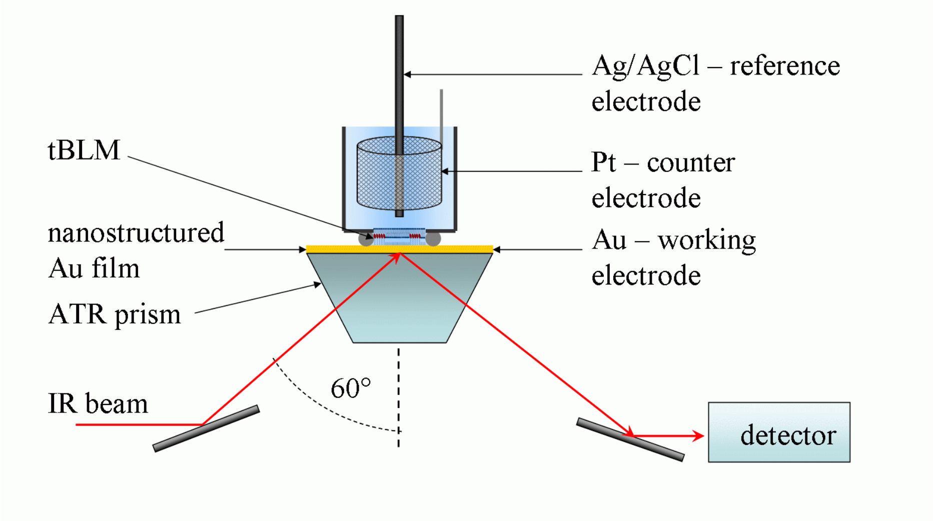

Figure 5.1: Schematic representation of the spectroelectrochemical SEIRA cell. The nanostructured SEIRA Au film serves as the IR signal amplifier and the the working electrode in one setup.

5.2. Instrumentation

5.2.1. Surface-Enhanced Infrared Absorption Spectroscopy

SEIRA spectra were recorded using a Bruker IFS66v/s FTIR-spectrometer equipped with an ATR set-up in the Kretschmann configuration, a photoconductive liquid N_2-cooled MCT-detector (HgCdTe), and a globar as the IR radiation source. The globar, the Michelson Interferometer, and the detector were operated under vacuum; solely the sample chamber was purged continuously with nitrogen gas. As the ATR prism, a trapezoidal Si crystal (L × W × H = 25 mm × 20 mm × 10 mm) was used and irradiated at an angle of incidence of 60° with a resulting measuring area of 7 mm × 3 mm. Spectra were acquired in the spectral region between 4000 and 1000 cm^{-1} with a spectral resolution of 4 cm^{-1}. Each spectrum is composed of 400 scans, taking 3 min to be accumulated. To perform SEIRA and EIS experiments, the ATR prism was coated with a nanostructured Au film. SEIRA spectra were evaluated using the OPUS 5.5 software.

Spectroelectrochemical Cell The Au-covered ATR prism was introduced into a home-made spectroelectrochemical SEIRA cell depicted in figure 5.1. Electrochemical treatments were performed using a three-electrode configuration: the Au film (real area of ca. 1.65 cm^2; geometric area of 0.79 cm^2 corrected by the roughness factor of 2.1 - *vide infra*; newly determined for each Au film using the Au-oxide reduction charge density method), a Pt-wire, and an Ag/AgCl (3 M KCl) electrode serving as working, counter, and reference electrodes, respectively (all potentials are referred to the Ag/AgCl electrode).

Electroless Au Deposition The nanostructured SEIRA Au film was prepared by electroless deposition.[153] For this purpose, first, the surface of the ATR Si prism was polished with alumina powder (Microgrit WCA-9, grain size: ca. 6 μm) and thoroughly rinsed with water. Subsequently, the prism was immersed into a 400 g/L NH_4F solution for 2 min to remove the oxide layer on the Si surface. Eventually, the Au film was deposited at a temperature of 65 °C by adding the Au plating solution onto the Si surface. After 1 min, the Au deposition was aborted by dilution with water. The plating solution is composed of an aqueous

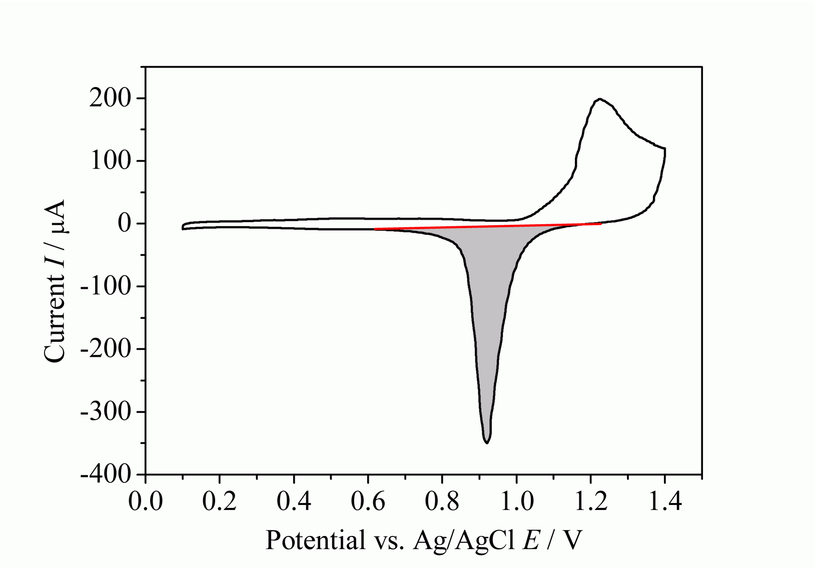

Figure 5.2: Electrochemical cleaning of the nanostructured Au electrode with cyclic voltammetry in 0.1 M H_2SO_4. The real area of the Au electrode was obtained from the Au-oxide reduction charge by calculating the area under the reduction peak at 790 mV (grey area).

1:1:1 (volume ratio) admixture of a 2 % (w/w) HF solution, a 0.03 M $NaAuCl_4 \cdot 2H_2O$ solution, and reduction solution comprised of 0.3 M Na_2SO_3, 0.1 M $Na_2S_2O_3 \cdot 5H_2O$, and 0.1 M NH_4Cl. The deposition is based on the reduction of Au^{III} and the associated oxidation of the Si surface:

$$\mathrm{Si^0(s) + 6F^-(aq) \rightarrow SiF_6^{2-}(aq) + 4e^-} \tag{5.1}$$

$$\mathrm{AuCl_4^-(aq) + 3e^- \rightarrow Au^0(s) + 4Cl^-}(aq) \tag{5.2}$$

Electrocleaning of Au Immediately after the electroless deposition, the Au film was cleaned electrochemically by conducting 6 oxidation/reduction cycles between the potentials of 0.1 and 1.4 V in a 0.1 M H_2SO_4 solution. During this procedure, the solution was purged constantly with Ar to remove O_2 and, thus, to avoid the generation of aggressive oxygen species. A typical voltammogram, shown in figure 5.2, includes a Au oxidation at potentials higher than 1.1 V and a single reduction peak centered at ca. 920 mV. On the basis of this reduction peak, the real area of the Au electrode was calculated using the Au-oxide reduction charge density method. For this purpose, the charge needed to reduce the surface Au-oxide was determined from the area of the reduction peak and compared with the specific charge density of 400 μC cm^{-2}.[154]

5.2.2. Electrochemistry

Electrochemical treatments were conducted using a μAutolabIII/FRA2. The application of static potentials for the measurements of potential-dependent SEIRA spectra was controlled using the Nova 1.8 software; electrochemical impedance spectra were recorded using the FRA software. Impedance spectra were monitored in a frequency range of 0.1 to 100 kHz using a static potential of 0 V and an amplitude of 25 mV (rms value).

Evaluation of EIS data Figure 5.4 shows typical EIS spectra of a CPEO3/6MH SAM and a tBLM obtained in this work and plotted in the Nyquist, Bode, and Cole-Cole plot.

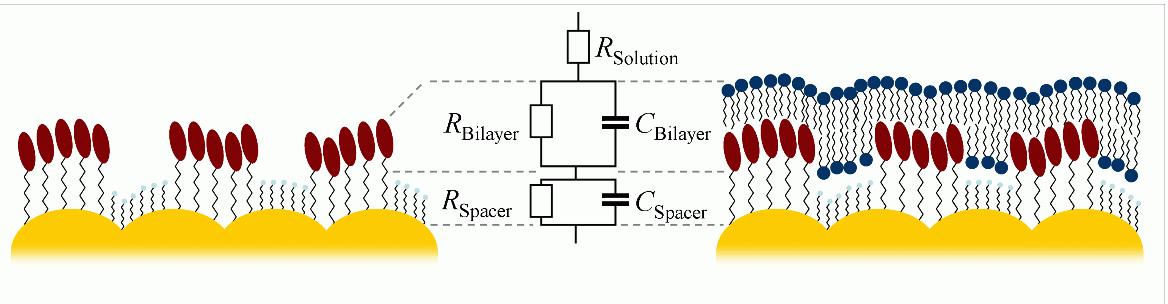

Figure 5.3: Equivalent circuit used to describe the dielectric properties of the mixed SAM (left) and the tBLM (right), respectively. The $R_{\text{Spacer}}C_{\text{Spacer}}$-element and the $R_{\text{Bilayer}}C_{\text{Bilayer}}$-element describe the spacer region (composed of 6MH and the polyethyleneoxy-linker) and the headgroup or bilayer region (composed of the POPC and the cholesteryl), respectively.

In contrast to the impedance spectra shown in figure 2.7, here, two dispersions are noted. This phenomenon is caused by the rough nanostructured surface of the SEIRA Au electrode which slightly disturbs the arrangement of the tBLM allowing water to penetrate below the cholesteryl groups. Hence, the two dispersions of the Nyquist and the Bode plot can be ascribed to the two hydrophobic components in the SAM and tBLM: the spacer region, composed of the polyethyleneoxy linkers and the 6MH molecules, and the bilayer region, composed of the cholesteryl headgroups and phospholipid molecules (see figure 5.3). In the Cole-Cole plot, however, the first half circle describes the dielectric properties of the entire system. Therefore, the capacitance of the entire SAM or tBLM (C_{SAM} and C_{tBLM}, respectively) was determined from the Cole-Cole plot by reading out the radius of the first half cirlce in analogy to figure 2.7. These values were used through out the whole work. An alternative way is to fit an equivalent circuit, describing a simplified model composed of the ideal components of capacitances and resistances, to the EIS data:

$$R_{\text{Solvent}}(R_{\text{Spacer}}C_{\text{Spacer}})(R_{\text{Bilayer}}C_{\text{Bilayer}}). \tag{5.3}$$

This analysis is performed using a non-linear least squares fit of this equivalent circuit (see figure 5.3) based on the Levenberg-Marquardt algorithm, which is included in the FRA software.[43] An alternative model would include a CPE-element instead of the capacitor, from which the capacitance could be calculated as well (see 2.50 on page 22). Although this model is commonly used in literature[36] and leads to better fit results, the lack of a maximum in the Nyquist plot prevents from conversion to the capacitance. Therefore the CPE-element lacks a physical meaning and will not be applied in this work. As shown in figure 5.4, the first half circle is approximated by this fit very well leading to similar values for the overall capacitances of the tBLM C_{tBLM} and the SAM C_{SAM}. The second half circle, however, shows considerable deviation, thus, rendering the capacitances of the C_{Spacer} and C_{Bilayer} more error-prone. Due to the two dispersions, the overall resistance of the tBLM is also split into a spacer and a bilayer component. As visible in the Nyquist plot, neither the first nor the second dispersion is resolved fully. As a consequence, neither the resistance of the complete tBLM R_{tBLM} (due to the large electrode area), nor the one of the components of the spacer region R_{Spacer} and the bilayer R_{Bilayer} can be approximated by the fit reliably. Solely the resistance of the bilayer region (R_{Bilayer}) lies within the range of the Nyquist plot. However, this value will be used rather semi-quantitatively.

Therefore, in the following, the capacitance determined by the radius of the Cole-Cole plot will be used for the discussion of the overall capacitance of the tBLM C_{tBLM} and interpretation of the data. The fit will be shown as well, when needed to demonstrate that the system

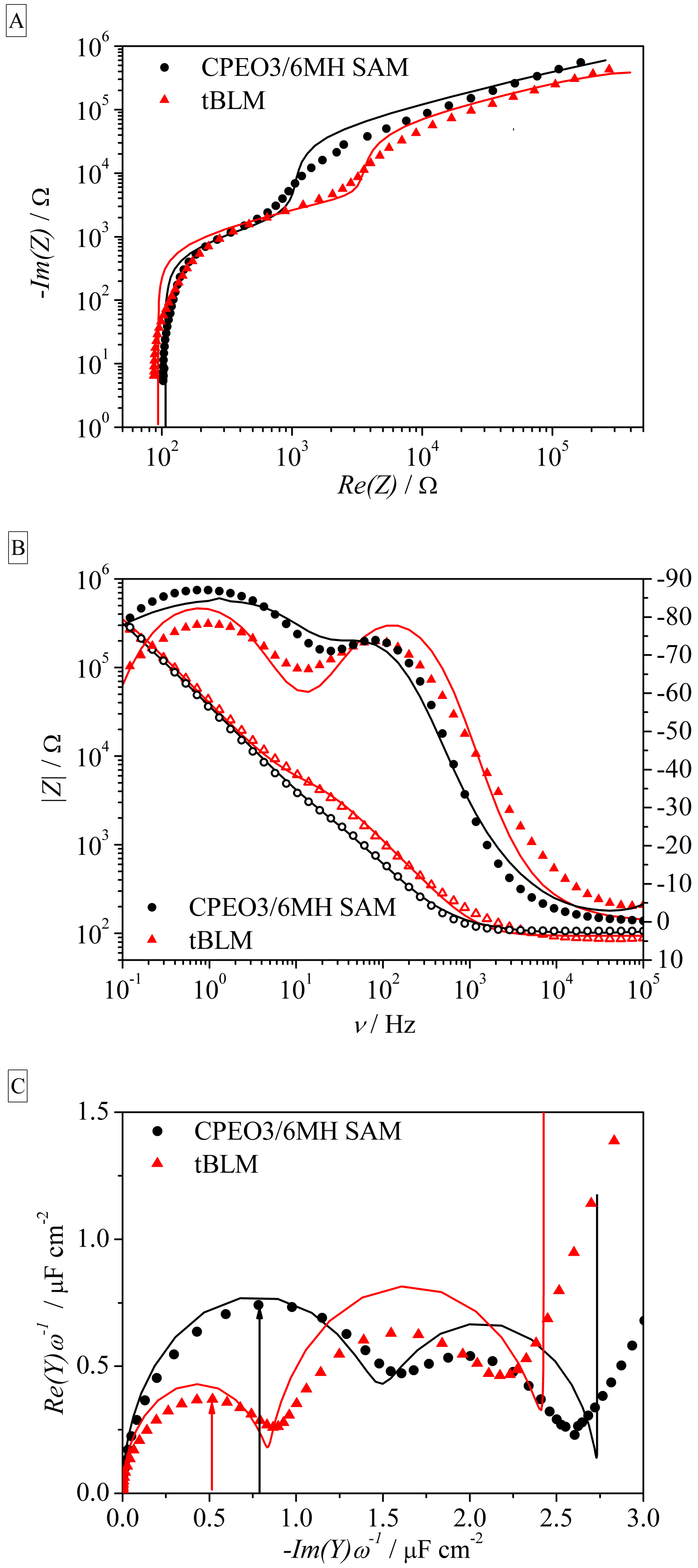

Figure 5.4: The Nyquist (**A**), Bode (**B**), and Cole-Cole plot (**C**) of a CPEO3/6MH (black circles) and a tBLM (red triangles) on the SEIRA Au electrode, respectively. In the Bode plot, filled and hollow symbols refer to the phase angle (right axis) and the magnitude of the impedance (left axis). Lines represent the fitting with the equivalent circuit $R_{\text{Solvent}}(R_{\text{Spacer}}C_{\text{Spacer}})(R_{\text{Bilayer}}C_{\text{Bilayer}})$ based on figure 5.3.

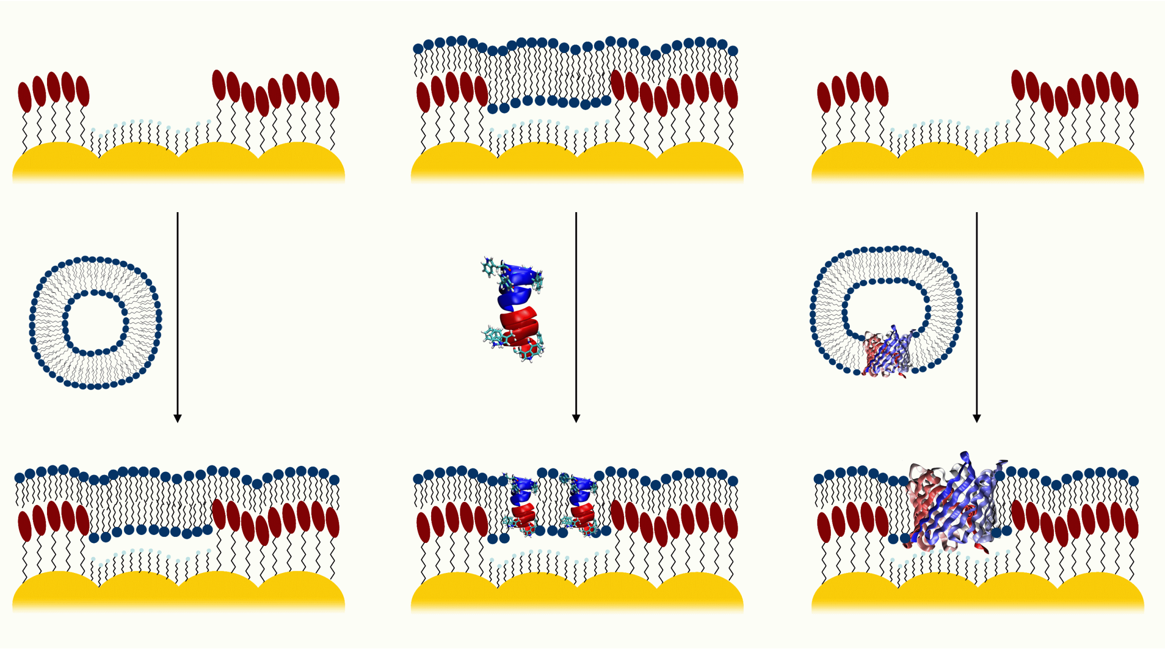

Figure 5.5: Schematic representation of the construction of pure tBLMs (left), gA-containing tBLMs (middle), and hVDAC-containing tBLMs by fusion of POPC vesicles, direct incorporation from the bulk solution, and fusion of hVDAC-containing POPC vesciles, respectively.

can be approximated by a model of resistances and capacitors, and to be able to discuss the insulating properties of the system semi-quantitatively using the resistance R_{Bilayer}.

5.3. Preparation

5.3.1. Membrane Proteins Incorporated into tBLMs

All buffers for the spectroelectrochemical SEIRA/EIS experiments contained 20 mM Tris-HCl, pH 7.4 with additional 100 mM of a chloride salt (i.e. $BaCl_2$, LiCl, NaCl, KCl, CsCl). Due to the poor solubility of TlCl in water, 20 mM Tris-HF, pH 7.4 with 100 mM TlF was used instead. These buffers will be referred to as e.g. the “Na^+-buffer”. The Na^+-D_2O-buffer was composed of 100 mM NaCl, 20 mM Tris-DCl, pD 7.8. All experiments with D_2O were performed under constant Ar purging to avoid D_2O-H_2O exchange with atmospheric H_2O.

Preparation of unilamellar vesicles For the preparation of unilamellar POPC vesicles 10 μL of a 25 mg mL^{-1} stock solution of POPC (in CH_3Cl) were diluted with 100 μL of CH_3Cl in a test tube and, subsequently, dried under an Ar stream and vacuum over night to obtain lipid multilayer films. The POPC film was covered with 500 μL of the Na^+-buffer. After 10 min of swelling, the test tube was vortexed 3 times for 30 sec with 10 min breaks in between. After the third time, the turbid vesicle solution was extruded through a polycarbonate filter with a pore size of 100 nm for 31 times to obtain 100 nm-sized unilamellar POPC vesicles.

Construction of Tethered Bilayer Lipid Membranes The tBLM was constructed by spreading and fusion of unilamellar POPC vesicles as follows (figure 5.5 left): A mixed monolayer of CPEO3 and 6MH was self-assembled on the SEIRA Au-electrode over night using 400 μL of a mixture of 0.05 mM CPEO3 and 0.05 mM 6MH in iso-propanol. After rinsing with iso-propanol and buffer, 500 μL of unilamellar POPC vesicles (0.5 mg mL^{-1} in 100 mM NaCl, 20 mM Tris-HCl, pH 7.4) were added onto the monolayer for 3-4 hours. Subsequently, the cell was rinsed extensively with fresh buffer to remove the excess of vesicles. After each step, an impedance spectrum was recorded to characterize the tBLM.

To evaluate the properties of the tBLM depending on the composition of the mixed SAM, the ratio between CPEO3 and 6MH was varied in such a way that the total molar concentration was 0.1 mM. All CPEO3/6MH mixtures were prepared one day before the SAM formation, since fresh solutions tend to result in scattered surface concentration ratios. After equilibration of the mixed CPEO3/6MH solutions over night at -30°C, reproducible SAMs were obtained.

Electrochemical Treatment (ECT) The application of an electrochemical treatment (ECT), comprised of switching between the open circuit potential E_{OCP} and a 60 mV higher potential every 6 min for 8 hours, improved the quality of the tBLM. This improved tBLM, however, was only used for the experiments conducted with hVDAC-containing tBLMs.

Incorporation of Gramicidin A Gramicidin A was incorporated directly into the tBLMs constructed on the SEIRA Au film (figure 5.5 middle): a gramicidin A solution in TFE was added into 4 mL of the supernatant Cs$^+$-buffer covering the tBLMs to yield a final concentration of 0.2 μM. After 1 hour, the incubation was stopped by buffer exchange. For this, prior to the addition of gA, the buffer was exchanged to the Cs$^+$-containing one, as Cs$^+$ ions promote the formation of helical dimer structures. Alternatively, the incorporation of gA was conducted in Ba^{2+}-buffer.

Incorporation of Human Voltage-Gated Anion Channel hVDAC was incorporated into the unilamellar vesicles prior to the tBLM formation (figure 5.5 right): unilamellar vesciles were prepared in 450 μL and mixed with 50 μL of a 65 mM LDAO solution (in Na$^+$-buffer) to yield 0.5 mg mL^{-1} POPC and 6.5 mM LDAO in Na$^+$-buffer ($\mathrm{CMC_{LDAO}}$ = 2 mM). hVDAC was incubated in this vesicle-detergent mixture at a final concentration of 1 μM for 30 min at room temperature. To remove the detergent, 25 mg BioBeads were added and shaked, first, for 2 hours at 4°C and subsequently over night at 4°C with freshly added 25 mg Biobeads. These hVDAC-reconstituted proteoliposomes were added onto the mixed CPEO3/6MH SAM to form a hVDAC-tBLM system in one step. After 3-4 hours the incubation was aborted by exchange with fresh buffer.

Experiments with D_2O The construction of the tBLM with and without hVDAC was carried out in D_2O, as well, to shift the H-O-H bending of water from 1646 cm^{-1} to the D-O-D bending at 1206 cm^{-1}. During these experiments the bulk solution was purged with Ar constantly, so that no D_2O-H_2O exchange with the atmospheric water was allowed to happen.

5.4. Execution of Experiments

5.4.1. Spectroelectrochemistry of Membrane Proteins Incorporated into tBLMs

Formation of Tethered Bilayer Lipid Membranes In each experiment, impedance spectra were taken of the mixed SAM and the tBLM after spreading of vesicles for 3-4 hours in the

Na^+-buffer. SEIRA spectra were measured during the entire tBLM formation process taking the spectrum of the SAM in Na^+-buffer as a reference. The reference spectrum contained 400 scans, as longer incubation times of the CPEO3 SAM with buffer resulted in worse tBLM properties. This is probably due to penetration of water molecules in between the CPEO3 chains (see section 6.1.1.2). This approach was repeated for SAMs composed of different CPEO3/6MH ratios. For the 1:1-CPEO3:6MH molar ratio (in solution), the tBLM formation was monitored in D_2O-buffer as well.

Incorporation of Gramicidin A The incorporation of gA into the tBLM was followed with SEIRA taking the spectrum of the tBLM in the Cs^+-buffer or Ba^{2+}-buffer as a reference spectrum. Impedance spectra were recorded of the pure tBLM and of the tBLM-embedded gA after 1 hour of incubation. The incorporation was stopped by removal of residual gA from the bulk solution and rinsing with fresh buffer.

Functionality of Gramicidin A The influence of different cations (Ba^{2+}, Li^+, Na^+, K^+, Cs^+, Tl^+) on the membrane-bound gA channel (incubated in presence of Cs^+) was investigated with SEIRA and EIS. After cation exchange, SEIRA difference spectra were recorded using the spectra recorded in Ba^{2+}-buffer as a reference. To guarantee a stable background, a new spectrum in Ba^{2+}-buffer was taken directly after the recording the spectrum in the presence of monovalent cations. All difference spectra were calculated taking 5 times 400 scans in the presence of each cation.

Evaluation of SEIRA difference spectra of the gA-tBLM sytem Exchanging cations leads to a change of the water content in the headgroup region of the bilayer. Hence, M^+ vs. Ba^{2+} SEIRA difference spectra show a broad negative band centered at ca. 1650 cm^{-1} due to the extended solvation shell of Ba^{2+} and the much smaller of monovalent cations. Unfortunately, this band overlaps with the amide I difference band of gA. To appreciate these peptide changes in more detail, the negative water band was fit by a combination of 4 Gaussian functions in the absence of gA (figure 5.6 bottom). This combination of Gaussians was then used to remove the negative water band from the spectrum in presence of gA (figure 5.6 top).

Incorporation and Functionality of Human Voltage-Gated Anion Channel The spreading of hVDAC-containing POPC vesicles was followed with SEIRA taking the spectrum of the mixed SAM in Na^+-buffer as reference. EIS was performed of the hVDAC-tBLM after incubation for 4 hour and subsequent exchange for fresh buffer. As a comparison, a tBLM was constructed on a SAM originating from the very same CPEO3/6MH solution to provide a common starting point. After the successful tBLM formation, a potential switch of +60 mV against the open circuit potential was applied. This procedure showed to have influence on the SEIRA data, EIS data, and the open circuit potential, increasing the quality of the tBLM. Thus, this procedure was applied prior to each experiment leading to a equilibrated and stable system.

The influence of the transmembrane potential on tBLM-embedded hVDAC was studied spectroelectrochemically with EIS and SEIRA. Here, all experiments were done under constant purging with Ar to remove oxygen from the bulk solution. For this purpose, first the open circuit potential (E_{OCP}) of this system was determined as the long-term stable potential with a current of 0 A. This open circuit potential was used to define the “open-state” of hVDAC. In the section on functional studies of hVDAC all potentials are referred to E_{OCP}. EIS was performed at this potential, and at +60 and -60 mV (vs. E_{OCP}) to characterize

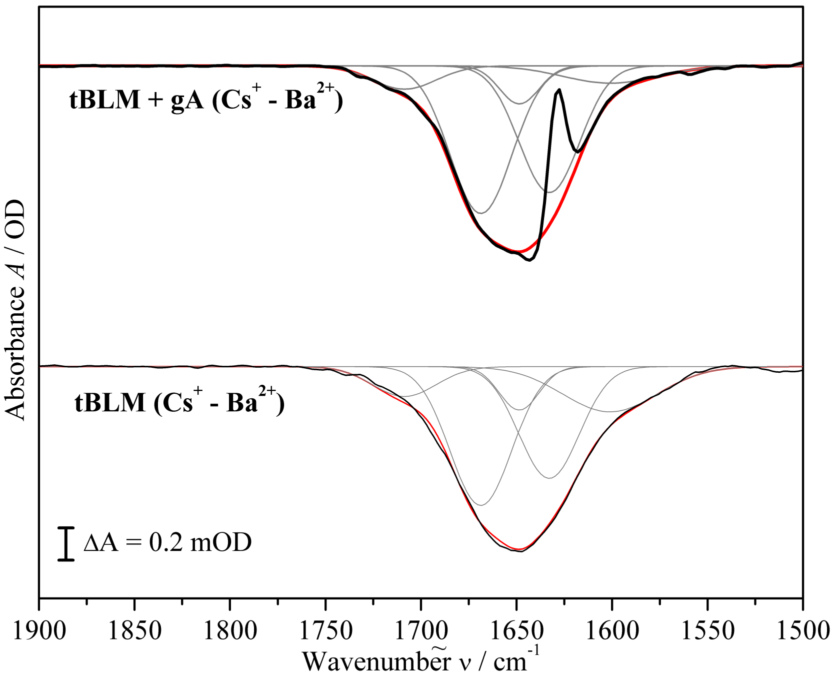

Figure 5.6: SEIRA difference spectra (black) of the tBLM with (top) and without gA (bottom) resulting from the exchange of Ba^{2+} to Cs^+. Both spectra show a broad negative band, which is caused by a rearrangement of the water molecules in the vicinity of the bilayer. To remove this contribution from the difference spectra of gA in the presence of different cations, the difference spectra (i.e M+ - Ba2+) have been baseline-corrected by subtracting an appropriate function (i.e. a linear combination of 4 Gaussian functions shown in red; single Gaussian components in grey) modeling negative water band.

the electrical properties of the open and closed-state of hVDAC, respectively. Additionally, the potentiostatic current was measured between -80 and +80 mV in 20 mV steps. Potential-induced structural changes were monitored with SEIRA difference spectroscopy. Here, spectra at +60 and -60 mV, respectively, were subtracted from the spectrum at 0 mV to obtain “closed-minus-open” spectra of hVDAC. To guarantee a high signal-to-noise ratio, the total accumulation time of one difference spectrum was 8 hours. In addition, long-term effects were efficiently avoided by measuring forward and backward-spectra, using the following loop which was repeated 40 times (40 × 4 × 3 min (400 scans) = 8 hours):

- **Spectrum 1:** open-state spectrum at 0 mV
- **Spectrum 2:** closed-state spectrum at ±60 mV
- **Spectrum 3:** closed-state spectrum at ±60 mV
- **Spectrum 4:** open-state spectrum at 0 mV

Subsequently, the forward and backward difference spectra were obtained as

- **Forward difference spectrum: Spectrum 2** at ±60 mV “minus” **Spectrum 1** at 0 mV
- **Backward difference spectrum: Spectrum 3** at ±60 mV “minus” **Spectrum 4** at 0 mV

and averaged to obtain the “closed-minus-open” hVDAC spectrum eventually.

These experiments were performed also in the absence of hVDAC to distinguish between potential-induced structural changes of the protein and of the phospholipids of the tBLM.

Part III.

Results and Conclusions

6. Results

In this chapter, the results of this work are presented in a systematic way. Since herein, tBLMs were constructed on a nanostructured substrate for the first time, first of all, the tBLM was characterized spectroelectrochemically by means of EIS and SEIRA, and compared with electrochemical data on tBLMs on flat Au surfaces published by Jeuken et al.[36,89] This includes the characterization of the mixed CPEO3/6MH SAM and its impact on the membrane quality. Furthermore, the tBLM formation process by spreading and fusion of unilamellar vesicles was monitored as well. In the next step, the transmembrane ion channel forming antibiotic gA was introduced into the tBLMs to examine the property of this artificial membrane system to act as a native-like environment for structural and functional studies. For this purpose, gA's channel activity was monitored spectroelectrochemically with EIS and SEIRA and provides information about the nature of gA-cation and phospholipid-cation interactions. Since most of the functional membrane proteins do not incorporate spontaneously into pre-formed tBLM without the use of further additives, the construction of a proteo-tBLM system from transmembrane protein-containing vesicles (or proteoliposomes) was investigated. For this purpose, hVDAC was chosen as, to date, this voltage-gated channel has not been studied in solid-supported systems such as tBLMs. Eventually, using the hVDAC-tBLMs, the suitability of this system in combination with the spectroelectrochemical approach provided by SEIRA will be examined. For this purpose, the voltage-gating mechanism was studied spectroelectrochemically by potential-induced SEIRA difference spectroscopy.

6.1. Construction of tBLMs on the nanostructured SEIRA Au film

The incorporation of membrane proteins into tBLMs requires the presence of patches of quasi free-standing phospholipid bilayers that are supported by a aqueous reservoir.[3] Pure CPOE3 SAMs, however, do not match this requirement. Therefore, inspired by the work of Jeuken et al.[89], in this work, tBLMs are engineered that are based on a mixed CPEO3/6MH SAM. The ratio between CPEO3 and 6MH on the Au surface plays a crucial role for the quality of the tBLM, as very low concentrations of CPEO3 do not induce vesicle fusion. However, at high concentrations, not enough space may be provided to insert integral membrane proteins. Therefore, in this section, first the dependence of the CPEO3-to-6MH mole fraction in solution on the molar CPEO3/6MH ratio of the SAM will be shown. Furthermore, SEIRA spectra of the SAMs will be presented since the knowledge about their spectroscopic signature is a prerequisite for the analysis of the SEIRA spectra of the complex protein-containing systems. In this respect, briefly, the influence of aqueous solutions on the SAM will be shown. Eventually, the formation of the tBLM on a mixed CPEO3/6MH SAM will be investigated more thoroughly. For this and throughout this whole work, a SAM composed of 80 % of CPEO3 and 20 % 6MH will be used as the system of choice, since it combines both requirements of pure phospholipid-phospholipid bilayer patches and good tBLM quality.

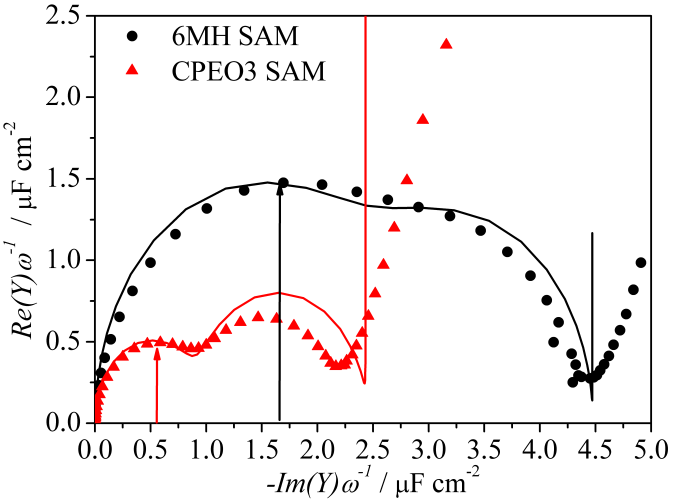

Figure 6.1: Cole-Cole plot of pure CPOE3 (black circles) and 6MH SAMs (red triangles), respectively. Lines represent the fitting with the equivalent circuit $R_{\mathrm{Solvent}}(R_{\mathrm{Spacer}}C_{\mathrm{Spacer}})(R_{\mathrm{Headgroup/Defect}}C_{\mathrm{Headgroup/Defect}})$ based on figure 5.3 on page 58.

	R_{Solvent} Ω	R_{Spacer} kΩ cm^2	C_{Spacer} μF cm^{-2}	$R_{\mathrm{Headgroup/Defect}}$ kΩ cm^2	$C_{\mathrm{Headgroup/Defect}}$ μF cm^{-2}	C_{SAM} μF cm^{-2}
CPEO3	110	910	2.44	1.99	1.73	1.02
6MH	107	2650	4.61	0.41	8.55	3.09

Table 6.1: Results of the fitting of the equivalent circuit $R_{\mathrm{Solvent}}(R_{\mathrm{Spacer}}C_{\mathrm{Spacer}})(R_{\mathrm{Headgroup/Defect}}C_{\mathrm{Headgroup/Defect}})$ to the EIS data of a pure CPEO3 and 6MH SAM, respectively. The last row is the result of reading out the capacitance of the entire SAM directly from the Cole-Cole plot. The error for the resistances and capacitances are 10 % and 5 %, respectively (n = 3).

6.1.1. Formation of the CPEO3/6MH SAM

6.1.1.1. EIS of CPEO3/6MH SAMs

As shown by Jeuken et al.[89], the surface concentration ratio between CPEO3 and 6MH differs from the ratio in solution due to different kinetics of binding. The formation of disulfide species is also a factor,[155] as, in this work, it was observed that freshly prepared CPEO3/6MH solutions gave monolayers with a scattering of the surface concentration ratio. Only after equilibration over night at -30°C (in iso-propanol) and incubation of the SEIRA Au electrode on the next day, reproducible monolayer coatings were achieved. The ratio of surface concentrations, given by the mole fraction of CPEO3 (χ_{CPEO3}) and 6MH (χ_{6MH}), was determined on the basis of the capacitance values of the mixed SAM obtained from EIS. For this purpose, first impedance spectra of pure CPEO3 and 6MH SAMs were recorded to obtain the capacitance values for both cases.

Pure CPEO3 SAMs Figure 6.1 shows the EIS data of pure CPEO3 and 6MH SAMs, respectively, plotted using the Cole-Cole plot. Both SAMs show two dispersions. This can be rationalized taking into account the nanostructure of the SEIRA Au electrode which induces heterogeneity to the SAM arrangement. In the case of the CPEO3 SAM, this leads to leaking of water molecules below the cholesteryl groups (*vide infra*), so that the spacer region and the cholesteryl headgroups can be perceived independently. Fitting with the simplified model of the equivalent circuit $R_{\mathrm{Solvent}}(R_{\mathrm{Spacer}}C_{\mathrm{Spacer}})(R_{\mathrm{Headgroup}}C_{\mathrm{Headgroup}})$ shown in figure 5.3 (on page 58; here, the index "bilayer" was exchanged to "headgroup" for increased clearness) accounts for both contributions which are described ideally as a parallel circuit of a resistance and a capacitor. In the Cole-Cole plot, the first half circle at high frequencies describes the capacitance of the entire SAM and is well reproduced by the fit; the second, however, shows considerable deviation. Since at the frequencies of the second half circle not the complete system is registered by EIS, the sole components C_{Spacer} and $C_{\mathrm{Headgroup}}$ may become more error-prone.

Table 6.1 shows the capacitance of the pure CPEO3 obtained from the Cole-Cole plot and the results of the fitting. The capacitance of the CPEO3 SAM obtained from the first half circle of the Cole-Cole plot yields a value of $\mathrm{C_{CPEO3}}$ = (1.02 ± 0.06) μF cm^{-2} which is in line with literature data[89]. The capacitance values of both components, i.e. the spacer and headgroup, are determined from the fit to C_{Spacer} = 2.44 μF cm^{-2} and $C_{\mathrm{Headgroup}}$ = 1.73 μF cm^{-2}. As mentioned before, these values may deviate from the physically correct values. However, they correspond to the expected values, as taking a dielectric constant of ca. ε_{r} = 2.5 for the cholesteryl group, a realistic size of ca. 1.3 nm is obtained (see figure 3.5). The resistances are only applicable semi-quantitatively for the cholesteryl groups with a value of $R_{\mathrm{Headgroup}} = 1.99$ kΩ cm^2. As discussed in section 5.2.2 the resistance of the entire SAM and the spacer molecule are not captured by the impedance spectrum and, therefore, the fitted value is not reliable.

Pure 6MH SAMs The impedance spectra of pure 6MH SAMs show two dispersions as well. In this case, however, due to the simpler structure of 6MH, it is not possible to argue on the basis of a spacer and a headgroup region. Here, heterogeneities of the SAM induced by the nanostructured Au electrode lead to a defect-containing 6MH SAM, so that the two components, perceived as two dispersions in the impedance spectra, are ascribed to 6MH molecules and defects, respectively. In analogy to the CPOE3 SAM, the capacitance of the total 6MH SAM is characterized by the first half circle in the Cole-Cole plot with a value of $\mathrm{C_{6MH}}$ = (3.09 ± 0.11) μF cm^{-2} (see table 6.1). This capacitance differs from the one published by Jeuken et al.[89] who found a value of ca. 4.8 μF cm^{-2}. This discrepancy can be explained, as well, on the basis of the rough, defect-causing surface structure of the SEIRA Au film. This is supported by the fact that one of the capacitances obtained from the fit (i.e. C_{Spacer}) leads to a value of ca. 4.6 μF cm^{-2} which is very similar to the one obtained by Jeuken et al.[89] and, thus, describes the dielectric properties of the self-assembled 6MH molecules. The other component, therefore, accounts for the defects (C_{Defect}). In general, the presence of defects is very as short alkanethiols form only weak van-der-Waals interactions between the alkyl chains and, consequently, do not form a tightly packed SAM.

In this work, the value of $\mathrm{C_{6MH}}$ = (3.09 ± 0.11) μF cm^{-2} was found to be reproducible for 6MH SAMs. Furthermore, for mixed CPEO3/6MH this value is the asymptote for small CPEO3 concentrations, as will be shown later in this section. Therefore, to calculate the composition of mixed CPEO3/6MH SAMs on nanostructured SEIRA Au films this value has to be considered.

Mixed CPEO3/6MH SAMs From the impedance spectra shown in figure 6.1, capacitances of the CPEO3 and 6MH SAM on the nanostructured SEIRA Au film of $\mathrm{C_{CPEO3}}$ = (1.02 ± 0.06) μF cm^{-2} and $\mathrm{C_{6MH}}$ = (3.09 ± 0.11) μF cm^{-2} are derived, respectively. The capacitance of a mixed CPEO3/6MH SAM results from the mole fraction-weighted average of these two values:

$$C_{\mathrm{CPEO3/6MH}} = \chi_{\mathrm{CPEO3}} C_{\mathrm{CPEO3}} + \chi_{\mathrm{6MH}} C_{\mathrm{6MH}}. \tag{6.1}$$

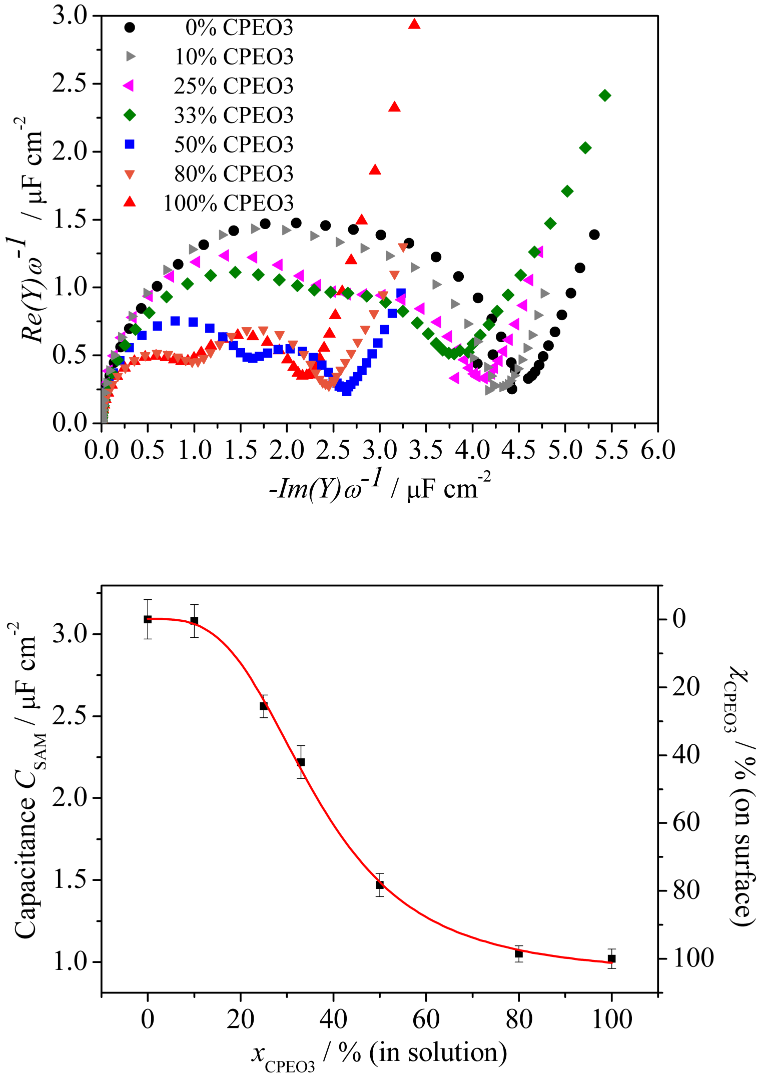

Figure 6.2: Top: Cole-Cole plots for mixed CPEO3/6MH SAMs resulting from solution with mole fractions of CPEO3 of 0, 10, 25, 33, 50, 75, 80, and 100%. For the sake of clarity, fitting curves are absent. Bottom: Capacitance values (left axis) and corresponding molar surface fractions of CPEO3 (right axis) of mixed CPEO3/6MH SAMs formed from solutions with different molar ratios of CPEO3 and 6MH on nanostructured SEIRA Au films. The values are obtained from the associated Cole-Cole plots (see top figure). The red line represents the fit with the Hill function $\chi_{\text{CPEO3}} = \chi_{\min} + (\chi_{\max} - \chi_{\min}) \cdot x^n_{\text{CPEO3}} (x^n_{\text{CPEO3}} + x^n_{1/2})^{-1}$ that describes a cooperative behavior of binding: $\chi_{\min} = 0 \pm 2$; $\chi_{\max} = 105 \pm 2$; $x_{1/2} = 36 \pm 1$; $n = 3.3 \pm 0.2$; $R^2 = 0.9985$. Each point results from an average of at least 3 values.

Converting this equation allows for the determination of the molar surface fraction of CPEO3:

$$\chi_{\text{CPEO3}} = \frac{C_{\text{CPEO3/6MH}} - C_{\text{6MH}}}{C_{\text{CPEO3}} - C_{\text{6MH}}} = \frac{C_{\text{CPEO3/6MH}} - 3.09\mu\text{Fcm}^{-2}}{1.02\mu\text{Fcm}^{-2} - 3.09\mu\text{Fcm}^{-2}}. \tag{6.2}$$

Figure 6.2 shows the dependence of the molar surface fraction on the mole fraction in solution for SAMs on nanostructured Au film. Similar to literature, a sigmoidal shape is noted which is in line with a cooperative binding behavior leading to a phase separated SAM composed of CPEO3 and 6MH domains, respectively.[89] This is also supported by the relatively accurate fit of the Hill function (see figure 6.2) with a Hill coefficient of $n = 3.2 \pm 0.2$ which is characteristic for a positive cooperative binding.[156] For mole fractions of CPEO3 of 0.75 > x_{CPEO3} > 0.15 in solution, mixed SAMs with different compositions are formed, whereas lower and higher ratios lead to (almost) pure CPEO3 or 6MH SAMs, respectively.

In the studies of Jeuken et al.,[89] the transition from pure 6MH to pure CPEO3 SAMs occurred in the range of ca. 0.15 > x_{CPEO3} > 0.05. The deviation in this work can be explained on the basis of two facts. On one hand, C_{6MH} is affected by the surface structure, as mentioned above, shifting the sigmoidal transition due to the lower density of 6MH molecules on the surface. On the other hand, the equilibration of the mixed CPEO3/6MH was found to have an influence on the SAM composition. Furthermore, the nanostructure may generate preferential binding spots for the rather short 6MH and the long CPEO3 molecules.

6.1.1.2. SEIRA spectroscopy of CPEO3/6MH SAMs

CPEO3/6MH SAMs in iso-propanol Figure 6.3 (A) depicts SEIRA spectra of pure CPEO3 and 6MH SAMs, respectively. The reference system for these spectra was the blank Au SEIRA film exposed to iso-propanol. During the SAM formation iso-propanol is removed from the surface and therefore its IR peaks are observed with negative intensities. The SAM forming CPEO3 and 6MH molecules, however, are characterized by positive IR bands as they adsorb onto the Au surface. The SEIRA spectrum of CPEO3 reveals several CH_n stretchings and bendings of both the cholesteryl headgroup and the polyethyleneoxy linker and, in addition, strong IR absorptions of the C-N carbamate group and of the C-O bonds of the linker. Interestingly, the C=O stretching shows two components indicating that only part of the CPEO3 molecules are involved in hydrogen bondings, shifting the IR absorption to 1692 cm^{-1}. Furthermore, the N-H bending shows as well several components at 1564, 1545, and 1515 cm^{-1} which characterize non, weakly, and strongly hydrogen bonded CPEO3 molecules.

As expected, the 6MH SAM reveals IR absorptions of CH_n stretchings and bendings, C-O stretchings, and a broad O-H stretching.

CPEO3/6MH SAMs in aqueous solution In electrochemical experiments on the formation of CPEO3-tethered tBLMs, it was observed that longer incubation times (> 30 min) of CPOE3 monolayers in aqueous solutions, prior to the addition of phospholipid vesicles, decreased the quality of the tBLMs or even impeded its formation. Upon addition of Na^+ or Na^+-D_2O-buffer onto a mixed CPEO3/6MH SAM, the SEIRA spectra in figure 6.3 (B) are obtained, taking the spectrum immediately after addition of water or heavy water as the background. Therefore, these spectra show the progressive effect of an aqueous solution on the SAM and not the IR spectrum caused by the exchange of iso-propanol for water. The spectrum of the SAM in H_2O clearly shows positive features of the SAM molecules due to a structural rearrangement: C-H stretchings at 2927 and 2855 cm^{-1}, the C=O stretching at 1662 cm^{-1}, and the N-H bending at 1545 cm^{-1}. In addition, the H-O-H bending coincides with the C=O stretching of the CPEO3 at ca. 1660 cm^{-1}. Both the H-O-H bending and the O-H stretching at 3257 cm^{-1} illustrate the penetration of water molecules in between the SAM molecules. In addition, the C=O bands of the CPEO3 molecules shift from 1724 and 1692 cm^{-1} to 1662 cm^{-1} due to the formation of a thin water layer beneath the cholesteryl headgroups which leads to strong hydrogen bonds with H_2O.

When D_2O is added instead of H_2O, the CPEO3 molecules undergo the same orientation changes indicated by positive bands at 2927, 2855, and 1662 cm^{-1}. The N-H bending displays negative intensity at 1545 cm^{-1} due to H/D-exchange and the corresponding positive

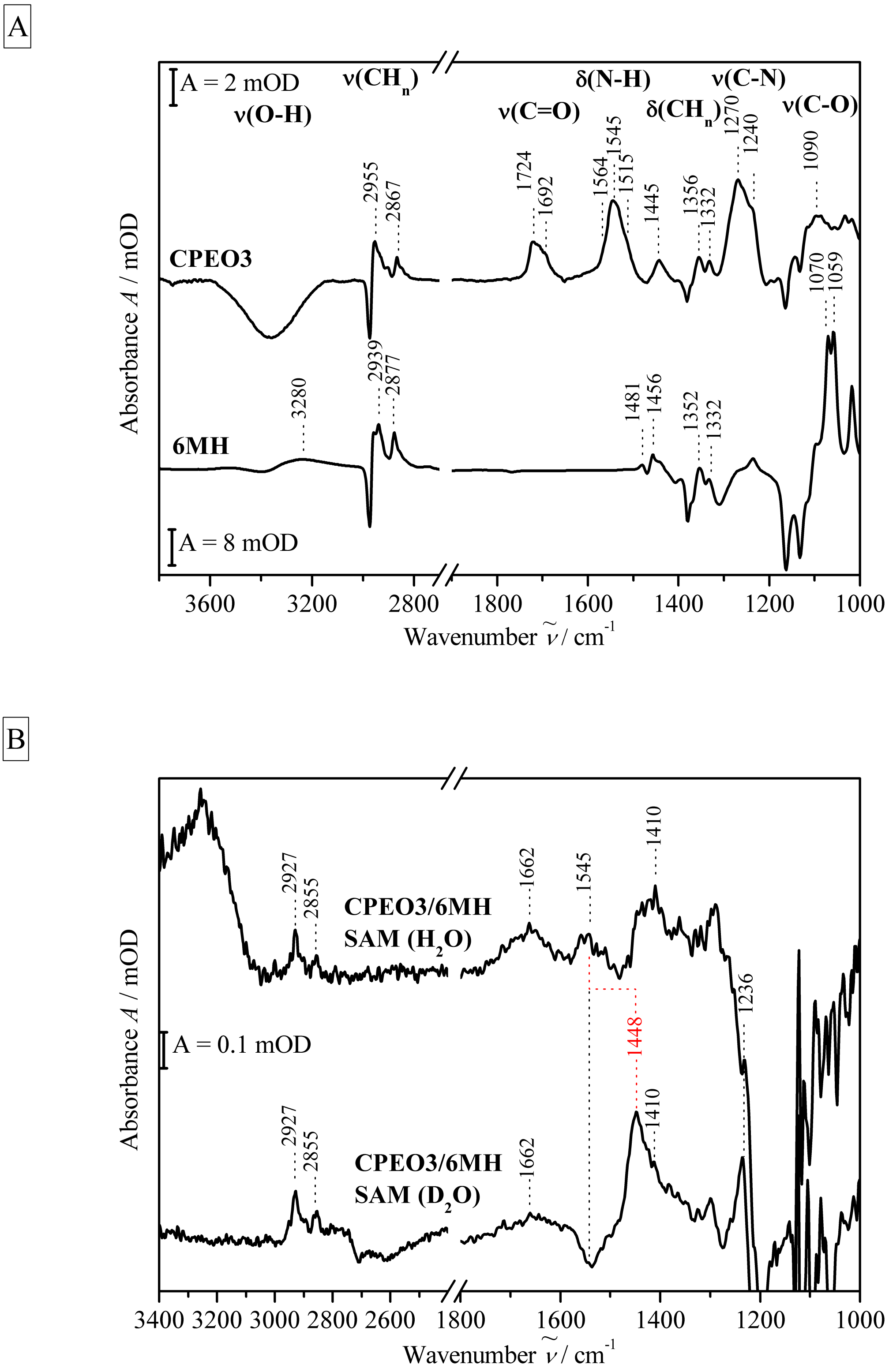

Figure 6.3: A: SEIRA spectra of self-assembled CPEO3 (top) and 6MH (bottom). In both cases, the spectrum of iso-propanol was taken as a reference and, thus, appears as negative IR absorption. B: SEIRA spectra of a mixed CPEO3/6MH SAM in the presence of H_2O (top) and D_2O (bottom), respectively. Band shifts upon H/D-exchange are marked in red.

N-D bending is found at 1448 cm^{-1}. The fact that the positive N-D bending has stronger intensity than the negative N-H bending is caused by the simultaneous reorientation of the SAM molecules which was already observed as a positive N-H bending absorption in the "H_2O-CPEO3" spectrum. The observed H/D-exchange proves the interpretation of water leaking below the cholesteryl headgroups causing two dispersions in the impedance spectra to arise: one accounting for the cholesteryl headgroups and the other for the polyethyleneoxy linker, separated by a thin water film. The broad O-D stretching band at ca. 2500 cm^{-1} shows a disturbed band structure which can be rationalized by the process of the H/D-exchange: D_2O molecules, that approach the Au surface and the CPEO3 SAM, are scavenged by protonated groups of the SAM. Due to this, the H-O-D bending arises at ca. 1450 cm^{-1} overlapping with the N-D bending of the CPEO3.

6.1.2. Formation of tBLMs on nanostructured Au

As discussed in the introduction of this section, the quantitative composition of the CPEO3/6MH SAM plays a key role for the stability of the tBLM on one hand and on the ability of the incorporation of membrane proteins on the other hand. Therefore, before the tBLM formation process will be discussed in more detail, the effect of the composition of the CPEO3/6MH SAM on the dielectric properties of the tBLM shall be addressed. Subsequently, the kinetics of POPC vesicle adsorption and spreading obtained from EIS and SEIRA will be discussed, providing more detailed information about the process of tBLM formation.

tBLM quality vs. CPEO3/6MH SAM composition To construct a CPEO3-tethered tBLM, 100 nm-sized unilamellar POPC vesicles were added onto the CPEO3/6MH SAM. As it was shown in literature, the interaction of vesicles with the SAM results in spreading and fusion of vesicles and, eventually, the formation of planar tBLMs with a specific capacitance of ca. 0.6 to 0.7 $\mu F\,cm^{-2}$.[89] For this process to happen, however, a certain concentration of CPEO3 molecules on the surface is required, otherwise surface-bound vesicles are obtained. In fact, Erbe et al.[92] have shown that for egg PC, planar tBLMs were formed on monolayers composed of at least 60 % of CPEO3. To evaluate this trend for tBLMs on SEIRA Au films, tBLMs were constructed on CPEO3/6MH SAMs of different compositions. Figure 6.4 (A) shows the capacitance values of tBLMs (after 4 hours of incubation of POPC vesicles and subsequent extensive washing with fresh buffer) versus the composition of the CPEO3/6MH SAM. Clearly, two regions can be recognized in this plot and are indicated by the dashed lines. At surface concentrations of more than 60 % of CPEO3 ($C_{\mathrm{CPEO3/6MHSAM}} > 1.7 \mu\mathrm{F\,cm^{-2}}$), capacitance values of less than 0.8 $\mu F\,cm^{-2}$ are observed. Below 60 % of CPEO3, the capacitance increases strongly converging against the values of the CPEO3-poor SAM. This clearly shows that in the first region ($\chi_{\mathrm{CPEO3}} > 0.6$) planar tBLMs are formed, whereas in the second region (($\chi_{\mathrm{CPEO3}} < 0.6$)) a different structural motif is obtained, i.e. CPEO3-bound vesicles, similar as reported in literature.[92,157] The fact that C_{tBLM} slightly increases from ca. 0.6 to 0.8 $\mu F\,cm^{-2}$ upon going from 100 to 60 % of CPEO3 can be explained by the increased concentration of 6MH that implies a higher amount of water molecules sealed between the bilayer and the Au surface. Since water has a considerably higher dielectric constant ($\varepsilon_{\mathrm{r}} = 80$) than the hydrophobic tBLM molecules ($\varepsilon_{\mathrm{r}} \sim 2-3$) an increase of the overall C_{tBLM} for lower CPEO3 surface concentration is intrinsically expected even without the presence of intact vesicles. In the region below 60 % the increase is substantially steeper indicating the increase in surface-bound vesicles. The bilayer resistances R_{tBLM} for tBLMs on differently composed CPEO3/6MH are shown in figure 6.4 (B). Although these values can be only evaluated in a semi-quantitative manner,

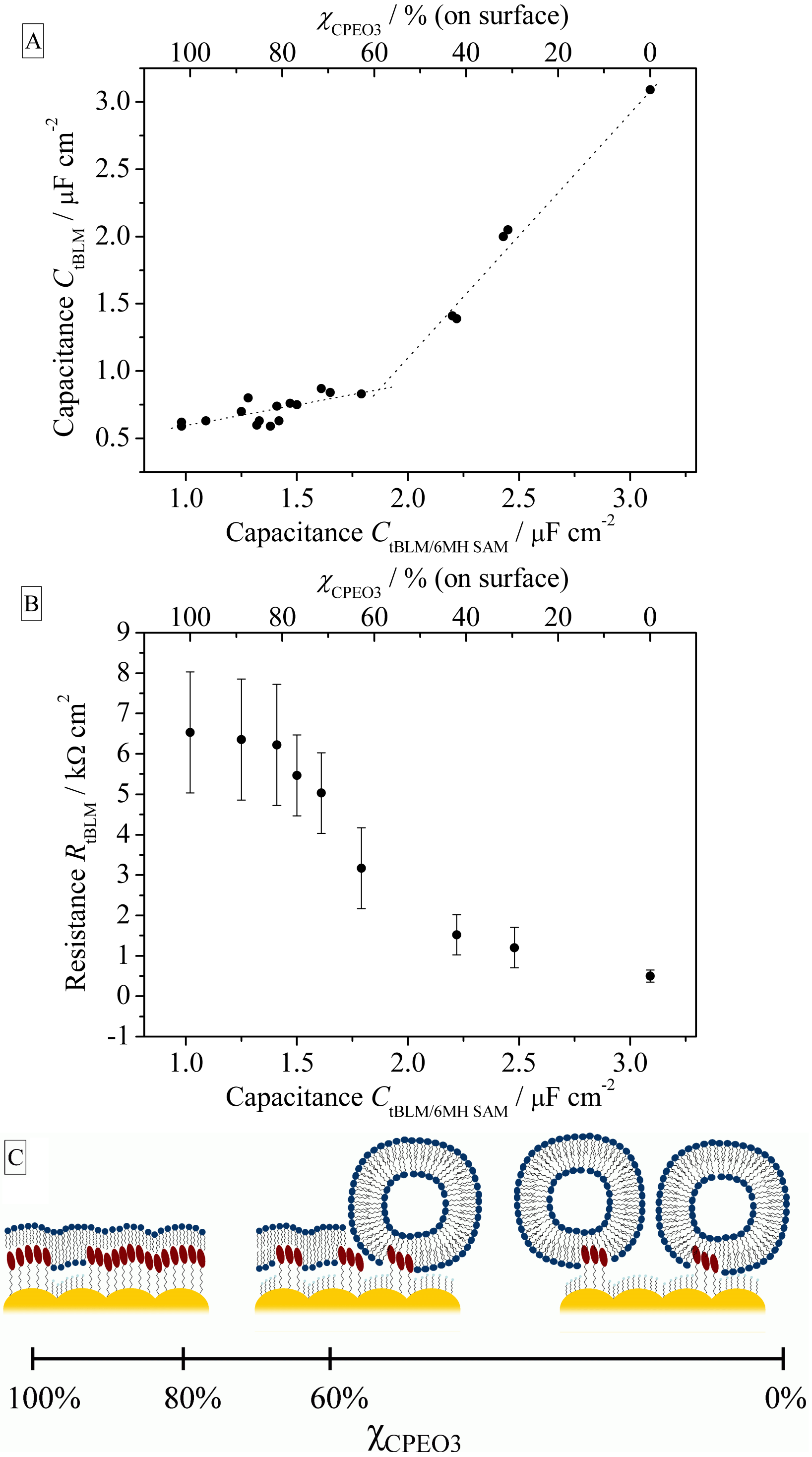

Figure 6.4: A: Graphical representation of the capacitance of tBLMs dependent on the composition of the CPEO3/6MH SAM. All capacitance values were obtained from the Cole-Cole plots of the respective system. The C_{tBLM} values were determined after 4 hours of POPC vesicles incubation and subsequent removal of the excess of vesicles. B: The resistance $R_{Bilayer}$ of the bilayer composed of POPC and cholesteryl headgroups depending on the composition of the CPEO3/6MH SAM. $R_{Bilayer}$ was extracted from a fit of the equivalent circuit $R_{Solvent}(R_{Spacer}C_{Spacer})(R_{Bilayer}C_{Bilayer})$ to the EIS data. Each point results from an average of at least 3 values. C: Schematic representation of the tBLM depending on the SAM composition.

as also experienced by substantial scattering between experiments performed on the same SAM compositions, the average values follow a clear trend. tBLMs on SAMs composed of 100 to 80 % of CPEO3 show a constant resistance of ca. 6.5 kΩ cm^2. This rather moderate magnitude can be ascribed to the presence of defects which, however, is an expected result due to the unavoidable nanostructure of the IR absorption enhancing Au film. Below 80 % the resistance drops considerably. This, together with the trend of the capacitance, can be interpreted in the following way shown in figure 6.4 (C). Between 100 and 80 % of CPEO3, planar tBLMs are formed. Below 80 % of CPEO3, the amount of defects increases and the vesicle fusion is impeded. Below 60 % of CPEO3, eventually, stable vesicles are favored with decreasing density on the surface when approaching pure 6MH SAMs.

As a consequence, for this work, tBLMs formed on SAMs composed of 80 % CPEO3 and 20 % 6MH were chosen as the system of choice, since they are characterized by the presence of planar tBLMs with quasi free-standing bilayer patches.

The process of tBLM formation - EIS The process of spreading and fusion of POPC vesicles on a CPEO3/6MH-functionalized SEIRA Au electrode was followed by EIS and SEIRA spectroscopy. Impedance spectra taken at different times during the process of tBLM formation as well as the tBLM capacitance and the resistance of the bilayer (R_{Bilayer}) are shown in figure 6.5. The capacitance of the tBLM (figure 6.5 B) follows a biexponential growth with a fast ($\tau_1 = (1.90 \pm 0.02)$ min) and a slower kinetics ($\tau_2 = (31.2 \pm 0.02)$ min) starting at a value of ca. 1.4 μF cm^{-2} which corresponds to a CPEO3/6MH SAM with a composition of $\chi_{CPEO3} = 80\%$ and reaches a value of ca. 0.65 μF cm^{-2}, accounting for a planar tBLM. The biexponential kinetics can be rationalized on the basis of a fast adsorption of POPC vesicles and a slower process involving the rupture and spreading of vesicles to form a planar tBLM. The long-term stability of the value of 0.65 μF cm^{-2} and the fact that extensive rinsing with fresh buffer does not alter this value is a prove for (a) the presence of a planar tBLM, (b) its high solidity, (c) the absence of a multilayer which would lead to further decrease of the capacitance, and (d) the fact that further vescile adsorption onto the tBLM leads to a weak, non-direct interaction.

The resistance of the bilayer shows a more complicated time course that could be fitted only to an exponential function of a higher degree. Thus, the resistance will be discussed qualitatively. Furthermore, the resistance results from a fit of an equivalent circuit describing an idealized system that may be not representative for tBLMs. Taking these constraints into account, one can qualitatively perceive three phases in the time course of the resistance which is in line with the interpretation of the capacitance values. In the beginning ($0 < t < 20$ min) a steep growth is noted which can be ascribed to the adsorption of vesicles onto the SAM. Subsequently, the resistance increases linearly. This is caused by the tBLM formation, combining the processes of vesicle rupture and spreading, rearrangement leading to a tighter packing of the bilayer, and removal of water located close to the SAM. After ca. 4 hours, the growth levels out slowly. Here, the loose adsorption of excess vesicles dominates, as exchanging for fresh buffer first causes a slight decrease in resistance and a subsequent plateau without altering the capacitance. The fact that further extensive rinsing does not change the capacitance nor the resistance of the system points at the formation of a mechanically highly stable planar tBLM construct.

The process of tBLM formation - SEIRA SEIRA spectroscopy performed the tBLM formation provides additional and complementary data. Figure 6.6 shows SEIRA spectra taken during the tBLM formation in H_2O and D_2O, respectively, using the spectrum of the mixed CPEO3/6MH SAM in the respective buffer as the reference spectrum. Therefore, negative contributions account for species removed from the surface, whereas positive bands describe

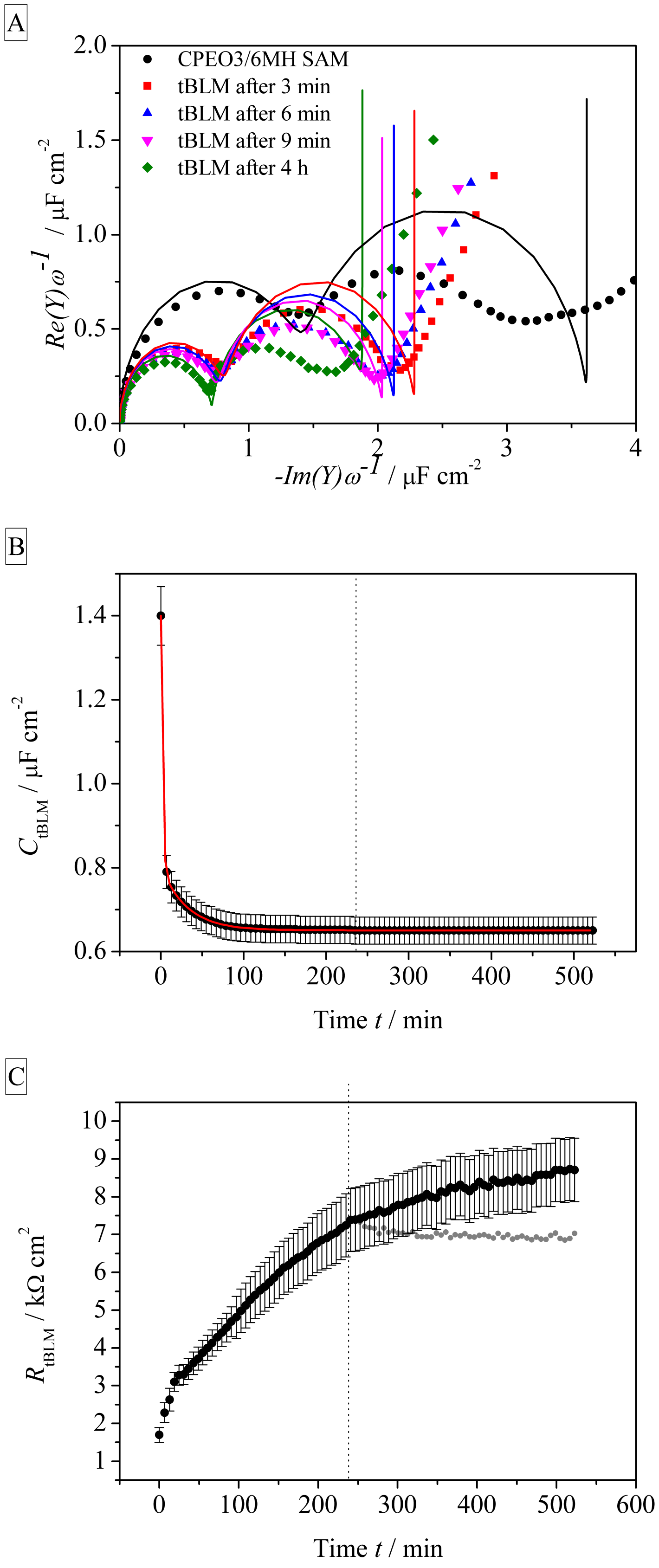

Figure 6.5: A: Cole-Cole plots of the EIS data taken during the tBLM formation for the SAM, and the tBLM after 3 min, 6min, 9 min, and 4 hours. Lines represent the fit. B: Time course of the capacitance values during the tBLM formation. The red line represents the fit with the biexponential function $C_{\mathrm{tBLM}} = C_0 + C_1 exp(-t/\tau_1) + C_2 exp(-t/\tau_2)$ resulting in: $C_0 = (0.6506 \pm 0.0001)\mu\mathrm{Fcm}^{-2}$, $C_1 = (0.151 \pm 0.002)\mu\mathrm{Fcm}^{-2}$, $\tau_1 = 31.2 \pm 0.2\mathrm{min}$, $C_3 = (0.598 \pm 0.002)\mu\mathrm{Fcm}^{-2}$, $\tau_2 = 1.90 \pm 0.02\mathrm{min}$, and $R^2 = 0.9997$. C: Time course of the resistance of the bilayer R_{Bilayer} obtained from the fit. Grey points present the time course after removing the excess of vesicles by washing with fresh buffer.

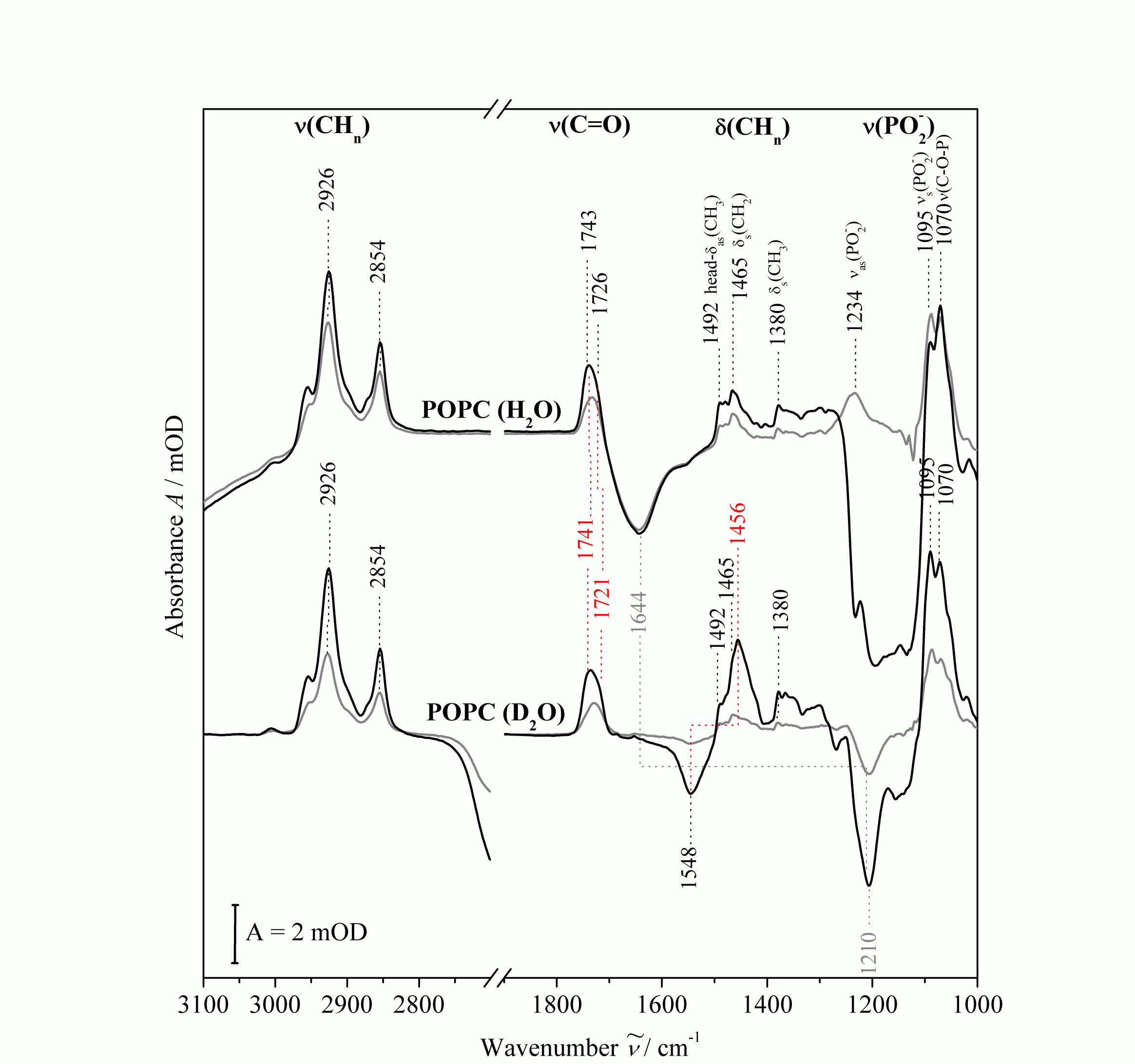

Figure 6.6: SEIRA spectra of POPC vesicle spreading and fusion in H_2O (top) and D_2O (bottom) after 3 min (grey) and 4 hours (black). The spectrum of the mixed CPEO3/6MH SAM in the respective buffer was used as the background spectrum. Lines and assignments in red indicate band shifts upon H/D-exchange; grey lines represent the shift of the vibrations δ(H-O-H) to δ(D-O-D).

	A_0 mOD	A_1 mOD	τ_1 min	A_2 mOD	τ_2 min
CH$_n$ stretchings					
2926 cm^{-1}	4.38 ± 0.01	3.73 ± 0.03	1.79 ± 0.04	0.65 ± 0.01	60 ± 4
2854 cm^{-1}	2.11 ± 0.01	1.80 ± 0.02	1.73 ± 0.05	0.305 ± 0.007	67 ± 5
2901 cm^{-1}	0.823 ± 0.002	0.82 ± 0.02	2.0 ± 0.1		
CO stretchings					
1741 cm^{-1}	1.55 ± 0.01	0.84 ± 0.03	2.7 ± 0.02	0.71 ± 0.01	72 ± 5
1721 cm^{-1}	1.11 ± 0.01	0.87 ± 0.03	1.8 ± 0.2	0.24 ± 0.01	70 ± 10

Table 6.2: Results of fitting the biexponential function $A = A_0 - A_1 exp(-t/\tau_1) - A_2 exp(-t/\tau_2)$ to the time course of the CH$_n$ bands (2926 cm^{-1}, $R^2 = 0.99803$; 2854 cm^{-1}, $R^2 = 0.99752$; 2901 cm^{-1}, $R^2 = 0.96945$) and C=O bands in D_2O (1741 cm^{-1}, $R^2 = 0.98997$; 1721 cm^{-1}, $R^2 = 0.97844$) in the time period $0 < t < 220$ min.

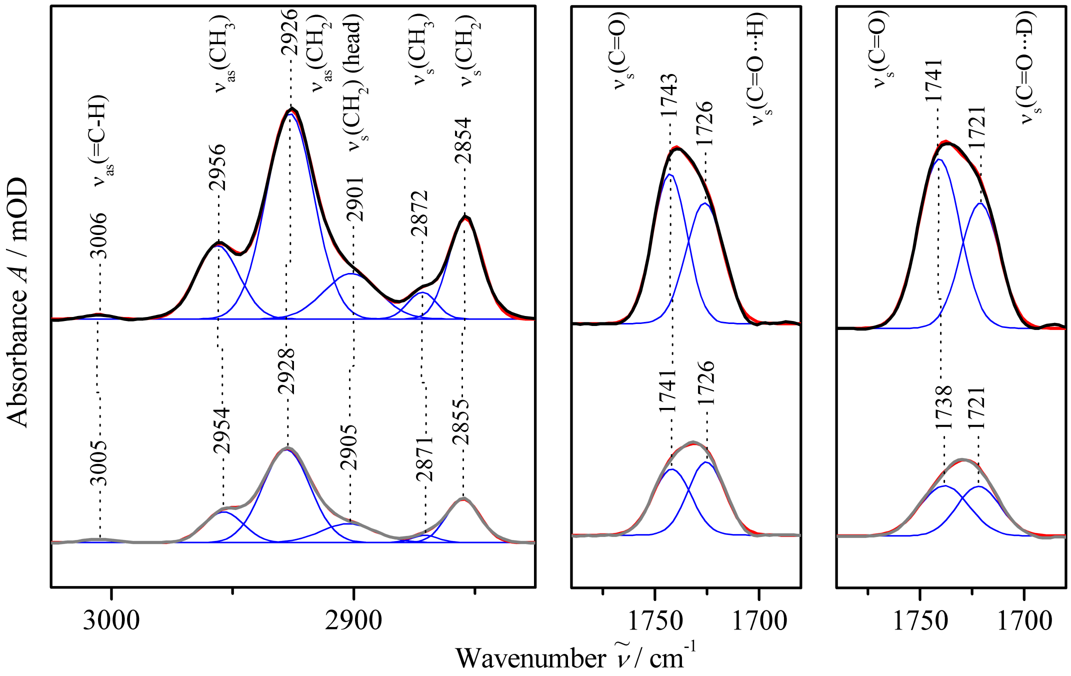

Figure 6.7: CH_n (left, in H_2O) and C=O stretching (middle, in H_2O; right, in D_2O) after 3 min (bottom, grey) and 4 hours (black, top) of vesicle fusion. Blue lines represent Gaussians fit to the baseline corrected data.

the adsorption of lipid material onto the SAM. Two prominent negative bands can be seen during this process in H_2O and D_2O at ca. 3400 and 1644 cm^{-1}, and ca. 2550 and 1210 cm^{-1}, respectively. These band are the O-H(D) stretching and H(D)-O-H(D) bendings of removed water molecules as POPC vesicles bind to the CPEO6/6MH SAM. In the case of D_2O, in addition, a negative band at 1548 cm^{-1} is observed. This band shifts to 1456 cm^{-1} and accounts for the N-H to N-D exchange of the carbamate group of the CPOE3 SAMs (as already observed in figure 6.3). Furthermore, a broad negative feature is present between 1250 and 1100 cm^{-1}. This is due to desorption of traces of anions such as sulfates. These bands shift below 1000 cm^{-1} in the presence of D_2O. The observed positive features arise upon POPC vesicle binding, displaying the CH_n (3050 - 2850 cm^{-1}), C=O (1750 - 1700 cm^{-1}), and P-O stretchings (1250 - 1000 cm^{-1}), as well as the CH_n bending and CH_n wagging vibrations (1500 - 1200 cm^{-1}) of the POPC molecules (see section 3.3 on page 33). Figure 6.7 highlights the CH_n and the C=O stretching region in H_2O and D_2O. To appreciate the spectral composition and the spectral changes in more detail, these band were fit with a set of Gaussian functions. The CH_n stretching region reveals the typical asymmetric and symmetric CH_n vibrations of the acyl chains at 3006 ($\nu_{as}(=C-H)$), 2956 ($\nu_{as}(CH_3)$), 2926 ($\nu_{as}(CH_2)$), 2872 ($\nu_s(CH_3)$), and 2854 cm^{-1} ($\nu_s(CH_2)$). In addition the symmetric CH_2 vibration of the choline headgroup is more pronounced at 2901 cm^{-1} due to its close proximity of the IR enhancing metal surface. The position of these bands, in particular of the $\nu_{as}(CH_2)$ and $\nu_s(CH_2)$, is characteristic of the liquid crystalline phase; in the solid-gel state they are shifted to lower frequencies of 2916 and 2850 cm^{-1}. During the incubation with POPC vesicles, these bands shift by 1-2 cm^{-1} due to structural rearrangements accompanied with the tBLM formation. The strongest shift of 4 cm^{-1} is experienced by the CH_2 vibration of the choline headgroup. This shift is caused by the drastic change

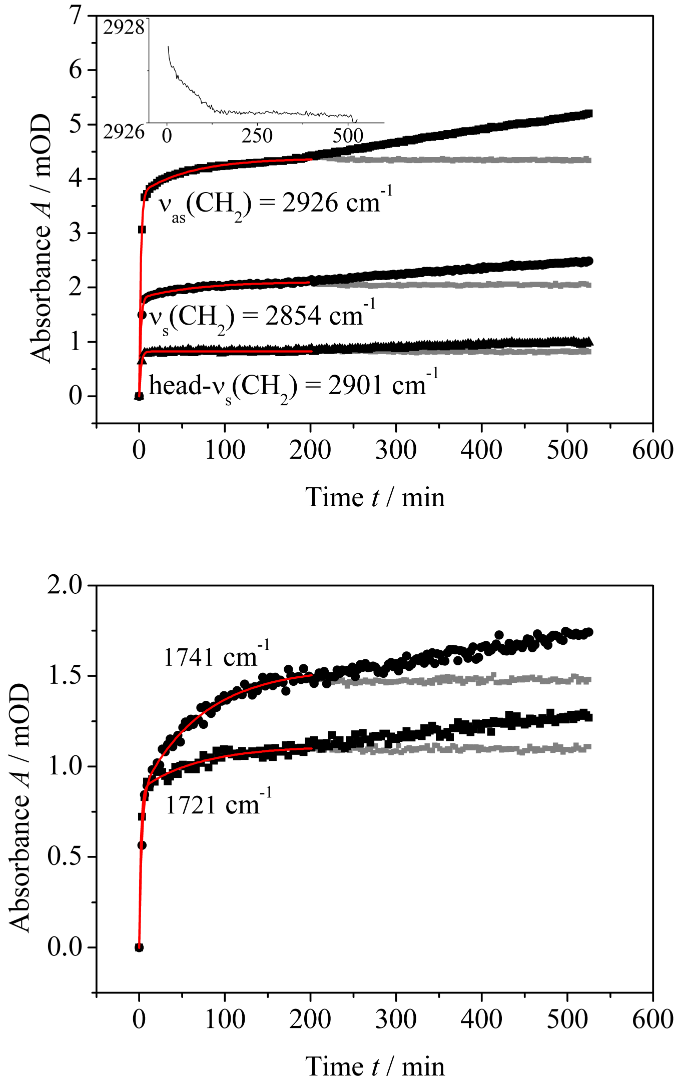

Figure 6.8: Time courses of the intensities of CH_n (top) and C=O stretchings (D_2O; bottom). Biexponential fits ($A = A_0 + A_1 exp(-t/\tau_1) + A_2 exp(-t/\tau_2)$) were done in the time period of $0 < t < 220$ min and are shown as red lines.

of environment during the vesicle absorption, as the headgroups approach towards the 6MH monolayer, and, possibly, an associated change in vesicle curvature. The C=O band is composed of two components, a high-frequency and a low-frequency one at 1743 and 1726 cm^{-1} or, in D_2O, at 1741 and 1721 cm^{-1}. These two components correspond to non (or weak-hydrogen bonded) and hydrogen/deuterium bonded C=O groups. Here, for the same reasons, the high-frequency (weak-hydrogen bonded) band changes slightly by 2 cm^{-1} indicating a weakening or a complete dissociation of the already weak hydrogen bondings.

The time courses of the intensities of both acyl CH_2, headgroup CH_2, and C=O stretchings (in D_2O) are shown in figure 6.8. Within the first ca. 200 min, these bands grow exponentially due to tBLM formation. This is followed by a linear increase which can be ascribed to adsorption of vesicles onto the bilayer, as washing with buffer impedes this linear growth. This is in line with the conclusions drawn from the time course of the bilayer resistance (*vide infra*). Within the tBLM formation phase (< 200 min), the prominent asymmetric and symmetric acyl CH_2 bands show a biexponential growth with consistent time constants of ca. 1.75 and 64 min (table 6.2). Here, the fast phase matches the one of the capacitance (1.9

min) well and, thus, describes the adsorption of POPC vesicles onto the SAM. The slower time constant of the increase in CH_2 intensity, however, deviates from the slow phase of the capacitance decrease (31.2 min). Still, both processes describe the formation of the tBLM, where the capacitance solely probes the thickness of the bilayer, SEIRA, however, monitors further rearrangements of the bilayer within its hydrophobic core. The time course of the band shift of the $\nu_{as}(CH_2)$ proceeds in a similar way reaching a stable value shortly before t = 200 min. This information proves the two previous interpretations that, first, the tBLM formation is completed after ca. 200 min and, second, the linear intensity increase at $t > 200$ min corresponds to further vesicle adsorption, happening more distant from the Au electrode and, thus, not affecting the spectral position considerably.

The C=O bands show a similar combination of a fast and a slow kinetics. Both bands display the above described processes with the time constants of 1.8 min and 70 min, and 2.7 min and 72 min for the 1721 cm^{-1}, and 1741 cm^{-1} components, respectively. Solely the fast phase of the 1741 cm^{-1} band with 2.7 min is slightly decelerated. This can be understood on the basis of the band shift by 2 cm^{-1} caused by loosening of hydrogen bonds. This process is associated with reorientations of the C=O groups and, thus, interferes with the approach of phospholipid material to the electrode. Interestingly, the fast process influences both bands to the same extent (0.84 and 0.87 mOD for the 1741 cm^{-1} and the 1721 cm^{-1}, respectively), pointing again to the plain vesicle adsorption. The slow process, however, is more pronounced with 0.71 mOD for the 1741 cm^{-1}, and 0.24 for the 1721 cm^{-1} band. Thus, it is the process of vesicle spreading and fusion causing the enrichment of the non-hydrogen bound C=O species, reflected by a higher relative intensity in the SEIRA spectra. This is caused by the associated rearrangements, including change in vesicle curvature, closing of ruptured vesicles, or POPC “flip over” events.

The head-$\nu_{as}(CH_2)$ stretching band increases monoexponentially (τ = 2 min) and reaches a plateau after several minutes. This corresponds to the previously obtained time constants for the vesicle adsorption. The absence of the slow phase for this band implies further that this vesicle adsorption process is limited to the 6MH-coated surface, since it is the only position at which POPC molecules remain unaffected during further rearrangements caused by the tBLM formation. Moreover, considering the penetration depth of the SEIRA enhancement, the 6MH-facing head-CH_2 groups, located ca. 1 nm from the Au surface, experience considerable stronger IR enhancement than the solution-exposed headgroups and, thus, rearrangements of the latter are not reflected by SEIRA significantly. Consequently, immediately after vesicle addition, the entire 6MH surface is covered with phospholipids, whereas the CPEO3 patches do not seem to be in direct contact with vesicles. This interpretation is reasonable, as the polar vesicle surface should prefer the proximity of the polar 6MH surface over the hydrophobic CPOE3 SAM in the early phase of vesicle absorption. Since the acyl CH_2 intensities increase further with the slower phase of ca. 64 min, this slow process, so far generally denoted as vesicle fusion and spreading, can be ascribed to the subsequent spreading of POPC molecules on the CPOE3-occupied surface (see figure 6.11). This can occur starting from 6MH-adsorbed vesicles that cause lateral tBLM “growth” along the CPOE3 SAM, as well as from non-6MH adsorbed vesicles directly from solution.[158] For the studied CPEO3/6MH SAM, the latter process does not happen initially, but could proceed as a later event.

Influence of Electrochemical Treatment After the formation and equilibration of the tBLM, it was found that an electrochemical treatment (ECT) influenced the properties of the system. This ECT consisted of switching the potential between the determined potential of zero charge (E_{PZC}), typically ca. -120 mV vs. Ag/AgCl, and +60 mV against the E_{PZC}, i.e. -60 mV vs. Ag/AgCl, in an alternated manner over night (see section 5.3.1 on page

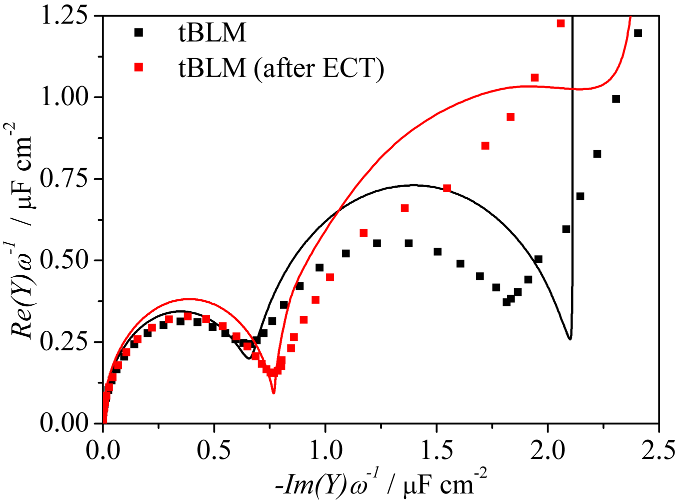

Figure 6.9: Cole-Cole plot of the tBLM before (black squares) and after the electrochemical treatment (red circles). Lines represent the fit.

	R_{Solvent} Ω	R_{Spacer} kΩ cm^2	C_{Spacer} μF cm^{-2}	R_{Bilayer} kΩ cm^2	C_{Bilayer} μF cm^{-2}	C_{tBLM} μF cm^{-2}
tBLM	114	930	2.11	5.3	1.04	0.63
tBLM (after EC)	106	410	2.69	21.3	1.09	0.66

Table 6.3: Results of the fitting of the equivalent circuit $R_{\text{Solvent}}(R_{\text{Spacer}}C_{\text{Spacer}})(R_{\text{Bilayer}}C_{\text{Bilayer}})$ to the EIS data of the tBLM before and after the electrochemical treatment (see section 5.4.1). The last row is the result of reading out the capacitance of the tBLM directly from the Cole-Cole plot. The error for the resistances and capacitances are 20 % or 10 % (before and after the ECT, respectively) and 5 %, respectively (n = 3).

60). Upon this treatment, the E_{PZC} shifted to a long-term stable value of ca. -350 mV (± 50 mV) not changing even upon further electrochemical procedures. The EIS data describing the system before and after the ECT are shown in figure 6.9 and table 6.3. Interestingly, the shape of the Cole-Cole plot changed considerably. Before the ECT, two half-circles were obtained, whereas afterwards the first one becomes more pronounced at the expense of the second one. The latter appearance of the Cole-Cole plot resembles the published EIS data by Jeuken et. al[89]. This shows that the ECT improves the quality of the tBLM by reorganization processes that "repair" defects and induce spreading of yet unruptured vesicles. This conclusion is supported by the observation that the resistance R_{Bilayer} increases considerably to 21.3 kΩ cm^2 while the capacitance C_{tBLM} shifts only slightly upon this treatment from 0.63 to 0.66 μF cm^{-2}. The results of the "R(RC)(RC)"-fit in table 6.3 reveal that this shift is attributed to changes of the spacer region increasing from 2.11 to 2.69 μF cm^{-2}. This can be rationalized on the basis of two processes: either diffusion of water into the spacer region, or a decrease of thickness of the spacer. However, the fact that the second half circle is not reproduced accurately by the fit may obscure these values.

SEIRA spectra of the system before and after the ECT are shown in figure 6.10. The most prominent changes are the positive features due to water at ca. 3400 and ca. 1650 cm^{-1} (or ca. 2600 and ca. 1210 cm^{-1} in the case of D_2O). Furthermore, the still ongoing H/D-exchange of the carbamate group of the CPEO3 molecules is reflected by the band

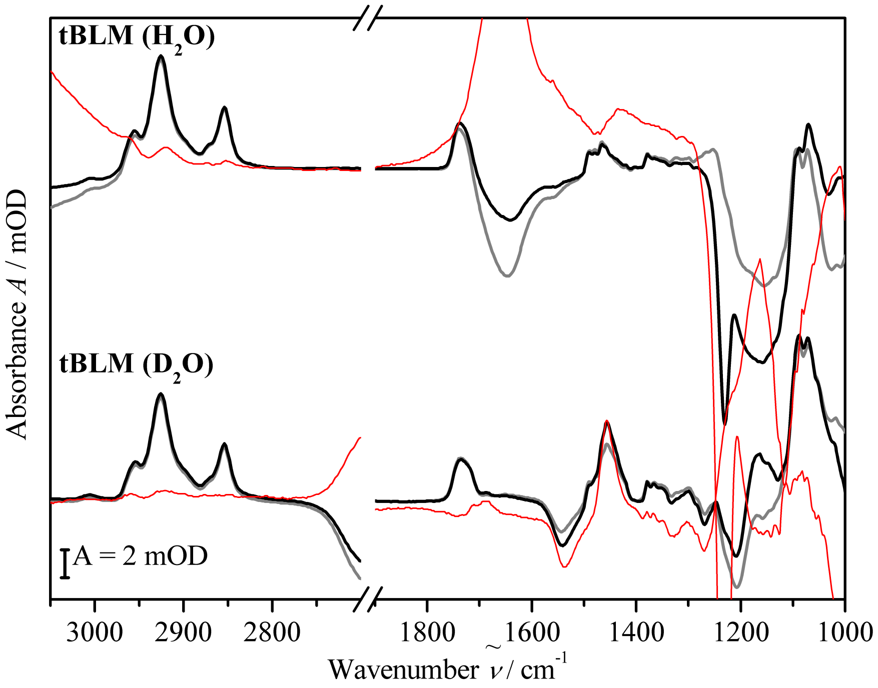

Figure 6.10: SEIRA spectra of the tBLM before (grey) and after (black) the electrochemical treatment in H_2O (top) and D_2O (bottom). The thin red lines represent the difference spectra between the system after and before the electrochemical treatment (multiplied with a factor of 4).

shifts (negative and positive band, respectively) from ca. 1740 to ca. 1690 cm^{-1} and ca. 1550 to 1450 cm^{-1} (see section 6.1.1.2). The CH$_n$ stretching and bending regions between 3050 and 2850 cm^{-1}, and 1500 and 1200 cm^{-1}, respectively, show only minor features that arise from rearrangements of the POPC molecules. Further changes below 1200 cm^{-1} are difficult to interpret as they originate from a superposition of several processes, such as desorption of ions. In D_2O, these changes shift below 1000 cm^{-1} and reveal a broad increase of the ν_{as}(CO-O-C) band at ca. 1170 cm^{-1}. Due to the absence of other prominent POPC difference bands, this observation points, as well, to reorganization processes of the bilayer region.

These findings suggest a process during which the amount of heterogeneities, defects, and remaining vesicles are removed from the tBLM. Since the CH$_n$ stretching region experiences only minor changes, the underlying processes correspond to those depicted in figure 6.11. For example, spots where POPC-POPC bilayers cover the CPEO3 SAMs fuse with cholesteryl headgroups. Taking into account the penetration depth of SEIRA, this explains the rather unchanged POPC vibrations and the increase of water vibrations, as a POPC-POPC bilayer is reduced to a POPC monolayer being located closer to the electrode. Furthermore, the quasi free-standing tBLM patches become more homogeneous involving the rupture of intact vesicles and some diffusion of water below the bilayer.

6.1.3. Summary

The Mixed CPEO3/6MH SAM Capacitance values obtained for the pure CPEO3 and 6MH SAM were determined to be C_{CPEO3} = (1.02 ± 0.06) μF cm^{-2} and C_{6MH} = (3.09 ± 0.11)

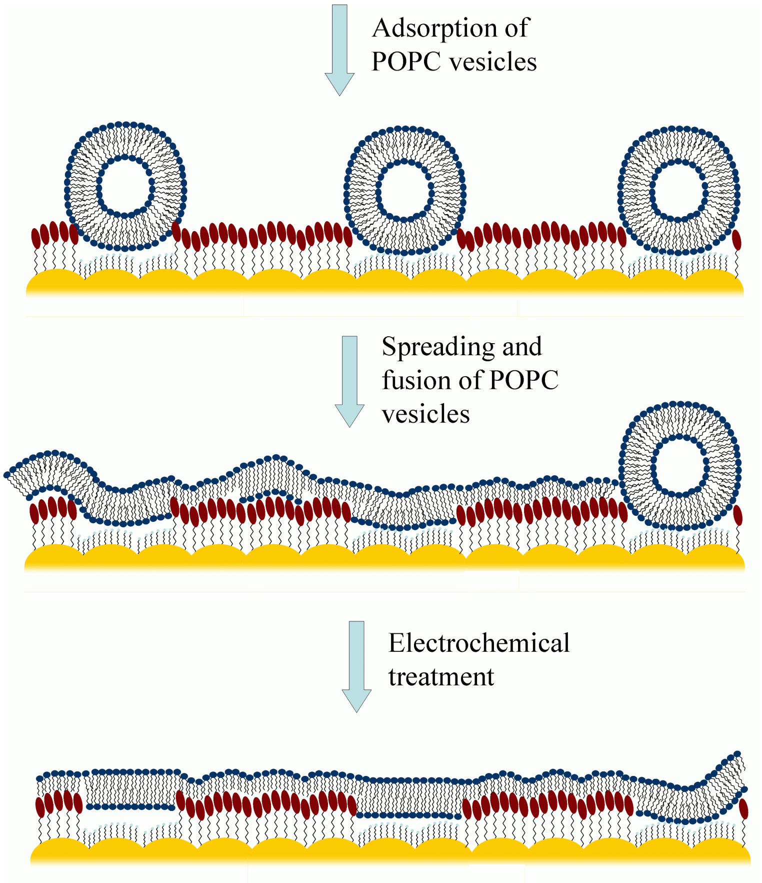
Adsorption of POPC vesicles
Spreading and fusion of POPC vesicles
Electrochemical treatment

Figure 6.11: Model for tBLM formation on CPEO3/6MH SAMs on SEIRA Au films. The first step is comprised of the adsorption of unilamellar vesicles onto the 6MH SAM islands with a time constant of ca. 2 min. This followed by spreading and fusion of vesicles to form a tBLM (time constant in the range of 30 - 60 min). Using the electrochemical treatment the amount of heterogeneities, defects, and remaining vesciles is reduced to improve the tBLM quality.

μF cm^{-2}, respectively. The former is in line with literature findings; the latter, however, deviates from the value obtained on flat Au surfaces due to the nanostructure of the SEIRA Au electrode. This is supported by the fact, that one dispersion of the EIS data corresponds to the 6MH molecules with C_{Spacer} = 4.6 μF cm^{-2} resembling the capacitance reported by Jeuken et al. (4.8 μF cm^{-2})[89]; the other is ascribed to defects (C_{Spacer} = 8.6 μF cm^{-2}). Mixtures of both molecules show cooperative binding and, thus, lead to mixed, but phase-separated CPEO3/6MH SAMs when solutions with a CPEO3 concentration of $0.75 > x_{\mathrm{CPEO3}} > 0.15$ were used. Above and below this concentration, pure CPEO3 and pure 6MH SAMs are formed. SEIRA spectra in H_2O and D_2O show a H/D-exchange of the carbamate group located below the cholesteryl headgroup of CPEO3. This proves the presence of an aqueous reservoir below the later formed tBLM and explains the appearance of two dispersions in the EIS data, ascribed to the polyethyleneoxy (and 6MH) spacer and the cholestryl groups.

tBLM on mixed CPEO3/6MH SAMs It was found that mixed monolayers with a composition of at least 60 % of CPEO3 ($C_{\mathrm{CPEO3/6MHSAM}}$ = 1.7 μF cm^{-2}) induce vesicle fusion and result in tBLMs, similar as on flat Au electrodes. Below this CPOE3 amount surface-bound vesicles seem to prevail. At a surface concentration of 80 % (or higher; $C_{\mathrm{CPEO3/6MHSAM}} <$ 1.4 μF cm^{-2}) planar tBLMs with capacitances of C_{tBLM} = 0.6 - 0.7 μF cm^{-2} and bilayer resistances of R_{Bilayer} = (6.5 ± 1.5) kΩ cm^2 are formed. In these tBLMs intact vesicles seem to be a minor feature, whereas defects are present in the bilayer, reflected by the moderate resistances. Here, again, two dispersions are noted in EIS data of tBLMs, pointing at the presence of the aqueous reservoir beneath the bilayer.

tBLM formation The formation of tBLMs on CPEO3/6MH SAMs with a composition of 80 % CPEO3 indicates a mechanism constituted of two processes with similar kinetics obtained from SEIRA and EIS. The initial adsorption of unilamellar POPC vesicles happens with a fast time constant of ca. 2 min and leads to a covering of the complete 6MH space, as indicated by the head-$\nu_{\mathrm{as}}(\mathrm{CH_2})$ stretching at 2901 $\mathrm{cm^{-1}}$. The second process with a slower time constant of ca. 60 - 70 min (determined from SEIRA; C_{tBLM} yields in τ = 30 min) can be ascribed to the spreading of vesicles to cover the CPEO3-functionalized parts of the SEIRA Au electrode. Only after planar tBLM patches are formed unspecific binding of further vesicles can be monitored. Washing the electrode with fresh buffer allows for removing these vesicles. Treating this system electrochemically improves its quality indicated by an increased bilayer resistance of ca. (21 ± 2) $\mathrm{k\Omega\,cm^2}$. The underlying process involves the reduction of the amount of heterogeneities, defects, and remaining vesciles of the tBLM as sketched in figure 6.11.

6.2. Spectroelectrochemistry of gA Incorporated into tBLMs

In the last section, it was shown by means of SEIRA and EIS that tBLMs are formed on CPEO3/6MH-functionalized nanostructured Au surfaces. Here, as a proof of principle, gA shall be used to demonstrate the ability of the tBLM to act as a native-like environment for the incorporation of membrane proteins. For this purpose, gA was incorporated under different conditions, leading to pore and channel configurations. Since the influence of the electrochemical treatment was discovered in retrospect, here, the tBLM system was used after 4 hours of vesicle incubation. Eventually, the functionality of the tBLM-embedded gA channel, denoted as $\beta^{6.3}\beta^{6.3}$, to translocate specifically monovalent cations across the membrane was monitored in a spectroelectrochemical manner with EIS and SEIRA.

6.2.1. Incorporation of gA into tBLMs

Pore vs. Channel The incorporation of gA into tBLMs was performed by adding a solution of gA in TFE directly into the supernatant buffer solution. In this way, the peptide incorporates spontaneously into the hydrophobic part of the tBLM. However, depending on the present cations, gA was incorporated either in its pore or its channel state. Figure 6.12 displays the spectra of gA incorporated into tBLMs in the presence of $\mathrm{Cs^+}$ and $\mathrm{Ba^{2+}}$ ions, respectively, taking the spectrum of the pure tBLM with the respective buffer as reference. In both cases small features appear at 3000 - 2800 $\mathrm{cm^{-1}}$ and ca. 1742 $\mathrm{cm^{-1}}$ which can be ascribed to the $\mathrm{CH_n}$ and C=O stretching vibrations of the phospholipids and indicates a structural rearrangement of the tBLM upon gA incorporation. The positions of these bands are shifted in comparison to the ones observed for the pure tBLM spectrum. This is caused by an interplay of several effects, i.e. the exchange of cations causing an altered complexation pattern of the C=O groups of the phospholipids and the presence of gA disturbing the original packing of the tBLM. Additionally, the $\mathrm{CH_n}$ vibrations of the highly hydrophobic gA interfere with the ones of the lipids causing a complicated band pattern. The incorporation of gA is characterized by the intense positive amide bands of the peptide. In the presence of $\mathrm{Cs^+}$ ions, the amide I and II bands are located at 1629 and 1554 $\mathrm{cm^{-1}}$,

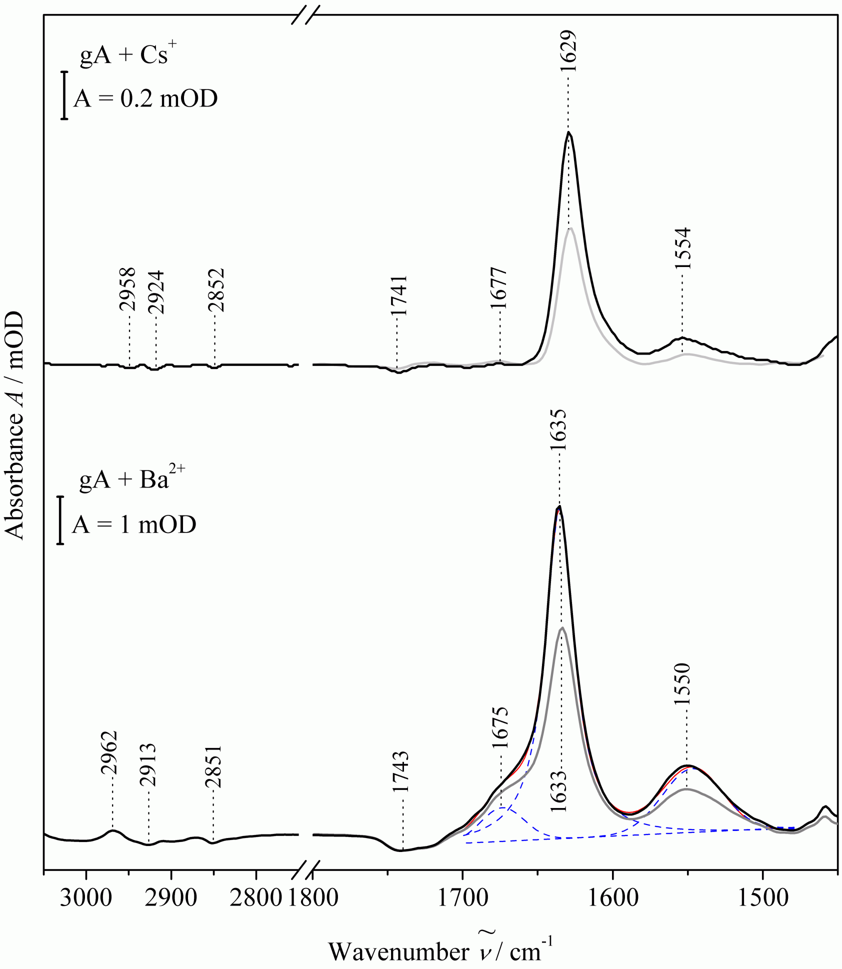

Figure 6.12: SEIRA spectra of gA incorporated into tBLMs in the presence of Cs^+ (top) and Ba^{2+} (bottom) ions yielding in channel and pore structures, respectively. Black spectra represent the system after 1 hour of incubation; grey spectra were taken after 3 min. In the bottom spectrum, dashed blue lines represent Gaussian (minor amide I and amide II) and Lorentzian functions (major amide I) used for fitting the shape of the amide I and amide II bands; the red line is sum of the fit.

respectively, and can be ascribed to the channel $\beta^{6.3}\beta^{6.3}$ conformation.[127] The high amide I/amide II intensity ratio (ca. 16 for peak areas; ca. 13 for peak intensities) is consistent with a perpendicular alignment of the β-helical dimer with respect to the electrode surface, since the transition dipole moments of the amide I and amide II are oriented in parallel and perpendicularly to the helix axis, respectively. This is supported also by the absence of the minor amide I component at ca. 1677 cm^{-1} which is polarized perpendicularly to the major component.

In the presence of Ba^{2+}, the spectrum of gA is altered considerably. The amide I is composed of a main band at 1635 cm^{-1} and a shoulder at ca. 1675 cm^{-1}; the amide II is centered at 1550 cm^{-1}. This band pattern is specific for the pore conformation of gA. To separate the two amide I bands from each other, the minor amide I and the amide II were simulated by with Gaussian functions, the main amide I at 1635 cm^{-1}, however, with a Lorentzian due to its narrow band shape. The latter can be rationalized on the basis of a uniform structure in respect to the conformation and the orientation. In contrast to the spectrum of the gA channel, the minor amide I component is present and the amide I/amide II intensity ratio

Amide band	A_0 mOD	A_1 mOD	τ_1 min	A_2 mOD	τ_2 min
Channel (gA + Cs^+)					
1629 cm^{-1}	1.68 ± 0.03	0.86 ± 0.01	1.11 ± 0.07	0.82 ± 0.03	46 ± 4
1554 cm^{-1}	0.18 ± 0.07	0.061 ± 0.005	1.2 ± 0.4	0.12 ± 0.07	97 ± 80
Pore (gA + Ba^{2+})					
1675 cm^{-1}	0.917 ± 0.003	0.92 ± 0.01	0.8 ± 0.1		
1635 cm^{-1}	8.68 ± 0.04	6.16 ± 0.08	1.78 ± 0.05	2.52 ± 0.06	22 ± 1
1550 cm^{-1}	1.137 ± 0.006	0.81 ± 0.02	1.8 ± 0.1	0.33 ± 0.02	22 ± 2

Table 6.4: Results of fitting the biexponential function $A = A_0$ - $A_1 exp(-t/\tau_1)$ - $A_2 exp(-t/\tau_2)$ to the time course of the amide I (1629 cm^{-1}, $R^2 = 0.99968$) and amide II bands (1554 cm^{-1}, $R^2 = 0.98334$) of gA incorporated in the presence of Cs^+ ions, and in the presence of Ba^{2+} ions (amide I: 1675 cm^{-1}, $R^2 = 0.997$; 1635 cm^{-1}; $R^2 = 0.99975$; amide II: 1550 cm^{-1}; $R^2 = 0.99977$).

(ca. 6 for intensities at maximum) is lower. However, this still corresponds to a perpendicular orientation with respect to the surface, as the peptide chain of both membrane-spanning monomers of the pore is inclined towards the helix axis (see section 4.2.1.1 on page 43). In this way, the angle between all C=O bonds and the surface normal is increased, and the one of the C-N bonds and the surface normal decreased, leading a weaker main amide I band, and stronger minor amide I and amide II bands. The exact conformational assignment of the pore is more complicated since the shoulder at ca. 1650 cm^{-1} is missing in the spectrum, and the related intensities are too weak due to the surface-selection rule. Furthermore, the 4 pore species were only characterized spectroscopically in organic solvents in literature. However, the position of the main amide I at 1635 cm^{-1}[111,112] points at species 3, the left-handed antiparallel $\uparrow\downarrow$ $\pi\pi^{5.6}$ double helix. For both conformers, the channel and the pore, no negative bands from water can be detected. This, in addition, proves the incorporation into the tBLM and the absence of unspecifically adsorbed gA onto the tBLM or in defects, as this would implicate a removal of water molecules from the surface.

Kinetics of the Incorporation In figure 6.12, the spectra of both species are shown obtained directly after the addition into the supernatant solution in grey. In the case of the channel (in Cs^+-Buffer), the positions of the amide I and II bands do not shift considerably by time and follow a biexponential growth with a fast and a slow kinetic (see table 6.4). It should be mentioned that for the amide II the biexponential fit leads to results with considerably lower accuracy which is ascribed to the low absolute intensity of this band (see R^2 value in table 6.14). Nevertheless, for both bands, the fast component has a time constant of ca. 1.1 min, describing the fast incorporation of the peptide from the supernatant solution. The slower phases with time constants of 46 min and 97 min for the amide I and amide II band, respectively, arise from the rearrangement and reorientation of the tBLM embedded peptide that involves a "flip over" (as the Trp containing C-termini face the lipid headgroups) from the upper, solution-exposed leaflet to the surface-facing leaflet of the tBLM[128] and the subsequent dimerization between the peptides in the upper and lower leaflet, respectively, to form the helical dimer channel. Although the absolute values of these slow time constants have to be considered with caution due to limited number of data points, the process of reorientation and dimerization is supported by the amide I/amide II intensity ratio that changes slightly from ca. 15 to 12 during the incorporation process; plain incorporation, however, would cause the amide I and II bands to increase equally. Thus, the spectra with

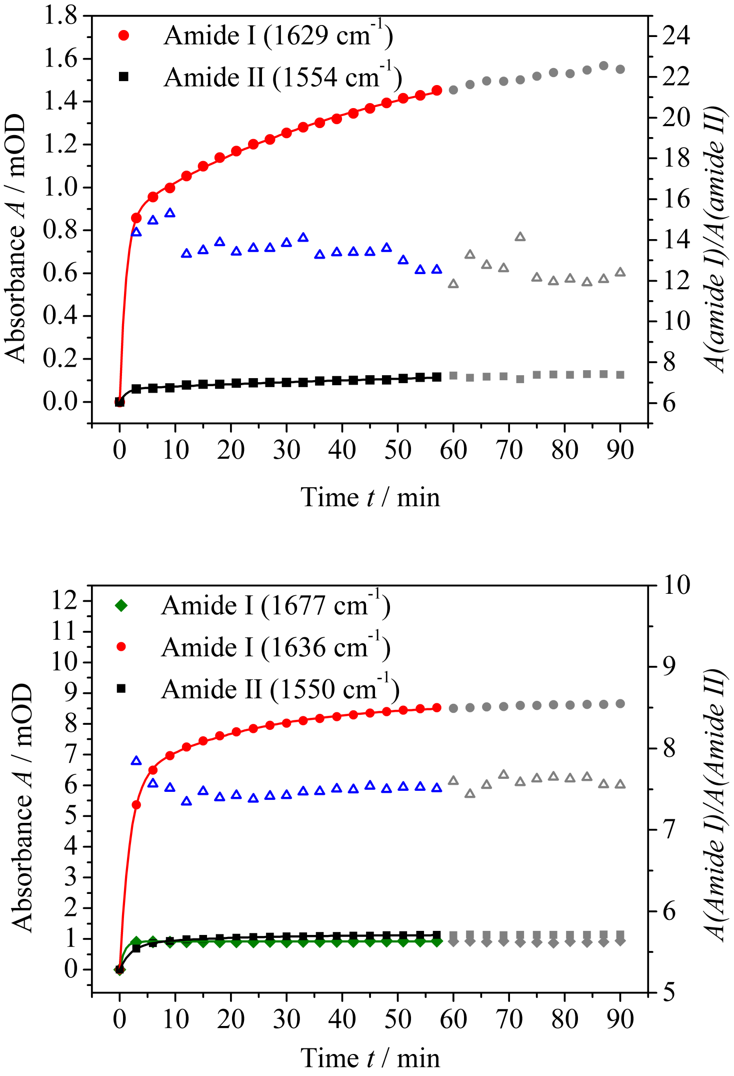

Figure 6.13: Time course of the amide I and amide II bands gA during the incorporation in the channel (Cs^+; top) and pore form (Ba^{2+}; bottom). Filled and hollow symbols refer to the absorbance and amide I/amide II intensity ratio, respectively; lines are result of the fit with the biexponential function $A = A_0 - A_1 exp(-t/\tau_1) - A_2 exp(-t/\tau_2)$ (results are presented in table 6.4). The intensities of the bands at 1675 cm^{-1} and 1635 cm^{-1} where obtained by fitting a Gaussian and a Lorentzian to the amide I band. Grey symbols refer to the intensities after buffer exchange and extensive rinsing.

amide I/amide II intensity ratios of 15 and 12 are ascribed to monomeric and dimeric $\beta^{6.3}$ helices, respectively.

During the incorporation of gA in presence of Ba^{2+} ions, the minor amide I and the amide II do not shift considerably. The main amide I, however, shifts from 1633 to 1635 cm^{-1} (grey and black spectra, respectively, in figure 6.13) indicating not only just rearrangements but also conformational transitions between the different pore species. In contrast to the incorporation of the gA channel, this process involves major structural alterations: the double-stranded helix forms hydrogen bonds along the entire peptide chain (and not only at the C-terminus as for the dimeric channel) and, thus, transitions between different "pores" cause all of these hydrogen bondings to rearrange. This interpretation is supported by the kinetics of the shift of the position of the main amide I component (figure 6.14). Under the assumption that this process can be traced back to $t = 0$ with the same kinetics, the

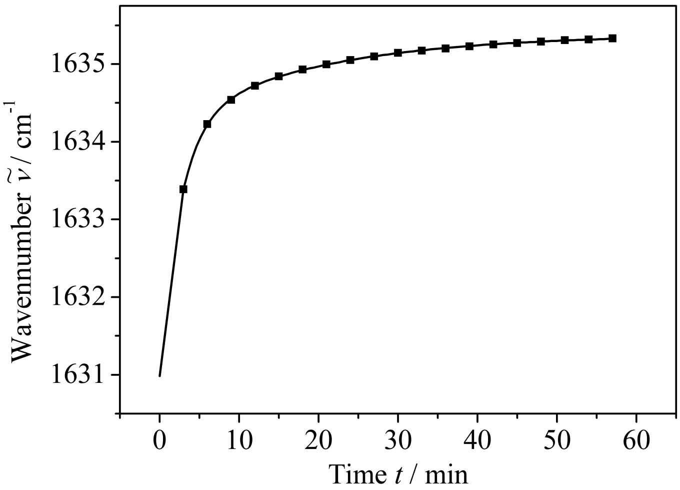

Figure 6.14: Time course of the position of the major amide I bands of gA during the incorporation of the pore form (Ba^{2+}). The line represents the result of the fit with the biexponential function $\tilde{\nu} = \tilde{\nu}_0 + \tilde{\nu}_1 exp(-t/\tau_1) + \tilde{\nu}_2 exp(-t/\tau_2)$: $\tilde{\nu}_0 = (1635.384 \pm 0.008)\text{cm}^{-1}$; $\tilde{\nu}_1 = (-3.2 \pm 0.08)\text{cm}^{-1}$; $\tau_1 = 2.5 \pm 0.1\text{min}$; $\tilde{\nu}_2 = (-1.20 \pm 0.03)\text{cm}^{-1}$; $\tau_1 = 18.7 \pm 0.7\text{min}$; $R^2 = 0.99984$.

frequency shifts from 1631 to 1635 cm^{-1}. Furthermore, as can be seen in figure 6.13, the amide I/amide II ratio stays constant during the entire incorporation process with a value of ca. 7.5. First of all, these findings rule out the presence of monomeric helix species which show a three times higher amide I/amide II ratio of ca. 15, whereas a smaller value for pores is in line with expectations (*vide supra*). Furthermore, supported by computational predictions[111] and experimental IR spectra[127] of gA, the amide I maxima at 1633 cm^{-1} and 1635 cm^{-1} can be ascribed to the right-handed $\uparrow\downarrow$ $\pi\pi^{7.2}$ and left-handed $\uparrow\downarrow$ $\pi\pi^{5.6}$ species, respectively. The amide I band at 1631 cm^{-1} (ν_0; at $t = 0$ min) then corresponds to the gA conformer formed directly upon inserting the solution species. NMR studies showed that bivalent cations lead to the gA conformer $\uparrow\uparrow$ $\pi\pi^{5.7}$.[159] Accordingly, the transition, $\uparrow\uparrow$ $\pi\pi^{5.7}$ $\longrightarrow$ $\uparrow\downarrow$ $\pi\pi^{7.2}$ $\longrightarrow$ $\uparrow\downarrow$ $\pi\pi^{5.6}$, thus is in line with the observed biexponential kinetics with time constants of 2.5 and 18.7 min. The time courses of the intensities of all three amide I bands support this interpretation. The minor component of the amide I at 1675 cm^{-1} follows a monoexponential growth, whereas the major amide I (1635 cm^{-1}) and the amide II (1550 cm^{-1}) rise in biexponential manner. In analogy to the incorporation in the presence of Cs^+ ions, here, the fast phase with similar time constants of ca. 1.7 min (for the main amide I and the amide II) represents the insertion from the supernatant solution and the transformation $\uparrow\uparrow$ $\pi\pi^{5.7}$ $\longrightarrow$ $\uparrow\downarrow$ $\pi\pi^{7.2}$ with similar time constant of 2.5 min. The slower components with time constants of 22 min (which lie close to the slow time constant of the amide I shift with 18.7 min) for the amide I and II describe the conformational transition of the incorporated gA. Upon conversion from $\pi\pi^{7.2}$ to $\pi\pi^{5.6}$, gA gets elongated from 27 Å to 36 Å and, thus, approaches the Au surface. This explains also the higher amplitude of the fast process of $A_1 = 6.16$ mOD corresponding to an increase of peptide content within the tBLM, and the lower amplitude of $A_2 = 2.52$ mOD describing the slower conformational transition. The monoexponential evolution of the minor amide I band may be contradictive at first glance, however, it reflects a more complex combination of exponential growth and decay behaviors due to the conformational transitions. This is supported by the observation that extensive rinsing with buffer did not affect either the position or the intensity of

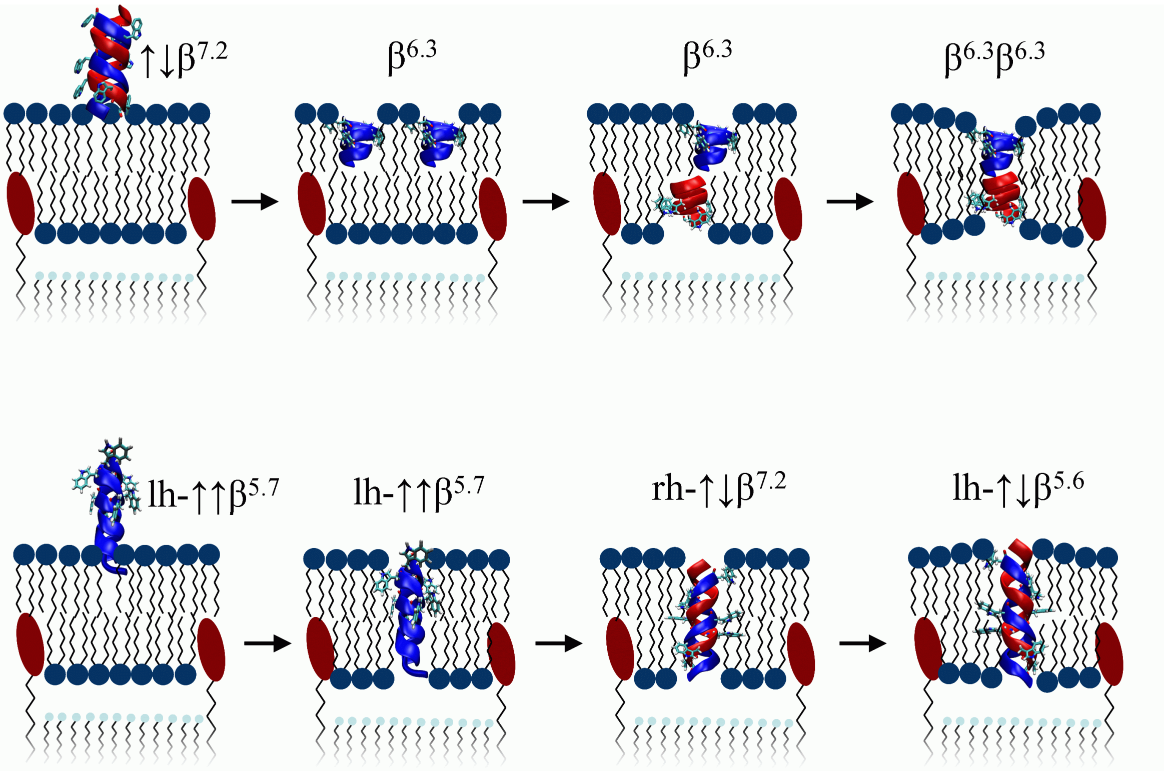
$\uparrow\downarrow\beta^{7.2}$
$\beta^{6.3}$
$\beta^{6.3}$
$\beta^{6.3}\beta^{6.3}$
lh-$\uparrow\uparrow\beta^{5.7}$
lh-$\uparrow\uparrow\beta^{5.7}$
rh-$\uparrow\downarrow\beta^{7.2}$
lh-$\uparrow\downarrow\beta^{5.6}$

Figure 6.15: Schematic representation of gA incorporation into tBLMs in the presence of Cs^+ ions (top) and Ba^{2+} (bottom) to form the channel or pore conformer, respectively. In the case of Cs^+, the cation is buried inside the channel interior, whereas Ba^{2+} is bound externally to the mouth of gA.

this band. Furthermore, ATR-IR spectra revealed a complex combination of bands in this region.[160] The constant amide I/amide II ratio fits into this model, as the double-stranded helix remains and only the pitch of the helix changes, which should not alter the direction of the overall dipole moment transition.

On the basis of these results, one can propose a mechanism for the incorporation of gA pores into membranes, supporting the existing model for channel formation.[128] The latter is initiated by the incorporation of helix monomers into the upper, solution-exposed membrane leaflet. Through a "flip over" mechanism, these helices also reach the bottom leaflet to finally form helical dimers. This process is in line with the present data. The presence of Cs^+ ions promotes this mechanism, and so the open $\uparrow\downarrow\ \pi\pi^{7.2}$ Cs-$^{+}$gA pore, formed in organic solvents, plays a crucial role for the incorporation and formation of gA channels: The lumen of this pore is a uniform hole with a diameter of > 3 Å. The presence of this hole is crucial for the separation into helical monomers, potentially, induced by interaction of the $N(CH_3)_3^+$ group with a cation binding side. In the presence of Ba^{2+}, however, the blocked left-handed $\uparrow\uparrow\ \pi\pi^{5.7}$ pore is formed which has a inner diameter of 2 Å. This much tighter conformation penetrates between the lipid headgroups without any helix rupture. Additionally, all Trp residues are located at one side of the pore, facilitating the penetration of the highly hydrophobic and narrow opposite pore ending into the bilayer. In this way, the pore conformation remains and transforms, first, into the right-handed $\uparrow\downarrow\ \pi\pi^{7.2}$ conformation and then, eventually, into the left-handed $\uparrow\downarrow\ \pi\pi^{5.6}$ double helix.

The EIS investigation of the incorporation process, shown in figure 6.16 and table 6.5, supports the interpretation for both gA types. In the presence of Cs^+ ions, C_{tBLM} increases from 0.75 to 0.89 μF cm^{-2} due to the activity of the gA channel[36] and, thus, the decrease in bilayer thickness brought about by the dimerization of two 13 Å long helix monomers

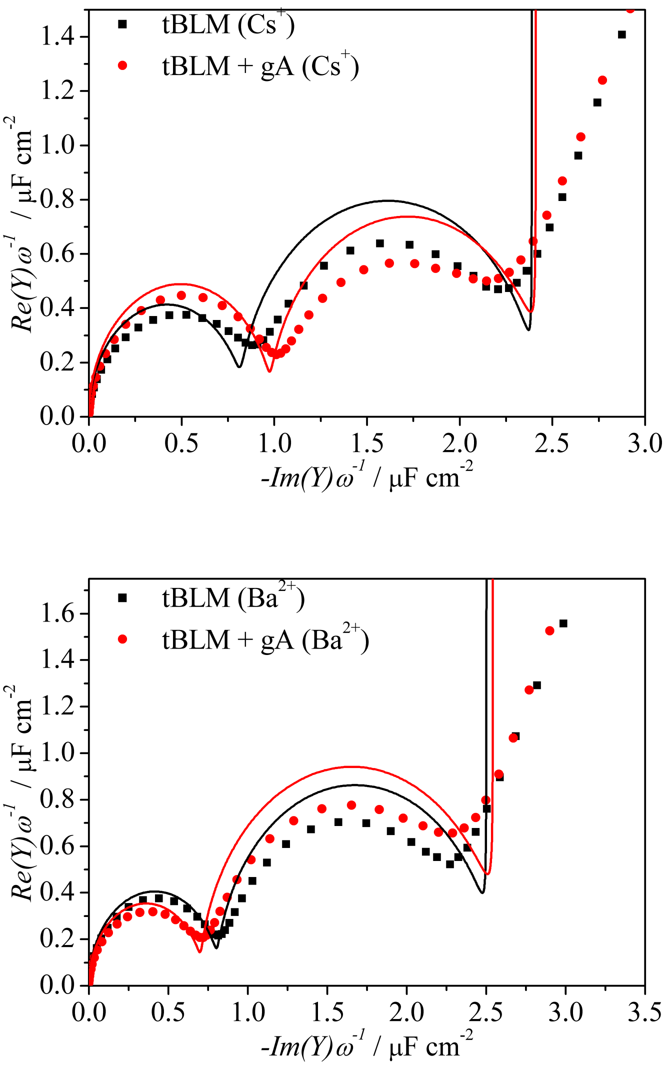

Figure 6.16: Cole-Cole plots recorded in the presence of Cs^+ (top) and Ba^{2+} ions (bottom), respectively. The tBLM on mixed CPEO3/6MH SAMs is presented in black squares; the tBLM with incorporated gA in red circles. Fits are represented as lines.

	R_{Solvent} Ω	R_{Spacer} kΩ cm^2	C_{Spacer} μF cm^{-2}	R_{Bilayer} kΩ cm^2	C_{Bilayer} μF cm^{-2}	C_{tBLM} μF cm^{-2}
tBLM (Cs^+)	98	1280	2.41	5.53	1.28	0.75
tBLM + gA (Cs^+)	94	1210	2.44	7.61	1.67	0.89
tBLM (Ba^{2+})	65	970	2.54	6.00	1.22	0.75
tBLM + gA (Ba^{2+})	68	790	2.59	6.84	0.99	0.64

Table 6.5: Results of the fitting of the equivalent circuit $R_{\text{Solvent}}(R_{\text{Spacer}}C_{\text{Spacer}})(R_{\text{Bilayer}}C_{\text{Bilayer}})$ to the EIS data of tBLMs before and after gA addition (in Cs^+ and Ba^{2+}-Buffer, respectively). The last row is the result of reading out the capacitance of the tBLM directly from the Cole-Cole plot. The error for the resistances and capacitances are 10 % and 5 %, respectively (n = 3).

to the 22 Å long helical dimer. Ba^{2+} ions cause the opposite trend of C_{tBLM} decreasing to 0.64 μF cm^{-2}. This is due to the formation of the pore species $\uparrow\downarrow\,\pi\pi^{5.6}$ which was already observed in the SEIRA spectra. This species is 36 Å long and, thus, leads to a dilation of the tBLM. These changes of the bilayer thickness are also in line with the data resulting from the fit. It shows only considerable changes for the value of C_{Bilayer} which increases for Cs^{+} from ca. 1.25 to 1.67 μF cm^{-2} and decreases for Ba^{2+} to 0.99 μF cm^{-2}. The influence on the bilayer resistance R_{Bilayer} is more difficult to rationalize and is ascribed to the weak resolution in the EIS data. However, also literature data do not correspond to the intuitive expectations.[36]

6.2.2. Structure-Function Relationship of tBLM-embedded gA

The functionality of tBLM-incorporated gA was studied by means of EIS and SEIRA with the goal to demonstrate the potential of nanostructured Au-supported tBLMs to act as a platform providing a native-like environment for membrane proteins. For this purpose, the system with gA incorporated as the helical dimer was used. In this conformation, gA acts as a ion channel that conducts monovalent cations across the membrane according to the series $Tl^{+} > Cs^{+} > K^{+} > Na^{+} > Li^{+}$, as demonstrated by electrochemical studies.[134,136]

EIS of tBLM-embedded gA Figure 6.17 and table 6.6 show the impedance spectra of the gA channel incorporated into tBLMs in the presence of the blocking Ba^{2+} and the conductible Tl^{+}, Cs^{+}, K^{+}, Na^{+}, and Li^{+} ions. Clearly, the non-conductive Ba^{2+} state can be distinguished from the conductive states in presence of the monovalent cations on the basis of the capacitances of the tBLM C_{tBLM} which are determined to be 0.7 μF cm^{-2} for Ba^{2+} and > 0.86 μF cm^{-2} for the monovalent cations. This change can be again attributed to the activity of the gA channel causing the formation of a gA-M^{+} complex with a length of ca. 22 Å and a consequent local compression of the bilayer thickness. This is supported by the fact that the capacitances of the spacer C_{Spacer} do not change considerably (except for the Tl^{+}), but that of the bilayer C_{Bilayer} varies with the same trend as C_{tBLM}. In contrast, binding of Ba^{2+} would elongate the gA channel as the capacitance decreases from 0.75 (with out gA) to 0.7 μF cm^{-2}. This interpretation, however, has to be taken with caution as both values are very close to each other and there is neither a X-ray nor a NMR structure of the Ba^{2+}-gA channel complex available for a comparison. The presence of Tl^{+} seems to cause a strong increase of C_{Spacer}. This result is obscured by the inaccurate fit of the second half circle. Similarly as in the work of Kendall et al.[36], the resistance R_{Bilayer} does not yield any rational trend that includes a functional information. In contrast, Steinem et al.[35] succeeded in reproducing the series and obtained decreasing resistances for the series Li^{+}, Na^{+}, K^{+}, and Cs^{+}. These results, however, were obtained using the concept of the Warburg impedance which is not applicable to the present EIS data due to their complexity. Here, such a trend can be derived from the data taking the magnitude of the impedance at a frequency that probes the bilayer, i.e. 45 Hz (table 6.6). The impedance decreases following the series $Ba^{2+} > Na^{+} > K^{+} > Cs^{+} > Tl^{+}$ which is in line with literature data and proves the functionality of gA channels when incorporated into tBLMs. The impedance for Li^{+} does not agree with this trend. This can be explained tentatively on the basis of the small size of Li^{+} and its high binding affinity to POPC bilayers[64] that allows this cation, after removal of its solvation shell, to diffuse through defects in the tBLM causing a sharp decrease of the impedance. This is supported by the increase of the capacitance of the bilayer (and thus, as well, of that of the entire tBLM) caused by the high dielectric constant of the cation.

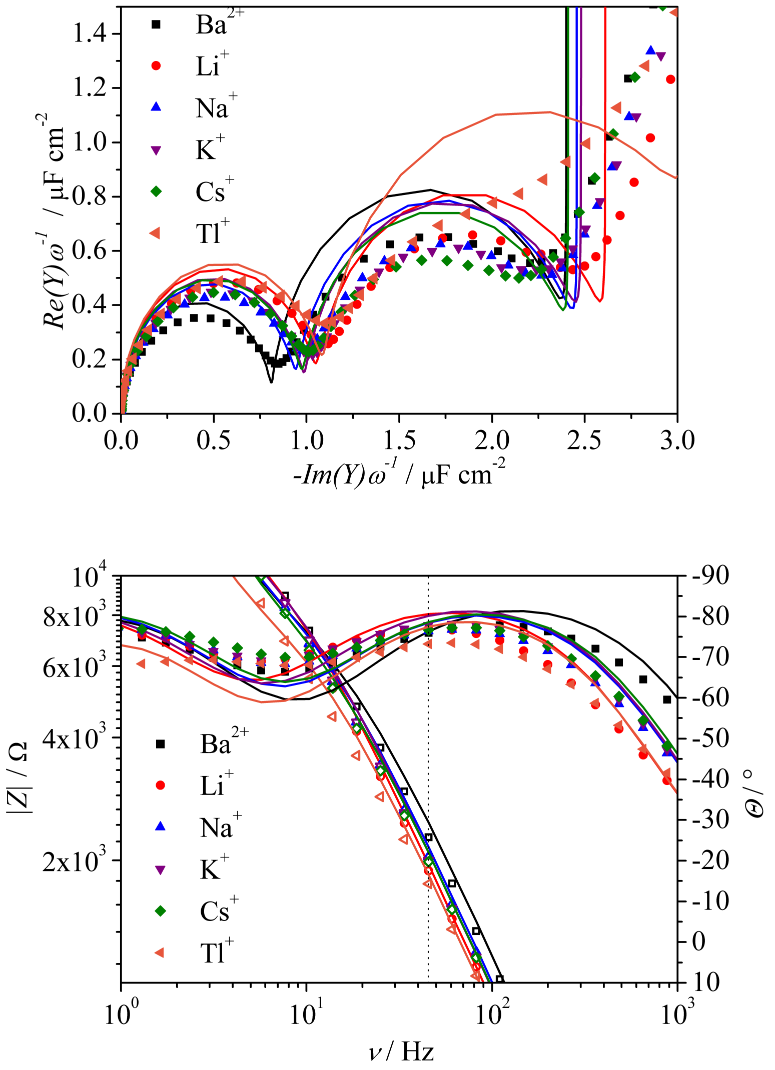

Figure 6.17: Cole-Cole and Bode plots of tBLM-embedded gA recorded in the presence of Tl^+, Cs^+, K^+, Na^+, Li^+, and Ba^{2+}. In the Bode plot, hollow and filled circles refer to the magnitude of the impedance and the phase angle. Fits are represented as lines; the dashed line marks the phase angle of 45 Hz.

	R_{Solvent} Ω	R_{Spacer} kΩ cm^2	C_{Spacer} µF cm^{-2}	R_{Bilayer} kΩ cm^2	C_{Bilayer} µF cm^{-2}	C_{tBLM} µF cm^{-2}	$\lvert Z\rvert_{@45\text{Hz}}$ kΩ cm^2
Ba^{2+}	66	1204	2.44	9.46	1.24	0.70	3420
Li^+	128	1510	2.65	9.52	1.79	0.96	2820
Na^+	105	1362	2.49	8.45	1.56	0.86	3060
K^+	99	1393	2.52	9.72	1.66	0.90	3000
Cs^+	94	1206	2.44	7.61	1.67	0.90	2970
Tl^+	117	401	3.24	8.30	1.69	0.97	2630

Table 6.6: Results of the fitting of the equivalent circuit $R_{\text{Solvent}}(R_{\text{Spacer}}C_{\text{Spacer}})(R_{\text{Bilayer}}C_{\text{Bilayer}})$ to the EIS data of tBLM-embedded gA in the presence of Tl^+, Cs^+, K^+, Na^+, Li^+, and Ba^{2+}. C_{tBLM} is the result of reading out the capacitance of the tBLM directly from the Cole-Cole plot. $\lvert Z\rvert_{@45\text{Hz}}$ is the magnitude of the impedance taken at a frequency of 45 Hz. The error for the resistances (and impedances), and capacitances are 10 % and 5 %, respectively (n = 3).

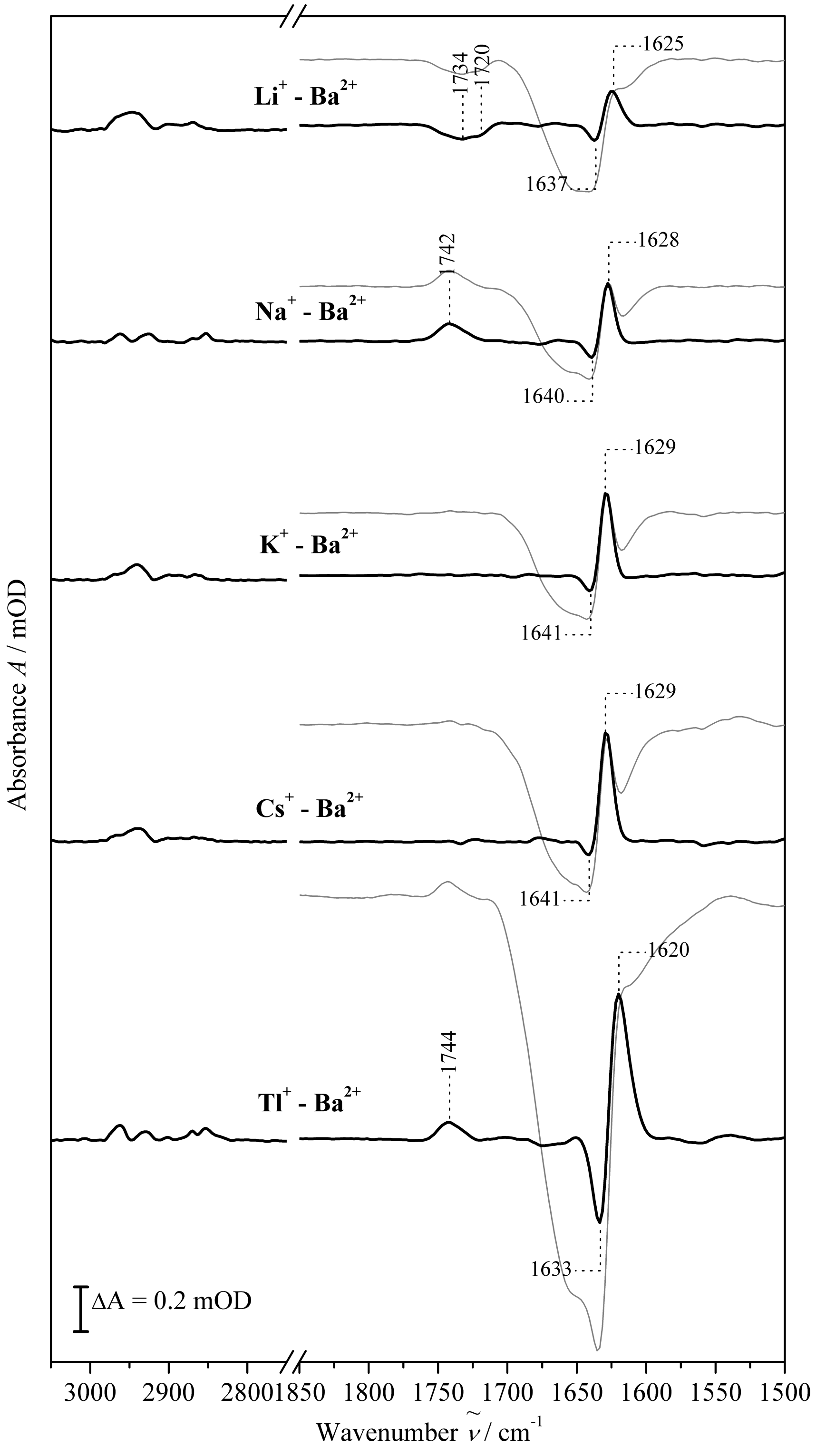

Figure 6.18: SEIRA difference spectra of gA incorporated into tBLMs in the presence of the monovalent cations Tl^+, Cs^+, K^+, Na^+, and Li^+, using the spectrum of the sample in the presence of Ba^{2+} as a reference. Grey spectra show the non-baseline corrected difference spectra showing, in addition, a broad negative water band. This band was removed as described in the experimental section (5.4).

SEIRA of tBLM-embedded gA The functionality of the incorporated gA was studied, as well, by measuring SEIRA difference spectra in the presence of Li^+, Na^+, K^+, Cs^+, and Tl^+, taking the spectrum in the Ba^{2+}-buffer as the reference. These spectra reveal several SEIRA difference bands of the phospholipids, i.e. CH_n stretchings (3000 - 2850 cm^{-1}) and C=O stretchings (1750 - 1700 cm^{-1}), of gA's amide I band (1650 - 1600 cm^{-1}), and of the broad negative band of water (H-O-H bending) centered at 1650 cm^{-1}. This H-O-H bending difference band arises from cation-phospholipid interactions, as shown for difference spectra in the absence of gA (figure 5.6). Upon the exchange of cations accumulated at the tBLM surface, water molecules are removed as well, since monovalent cations carry a substantially smaller hydration shell than the bivalent Ba^{2+}. This is in line with the intensity of this negative water band which increases (with a negative sign) with ion size. Li^+, as a small ion, has a more extended solvation shell comprising a high amount of water; bigger cations, however, carry less water molecules in their solvation shell. Hence, the difference between Li^+ and Ba^{2+} leads to a rather small negative difference water band and the difference between a bigger cation and Ba^{2+} to an stronger negative difference band. To appreciate the structural changes of gA more clearly, this broad negative band was removed by subtraction of a set of Gaussian functions to yield the black spectra in figure 6.18, as described in section 5.4. The now clearly observable reversible amide I changes result from replacing Ba^{2+} ions at the binding site in the gA channel by the various monovalent cations. Thus, these spectral changes describe an increase of the conducting state and a decrease of the non-conductive Ba^{2+}-bound state, reflected by the positive difference band between 1629 and 1620 cm^{-1}, and negative difference band between 1641 and 1633 cm^{-1} shifted by 12 - 13 cm^{-1} in each spectrum. In this regard, as will be shown, the spectral position provides structural insight, whereas the intensity yields functional information upon ion conductance.

The structure of the conducting state of gA, in the presence of Na^+, K^+ and Cs^+, can be confidently ascribed to the cation-bound $\beta^{6.3}\beta^{6.3}$ conformation, due to their the amide I positions of 1629 and 1628 cm^{-1}.[127] For Li^+ and Tl^+, this position is shifted to 1625 and 1620 cm^{-1}, respectively. In the case of Li^+, this indicates the formation of a helix conformer with a different number of residues per turn and, thus, an decreased channel diameter to fit the size of the cation. This is supported by the following: the empty gA channel has a lumen diameter of 3.6 Å[132] which does not change substantially upon Na^+ binding. Since Na^+ has a ion diameter of ca. 1.96 Å, one can assume that it will not change as well for K^+ and Cs^+ with ion diameters of 2.66 and 3.34 Å, respectively, which fit into the binding site even better. Li^+, however, is considerably smaller (1.36 Å) and, thus, tightens the channel as displayed by the shifted amide I position. This interpretation does not hold for Tl^+ (1620 cm^{-1}), at first sight, which has a ion diameter of 2.94 Å , lying in between the ones of K^+ and Cs^+. This discrepancy can be rationalized in two ways. On one hand, Tl is much more polarizable than the alkali ions due to the presence of filled f-orbitals which alter the Tl^+-gA interaction. On the other hand, Tl^+ has a considerably stronger affinity producing a doubly Tl^+-bound channel whereas the alkali cations rather yield a steady state equilibrium of the single-occupied gA. The latter interpretation is in line with literature findings where the generation of the doubly occupied K^+-gA complex required substantially higher cation concentrations than for Tl^+-gA complex which was already formed at low Tl^+-concentrations.[161] In this respect, the observed shift to 1620 cm^{-1} accords to the observation, that double occupancy leads to an outward movement of the cations,[162] which causes a narrowing of the helix.

The negative band amide I difference band of the non-conductive Ba^{2+}-bound gA state is observed at different positions between 1641 and 1633 cm^{-1}. At first glance, this seems to be irrational, as the Ba^{2+}-bound gA should be characterized by only one species displaying a single amide I difference band. This phenomenon, however, can be attributed to (and again proves) the presence of a planar, aqueous reservoir below the tBLM on the nanostructured Au film. Monovalent cations are conducted across the membrane by gA and, thus, fill the aqueous reservoir. Upon exchange to Ba^{2+} ions, the channel gets blocked from the bulk solution exposed side and prevents the monovalent cations from exiting the sub-membrane reservoir. Consequently, this leads to the formation of a hetero dimeric gA channel of the type M^{+}-$\beta^{6.3}\beta^{6.3}$-Ba^{2+} bound to one monovalent cation and one Ba^{2+}. This also explains the same band shift of 12 - 13 cm^{-1} for each cation pair.

The intensity of the positive amide I difference band increases in the series $Li^{+} < Na^{+} < K^{+} < Cs^{+} < Tl^{+}$. This is in accord with electrochemical conductivity studies of membrane-bound gA and, thus, allows for monitoring the functionality of gA. The reason for this is that the binding of the cations to the gA binding site represents the limiting step of ion conductance.[137] This binding affinity increases in the very same series leading to a higher steady state concentration of the cation-bound gA. This, eventually, is observed in the SEIRA difference spectrum as a more intense difference band.

6.2.3. Cation-Phospholipid Interactions

In addition to structural and functional information on gA, SEIRA difference spectra in figure 6.18 give insight into the nature of cation-phospholipid interactions by displaying changes in the CH_n and C=O stretching region (3000 - 2850 cm^{-1} and 1750 - 1700 cm^{-1}). The CH_n region shows a rather complicated pattern composed of several positive and negative difference bands. However, the C=O difference band displays a simpler picture. In the case of the alkali cations vs. Ba^{2+}, one can identify three situations: for Li^{+} a negative C=O difference band at 1734 cm^{-1} with a shoulder at 1720 cm^{-1}, for Na^{+} a positive difference band centered at 1742 cm^{-1}, and for K^{+} and Cs^{+} no spectral features. These spectral changes can be interpreted on the basis of theoretical[163,164] and experimental[64] data on cation binding to POPC. Accordingly, Li^{+}, Na^{+}, and Ba^{2+} ions bind very strongly to the POPC headgroups, whereas K^{+} (and, thus, Cs^{+} as well) does not penetrate the headgroup region, but remains in the solution. In this scenario, calculations of cation-bound DPPC bilayers[164] revealed that these ions bind with different coordination patterns and are located at different positions within the lipid headgroup region, i.e. 1.86 nm (Li^{+}), 1.79 nm (Na^{+}), and 1.90 nm (Ba^{2+})[164] away from the center of the membrane. Furthermore, measurements of the zeta potential of cation-bound vesicles showed that Li^{+} binds in such high amounts that the surface of the vesicles becomes positively charged, whereas Na^{+} renders the vesicles neutral. In the presence of K^{+} and Cs^{+}, the vesicles were negatively charged supporting the finding that these cations do not bind to the lipid headgroups. Due to the combination of these effects, exchanging Ba^{2+} by Li^{+} or Na^{+} leads to notable difference bands in the C=O stretching region of the present SEIRA spectra, albeit of opposite sign. This is attributed to a different vertical displacement or tilt angle of the Li^{+} and Na^{+}-bound lipid head groups with respect to the surface, thereby accounting for the negative and positive signals in the difference spectrum. An analogous interpretation may hold for the binding of Tl^{+} ions. As mentioned before, K^{+} and Cs^{+} ions do not interact directly with the C=O groups of POPC. This is consistent with the lack of difference bands in the present SEIRA spectra, as these cations are not capable of penetrating the POPC headgroup region and, thus, do not alter the ion content of the headgroups.

6.2.4. Summary

Incorporation of the gA Channel In the presence of Cs^{+} ions, gA incorporates into the tBLM in its channel conformation denoted as the helical dimer $\beta^{6.3}\beta^{6.3}$. This finding is in

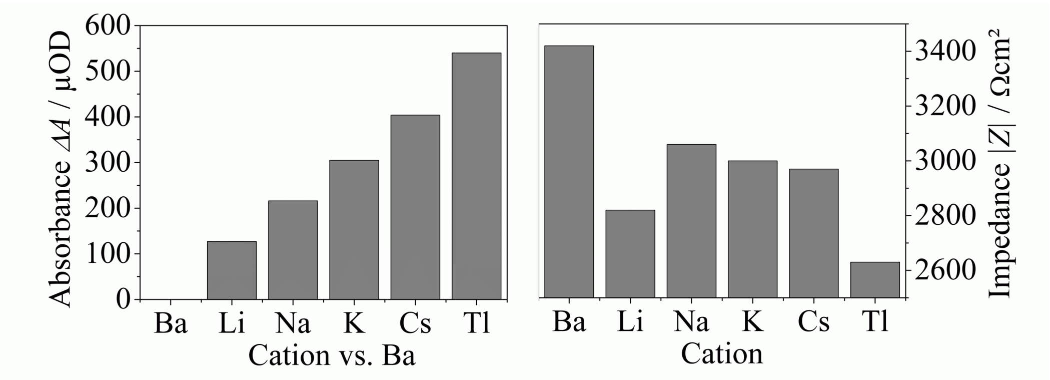

Figure 6.19: Left: Intensities of the positive amide I band (1620 - 1629 cm^{-1}) of the conductive state in the SEIRA difference spectra (figure 6.18). Right: Impedance values at a frequency of 45 Hz of the tBLM with gA in the presence of different cations (figure 6.17; table 6.6). The errors of the absorbance and the impedance values are within 10 and 5 %, respectively.

line with literature data.[128] As the presence of $\uparrow\downarrow\ \pi\pi^{7.2}$ gA-Cs$^+$ complex in organic solutions and helix monomers in membranes is established, the incorporation process proceeds in the following order according to the present results:

$$\uparrow\downarrow\ \pi\pi^{7.2}\ \text{(TFA)} \longrightarrow \beta^{6.3}\ \text{(upper leaflet)} \longrightarrow \beta^{6.3}\ \text{(bottom leaflet)} \longrightarrow \beta^{6.3}\beta^{6.3}$$

The presence of the open $\uparrow\downarrow\ \pi\pi^{7.2}$ conformer is critical for the channel formation, as the open pore of > 3 Å is a predetermined breaking point for the separation into helix monomers by penetration of the positively charged choline $N(CH_3)_3^+$ group.

Incorporation of gA Pores In the presence of Ba^{2+} ions, a gA pore is formed when inserted into tBLMs. SEIRA spectra point at the left-handed $\uparrow\downarrow\ \pi\pi^{5.6}$ double helix. Here, no unified model is present. However, starting from the closed $\uparrow\uparrow\ \pi\pi^{5.7}$ pore, known to be formed in the presence of bivalent cations, the following mechanism is proposed:

$$\text{lh-}\uparrow\uparrow\ \pi\pi^{5.7}\ \text{(TFA)} \longrightarrow \text{lh-}\uparrow\uparrow\ \pi\pi^{5.7} \longrightarrow \text{rh-}\uparrow\downarrow\ \pi\pi^{7.2} \longrightarrow \text{lh-}\uparrow\downarrow\ \pi\pi^{5.6}$$

As the $\uparrow\uparrow\ \pi\pi^{5.7}$ pore is wedge-shaped (all Trp are located at the C-terminus) and highly hydrophobic at its N-terminus, it inserts in between the headgroups without being split into monomers. The subsequent transition involves a change in handedness of the pore from left-handed (lh) over right-handed (rh) to left-handed. This could be a general mechanism for pore transitions, as these conformers only exist in the structures with these head directions.

Functionality of the gA Channel The tBLM-incorporated gA channel was used to test the biomimetic properties of the tBLM. As shown in figure 6.19, the activity of the gA channel was probed successfully with both, EIS and SEIRA. EIS allows for distinguishing between the conductive and non-conductive state with the specific tendency of conductance Na$^+$ < K$^+$ < Cs$^+$ < Tl$^+$ which is in line with literature data. Li$^+$ is conducted as well, however, does not fit the expected trend. This can rationalized on the basis of present defects which allow spatial diffusion of the small Li$^+$ across the bilayer. SEIRA difference spectra probe the functionality very accurately using the intensity of the amide I difference band increasing in the following series Li$^+$ < Na$^+$ < K$^+$ < Cs$^+$ < Tl$^+$, specific for the gA channel in membranes. This functional information can be combined with structural insight provided by the position of the amide I difference band. The amide I position is modulated depending on the size of the present monovalent cation. Na^+, K^+, and Cs^+ fit the inner diameter without changing the inner helix diameter considerably and, thus, the amide I position maintains at ca. 1629 cm^{-1}, the same spectral position as for the emtpy pore. The much smaller Li^+ narrows the pore upon binding, shifting the amide I to lower wavenumbers (1625 cm^{-1}). For Tl^+, the amide I appears at even smaller wavenumbers of 1620 cm^{-1} due to double occupancy associated with outward movement of the ions and a thereby decreased helix diameter. Here, the high polarizability of Tl^+ changes the cation-gA interactions, as well.

Cation-Phospholipid Interactions The effect of cation-lipid interactions as reflected by the SEIRA difference spectra is in line with previous findings. K^+ and Cs^+ do not penetrate the membrane headgroup region. As a consequence, they do not exchange the tightly lipid-bound Ba^{2+} ions and the C=O stretching region remains unaffected. Li^+ and Na^+, however, penetrate into the bilayer headgroup region and are capable of replacing the bound Ba^{2+} ions. This causes a change in the orientation and position of the C=O bonds, visible in SEIRA spectra. Tl^+ affects the SEIRA spectrum similarly as Na^+ and, thus, probably leads to a similar binding situation.

6.3. Spectroelectrochemistry of hVDAC Incorporated into tBLMs

Since not every membrane protein shows the ability to integrate spontaneously into a preformed tBLM, an alternative way to incorporate transmembrane proteins into tBLMs makes use of protein-reconstituted vesicles forming proteo-tBLMs by spreading and fusion in one step. To study the suitability of CPOE3/6MH-supported tBLMs for the construction of such a system, the voltage-gated channel hVDAC was used. hVDAC was proposed to exert voltage-gating ion conductance when incorporated into membranes, although unpublished data by Steinem et al. show that the closing probability of the channel is much less pronounced (ca. 5 %) than present literature suggests (ca. 40 %). Thus, one goal is to clarify if structural changes of the hVDAC are in line with these observed electrophysiological properties. To date, *in situ* structural studies on the function of the voltage-gating of hVDAC were accompanied by the limitation of spectroscopic methods to address the membrane-incorporated protein electrochemically and spectroscopically at the same time. SEIRA spectroscopy is the method of choice for this aim and, thus, tBLM-embedded hVDAC is studied with this spectroelectrochemical approach for the first time in this work. Furthermore, the suitability of the CPEO3/6MH-supported tBLM for potential-induced SEIRA spectroscopy will be addressed in general.

6.3.1. Formation of hVDAC-containing tBLMs

EIS of tBLM-embedded hVDAC hVDAC was immobilized onto the SEIRA electrode by spreading and fusion of hVDAC-reconstituted POPC vesicles. This system was compared with pure tBLMs formed on CPOE3/6MH SAMs originating from the same CPEO3/6MH solution. In this way, SAMs with the same electrical properties were obtained as a starting point for both systems, so that tBLMs with and without hVDAC can be compared quantitatively. Figure 6.20 and table 6.7 show the results of the EIS investigation before and after the ECT. Before the ECT, tBLMs with comparable electrical properties were achieved. The capacitances C_{tBLM} and resistances R_{Bilayer} of both systems were determined to be ca. 0.63 μF cm^{-2} and ca. 5.2 kΩ cm^2, respectively, pointing at the formation of tBLMs also in the case of hVDAC-reconstituted vesicles (hVDAC is in deed present in the tBLMs as will be

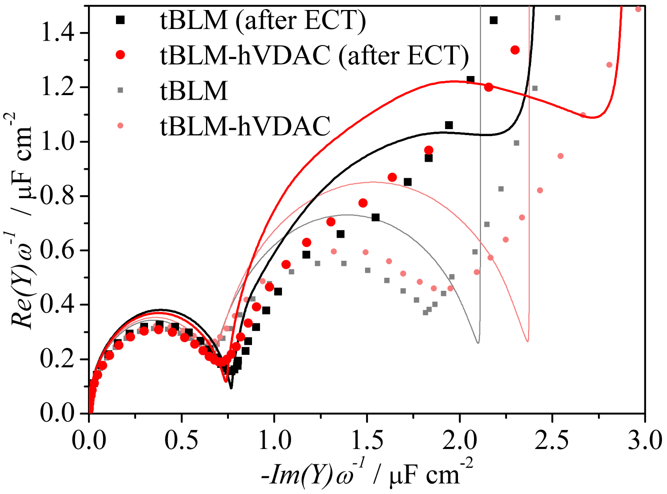

Figure 6.20: Cole-Cole plots of hVDAC-tBLMs (red) and pure tBLMs (black) before and after the ECT (in pale and intensive colors). Lines represent the result of the fit.

	R_{Solvent} Ω	R_{Spacer} kΩ cm^2	C_{Spacer} μF cm^{-2}	R_{Bilayer} kΩ cm^2	C_{Bilayer} μF cm^{-2}	C_{tBLM} μF cm^{-2}
tBLM	114	930	2.11	5.3	1.04	0.63
tBLM-hVDAC	109	1110	2.39	5.1	1.02	0.64
After electrochemical treatment (ECT)						
tBLM	106	410	2.69	21.3	1.09	0.66
tBLM-hVDAC	104	363	3.13	13.7	0.99	0.61

Table 6.7: Results of the fitting of the equivalent circuit $R_{\text{Solvent}}(R_{\text{Spacer}}C_{\text{Spacer}})(R_{\text{Bilayer}}C_{\text{Bilayer}})$ to the EIS data of the pure and hVDAC-containing tBLM before and after the electrochemical treatment (see section 5.4.1). The last row is the result of reading out the capacitance of the tBLM directly from the Cole-Cole plot. The error for the resistances and capacitances are 20 % or 10 % (before and after the ECT, respectively) and 5 %, respectively (n = 3).

shown by means of SEIRA; *vide infra*). The fact that hVDAC-tBLMs and pure tBLMs do not differ significantly from each other can be attributed to the relatively low concentration of hVDAC, the presence of defects associated with a higher conductivity than the protein, and unfavorable positioning and orientation of the hVDACs (see figure 6.21).

Applying the ECT, the capacitances change only insignificantly, but differences of the bilayer resistance of the hVDAC-tBLMs and pure tBLMs are revealed: in the presence and absence of hVDAC, R_{Bilayer} is determined to be (14 ± 2) and (21 ± 2) kΩ cm^2, respectively. This is an expected result, since the hVDAC pore allows for the free diffusion of ions across the membrane lowering the resistance and, thus, proves the presence of the ion channel in the tBLM. Thus, this result points to the successful construction of a hVDAC-tBLM system by spreading proteoliposomes.

SEIRA of tBLM-embedded hVDAC As shown in table 6.7, spreading hVDAC-containing vesciles on CPEO3/6MH SAMs leads to comparable dielectric properties as for pure POPC vesicles. This is displayed as well in the SEIRA spectra by the CH$_n$ stretching region (figure

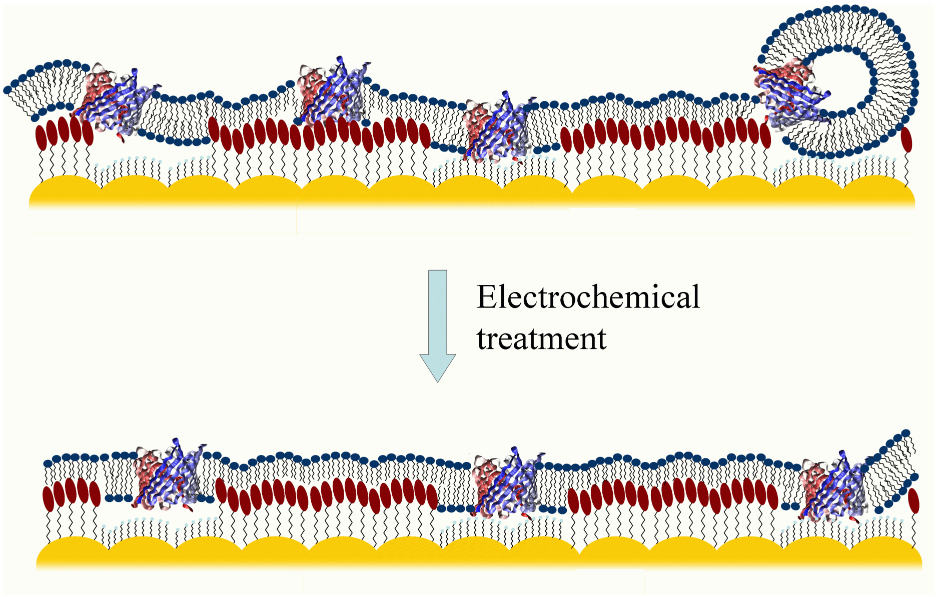

Figure 6.21: Schematic representation of the hVDAC-tBLM before and after the ETC

6.22) that show approximately the same intensities and only slight changes in the band pattern induced by the presence of hVDAC. The intensity of the C=O stretching vibration of the POPC molecules, however, differs significantly between hVDAC-tBLMs and pure tBLMs. This can be explained tentatively on the basis of POPC-hVDAC interactions that affect the molecular arrangement of the POPC molecules within the tBLM and, thus the orientation of the C=O bond with respect to the surface. Upon ECT this difference diminishes to reach almost the same intensity as the pure tBLM system. The remaining difference is associated partially with the lower number of POPC molecules within the POPC-POPC bilayer fragments in the presence of hVDAC. This is supported by the head-$\nu_{\mathrm{as}}(\mathrm{CH}_3)$ at 1492 cm^{-1} that appears with negative intensity in all "hVDAC-tBLM minus tBLM" difference SEIRA spectra in figure 6.23.

The fact that hVDAC is in deed present in the tBLMs is proven by the amide region of the SEIRA spectra. Figure 6.22 shows SEIRA spectra of tBLMs and hVDAC-tBLMs before the ECT in grey and black color, respectively. In the spectrum recorded in H_2O buffer (1$^{\mathrm{st}}$ spectrum from top), the broad negative water band at ca. 1645 cm^{-1} interferes severely with the amide I band and, in this way, impedes the direct observation of the amide I band. The amide II band, however, can be identified easily by comparison with the spectrum of pure tBLMs (marked with red color in the spectra). Subtracting the SEIRA spectrum of the pure tBLM from the one of the hVDAC-tBLM (see figure 6.23; 1$^{\mathrm{st}}$ spectrum from top) reveals the SEIRA spectrum of the immobilized hVDAC more clearly. Here, the amide I band is visible as well, however, with a distorted structure due to the subtraction of the negative water H-O-H bending. With the help of the second derivatives, 4 components located at 1695, 1681, 1655 and 1633 cm^{-1} can be indentified. These bands are ascribed to the minor β-sheet band, turns, random coils, and the major β-sheet band of hVDAC, respectively.[151] A contribution of the α-helix at 1655 cm^{-1} can not be excluded, but is rather improbable as its transition dipole moment should be directed approximately in parallel to the Au surface. The amide II band is relatively sharp and centered at 1558 cm^{-1}. This may be contradictive at first glance, since ATR-IR spectra of hVDAC (see figure 4.10 on page 51) show a broad band ranging from 1570 to 1510 cm^{-1} with a maximum at ca. 1530 cm^{-1}. Here, however, the preferential enhancement of the structural motifs located closely to the Au film have to be considered, i.e. the β-sheet-connecting turns, random coils, and amino acid residues

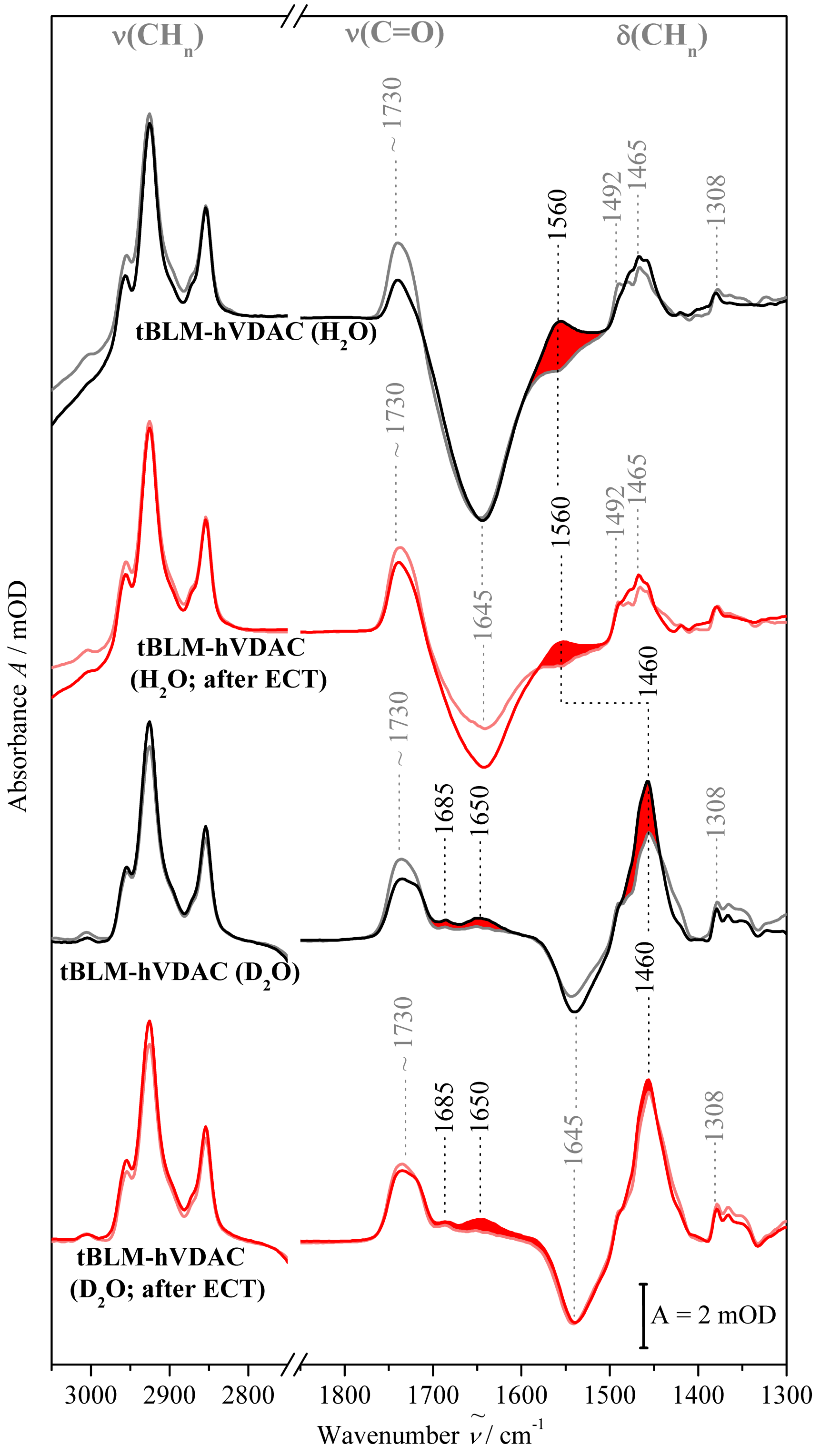

Figure 6.22: SEIRA spectra of hVDAC-tBLMs and pure tBLMs are shown in intensive and pale colors, respectively. The spectra before the ECT are depicted in black, and those after the ECT in red. The amide I and amide II or amide I' and amide II' bands recorded in H_2O and D_2O, respectively, are indicated by the areas filled with red color.

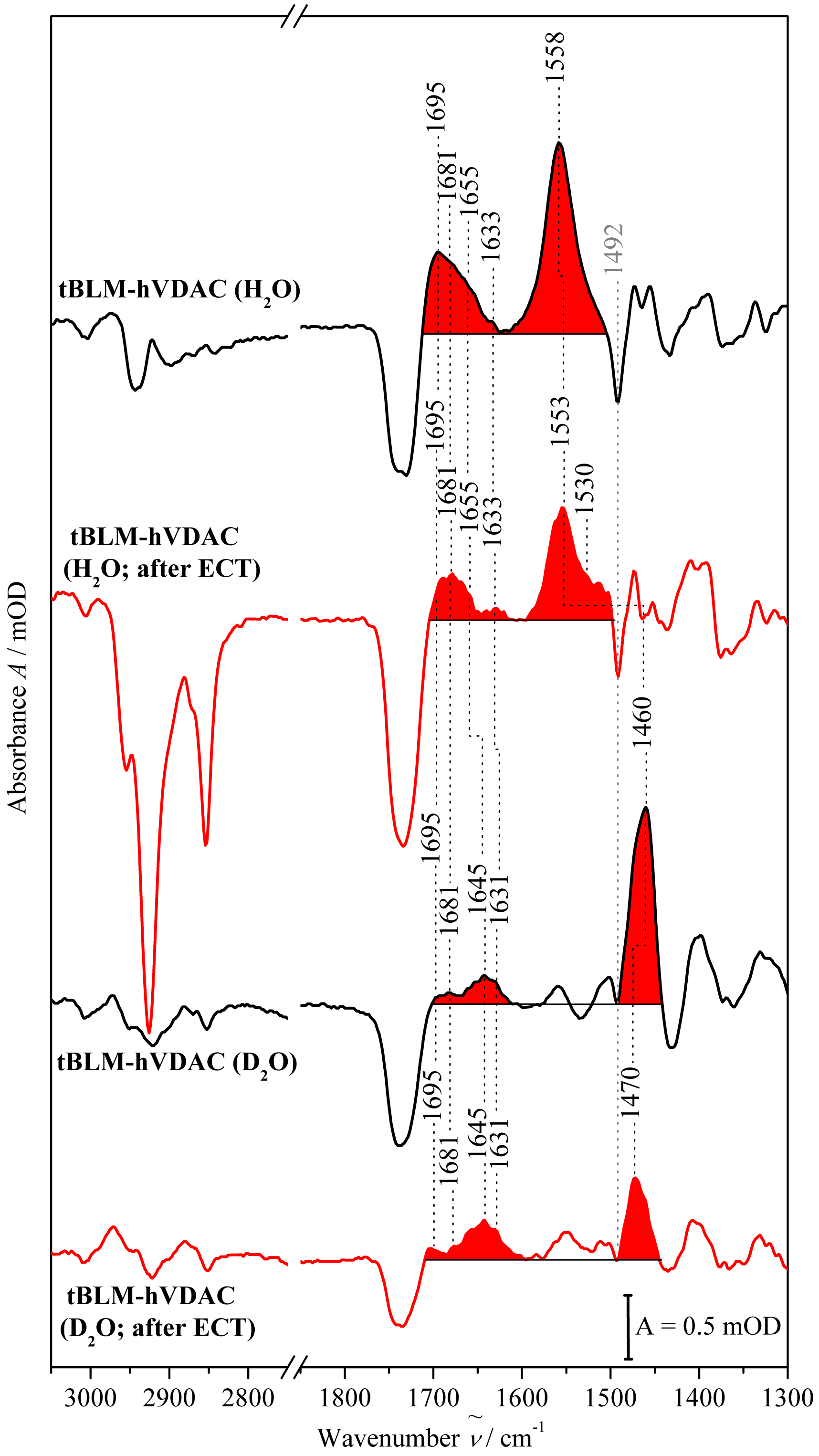

Figure 6.23: SEIRA difference spectra “hVDAC-tBLM minus tBLM” calculated from the spectra in figure 6.22. The spectra before the ECT are depicted in black, and those after the ECT in red. The amide I and amide II or amide I’ and amide II’ bands recorded in H_2O and D_2O, respectively, are indicated by the areas filled with red color. The spectrum after the ECT in H_2O was calculated in such a way that the negative water band at ca. 1645 cm^{-1} is compensated. Thus, the CH_n stretching vibrations appear as strong negative bands.

such as aspargine and glutamine containing an additional amide group (see figure 6.24). All of these structural features display vibrations at wavenumbers above ca. 1550 cm^{-1}.[108] Furthermore, the amide II transition dipole moment of the α-helix is directed along the polarized electromagnetic field and is more enhanced in the SEIRA spectrum. In addition, the negative head-CH_3 vibration at 1492 cm^{-1} reduces the intensity of the shoulder of the amide II band at ca. 1530 cm^{-1}. A combination of these factors is responsible for the sharp but asymmetrical band shape of the amide II band at 1558 cm^{-1}.

Figure 6.22 shows the spectra of hVDAC in D_2O (3rd spectra from top). Here, the amide II' is superimposed by the CH_n and N-D bendings. Subtraction with the spectrum of the tBLM (see figure 6.23) reveals a amide II' at 1460 cm^{-1}. In analogy to the spectrum in H_2O, the position is shifted as well when compared to ATR-IR data[151] which show a broad band at 1445 cm^{-1}. Here, again negative peaks at the high and low-frequency flank distort the amide II' band shape. The amide I' region, however, is isolated mostly from other contributions; solely C=O vibrations of the CPOE3 molecules are visible as weak and broad bands in this region. The amide I' band pattern of hVDAC is comprised of the same components as in the case of H_2O at 1695, 1681, 1645, and 1631 cm^{-1}. The most pronounced effects upon H/D-exchanged is observed for the bands shifting from 1655 to 1645 cm^{-1} and 1633 to 1631 cm^{-1}. This is in line with findings in literature.[151] In D_2O, the relative intensities of the amide I' components agree very well with the ATR-IR spectra (see figure 4.10 right). Since the β-sheets are farther away from the Au surface than the turn and random coil region of the hVDAC channel entrance, it is expected that the amide I component of the β-sheets at ca. 1631 cm^{-1} displays weaker intensity than in the ATR-IR spectra (see figure 6.24). This, indeed, is the case for these spectra, as the component at 1645 cm^{-1} overrides the band at 1631 cm^{-1} in comparison to ATR-IR spectra. This is also in line with the observed amide II band in H_2O where the β-sheet component (ca. 1530 cm^{-1}) is considerably weaker in the SEIRA spectra than in the ATR-IR spectra. The maximum intensity of the amide I' of ca. 0.3 mOD points to a low protein density within the tBLM. In comparison, protein monolayers on SEIRA Au films yield 10 - 30 times higher intensities. Thus, with CPEO3/6MH SAMs composed of 20 % 6MH, enough space is provided for all hVDAC molecules to occupy the 6MH-supported POPC-POPC bilayers.

The ECT changes the water content in the SEIRA spectrum of the tBLM (see section 6.1.2) and, thus, the hVDAC SEIRA difference spectrum in H_2O in figure 6.23 has to be adjusted to the negative water band to visualize the amide I band more clearly. Here, the amide I band in the difference spectrum does not change significantly. The most prominent change is experienced by the amide II band which shifts slightly to 1553 cm^{-1} and reveals a broad shoulder at the low-frequency flank which corresponds to the amide II band observed in ATR-IR spectra. The fact that this band undergoes such changes can be attributed to the reorganization of the entire tBLM which relocates hVDACs within the tBLM and causes the negative head-CH_3 vibration at 1492 cm^{-1} to disappear (see figure 6.21). In D_2O, the amide I' region maintains its band structure with a slight increase in intensity. This increase can be interpreted as well in terms of the rearrangement processes initiated by the ECT. This process leads to a more homogeneous tBLM structure and, thus, to a higher density of hVDACs within the 6MH-supported bilayer patches. The amide II' is shifted to 1470 cm^{-1} in the D_2O spectrum. Since this band is generally superimposed by CH_n and N-D bendings of the tBLM, this shift is caused by interfering with negative difference bands.

The amide I/amide II (or amide I'/amide II') intensity ratio is difficult to evaluate, since the amide I' is the only non-superimposed band in the SEIRA spectra. However, in each case the amide II or amide II', respectively, was experienced to be more intense. This observation is in line with expectation when compared to dichroic ATR-IR spectra of hVDAC by Abrecht et al.[151] (see figure 4.10 right). Since the β-sheets are farther away from the

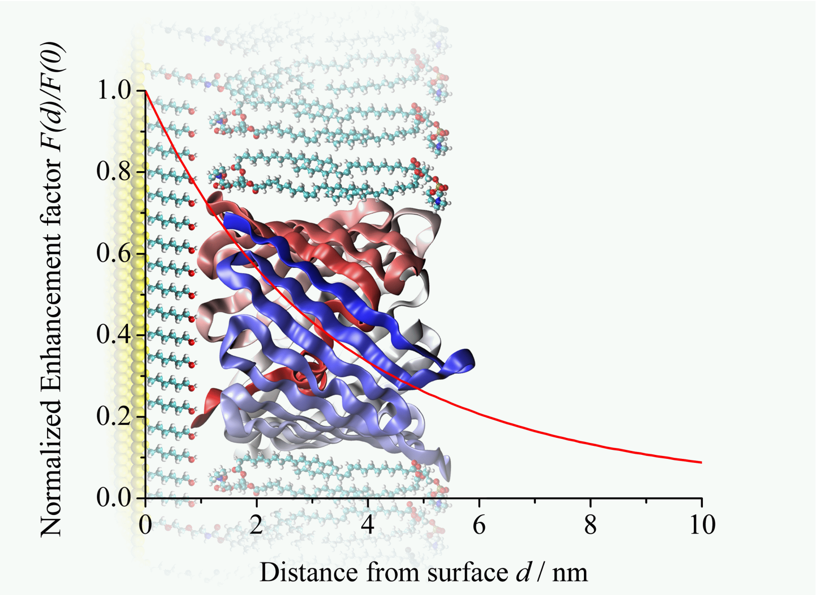

Figure 6.24: Schematic representation of the SEIRA enhancement profile (according to equation 2.30; a_0 = 20 nm) applied to the hVDAC-tBLM system.

surface, the intensity of the β-sheet components at ca. 1633 and ca. 1530 cm^{-1} is reduced and a spectrum is obtained which resembles the present spectrum with a amide II centered at ca. 1560 - 1550 cm^{-1}, an amide I with a weaker 1633 cm^{-1} component, and amide I/amide II intensity ratio < 1. Unfortunately, due to the complex mechanism of SEIRA and the heterogeneous roughness of the Au film, a reliable quantification of this effect is not straightforward. However, taking into account only the EM mechanism of the enhancement for a homogeneous surface composed of spherical particles with a radius of a_0 = 20 nm, one can estimate the surface enhancement profile across the tBLM (see figure 6.24) on the basis of equation 2.30.[5] Accordingly, the turn region experiences a normalized SEIRA enhancement of ca. 0.75, whereas in the core of the hydrophobic bilayer region the enhancement decays to ca. 0.4. This is in line with the observed amide band intensities. Thus, the measured SEIRA spectra show the successful immobilization of hVDAC in the CPEO3/6MH-supported tBLM on the SEIRA Au electrode and indicates the presence of hVDAC in its native conformation and in a uniform orientation.

Kinetics of hVDAC Immobilization The kinetic investigation of the hVDAC immobilization from the SEIRA spectra is aggravated by the low intensity of the amide bands and the interference of the amide region with IR absorptions of the tBLM. The most reliable result was obtained from the amide II band. For this purpose, SEIRA difference spectra were calculated in the same way as in figure 6.23, but using the hVDAC-tBLM and tBLM spectra obtained at the same time (hVDAC-tBLM at time t “minus” tBLM at time t). The time course of the intensity of the amide II and the results of the exponential fit is shown in figure 6.25. The amide II band increases biexponentially with the time constants τ_1 = (3 ± 2) min and τ_2 = (32 ± 6) min. In comparison to that, the CH$_n$ stretchings of the POPC molecules and the capacitance of the tBLM evolve with time constants of ca. 2 and 65 min, and 2 and 30 min, respectively (see sections 6.1.2 and 6.1.2). Hence, the here observed kinetics of the amide II band are in line with the observed evolution of the capacitance C_{tBLM} and the increase of the amide II can be ascribed to the binding and a subsequent spreading of hVDAC-tBLM vesicles. However, rearrangement processes of the POPC molecules

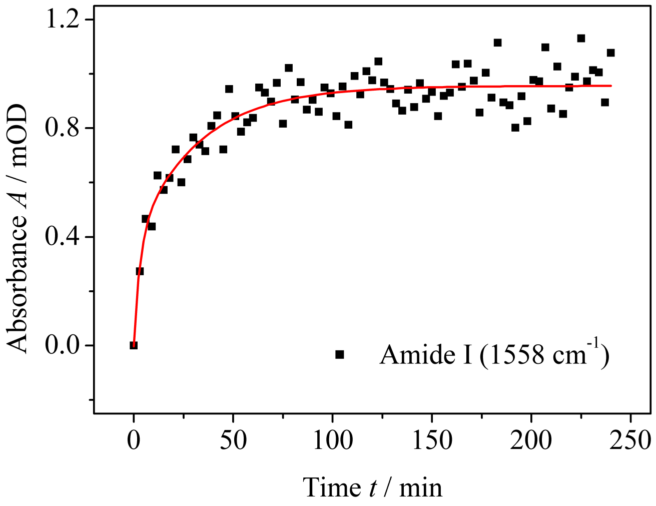

Figure 6.25: Time course of the amide I intensity obtained from the "hVDAC-tBLM minus tBLM" difference SEIRA spectra. For this purpose, hVDAC-tBLM and tBLM spectra taken at the same time after the addition of vesicles were used for each difference spectrum. Red line represents the biexponential fit $A = A_0 - A_1 exp(-t/\tau_1) - A_2 exp(-t/\tau_2)$ with the result: A_0 = (0.96 ± 0.01) mOD; A_1 = (0.4 ± 0.1) mOD; τ_1 = (3 ± 2) min; A_2 = (0.57 ± 0.09) mOD; τ_2 = (32 ± 6) min; R^2 = 0.84234

(derived from the slow kinetics with ca. 65 min) do not affect the protein. Since this process involves the coating of CPEO3-covered fragments, the protein is partially located at CPOE3-supported bilayer fragments. This is also an explanation for the similar resistance in hVDAC-tBLMs and pure tBLMs.

Since the ECT leads to the expected difference in bilayer resistance, it can be assumed that rearrangements take place. This involves a movement of CPEO3-supported hVDACs to 6MH-supported tBLM fragments or a removal of unfavorably bound hVDACs. The exact underlying rearrangement processes, however, can not be elucidated on the basis of these results.

6.3.2. Structure-Function Relationship of hVDAC in tBLMs

The successfully constructed hVDAC-tBLM system was used to investigate the suitability of CPEO3/6MH-supported tBLMs for functional and spectroelectrochemical studies. For this purpose, current measurements and SEIRA difference spectroscopy were performed to characterize the closed and open state of hVDAC. Concerning the latter, a crucial aspect is the choice of the potential at which hVDAC remains in its open state. In experiments using free-standing black lipid membranes with two equal electrodes, this potential is defined by the potential at which no current is observed and, thus, is close to 0 V. In analogy to this approach, in the present experiments the open circuit potential E_{OCP} of the tBLM was used as the "zero-potential". Therefore, prior to examining structural changes of hVDAC, SEIRA difference spectra of pure tBLMs were measured at different potentials to support the choice of E_{OCP}. In the next step, the hVDAC-tBLM system was studied spectroelectrochemically to compare the structural changes with the electrophysiological properties.

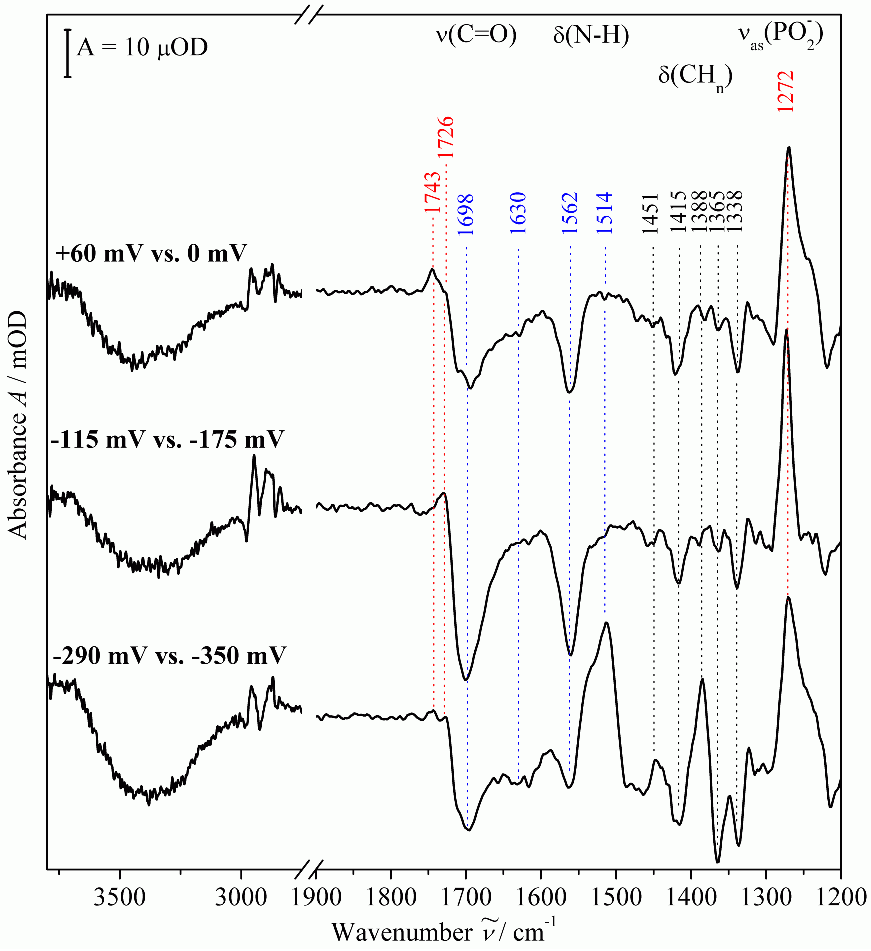

Figure 6.26: Potential-dependent SEIRA difference spectra of pure tBLMs recorded between the potential +60 and 0 mV, -115 and 175 mV, and -290 and -350 mV (against Ag/AgCl). POPC band and CPOE3 bands are highlight with red and blue color, respectively.

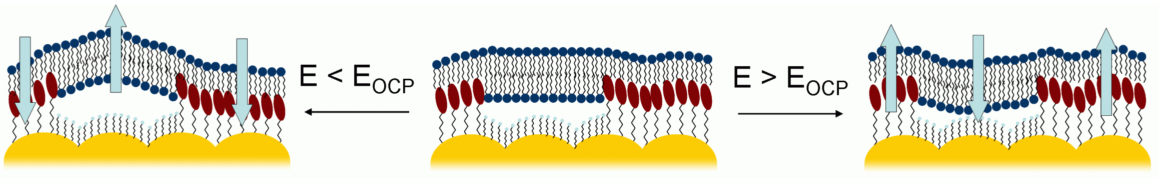

Figure 6.27: Schematic representation of the effect of potentials on CPEO3/6MH-supported tBLMs. Upon application of potentials above E_{OCP}, water molecules exit the aqueous reservoir below the tBLM and cause the POPC-POPC bilayer fragments to approach the Au surface. To compensate the associated tension of the bilayer, the CPOE3-supported bilayer fragments counteract this motion and move away from the surface. At potentials below E_{OCP} the opposite process takes place.

Influence of Electrical Potentials on the SEIRA spectra of tBLMs Figure 6.26 presents the potential-dependent SEIRA difference spectra of pure tBLMs taken at different potentials. The potential difference within one difference spectrum was +60 mV, so that - as shown above - positive and negative bands largely correspond to molecular oscillators moving towards and away from the surface, respectively. All difference spectra are comprised of bands of CPEO3, 6MH, and POPC molecules. Between 1500 and 1300 cm^{-1} the CH_n bendings of all three components interfere and create a complicated band pattern. Above and below this region, however, the C=O stretching (1750 - 1720 cm^{-1} for POPC; 1700 - 1600 cm^{-1} for CPOE3), PO_2^- stretching (1272 cm^{-1}), and N-H bending vibrations (1600 - 1500 cm^{-1}) of POPC and CPEO3 can be discriminated efficiently.

Clearly, the difference spectra “+60 mV vs. 0 mV” and “-115 mV vs. -175 mV” show an similar picture with alternated relative intensities. The region between 1700 and 1300 cm^{-1} is entirely composed of negative difference bands. Since the transition dipole moments of the C=O stretching and the N-H bending in CPEO3 are oriented nearly perpendicularly, these bands can not be ascribed to a reorientation, but to a tilt up of CPEO3 molecules due to the removal of water (as observed as a negative band at 3400 cm^{-1}) and the associated increase in distance of the CPEO3 carbamate group from the electrode. Such a movement compensates the bending of the 6MH-supported POPC-POPC bilayer fragments in the opposite direction to minimize friction within the tBLM (see figure 6.27). Positive features supporting this motion are found at 1743, 1726, and 1272 cm^{-1} which can be ascribed to the C=O and the asymmetric PO_2^- stretching of POPC molecules. Their positive intensity is in line with the deletion of water which decreases the distance of the POPC-POPC bilayer and the electrode. The difference of the position of the C=O stretching at the different potentials can be ascribed to different protonation patterns or to a different orientation of both C=O components associated with the varying electric field.

The “-290 mV vs. -350 mV” difference spectrum differs considerably from the other spectra. The POPC difference bands still show a band pattern indicating the approach of the POPC-POPC bilayer fragment towards the electrode. The weak intensity of the C=O band is caused by a unfavorable orientation of nearly 90° to the surface normal. However, the CPOE3 bands reveal a slightly different rearrangement process. The bands at 1689 and 1562 cm^{-1} have negative intensity, similarly to higher potentials. However, a additional band at 1514 cm^{-1} arises with positive intensity. Since this band originates from strongly hydrogen bound N-H groups, it is attributed to CPOE3 molecules located at the boundary to the 6MH SAM islands. The fact that this band only appears in difference spectra where the spectrum at E_{OCP} was taken as the reference can be rationalized on the basis of a “relaxed” state of the tBLM at E_{OCP} in which the bilayer is pressed neither towards nor away from the Au surface. The application of a potential higher by 60 mV, perturbs the system and leads either to a more favorable orientation of the transition dipole moment of N-H groups with respect to the surface or to a change in the quality of protonation. Only after the system is already perturbed by the electric field, the CPOE3 molecules are stretched to increase the distance to the electrode. All in all, these spectra indicate that the choice of E_{OCP} as a reference seems to be applicable to this system.

Functionality of hVDAC - EIS After the ECT, the open circuit potential of the hVDAC-tBLM system reached a similar value of E_{OCP} = (-350 ± 50) mV as for pure tBLMs (see section 6.1.2 on page 80). Since a comparison of EIS data of the system with and without hVDAC showed a difference in bilayer resistance ((14 ± 2) and (21 ± 2) kΩ cm^2, respectively), here, the difference between the closed and open state of the protein was examined and, thus, all potentials will be given against E_{OCP} which defines the open state of hVDAC.

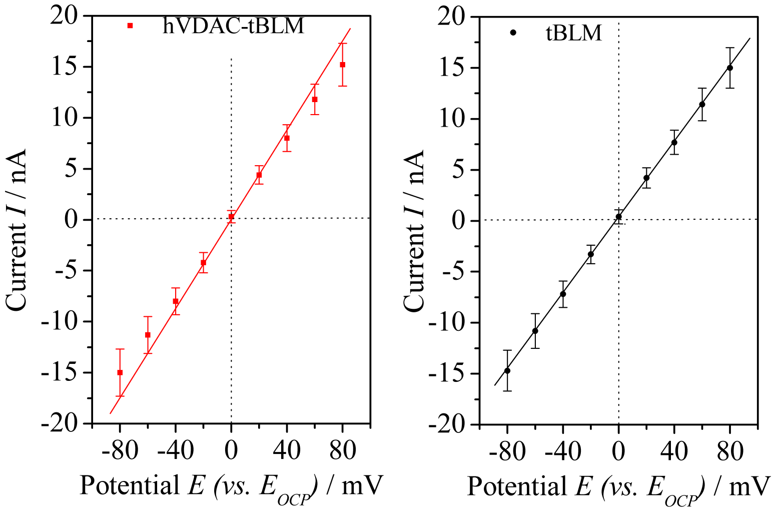

Figure 6.28: Currents recorded at different potentials of hVDAC-tBLMs (left) and of pure tBLMs (right; n=3). The lines represent the conductivity of the hypothetically non-voltage sensing open hVDAC channel determined from the line of best fit between -20 and +20 mV. The dotted lines at 0 mV and 0 nA are shown to lead the eye.

For this purpose, the current across the hVDAC-containing tBLM was recorded at different potentials above and below the E_{OCP} (figure 6.28 left). Since the currents between -20 and +20 mV can be ascribed to ion conductance of the open hVDAC channel, the line of best fit between these points describes the currents of the channel at every potential for the case of no observable voltage-gated closing. Clearly this line deviates from the measured currents at potentials below -20 and above + 20 mV, showing an increased resistance of the tBLM and, thus, demonstrating that the voltage-gated closing of hVDAC can be monitored when incorporated into tBLMs on SEIRA Au films. This is supported by the fact that the same experiment performed with pure tBLMs does not show such a behavior, but a constant resistance in the observed potential window. Furthermore, this result proves the conclusion drawn from the previous section that hVDAC is incorporated into the POPC-POPC bilayer fragments in its native conformation and with a uniform orientation.

Functionality of hVDAC - SEIRA In addition to the electrochemical experiment that shows a voltage-gated closing of hVDAC, potential-dependent SEIRA difference spectroscopy was applied to visualize potential-induced structural changes of hVDAC when switching between the open and the closed state. For this purpose, the SEIRA spectrum at 0 mV was subtracted from those measured at +60 mV and -60 mV, respectively. Since, the pure tBLM system reacts as well to the application of potentials (*vide supra*),[160] the same experiment was conducted for pure tBLMs. Figure 6.29 shows these difference spectra for the hVDAC-tBLM and the pure tBLM. The difference spectra of pure tBLMs (black spectra) for positive and negative potentials against the E_{OCP} show mirror-like features which can be ascribed to changes in water content (ca. 3400 cm^{-1}) and potential-induced rearrangements of the tBLM (*vide supra*).

Upon insertion of hVDAC, these difference spectra show several changes caused by the presence of the channel. First, the water band at ca. 3400 cm^{-1} is decreased considerably. This can be rationalized in the following way. Upon application of voltage, the aqueous reservoir below the bilayer is filled or depleted. When hVDAC is present in the tBLM, the addition or removal of water at negative or positive potentials against E_{OCP}, respectively,

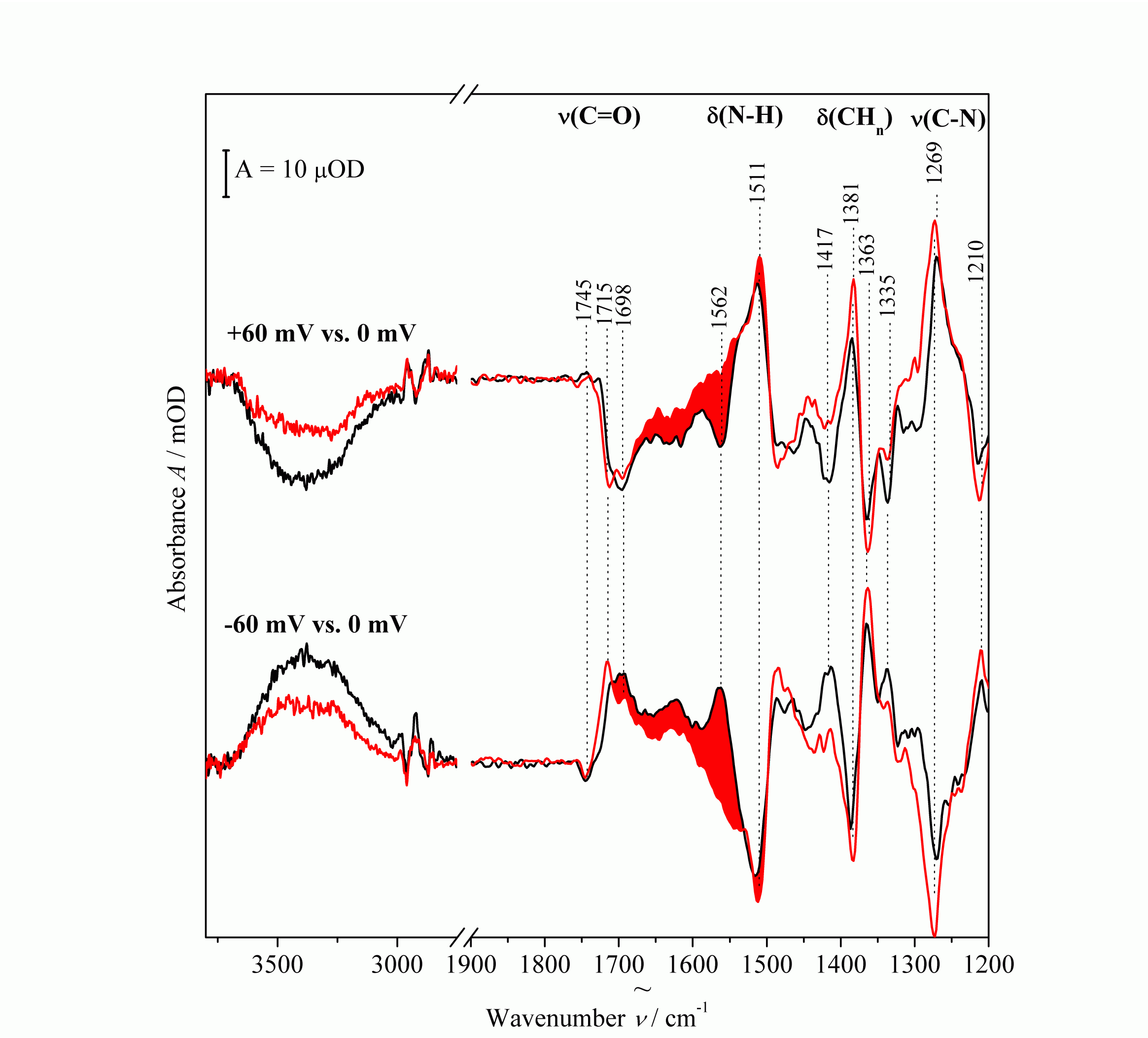

Figure 6.29: Potential-dependent SEIRA difference spectra of hVDAC-tBLMs (red) and pure tBLMs (black). The changes of the amide region of the protein are marked with red color.

can be compensated by the hVDAC pores which allow for water diffusion. This prevents the accumulation or depletion of water, respectively, and, thus, reduces the extent of changes of the water content. The spectral changes of the POPC molecules in hVDAC-tBLMs are equivalent to those in pure tBLMs in terms of position and intensity of the SEIRA difference signals. Below 1720 cm^{-1}, considerable alterations of the SEIRA difference spectrum are noted due to the presence of hVDAC. First, a C=O stretching difference band appears at ca. 1715 cm^{-1}. Furthermore, the spectral region below 1500 cm^{-1} is affected by changes of amino acid residues and SAM-hVDAC interactions. However, most remarkable is the amide region between 1700 and 1500 cm^{-1} which is marked in red. Unfortunately, since CPEO3 contains as well a C=O stretching and a N-H bending, these bands coincide with the less pronounced amide I and amide II changes. SEIRA double-difference spectra obtained by subtracting the difference spectra of the tBLM from those of the hVDAC-tBLM make all these changes clearly visible. Without any further correction of neither the baseline nor the overall intensity of these spectra, the subtraction eliminates almost all contributions of the POPC molecules and, thus, as well those of the CPEO3/6MH SAM. Hence, the SEIRA double-difference spectra in figure 6.30 display solely spectral changes attributable to hVDAC. These changes involve potential-induced structural changes of the protein itself

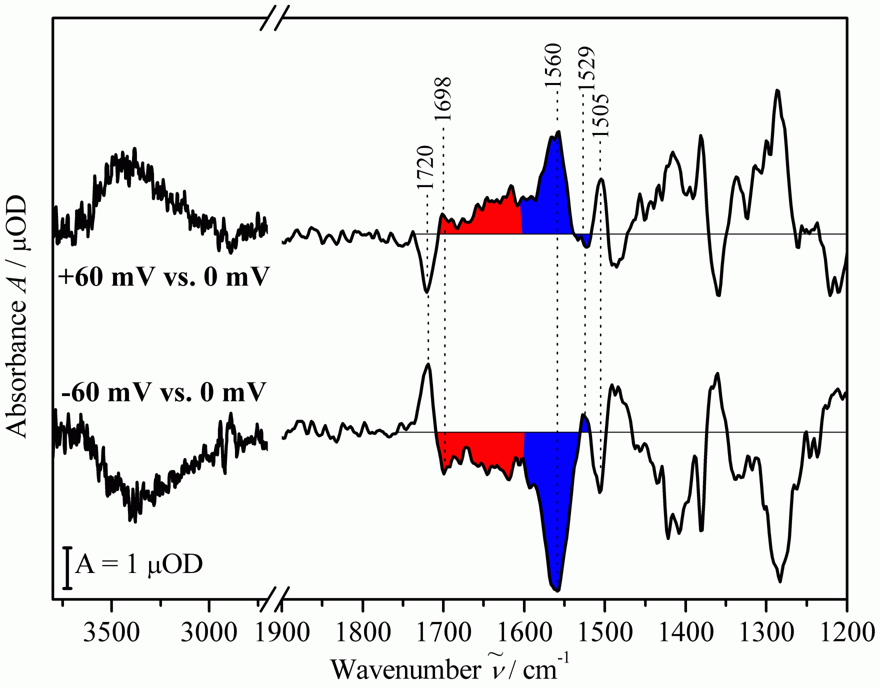

Figure 6.30: Potential-dependent SEIRA double-difference spectra resulting from the subtraction of potential-dependent SEIRA difference spectra of hVDAC-tBLMs and pure tBLMs from figure 6.29. The amide I and amide II regions are indicated with red and blue color, respectively.

as well as changes of its surrounding. To guide the eye, difference bands of the amide I and amide II region are highlighted using red and blue color, respectively. For the sake of simplicity, the "+60 mV vs. 0 mV" double-difference spectrum will be discussed unless noted otherwise.

The amide I region shows a broad positive feature which is composed of amide I changes superimposed by amino acid residues and an altered rearrangement of water molecules. The rather weakly defined band pattern accounting for changes of hVDAC is ascribed to the poor absolute intensity of the amide I band. The amide II region reveals a clearer band pattern including an intense positive difference band at 1560 cm^{-1} and a weak negative band at 1529 cm^{-1}. The band at 1560 cm^{-1} originates from the difference spectra in figure 6.29 due to the absence of the negative band at 1562 cm^{-1} in the spectrum of hVDAC-tBLMs. Since the CPEO3 C=O stretching difference band at 1698 cm^{-1} does not show any considerable alterations upon hVDAC insertion, the disappearance of the 1560 cm^{-1} band is related to a positive band of hVDAC and not to the disappearance of the N-H bending of CPEO3. This difference band located at 1560 cm^{-1} in the spectra in figure 6.30 can be ascribed confidently to changes of turns which link the β-sheets of hVDAC. This is in line with observations of SEIRA difference spectra of cytochrome c which showed redox-linked structural changes of β-turns (type III) reflected by a difference signal at this position.[19] The weak difference band at 1529 cm^{-1} originates from changes of the β-sheets of the barrel. Besides these backbone changes, a negative and a positive difference band at 1720 and 1505 cm^{-1}, respectively, appear in the hVDAC difference spectrum. Difference bands located below 1500 cm^{-1} originate from all components of the tBLM system and, thus,

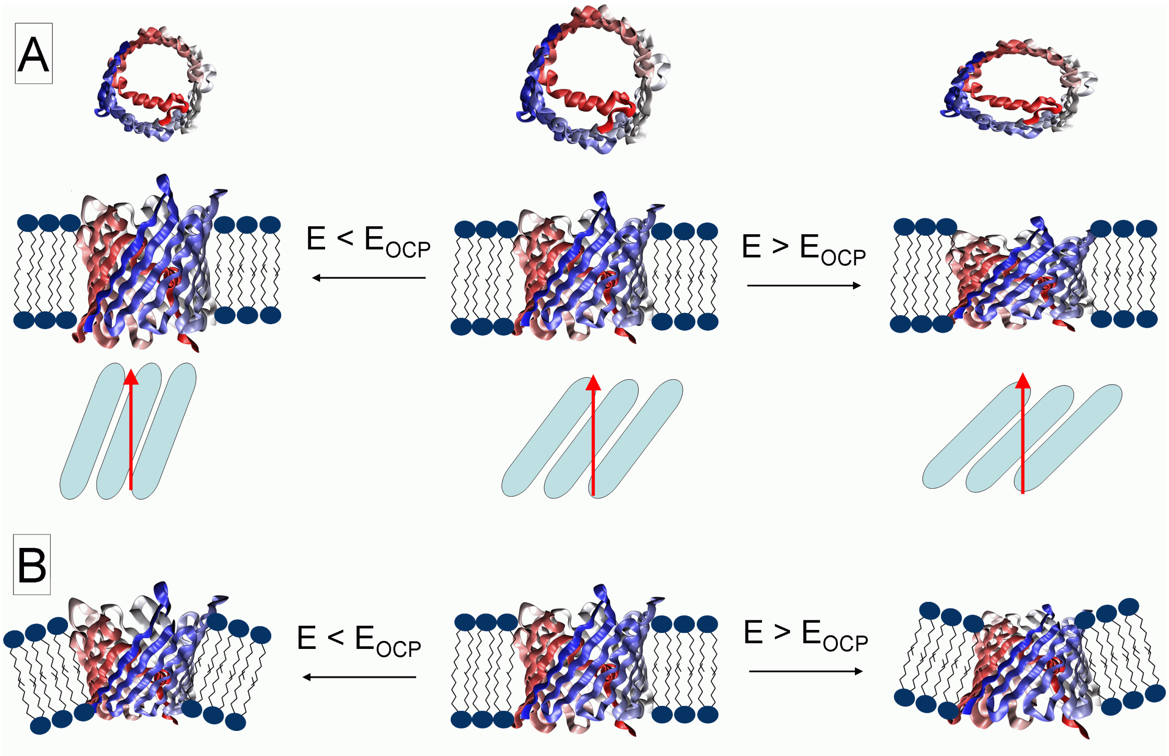

Figure 6.31: Two possible models for voltage-gating of hVDAC. A: Upon application of potential the channel elongates or compresses. In both cases this leads to a narrowing of the pore. This inclinates the β-sheet in such a way that the transition dipole moment of the β-sheet amide II at 1529 cm^{-1} matches the polarized electromagnetic field (red arrow) present in SEIRA worse or better, respectively. This is perceived as a negative or positive difference band, respectively, in the spectrum. B: The bending of the bilayer upon application of potentials narrows the pore on the concave side of the membrane. In this scenario, the bottom part of hVDAC (facing the Au surface) adapts an alike β-sheet arrangement as in A.

show a pattern that is too complex to be interpreted in terms of specific structural changes of hVDAC.

First, the broad amide I region and the amide II difference band at 1560 cm^{-1} can be assigned to the motion of the hVDAC-containing POPC-POPC bilayers as discussed above. This is supported by the fact that at positive potentials, both, the POPC vibrations and the hVDAC amide bands show positive difference bands (and *vice versa* at negative potentials). This observation shows as well that the majority of hVDAC is located within the POPC-POPC fragments and not on top of the CPOE3 SAM, since the hVDAC “moves together” with the POPC-POPC bilayer and not with the CPOE3 SAM fragments covering the majority of the surface.

The weak amide II difference band at 1530 cm^{-1}, having opposite intensity with respect to the entire amide region, and the bands at 1720 and 1505 cm^{-1} originate from structural changes of the protein. The band at 1720 can be ascribed to a C=O stretching of Asp or Glu residues of hVDAC. The 1505 cm^{-1} difference band is more difficult to assign, however, originates either from the amino acid Tyr or from Trp.[108] Since both bands show relatively high intensity, these amino acids belong most likely to those located in the turn region of hVDAC and, thus, in close proximity to the Au surface. The fact that all of these hVDAC bands show a mirrored picture for positive and negative intensities, clearly points at the fact that positive and negative potential differences cause different structural changes. This observation is in line with the slightly asymmetric open probability of hVDAC observed in conductance experiments[7,140] and points at two possible mechanisms of the voltage-gating, both involving a structural change of the entire barrel as proposed recently:[149]

- The first involves a compression and elongation of the barrel at positive and negative potentials, respectively, both leading to a decreased diameter of the pore albeit upon principally different changes. In both cases, the distortion of the protein changes the inclination angle of the β-sheets with respect to the surface normal (see figure 6.31 A). In difference spectra at positive potentials the angle between the transition dipole moment of the amide II of the β-sheet and the surface normal increases and causes a negative difference band; for negative potentials this angle decreases and gives rise to a positive difference band. Associated with this rearrangement, the pore narrows. The narrowing upon elongation can be understood easily. During the compression, however, the α-helix acts as a stabilizing sequence forcing the channel into an oval structure. This mechanism explains the slight asymmetric behavior and the fact that the closed state still shows conductivity. Furthermore, the β-sheets 1 and 19 forming a parallel pair may play a crucial role for the oval-shaped closed state. The tension caused by the compression releases its weak interaction, the α-helix, however, stabilizes the overall barrel structure forcing the pore into the oval-like shape.
- The second possible mechanism accounts for the small closing probability of ca. 5 %, which is not in line with the usually high efficiency of channel proteins, and for the fact that this voltage-gated behavior was yet only observed in artificial membrane systems. As shown in the previous paragraph, upon applying a potential, the POPC-POPC bilayer fragments move towards or away from the surface in a “breathing-like” motion. This is accompanied by a local bending of the bilayer. Such a bending could distort the hVDAC structure as shown in figure 6.31 B turning into a cone-like structure. This would cause a similar local β-sheet orientation of the Au surface facing hVDAC part as for the first mechanism. Since such strong distortions of the bilayer curvature occur only transiently, only these hVDACs located in this very region will experience a closing event. Here, again the combination of the parallel β1-β19 fragment and the stabilizing α-helix allow for such a channel distortion. However, this mechanism implies that the voltage-gating may only be an artifact caused by the high flexibility of artificial membranes.

6.3.3. Summary and Discussion

Suitability of CPOE3/6MH-supported tBLM for Spectroelectrochemistry tBLMs constructed on a CPEO3/6MH SAM show a rich SEIRA spectrum in the region between 1750 and 1000 cm^{-1}. In particular the C=O and N-H vibration of the carbamate group of CPOE3 interfere with the amide I and amide II region and aggravate the direct evaluation of the spectra. Thus, pure tBLMs have to be constructed on the same SAM as a control experiment for absolute and difference spectra of the incorporated protein. Although this approach affords promising successful results, alternative CPEO3 derivatives would facilitate the SEIRA spectroscopy on tBLMs.

However, the presence of these IR active groups are also beneficial for studying the influence of electrical potentials on the tBLMs, which are of utmost importance for the application of SEIRA to hVDAC-tBLMs. SEIRA difference spectra show a “breathing motion” of the tBLM when potentials are applied. At positive potentials (vs. E_{OCP}) the POPC-POPC bilayer fragments are pulled towards the Au surface. The CPOE3-POPC fragments compensate this movement by tilting up. In the same way, at negative potentials, the POPC-POPC bilayers are pushed away from the surface and, thus, CPEO3 molecules approach the Au surface.

Formation of hVDAC-tBLMs from proteoliposomes Spreading of hVDAC-containing vesicles led to a successfully assembled hVDAC-tBLM. The direct comparison of pure tBLMs and hVDAC-tBLMs before the ECT showed similar tBLM capacitances and bilayer resistances of ca. 0.63 (± 0.03) μF cm^{-2} and 5 (± 1) kΩ cm^2. This indicates that although the bilayer is formed, the majority of the hVDAC channels are bound non-specifically, either still in intact vesicles, or on the CPOE3 SAM fragments which occupy the majority of the Au film. After the ECT the capacitances remain, but the resistances increase to 14 (± 2) kΩ cm^2 and 21 (± 2) kΩ cm^2 for pure and hVDAC-containing tBLMs, respectively, proving a more sealed and well-ordered tBLM in which hVDAC is located inside the POPC-POPC bilayer fragments.

SEIRA spectra of the spreading of hVDAC/POPC-vesicles reveal a amide I and amide II band indicative of hVDAC immobilization. The spectrum is in line with previously reported ATR-IR spectra when the surface-selection rule and the sharply decaying electromagnetic field of SEIRA is taken into account. The ETC shows only slight rearrangements of the protein which are in line with the described rearrangement processes. The relatively weak amide signals are in line with rather low hVDAC concentrations, allowing, in principle, for the embedment of all proteins in POPC-POPC bilayer fragments. These data indicate that hVDAC is immobilized onto tBLMs in its native conformation.

Functionality of hVDAC The measurement of the currents across the hVDAC-tBLM shows a slight closing of hVDAC at potentials of E > |+/- 20mV|. This in line with literature data and proves the successful immobilization of hVDAC in its native conformation into POPC-POPC bilayer fragments of the tBLM. SEIRA difference spectra between the open and closed state for positive and negative potentials are dominated by the movement of the POPC-POPC bilayer, but show as well slight structural changes of the channel. These changes can be interpreted on the basis of two possible mechanisms. The first displays a compression and elongation of hVDAC that leads to a narrowing of the pore for positive and negative potentials. This mechanism may induce an oval-shaped structure of hVDAC in its "closed state" in which both, the weak β1-β19 interaction and the stabilization by the α-helix, play a crucial role. On the basis of the "breathing motion" of the bilayer, it is also possible that bilayer curvature induces a distortion of hVDAC. In this way a cone-shape structure is adopted which narrows the pore as well. This mechanism is in line with the small closing probability of 5 % which, thus, is induced not by the channel itself, but by the membrane curvature. To evaluate this further, polymerizable lipids could be used to build a less flexible network and prevent the possible coning of hVDAC. Furthermore, tether molecules absent of C=O and N-H bonds are required to resolve the amide region of the protein without the indirect route of subtracting spectra of pure tBLMs.

7. Conclusions

Construction of tBLMs In this work, the successful construction of a tBLM on a CPOE3/6MH-functionalized nanostructured SEIRA-active Au film was demonstrated. As the system of choice, a SAM composed of 80 % CPEO3 and 20 % 6MH was used, leading to stable tBLM with sufficient space to incorporate membrane proteins into POPC-POPC bilayer fragments and extended aqueous reservoirs. Due to the nanostructured surface required for SEIRA spectroscopy, the bilayer contains defects reflected by two dispersions of in the EIS data and rather moderate resistances of R_{Bilayer} = (6.5 ± 1.5) kΩ cm^2. The capacitance of the tBLM C_{tBLM} = 0.6 - 0.7 μF cm^{-2}, however, is in line with literature data and, thus, proves the successful bilayer formation. This conclusion is supported by the fact that the system displays a long-term mechanical stability.

Monitoring the time-dependence of tBLM formation reveals a biexponential behavior of both the capacitance and the IR absorptions of POPC in the SEIRA spectra. The fast phase, with a time-constant of ca. 2 min determined by both techniques, describes the absorption of vesicles onto the 6MH-coated parts of the Au film. The slow phase has a time constant of ca. 30 min for the capacitance and ca. 60 - 70 min for the IR absorptions of POPC molecules. This process describes the spreading of vesicles and the covering of the CPEO3-supported bilayer fragments. The reason for the difference between the kinetics determined from the two techniques can be ascribed to rearrangements on the molecular level causing a tighter tBLM packing which can not be monitored with EIS.

The quality of the tBLM can be improved by an electrochemical treatment. This procedure causes the repair of defects and the rupture of intact vesicles increasing the resistance to a value of (21 ± 2) kΩ cm^2, while the capacitance remains rather constant. The shape of the Cole-Cole plot changes considerably approaching the EIS data obtained for tBLMs on flat Au surfaces.

gA incorporated into tBLMs The spontaneous incorporation of gA leads to different species, i.e. the helical dimer and double helices in presence of Cs^+ and Ba^{2+}, respectively. This difference can be ascribed to the species persisting in the TFA solution prior to the incorporation. In the presence of Cs^+, a $\uparrow\downarrow \pi\pi^{7.2}$ gA-Cs^+ complex is formed. The open pore probably interacts with the choline headgroup splitting into monomers which then form helical dimers in the following way:

$$\uparrow\downarrow \pi\pi^{7.2}\ (\text{TFA}) \longrightarrow \beta^{6.3}\ (\text{upper leaflet}) \longrightarrow \beta^{6.3}\ (\text{bottom leaflet}) \longrightarrow \beta^{6.3}\beta^{6.3}$$

In contrast, Ba^{2+} causes the formation of the $\uparrow\uparrow \pi\pi^{5.7}$ double helix with a closed pore, which can penetrate into the headgroup region without dissociation into monomers. The incorporation into membranes observed in this work is suggested to follow according to:

$$\text{lh-}\uparrow\uparrow \pi\pi^{5.7}\ (\text{TFA}) \longrightarrow \text{lh-}\uparrow\uparrow \pi\pi^{5.7} \longrightarrow \text{rh-}\uparrow\downarrow \pi\pi^{7.2} \longrightarrow \text{lh-}\uparrow\downarrow \pi\pi^{5.6}$$

The incorporated channels (helical dimers) were used to examine the tBLM system with respect to its suitability for providing a native-like environment for membrane proteins and to study such systems by spectroelectrochemical approach. Using the blocking Ba^{2+} and the conductible monovalent cations Li^+, Na^+, K^+, Cs^+, and Tl^+, it was possible to distinguish between the non-conductive and conductive state on the basis of the magnitude of the impedance. Furthermore, a slight tendency according to the series (Li^+ <) Na^+ < K^+ < Cs^+ < Tl^+ was reproduced, demonstrating the biomimetic environment of tBLM. Li^+ is able to diffuse through defects, however, it is not clear if such a behavior is observable as well on tBLMs built on flat Au surfaces. "M^+ vs. Ba^{2+}" SEIRA difference spectra reveal structural changes of the peptide observed by a difference signal of the amide I band. The intensity of the positive band, corresponding to the monovalent cation, follows the series $Li^+ < Na^+ < K^+ < Cs^+ < Tl^+$. This demonstrates the suitability of this technique for functional studies of membrane proteins. Furthermore, the frequency of the positive amide I band increases with increasing ion size. Tl^+ probably forms doubly-occupied and tighter bound complexes reflected by a difference band that suggests a strongly tightened gA pore.

Interactions of cations with the lipid headgroups show a similar behavior as expected on the basis of experimental and theoretical studies of lipid-cation interactions. K^+ and Cs^+ are not capable of competing with Ba^{2+} for binding to the charged headgroup region and, thus, do not affect the POPC C=O stretching vibrations. Li^+ and Na^+, however, replace Ba^{2+} and show a rearrangement or reorientation of the C=O group as indicated by the corresponding stretching mode in the SEIRA spectrum. The Tl^+ ion reveals a similar band pattern as for Na^+ suggesting an analogous cation-lipid interaction.

Potential-induced effects on tBLMs In the spectrum of the tBLM, the C=O and PO_2^- stretchings as well as the N-H bending of CPOE3 and POPC can be used to monitor structural changes induced by variation of the electrode potential. The application of positive potential differences removes water from the aqueous reservoir and, thus, pulls the POPC-POPC bilayer towards the 6MH SAM. The neighboring CPOE3-POPC fragments counteract the bending friction by tilting up. Negative potential differences lead to the opposite behavior. At the open circuit potential E_{OCP}, the tBLM system adopts a "relaxed" structure.

hVDAC incorporated into tBLMs Spreading of hVDAC-containing vesicles leads to a successfully formed hVDAC-tBLM with tBLM capacitances of 0.6 - 0.7 μF cm^{-2}, similar to pure tBLMs. The resistance, however, is smaller with a value of 14 (± 2) kΩ cm^2 caused by the presence of hVDAC which allows for free diffusion of ions across the tBLM. The amide band region of the SEIRA spectra indicates the native hVDAC conformation within the POPC-POPC fragments of the tBLMs, taking into account the distance-dependence of the surface-enhancement and the surface-selection rules. This conclusion is supported by lower conductivity across the tBLM when potentials higher than +20 mV and lower than -20 mV were applied (vs. E_{OCP}).

Potential-dependent SEIRA difference spectra reflect mainly the movement of hVDAC together with the POPC-POPC fragments towards and away from the Au surface. Weak changes of the amide II attributable to the β-sheet elements, however, point at a pore-closing mechanism which involves a distortion of the barrel structure. On one hand, the electric field leads to an elongation and compression of the barrel accompanied by a tightening of the pore. In the case of the compression an oval-shape may be adopted due to the weak β1-β19 interaction and the stabilizing α-helix. On the other hand, the barrel is distorted into a cone-shaped structure resulting in a tighter pore. This mechanism may be caused by the bending of the bilayer, as the spectral changes of the tBLM and hVDAC reflect a common bending. Both hypotheses can well account for the slight asymmetry in voltage-gating for negative and positive potentials. The low closing probability of ca. 5 % would be in line with the bending process which, thus, is experienced only by a minority of hVDAC molecules.

Outlook This work has demonstrated the successful construction of tBLMs on CPEO3/6MH-coated SEIRA-active Au electrodes and the potential to apply this system to studies of the structure, function, and dynamics of membranes and membrane proteins by spectroelectrochemical approaches. However, further optimization will be the focus of the next steps on this field. Central points are the design of other lipid tethers and the improvement of the tBLM. Although the CPOE3-carbamate group is advantageous for analyzing the potential-dependent SEIRA difference spectra of hVDAC-tBLMs, more detailed information on the protein structure may be obtained in the absence of the C=O and N-H vibrations of the CPOE3 molecule. Optimizing the bilayer constructs requires the improvement of the sealing properties of the tBLM and the increase of protein concentration within the bilayer. However, even at the current state of the art, the tBLM-approach can be extended to other membrane proteins, or molecules targeting the membrane system. In this way, one can contribute greatly to the understanding of the membrane-confined fundamental processes and to the design of novel biomimetic constructs.

Bibliography

[1] J. Drews, *Science* **2000**, *287*, 1960–1964.

[2] I. Willner, E. Katz (Eds.:), *Bioelectronics*, Wiley-VCH, Weinheim, **2005**.

[3] L. J. C. Jeuken, *Nat. Prod. Rep.* **2009**, *26*, 1234–1240.

[4] A. Janshoff, C. Steinem, *Anal. Bioanal. Chem.* **2006**, *385*, 433–451.

[5] F. Siebert, P. Hildebrandt, *Vibrational Spectroscopy in Life Science*, 1^{st} ed. , Wiley-VCH, Weinheim, **2008**.

[6] J. A. Killian, *Biochim. Biophys. Acta* **1992**, *1113*, 391–425.

[7] V. Shoshan-Barmatz, V. De Pinto, M. Zweckstetter, Z. Raviv, N. Keinan, N. Arbel, *Mol. Aspects Med.* **2010**, *31*, 277–285.

[8] G. Herzberg, *Molecular Spectra and Molecular Structure: II, Infrared and Raman Spectra of Polyatomic Molecules*, Van Nostrand Reinhold, New York, **1945**.

[9] J. Herbst, K. Heyne, R. Diller, *Science* **2002**, *297*, 822–825.

[10] P. Kukura, D. W. McCamant, S. Yoon, D. B. Wandscheider, R. A. Mathies, *Science* **2005**, *310*, 1006–1009.

[11] K. Ataka, J. Heberle, *J. Am. Chem. Soc.* **2003**, *125*, 4986–4987.

[12] D. H. Murgida, P. Hildebrandt, *Acc. Chem. Res.* **2004**, *37*, 854–861.

[13] E. B. Wilson, J. C. Decius, P. C. Cross, *Molecular Vibrations: The Theory of Infrared and Raman Vibrational Spectra*, McGraw-Hill, New York, **1955**.

[14] E. Goormaghtigh, V. Raussens, J.-M. Ruysschaert, *Biochim. Biophys. Acta* **1999**, *1422*, 105–185.

[15] Z. Kóta, T. Páli, D. Marsh, *Biophys. J.* **2004**, *86*, 1521–1531.

[16] A. Hartstein, J. R. Kirtley, J. C. Tsang, *Phys. Rev. Lett.* **1980**, *45*, 201–204.

[17] M. Osawa, *Bull. Chem. Soc. Jpn.* **1997**, *7*, 2861–2880.

[18] N. Wisitruangsakul, I. Zebger, K. H. Ly, D. H. Murgida, S. Ekgasit, P. Hildebrandt, *Phys. Chem. Chem. Phys.* **2008**, *10*, 5276–5286.

[19] K. Ataka, F. Griess, W. Knoll, R. Naumann, S. Haber-Pohlmeier, B. Richter, J. Heberle, *J. Am. Chem. Soc.* **2004**, *126*, 16199–16206.

[20] X. Jiang, E. Zaitseva, M. Schmidt, F. Siebert, M. Engelhard, R. Schlesinger, K. Ataka, R. Vogel, J. Heberle, *Proc. Nat. Ac. Sci.* **2008**, *105*, 12113–12117.

[21] N. Wisitruangsakul, O. Lenz, M. Ludwig, B. Friedrich, F. Lendzian, P. Hildebrandt, I. Zebger, *Angew. Chem.* **2009**, *48*, 611–613.

[22] D. Millo, P. Hildebrandt, M.-E. Pandelia, W. Lubitz, I. Zebger, *Angew. Chem.* **2011**, *50*, 2632–2634.

[23] F. Griess, M. G. Friedrich, J. Heberle, R. L. Naumann, W. Knoll, *Biophys. J.* **2004**, *87*, 3213–3220.

[24] M. Osawa, *Topics Appl. Phys.* **2001**, *81*, 163–187.

[25] R. F. Aroca, D. J. Ross, *Appl. Spectr.* **2004**, *58*, 324A–338A.

[26] M. Osawa, K. Ataka, K. Yoshii, Y. Nishikawa, *Appl. Spectrosc.* **1993**, *47*, 1497–1502.

[27] Y. Suzuki, M. Osawa, A. Hatta, W. Suëtaka, *Surf. Sci.* **1988**, *33/34*, 875–881.

[28] M. Osawa, „Surface-enhanced Infrared Spectroscopy“ in *Handbook of Vibrational Spectroscopy* (Eds.: J. Charmers, P. R. Griths), Wiley, New York, **2002**, pp. 785–799.

[29] J. R. MacDonald, E. Barsoukov, *Impedance Spectroscopy Theory, Experiment, and Application*, 2$^{\text{nd}}$ ed. , John Wiley & Sons, Inc., Hoboken, **2005**.

[30] Y. Nabae, I. Yamanaka, *Applied Catalysis A: General* **2009**, *369*, 119–124.

[31] S. Brosda, T. Badas, C. G. Vayenas, *Topics in Catalysis* **2011**, *54*, 708–717.

[32] F. Lisdat, D. Schäfer, *Anal. Bioanal. Chem.* **2008**, *391*, 1555–1567.

[33] C.-P. Chen, A. Ganguly, C.-H. Wang, C.-W. Hsu, S. Chattopadhyay, Y.-K. Hsu, Y.-C. Chang, K.-H. Chen, L.-C. Chen, *Anal. Chem.* **2009**, *81*, 36–42.

[34] F. Asphahani, K. Wang, M. Thein, O. Veiseh, S. Yung, J. Xu, M. Zhang, *Phys. Biol.* **2011**, *8*, 015006.

[35] C. Steinem, A. Janshoff, H.-J. Galla, M. Sieber, *Bioelectrochem. Bioenerg.* **1997**, *42*, 213–220.

[36] J. Kendall, B. R. G. Johnson, P. H. Symonds, G. Imperato, R. J. Bushby, J. D. Gwyer, C. van Berkel, S. D. Evans, L. J. C. Jeuken, *ChemPhysChem* **2010**, *11*, 2191–2198.

[37] C. P. Smith, H. S. D. Byler, *Anal. Chem.* **1992**, *64*, 2398–2405.

[38] L. Becucci, I. Guryanov, F. Maran, F. Scaletti, R. Guidelli, *Soft Matter* **2012**.

[39] V. F. Lvovich, *Impedance Spectroscopy: Applications to Electrochemical and Dielectric Phenomena*, Jon Wiley & Sons Inc., Hoboken, **2012**.

[40] E. K. Schmitt, Dissertation, Georg-August-Universität Göttingen, **2009**.

[41] G. Valincius, T. Meškaukas, F. Ivanauskas, *Langmuir* **2012**, *28*, 977–990.

[42] P. M. Gomadam, J. W. Weidner, *Int. J. Energy Res.* **2005**, *29*, 1132–1151.

[43] B. A. Boukamp, *Solid State Ionics* **1986**, *20*, 31–44.

[44] S. Ohki, *J. Theo. Biol.* **1970**, *26*, 277–287.

[45] H. Coster, J. Smith, *Biochim. Biophys. Acta - Biomembranes* **1974**, *373*, 151–164.

[46] V. Jovic, B. Jovic, *J. Electroanal. Chem.* **2003**, *541*, 1–11.

[47] A. S. Achamlkumar, R. J. Bushby, S. D. Evans, *Soft Matter* **2010**, *6*, 6036–6051.

[48] C. Steinem, A. Janshoff, *Chem. Unserer Zeit* **2008**, *42*, 116–127.

[49] S. J. Singer, N. G. L, *Science* **1972**, *175*, 720–731.

[50] S. Takamori, M. Holt, K. Stenius, E. A. Lemke, M. Grø nborg, D. Riedel, H. Urlaub, S. Schenk, B. Brügger, P. Ringler, S. A. MuÏler, B. Rammner, G. Gräter, H. Grubmüller, J. Heuser, F. Wieland, R. Jahn, *Cell* **2006**, *127*, 831–846.

[51] D. F. Stamatialis, B. J. Papenburg, M. Giroñes, S. Saiful, S. N. M. Battahalli, S. Schmitmeier, M. Wessling, *J. Membr. Sci.* **2008**, *308*, 1–34.

[52] G. Cevc, *Phospholipids Handbook*, Dekker, New York, **1993**.

[53] M. N. Jones, D. Chapman, *Micelles, Monolayers, and Biomembranes*, Wiley-Liss, New York, **1995**.

[54] R. M. Epand (Ed.:), *Lipid Polymorphism and Membrane Properties*, Academic, SanDiego, **1997**.

[55] J. H. Collier, P. B. Messersmith, *Annu. Rev. Mater. Res.* **2001**, *31*, 237–263.

[56] J. R. Silvius, *Lipid-Protein Interactions*, John Wiley & Sons Inc., New York, **1982**.

[57] A. P. Lipids, „Physical Properties of Phospholipids“, http://avantilipids.com/index.php?option=com_content&view=article&id=1699&Itemid=418, **2012**.

[58] K. Olbrich, W. Rawicz, D. Needham, E. Evans, *Biophys. J.* **2000**, *79*, 321–327.

[59] H. Hauser, D. Oldani, M. C. Philips, *Biochemistry* **1973**, *12*, 4507–4517.

[60] R. P. Richter, Dissertation, Université Bordeaux I - Institut Européen de Chimie et Biologie, **2004**.

[61] R. B. Gennis, *Biomembranes: Molecular Structure and Function*, Springer Verlag, New York, **1989**.

[62] R. J. Clarke, *Adv. Colloid Interface Sci.* **2001**, *89-90*, 263–281.

[63] B. Hille, *Ionic Channels of Excitable Membranes*, 2nd ed. , Sinauer Associates Inc., Sunderland, MA, **1992**.

[64] B. Klasczyk, V. Knecht, R. Lipowsky, R. Dimova, *Langmuir* **2010**, *26*, 18951–18958.

[65] L. Wang, *Annu. Rev. Biochem.* **2012**, *81*, 615–635.

[66] M. Menke, V. Gerke, C. Steinem, *Biochemistry* **2005**, *44*, 15296–15303.

[67] S. Faiss, S. Schuy, D. Weiskopf, C. Steinem, A. Janshoff, *J. Phys. Chem. B* **1993**, *111*, 13979–13986.

[68] A. Herrig, M. Janke, J. Austermann, V. Gerke, A. Janshoff, C. Steinem, *Biochemistry* **2006**, *45*, 13025–13034.

[69] C. Steinem, A. Janshoff, W. P. Ulrich, M. Sieber, H. J. Galla, *Biochim. Biophys. Acta* **1996**, *1279*, 169–180.

[70] C. W. Meuse, G. Niaura, M. L. Lewis, A. L. Plant, *Langmuir* **1998**, *14*, 1604–1611.

[71] D. Millo, A. Bonifacio, M. R. Moncelli, V. Sergo, C. Gooijer, G. Van Der Zwan, *Colloids and Surfaces B: Biointerfaces* **2010**, *81*, 212–216.

[72] J. Güldenhaupt, Y. Adigüzel, J. Kuhlmann, H. Waldmann, C. Kotting, K. Gerwert, *FEBS* **2008**, *275*, 5910–5918.

[73] M. R. Hernandez, E. N. Towns, T. C. Ng, B. C. Walsh, R. Osibanjo, A. N. Parikh, D. P. Land, *Applied Optics* **2012**, *51*, 2842–2846.

[74] J. Kozuch, C. Steinem, P. Hildebrandt, D. Millo, *Angew. Chem. Int. Ed.* **2012**, *51*, 8114–8117.

[75] K. Blodgett, *J. Am. Chem. Soc.* **1935**, *57*, 1007–1022.

[76] I. Langmuir, V. Schäfer, *J. Am. Chem. Soc.* **1935**, *60*, 1351–1360.

[77] P. S. Cremer, S. G. Boxer, *J. Phys. Chem. B* **1999**, *103*, 2555–2559.

[78] G. A.-L. N. Wiegand, H. Hillebrandt, E. Sackmann, P. Wagner, *J. Phys. Chem. B* **2002**, *106*, 4245–4254.

[79] A. Ulman, *Chem. Rev.* **1996**, *96*, 1533–1554.

[80] A. L. Plant, *Langmuir* **1999**, *15*, 5128–5135.

[81] E. L. Florin, H. E. Gaub, *Biophys. J* **1993**, *64*, 375–383.

[82] J. Aittoniemi, P. S. Niemelä, M. T. Hyvönen, M. Karttunen, I. Vattulainen, *Biophysical Journal* **2007**, *92*, 1125–1137.

[83] B. A. Cornell, V. L. B. Braach-Maksvytis, L. G. King, P. D. J. Osman, B. Raguse, L. Wieczorek, P. R. J, *Nature* **1997**, *387*, 580–583.

[84] J. Hrabakova, K. Ataka, J. Heberle, P. Hildebrandt, D. H. Murgida, *Phys. Chem. Chem. Phys.* **2006**, *8*, 759–766.

[85] H. Lang, C. Duschl, H. Vogel, *Langmuir* **1994**, *10*, 197–210.

[86] T. Dewa, S. L. Regan, *J. Am. Chem. Soc.* **1996**, *118*, 7069–7074.

[87] R. Naumann, S. M. Schiller, F. Giess, B. Grohe, K. B. Hartman, I. Kärcher, I. Köper, J. Lübben, K. Vasilev, W. Knoll, *Langmuir* **2003**, *19*, 5435–5443.

[88] E. K. Schmitt, M. Vrouenraets, C. Steinem, *Biophysical Journal* **2006**, *91*, 2163–2171.

[89] L. J. C. Jeuken, N. N. Daskalakis, X. Han, K. Sheikh, A. Erbe, R. J. Bushby, S. D. Evans, *Sensors and Actuators B: Chemical* **2007**, *124*, 501–509.

[90] S. A. Weiss, R. J. Bushby, S. D. Evans, P. J. F. Henderson, L. J. C. Jeuken, *Biophysical Journal* **2009**, *47*, 555–560.

[91] L. J. C. Jeuken, *Biophysical Journal* **2008**, *94*, 4711–4717.

[92] A. Erbe, R. J. Bushby, S. D. Evans, L. J. C. Jeuken, *J. Phys. Chem. B* **2007**, *111*, 3515–3524.

[93] T. Le Bihan, M. Pézolet, *Chem. Phys. Lipids* **1998**, *94*, 13–33.

[94] A. Blume, *Curr. Opin. Colloid Interface Sci.* **1996**, *1*, 64–77.

[95] L. Tamm, S. A. Tatulian, *Quart. Rev. Biophys.* **1997**, *30*, 365–429.

[96] S. Krishnamurty, M. Stefanov, T. Mineva, S. Bégu, J. M. Devoissell, A. Goursot, R. Zhu, D. R. Salahub, *J. Phys. Chem. B* **2008**, *112*, 13433–13442.

[97] D. C. Lee, D. Chapman, *Biosci. Rep.* **1986**, *6*, 235–256.

[98] H. H. Mantsch, R. N. McElhaney, *Chem. Phys. Lipids* **1991**, *57*, 213–226.

[99] M. A. Davies, J. W. Brauner, H. F. Schuster, R. Mendelsohn, *Biochemistry* **1990**, *168*, 213–226.

[100] J. W. Davies, M. A. Schuster, H. F. Brauner, R. Mendelsohn, *Biochemistry* **1990**, *29*, 4368–4373.

[101] H. L. Casal, R. N. McElhaney, *Biochemistry* **1990**, *29*, 5423–5427.

[102] R. N. A. H. Lewis, R. N. McElhaney, W. Pohle, H. H. Mantsch, *Biophysical Journal* **1994**, *67*, 2376–2375.

[103] A. Blume, W. Hübner, G. Messner, *Biochemistry* **1988**, *27*, 8239–8249.

[104] K. Melén, A. Krogh, G. von Heijne, *J. Mol. Biol.* **2003**, *327*, 735–744.

[105] R. Khurana, A. L. Fink, *Biophys. J.* **2000**, *78*, 944–1000.

[106] B. A. Wallace, *J. Struc. Biol.* **1998**, *121*, 123–141.

[107] S.-Y. Park, T. Yokoyama, N. Shibayama, J. R. H. Tame, *J. Struc. Biol.* **2006**, *360*, 690–701.

[108] A. Barth, C. Zscherp, *Quart. Rev. Biophys.* **2002**, *35*, 369–430.

[109] A. Barth, *Biochim. Biophys. Acta* **2007**, *1767*, 1073.

[110] H.-J. Steinhoff, R. Mollaoghababa, C. Altenbach, K. Hideg, M. Krebs, H. G. Khorana, W. L. Hubbell, *Science* **1994**, *266*, 105–107.

[111] V. M. Naik, S. Krimm, *Biophys. J.* **1986**, *49*, 1131–1145.

[112] V. M. Naik, S. Krimm, *Biophys. J.* **1986**, *49*, 1147–1154.

[113] A. M. Dwivdi, S. Krimm, *J. Phys. Chem.* **1984**, *88*, 620–627.

[114] H. Susi, D. M. Byler, *Arch. Biochem. Biophys.* **1987**, *258*, 465–469.

[115] E. Goormaghtigh, V. Cabiaux, J.-M. Ruysschaert, *Subcell. Biochem.* **1994**, *23*, 405–450.

[116] D. Marsh, *Biophys. J.* **1997**, *72*, 2710–2718.

[117] D. Marsh, *Biophys. J.* **1998**, *75*, 354–358.

[118] D. Marsh, M. Müller, F. J. Schmitt, *Biophys. J.* **2000**, *78*, 2499–2510.

[119] T. Páli, D. Marsh, *Biophys. J.* **2001**, *80*, 2789–2797.

[120] R. D. Hotchkiss, R. J. Dubos, *J. Biol. Chem.* **1940**, *14*, 65–78.

[121] A. S. Bourinbaiar, S. Lee-Huang, *Contraception* **1994**, *49*, 131–137.

[122] N. Sarkar, D. Langley, H. Paulus, *Proc. Natl. Acad. Sci. USA* **1977**, *74*, 1478–1482.

[123] D. A. Kelkar, A. Chattopadhyay, *Biochim. Biophys. Acta* **2007**, *1768*, 2011–2025.

[124] S. Weinstein, B. A. Wallace, J. S. Morrow, W. R. Veatch, *J. Mol. Biol.* **1980**, *143*, 1–19.

[125] D. W. Urry, *Proc. Natl. Acad. Sci. USA* **1972**, *68*, 672–676.

[126] W. R. Veatch, E. T. Fossel, E. R. Blout, *Biochemistry* **1974**, *13*, 5249–5256.

[127] S. V. Sychev, L. I. Barsukov, V. T. Ivanov, *Eur. Biophys. J.* **1993**, *22*, 279–288.

[128] B. A. Wallace, *Ann. Rev. Biophys. Biophys. Chem.* **1990**, *19*, 127–157.

[129] T. P. Galbraith, B. A. Wallace, *Faraday Discuss.* **1998**, *111*, 159–164.

[130] E. Bamberg, H. J. Apell, H. Alpes, *Proc. Nat. Acad. Sci. USA* **1977**, *74*, 2402–2406.

[131] G. Szabo, D. W. Urry, *Science* **1979**, *203*, 55–57.

[132] R. R. Ketchem, W. Hu, T. A. Cross, *Science* **1993**, *261*, 1457–1460.

[133] R. R. Ketchem, B. Roux, T. A. Cross, „Computantional refinement through solid state NMR and energy constraints of a membrane bound polypeptide“ in *Biological Membranes* (Eds.: K. J. Mertz, B. Roux), Birkhauser Press, **1996**, pp. 299–322.

[134] V. B. Myers, D. A. Haydon, *Biochim. Biophys. Acta* **1972**, *274*, 313–322.

[135] F. Hofmeister, *Arch. Exp. Pathol. Pharmacol.* **1888**, *24*, 247–260.

[136] Y. Zhang, P. S. Cremer, *Curr. Opin. Chem. Biol.* **2006**, *10*, 658–663.

[137] D. D. Busath, *Annu. Rev. Physiol.* **1993**, *55*, 473–501.

[138] D. W. Urry, *Bull. Mag. Res.* **1987**, *9*, 109–131.

[139] D. W. Urry, K. U. Prasad, T. L. Trapane, *Proc. Natl. Acad. Sci. USA* **1982**, *79*, 390–394.

[140] M. Bayrhuber, T. Meins, M. Habeck, S. Becker, K. Giller, S. Villinger, C. Vonrhein, C. Griesinger, M. Zweckstetter, K. Zeth, *Proc. Natl. Acad. Sci. USA* **2008**, *105*, 15370–15375.

[141] D. Brdiczka, *Biochim. Biophys. Acta* **1991**, *3*, 291–312.

[142] R. Benz, *Biochim. Biophys. Acta* **1994**, *1197*, 167–196.

[143] R. Ujwal, P. Ping, J. Zhang, G. Mercado, T. M. Vondriska, H. R. Kabeck, J. Abramson, *J. Fed. Am. Soc. Exp. Biol.* **2008**, *20*, LB17–LB18.

[144] S. Hiller, R. Garces, T. Malia, V. Orekhov, M. Colombini, G. Wagner, *Science* **2008**, *321*, 1206–1210.

[145] M. Colombini, *Mol. Cell. Biochem.* **2004**, *256-257*, 107–115.

[146] B. M. McDonald, M. M. Wydro, R. N. Lightowlers, J. H. Lakey, *FEBS Lett.* **2009**, *583*, 739–742.

[147] R. Ujwal, D. Cascio, V. Chaptal, P. Ping, J. Abramson, *Channels* **2009**, *3:3*, 167–170.

[148] L. Thomas, E. Blachyl-Dyson, M. Colombini, M. Forte, *Proc. Natl. Acad. Sci. USA* **1993**, *90*, 5446–5449.

[149] O. Teijido, R. Ujwal, C.-O. Hillerdal, L. Kullman, T. K. Restovtseva, J. Abramson, *J. Biol. Chem.* **2012**, *287*, 11437–11445.

[150] R. Schneider, M. Etzkorn, K. Giller, V. Daebel, J. Eisfeld, M. Zweckstetter, C. Griesinger, S. Becker, , A. Lange, *Angew. Chem. Int. Ed.* **2010**, *49*, 1882–1885.

[151] H. Abrecht, E. Goormaghtigh, J.-M. Ruysschaert, F. Homblé, *J. Biol. Chem.* **2000**, *275*, 40992–40999.

[152] H. Engelhardt, T. Meins, M. Poynor, V. Adams, S. Nussberger, W. Welte, K. Zeth, *J. Membr. Biol.* **2007**, *216*, 93–105.

[153] H. Miyake, S. Ye, M. Osawa, *Langmuir* **2002**, *4*, 973–977.

[154] S. Trasatti, O. Petrii, *Pure & Appl. Chem.* **1991**, *63*, 711–734.

[155] C. D. Bain, H. A. Biebuyck, G. M. Whitesides, *J. Am. Chem. Soc.* **1989**, *111*, 7164–7175.

[156] A. V. Hill, *J. Physiol.* **1910**, *40*, iv–vii.

[157] N. N. Daskalakis, S. D. Evans, L. J. C. Jeuken, *Electrochim. Acta* **2011**, *56*, 10398–10405.

[158] A. T. A. Jenkins, T. Neumann, A. Offenhäusser, *Langmuir* **2001**, *17*, 265–267.

[159] Y. Chen, B. A. Wallace, *Biophys. J.* **1996**, *71*, 163–170.

[160] T. Laredo, J. R. Dutcher, J. Lipkowski, *Langmuir* **2011**, *27*, 10072–10087.

[161] G. A. Olah, H. W. Huang, W. H. Liu, Y. L. Wu, *J. Mol. Biol.* **1991**, *218*, 847–858.

[162] T. Bastug, S. Kuyucak, *J. Chem. Phys.* **2007**, *126*, 105103.

[163] A. Cordomì, O. Edholm, J. J. Perez, *J. Phys. Chem. B* **2008**, *112*, 1397–1408.

[164] R. Vacha, S. W. I. Siu, M. Petrov, R. A. Böckmann, J. Barucha-Kraszewska, P. Jurkiewicz, M. Hof, P. Jungwirth, *J. Phys. Chem. A* **2009**, *113*, 7235–7243.

Acknowledgements

Mein besonderer Dank gilt folgenden Personen, die mich während dieser Zeit unterstützt haben:

- Prof. Dr. Peter Hildebrandt für die Betreuung und Unterstützung. Vielen Dank für die bereitgestellten Möglichkeiten und die Hilfe während der Doktorarbeit.
- Prof. Dr. Claudia Steinem und Conrad Weichbrodt für die nette und fruchtbare Zusammenarbeit, die Unterstützung auf dem Gebiet der Bilayer sowie die Bereitstellung des CPEO3, der gA- und der hVDAC-Proben.
- Dr. Diego Millo für die Betreuung und die Zusammenarbeit im Labor und auf den Gitarren in der "Hilde-Band".
- Dr. Inez Weidinger für die Zusammenarbeit, Betreuung und das stets offene Ohr.
- Dr. Uwe Kuhlmann und Dr. Ingo Zebger für die Hilfe mit Spektrometern.
- Dr. Lars Jeuken für die Hilfe bei der Auswertung der Impedanzdaten.
- Claudia Schulz für Ihre nette Hilfe im Labor.
- Jürgen Krauss, Dr. Hendrik Naumann und Lars Paasche für die Hilfe bei technischen Problemen.
- Nina Heidary und Hoang Khoa Ly für die nette Zusammenarbeit und die gegenseitige psychologische Unterstützung.
- Murat Sezer für die nette Zusammenarbeit und die interessanten Geschichten.
- Francisco Velazquez-Escobar für die nette gemeinsame Zeit im Studium und während der Doktorarbeit.
- Marina Böttcher für die Hilfe bei organisatorischen Angelegenheiten.
- Sara Bruun, Prof. Dr. Thomas Friedrich, Kirstin Hobiger, Marius Horch, Anke Keidel, Dr. Friedhelm Lendzian, Wiebke Meister, Nobert Michael, Prof. Dr. Maria Andrea Mroginski, Yvonne Rippers, Johannes Salewski, Matthias Schenderlein, Gal Schkolnik, Elisabeth Siebert, Dr. Arumugam Sivanesan, Tillmann Utesch und allen weiteren Mitgliedern des Max-Volmer Laboratoriums für die angenehme Arbeitsatmosphäre.
- Dem EPC-Team für erfolgreiche Zusammenarbeit in der Lehre.
- Prof. Dr. Maria Rosa Moncelli und Dr. Serena Smeazzetto für die Betreuung beim Aufbau meiner ersten BLMs.
- Meinen Schullehrern Ralph-Dieter Feigel, Arnim Schmidt und Sven-Erek Schramm für die Einführung in die Naturwissenschaften sowie Sigrid Schmidt für die dafür nötigen Grundlagen.
- Prof. Dr. Reinhard Schomäcker und Dr. Jean-Philippe Lonjaret für die Betreuung bei der BIG-NSE sowie Bartek Krawczyk, Jan Laudenbach, Xiao Xie und allen weiteren Mitgliedern der BIG-NSE.
- Swantje Wiebalck für den Halt während des Zusammenschreibens.

Mein herzlichster Dank gilt meiner Familie, besonders meinen Eltern, die mir das Studium ermöglichten und mich bei allem unterstützten.

Selbständigkeitserklärung

Die selbstständige und eigenhändige Anfertigung dieser Arbeit versichere ich an Eides statt.

Jacek Kozuch

Berlin, 24.09.2012